WCRP REPORT
World Climate Research Programme

WMO | IOC | ICSU International Council for Science

Global Energy and Water Cycle Experiment

GEWEX
WCRP

Assessment of Global Cloud Data Sets from Satellites

A Project of the World Climate Research Programme
Global Energy and Water Cycle Experiment (GEWEX)
Radiation Panel

Lead Authors:

Claudia Stubenrauch
Laboratoire de Météorologie Dynamique IPSL/CNRS, France

William Rossow
CREST Institute at City College of New York, USA

Stefan Kinne
Max Planck Institute for Meteorology, Hamburg, Germany

November 2012

WCRP Report No. 23/2012

Foreword

The charge given by the then GEWEX Radiation Panel (GRP) to the Cloud Assessment Working Group was to evaluate the overall quality of available, global, long-term cloud data products, including the ISCCP product that has been adopted by GEWEX as its standard product for clouds. The need of periodic assessments is obvious. Climate change requires long term, consistent data products while sensors technology is constantly being improved and re-invented. As such, it is imperative that the long-term products be compared with more recent state of the art products to assess not only their fidelity, but their quality in light of increasingly accurate measurements. Absolute quality, unfortunately, is often very difficult to assess with cloud products for which there are few in-situ measurements. Instead, a more appropriate question is often whether or nor a specific cloud product is accurate enough to meet a specific application. As such, the Cloud Assessment Working Group was further asked to go beyond simple product comparisons at fixed space and time resolutions to provide expert insight into their findings. We hope that this insight is useful for those contemplating the suitability of specific products for their own applications. While all the assessed products are covered, special emphasis was placed on the ISCCP product. As the standard GEWEX product, the panel specifically asked if it meets the panel goals for understanding the variability and trends in the regional and global water and energy budgets. We think the Assessment has met the overall objectives given to the team. This formal evaluation and insight will become increasingly important as the panel, which has been renamed as the GEWEX Data and Assessments Panel (GDAP) undertakes the important step of bringing together the diverse Water and Energy variables to produce a single "Integrated Water and Energy" product designed to not only assess the state of current closure of the water and energy budgets, but to provide a simple tool to explore the co-variance of the key water and energy parameters. The work of the previous Chair of this panel, Dr. William Rossow of The City University of New York, who began this activity, Dr. Claudia Stubenrauch of CNRS / IPSL Laboratoire de Meteorologie Dynamique, who led the effort, and all those who contributed to this successful assessment are of course greatly appreciated and acknowledged.

Christian Kummerow, Chair, GEWEX Data and Assessments Panel

Table of Contents

Appendices

W.B. Rossow
    1.1.1.1 Measurements
    1.1.1.2 Cloud Detection
    1.1.1.3 Retrieval
    1.1.1.4 Standard Products and Characteristics of GEWEX-Archived Version
    1.1.1.5 Uncertainty Estimates

A. Heidinger, A. Walther, M. Foster
    1.1.2.1 Measurements
    1.1.2.2 Cloud Detection
    1.1.2.3 Retrieval
    1.1.2.4 Standard Products and Characteristics of GEWEX-Archived Version
    1.1.2.5 Uncertainty Estimates

P. Menzel, D. Wylie, E. Olson, B. Baum
    1.1.3.1.1 Measurements
    1.1.3.1.2 Cloud Detection
    1.1.3.1.3 Retrieval
    1.1.3.1.4 Standard Products and Characteristics of GEWEX-Archived Version
    1.1.3.1.5 Uncertainty Estimates

C.J. Stubenrauch
    1.1.3.2.1 Measurements
    1.1.3.2.2 Cloud Detection
    1.1.3.2.3 Retrieval
    1.1.3.2.4 Standard Products and Characteristics of GEWEX-Archived Version
    1.1.3.2.5 Uncertainty Estimates

S. Ackerman, S. Platnick, B. Maddux, R. Pincus
    1.2.1.1.1 Cloud Detection
    1.2.1.1.2 Retrieval
    1.2.1.1.3 Standard Products and Characteristics of GEWEX-Archived Version
    1.2.1.1.4 Uncertainty Estimates

Executive Summary

Objective:

Clouds cover about 70% of the earth's surface and play a dominant role in the *energy and water cycle* of our planet. Only satellite observations provide a continuous survey of the state of the atmosphere over the whole globe, at space-time scales at which cloud processes occur. Satellite cloud data records now exceed more than 25 years in length. While not as long as records from human observers, satellites provide the only globally complete data record at spatial and temporal scales consistent with cloud processes (approximately 3 hr, 25 km). The International Satellite Cloud Climatology Project (ISCCP), which is the GEWEX cloud project, uses multi-spectral imager data from a combination of polar orbiting and geostationary weather satellites to achieve the necessary sampling. During the past decade, other global cloud data records have been established from various instruments, mostly onboard polar orbiting satellites. New sensors such as MODIS, POLDER, CALIPSO and CloudSat have expanded cloud measurement capabilities. It is imperative that the longer time series products such as ISCCP be compared to recent intruments to assess the accuracy and error sources relevant for climate studies and for evaluation of general circulation models (GCM). In 2005, the GEWEX Radiation Panel (GRP, now GEWEX Data and Assessments Panel) initiated the GEWEX Cloud Assessment to intercompare these cloud data with ISCCP. The GEWEX Cloud Assessment was focused on the intercomparison of global Level-3 (L3) cloud products (gridded, monthly statistics), retrieved from measurements of ***multi-spectral imagers*** (ISCCP, PATMOS-x, MODIS-ST, MODIS-CE), ***multi-angle multi-spectral imagers*** (ATSR-GRAPE, MISR, POLDER, the latter also using polarization), ***IR sounders*** (HIRS-NOAA, TOVS Path-B, AIRS-LMD) and ***active lidar*** (CALIPSO-ST, CALIPSO-GOCCP). Cloud properties under study include cloud amount (fractional cloud cover), cloud height (in terms of pressure, temperature or altitude), cloud radiative properties (visible optical depth or infrared emissivity), cloud thermodynamic phase (liquid or ice) and bulk microphysical properties (effective particle size and water path).

Conclusions, Recommendations and Outlook:

Discussions during four workshops led to the creation of the GEWEX Cloud Assessment L3 database, in common format and available at ***http://climserv.ipsl.polytechnique.fr/gewexca/***, allowing for the first time an inter-comparison of L3 cloud essential climate variables (ECVs) of twelve 'state of the art' data sets. In addition to self-assessments (summarized in Annex I), which show the maturity of the various data sets, the analyses have shown how cloud properties are perceived by instruments measuring different parts of the electromagnetic spectrum and how their averages and distributions are affected by instrument choice as well as some methodological decisions. *These satellite cloud products are very valuable for climate studies or model evaluation*: even if absolute values, especially those of high-level cloud statistics depend on instrument (or retrieval) performance to detect and/or identify thin cirrus, relative geographical and seasonal variations in the cloud properties agree very well (with only a few exceptions like over deserts and snow-covered regions). Probability density functions of optical and bulk microphysical properties also agree well, when one considers retrieval filtering or possible biases due to partly cloudy samples and to ice-water misidentification. The study of long-term variations with these data sets requires consideration of many factors, which have to be carefully investigated before attributing any detected trends to climate change. This database will facilitate future assessments, climate studies and the evaluation of climate models. ISCCP cloud properties have also been assessed during the GEWEX Assessment of Global Radiative Flux Data Sets, revealing excellent quantitative agreement between fluxes.

Coordinated comparison of satellite derived cloud ECVs continues with the Cloud Retrieval Evaluation Workshop (CREW, initiated by EUMETSAT), focusing on detailed L2 data comparisons over limited areas and time periods, and within the ESA Climate Change Initiative.

Key Results:

Important Considerations for the Interpretation of Satellite Retrievals

The use of different spectral domains was identified as the main reason for discrepancies in retrieved cloud properties: Systematic biases in the retrieved cloud properties depend on the instrument (electromagnetic part of the spectrum used) and on the cloud scene. Differences in average cloud properties, especially in high-level cloud amount, are mostly explained by instrument performance to identify thin cirrus, especially when overlying low-level clouds. These cases make out about <20% of all cloudy cases, according to the lidar of the CALIPSO mission. Active lidar measurements, IR sounding and methods using IR spectral radiance differences allow determination of the properties of the semi-transparent cirrus (with decreasing performance from the former to the latter), whereas reflected solar radiation (during daytime) is more influenced by the properties of the low-level clouds underneath.

The 'radiative' height of a cloud with diffuse cloud top (optical depth slowly increasing from the top downward over a considerable vertical extent) may lie a few kilometres below the physical cloud top. According to an analysis of ISCCP and limb-viewing observations of the Stratospheric Aerosol Gas Experiment (SAGE) (Liao et al. 1995), almost 70% of the high-level clouds in the tropics have a diffuse cloud top, leading to an average positive bias of ISCCP in cloud top pressure of about 150 hPa. At higher latitudes, only 30 - 40% of the high-level clouds are in this category, leading to an average positive bias of about 50 hPa.

Total Cloud Amount

- Global total cloud amount (fractional cloud cover) is about 0.68 (±0.03), when considering clouds with optical depth > 0.1. The value increases to 0.74 when considering clouds with optical depth < 0.01 (e.g., CALIPSO) and decreases to about 0.56 when clouds with optical depth > 2 are considered (e.g., POLDER).
- According to most data sets, there is about 0.10 – 0.15 more cloudiness over ocean than over land. HIRS-NOAA and MISR detect a difference of 0.30, which can be attributed to uncertainties in cloud detection over land (low-level clouds for HIRS and thin cirrus for MISR) and to poor diurnal sampling at only 10:30 AM local time for MISR.

Cloud Height

- Cloud top height can be accurately determined with lidar (e.g., CALIPSO).
- Apart from the MISR stereoscopic height retrieval for optically thick clouds, passive remote sensing provides a 'radiative height'. It was found that the 'radiative cloud height' may lie as much as a few kilometers below the 'physical height' of the cloud top, depending on the cloud extinction profile and vertical extent. Especially high-level clouds in the tropics have such 'diffusive' cloud tops, for which retrieved cloud top temperature may be up to 10 K larger than cloud top temperature.
- In general, the 'radiative height' lies near the middle between cloud top and 'apparent' cloud base (for optically thick clouds height at which the cloud reaches an optical depth of 3). When cloud height is determined via O_2 absorption (e.g., POLDER), it corresponds to a location even deeper inside the cloud.
- Global uncertainties in retrieved cloud pressure are estimated to 100 hPa for ISCCP, compared to about 50 hPa for IR sounding.
- During night, ISCCP may misidentify thin cirrus as mid-level cloud, because only one IR radiance is measured, leading to a positive bias of about 75 hPa, in comparison with IR sounder retrievals.

Height-Stratified Cloud Amount

Clouds in all data sets are vertically stratified according to their pressure into high-level, mid-level and low-level clouds. Separation levels are at 440 hPa and 680 hPa (corresponding to altitudes of about 6 km

and 3 km, respectively). We consider height-stratified cloud amounts relative to total amount, because these values are less influenced by differences in cloud detection.

- About 42% of all clouds are high-level clouds with optical depth > 0.1. The value increases to 50% when including subvisible cirrus, and it decreases to 20% when considering clouds with optical depth > 2.
- About 16% (±5%) of all clouds correspond to mid-level clouds with no other clouds above. Values from ISCCP are 27% (day: IR and VIS information) and 40% (day and night: night only one IR channel), respectively. These biases are due to semi-transparent cirrus overlying low-level clouds during day and in addition due to semi-transparent cirrus during night.
- According to the majority of data sets, about 42% (±5%) of all clouds are single-layer low-level clouds. Outliers are HIRS-NOAA with 26% (only one IR channel for low-level clouds) and MODIS-ST with 53% (misidentification of optically thin cirrus).
- When including low-level clouds underneath semi-transparent higher lying clouds (considering CALIPSO and MISR results), about 60% of all clouds correspond to low-level clouds.
- Most data sets show similar latitudinal variations in total and height-stratified cloud amount. Exceptions are polar latitudes and relative low-level cloud amount from HIRS-NOAA (underestimation of low-level clouds with minimal thermal contrast).
- Geographical maps show some differences in total cloud amount over deserts and land areas which may be linked to aerosols.
- Regional anomalies (difference between regional averages and global average cloud properties) agree better between the data sets than regional absolute values. The spread in regional cloud amount anomaly is less than 0.10 and in relative high-level cloud amount anomaly varies between 10 to 20% (polar regions and regions with frequent cirrus).
- Most data sets agree on the seasonal cycle. In general, seasonal variations are smaller than latitudinal variations, except for the transition of the InterTropical Convergence Zone (ITCZ). The seasonal cycle is generally larger over land than over ocean.

Effective Cloud Amount

- Global effective cloud amount (cloud amount weighted by cloud emissivity) is about 0.50 (±0.05).
- Global effective cloud amount of high-level clouds (0.15) is very similar for the different data sets, because a smaller cloud amount due to missing optically thin clouds is compensated by a larger average cloud emissivity.

Cloud Optical Properties

Cloud optical depth is in general determined from reflectances in the solar spectrum and therefore only available during daytime conditions.

- The data sets provide global average cloud optical depth between 4 and 9. However, given that the global mean cloud amount is larger than 0.65, we know that the average cloud optical depth has to be smaller than 5 to give a consistent planetary albedo.
- Probability density functions of cloud optical depth agree for cloud optical depth between 1 and 10. The relative contributions outside this range (< 1 and > 10) essentially reflect differences in retrieval filtering and limits (< 10) due to conversion from cloud emissivity.
- The transition of the ITCZ is reflected in the seasonal cycle of ice cloud optical depth, with larger optical depth when more high-level clouds are present (except for PATMOS-x which shows the opposite behaviour).

Bulk Cloud Microphysical Properties

Remote sensing determines an effective particle size by assuming particle shape and size distribution within the cloud. The height contributions in the retrieval of the effective particle size depend on the absorbing spectral band used: in general, absorption increases with increasing wavelength. However, with increasing cloud optical depth the retrieved particle size corresponds more and more to particles near the cloud top, leading typically to overestimates for liquid clouds and underestimates for ice clouds.

- Global effective droplet radius of liquid clouds is about 14 μm (±1 μm).
- Global effective ice crystal radius of high-level ice clouds is about 25 μm (±2 μm).
- Effective cloud droplet radii are on average about 15–20% larger over ocean than over continents, whereas the difference in effective ice crystal radius is only about 5%.
- Global cloud water path varies from 30 to 60 gm^{-2} for liquid clouds and from 60 to 120 gm^{-2} for clouds with ice tops. Retrieval filtering of ice clouds leads to smaller (25 gm^{-2} for semi-transparent cirrus) or larger values (225 gm^{-2} for clouds with optical depth larger than 1) of average cloud water path.
- Differences in probablility density functions have been identified due to thermodynamical phase misidentification (leading to larger droplet radii or smaller ice crystal radii, respectively), partly cloudy samples (leading to slightly smaller particle sizes and water path) and retrieval filtering.
- Seasonal cycles of water path are similar to those of optical depth, with smaller relative amplitudes. Seasonal cycles of effective particle sizes are in general small and have to be considered with care, because they may be affected by misidentification of thermodynamical phase.

Diurnal Variation

Most notable features of the diurnal cycle of clouds, revealed by ISCCP (and TOVS Path-B), have been summarized in the report, but the Cloud Assessment was mainly focused on averages and longer-term variations. We have therefore investigated how diurnal variations may affect these results. Three of the twelve cloud data sets change their method in cloud detection between day and night (ISCCP, PATMOS-x and MODIS-CE) and three only sample daylight conditions (MISR, POLDER and ATSR-GRAPE).

- Day – night differences and daytime sampling differences among data sets with no change in method (IR sounders and lidar) reflect random differences of a few percent.
- CALIPSO seems to have a slightly smaller detection sensitivity of optically thin cirrus during day (5 - 10% in relative high-level cloud amount over tropical land), linked to solar radiance noise.
- Day – night differences for original ISCCP products correspond to 5 – 10% in total cloud amount over land and approach 25% in relative high-level cloud amount in the tropics. However, adjustments in the distributed ISCCP monthly products reduce the magnitude of this difference.

Longterm Variations

- Global interannual variability lies between 2 - 3% in cloud amount, 2.5 - 3.5% in relative high-level / low-level cloud amount and 2 K in cloud temperature.
- Larger interannual variability (5%) is found for data sets with smaller instantaneous sampling coverage (ATSR and MISR) and for data sets characterized by larger retrieval noise due to coarse spatial resolution (100 km for TOVS Path-B).
- The most prominent feature in regional interannual variability seems to be linked to the El Niño Southern Oscillation (about 10% in relative high-level cloud amount).
- ISCCP exhibits a slow variation over the time period (1984 to 2008) that is not reflected in any other data set (with coarser time sampling). Detailed investigations (Annex 2) show that spurious changes in calibration and sampling do affect the magnitude but do not eliminate this slow variation.
- At present, one can only conclude that global monthly mean cloud amount is constant over the last 25 years to within 2.5%, within the range of interannual variability.

1. Introduction

1.1 Satellite Remote Sensing of Cloud Properties

Only satellite observations are capable of providing a continuous synoptic survey of the state of the atmosphere over the whole globe. Operational weather satellite sensors provide time records extending for at least 30 years.

Cloud sensors are deployed on *polar-orbiting and geostationary satellites*. Polar-orbiting sensors with cross-track scanning capabilities provide global coverage with one daytime (at a particular local time) and one nighttime overpass (12 hours later). Geostationary satellites are placed at particular longitudes along the equator, covering about 100° in longitude and in latitude. Sensors aboard these satellites permit high frequency temporal sampling (15 minute to 3 hour intervals for whole Earth images).

The relevant satellite sensors measure radiation scattered or emitted by the earth's surface, atmosphere and clouds. To maximize the sensitivity to the presence of clouds and to determine key cloud properties, specific spectral domains are selected. The conversion of the measured radiances into cloud properties requires two steps:

- Cloud detection (or scene identification)
- Cloud property retrieval, based on radiative transfer and employing ancillary data to isolate the cloud from surface and atmospheric contributions

Cloud signatures are generally larger reflectances at solar wavelengths and smaller infrared radiances (lower brightness temperatures) compared to clear sky. Cloudy scenes also generally exhibit larger spatial and temporal variability than cloud-free (clear) scenes. However, difficulties in detecting clouds may arise when the radiance contrast between cloudy and clear scenes is small (e.g. clouds over already highly solar reflecting surfaces such as snow or ice, clouds with small thermal contrast to the surface below as for low-level clouds, or cloud edges) or when clear-scene variability is larger than usual (e.g. optically thin clouds over land areas or clouds over winter land areas).

1.1.1 Satellite Sensors

Multi-spectral imagers are radiometers that make measurements at usually only a few discrete wavelengths, usually from the solar to thermal infrared spectrum. Nadir viewing with cross-track scanning capabilities, they have a spatial resolution from about 0.5 to 7 km (at nadir) and are the only sensors aboard geostationary weather satellites. The International Satellite Cloud Climatology Project (ISCCP) uses a combination of these sensors from both, geostationary and polar orbiting satellites. Multi-spectral imagers aboard polar orbiting satellites are the Advanced Very High Resolution Radiometer (AVHRR, with 5 spectral channels) and the MODerate resolution Imaging Spectroradiometer (MODIS with 36 spectral channels).

Multi-angle, multi-spectral imagers make measurements of the same scene with different viewing angles, allowing a *stereoscopic retrieval of cloud top height*. Together with the use of *polarization* the *cloud thermodynamic phase* can be determined (since non-spherical ice particles depolarize the reflected light less than liquid droplets). The Cloud Assessment database includes data sets derived from the Multi-angle Imaging SpectroRadiometer (MISR, with 4 solar spectral channels and 9 views) and a sensor using POLarization and Directionality of the Earth's Reflectances (POLDER, with 8 solar sub-spectral channels (3 polarized) and up to 16 views), both operating only during daylight conditions. Results from the Along Track Scanning Radiometer (ATSR, with 7 channels exploring solar to thermal infrared spectrum and 2 views) are provided only for daylight, but a stereoscopic retrieval is not yet developed.

IR sounders, originally designed for the retrieval of atmospheric temperature and humidity profiles, use IR channels in absorption bands of CO_2, water vapor and ozone. Measured radiances near the centre

of the CO_2 absorption band are only sensitive to the upper atmosphere while radiances from the wing of the band stem from successively lower levels in the atmosphere. The operational High resolution Infrared Radiation Sounder (HIRS, with 19 channels in the IR) is a multi-channel radiometer, whereas the Atmospheric Infrared Sounder (AIRS) and Infrared Atmospheric Sounding Interferometer (IASI) are infrared spectrometers. Their spatial resolution is only about 15 km (at nadir). Several MODIS channels are similar to those of HIRS. This allows for a similar analysis as HIRS. The *good spectral resolution* of these IR sounding instruments allows a *reliable identification of cirrus* (semi-transparent ice clouds), *day and night*. Sounder systems usually include **microwave sounders** (Microwave Sounding Unit, MSU, and Advanced Microwave Sounding Unit, AMSU) as well. Because these instruments operate at wavelengths insensitive to clouds (sensitive to precipitation, however), they are also used in the retrieval of atmospheric profiles and may be used for *cloud detection* (by predicting IR clear sky radiances).

Limb sounders, such as the spectrometer of the Stratospheric Aerosol Gas Experiment (SAGE) that measures the solar occultation along the earth's limb at 4 solar wavelengths, provide *good vertical resolution* (1 km) at the expense of a low horizontal resolution along the viewing path (about 200 km). On the other hand, the *long path* leads to detection of *subvisible (very thin) cirrus*.

Passive microwave imagers, like the Special Sensor Microwave Imager (SSM/I) and the Advanced Microwave Sounding Radiometer-EOS (AMSR-E), make use of spectral features sensitive to water vapour and liquid water to estimate *cloud liquid water path over ocean* (especially if precipitation and drizzle contamination are removed). These measurements are also sensitive to precipitation-sized ice particles.

Active sensors extend the measurements of passive radiometers to cloud vertical profiles. Since 2006 the CALIPSO lidar and CloudSat radar, together, determine cloud top and base heights of all cloud layers. Whereas the *lidar* is *highly sensitive* and can even detect *sub-visible cirrus*, its beam reaches cloud base only for clouds with an optical depth less than 3. When the optical depth is larger, the radar is still capable to provide a cloud base location. However, its signal needs an optical depth greater than about 0.1 to detect a cloud (Stephens *et al.* 2002). Even though the nadir-pointing, active instruments have poor global sampling, the *synergy with the passive instruments* participating in the A-Train satellite formation (MODIS, AIRS and POLDER) can be used to better study the v*ertical structure of different cloud types*.

In general, ***passive remote sensing provides cloud properties as observed from above***. CALIPSO data in the GEWEX Cloud Assessment database have been produced in a similar way for a better comparison: only the uppermost cloud layer is kept in the case of multi-layered clouds.

1.1.2 Cloud Properties

Cloud properties that can be inferred from these measurements include:

Cloud amount (or fractional cloud cover, CA) is usually the ratio between the number of samples (pixels) that contain cloud and the number of all measurement samples. Methods may be developed, especially for large instrument footprints that scale the within-pixel cloud amount by radiance value or heterogeneity (cf. Rossow *et al.* 1993 and references within). How instrument resolution (footprint size) affects the estimate of cloud amount has already been studied by Wielicki and Parker (1992) and Rossow *et al.* (1993): one would expect an increase in cloud amount by decreasing the spatial resolution (with the same detection sensitivity), especially in the case of low-level clouds which appear to be broken and more variable at smaller scales than upper-level clouds. However, the *total cloud amount* determined by a particular instrument also *depends on the sensitivity of its measurements to the presence of clouds.*

Differences in detection sensitivity also appear as differences in the average radiative properties: less sensitive instruments will detect fewer optically thin clouds (low visible radiance contrast) so that average cloud optical depth will be larger, or they will detect fewer low-level clouds (low IR radiance contrast) so that average cloud temperature will be smaller.

Cloud top location can be indicated by cloud top temperature (CT), pressure (CP) or height (CZ) above topography or above mean sea level.

- Lidars and instruments that use stereoscopic views (e.g. CALIPSO, MISR) measure the cloud top height.
- Most sensors measuring atmospheric IR window radiances directly retrieve cloud top temperature, when clouds act as blackbody emitters (especially low-level clouds). For semi-transparent clouds the retrieved cloud temperature is biased high because of the atmospheric and surface radiation passing through these clouds and needs to be corrected, in general by using information on the cloud optical depth or emissivity.
- *When the cloud top is diffuse* – meaning that the optical depth does not increase from the top downward from zero to a large value in a very small vertical extent, the *radiometric top does not coincide with the physical top* (especially for high-level clouds, *cf*. Liao *et al*. 1995, Wang *et al*. 1999, Sherwood *et al*. 2004).
- Alternate methods to determine the cloud top location involve differential measurements in strong absorption bands (CO_2 or O_2). These methods determine cloud pressure (CP). Whereas the sounding of the thermal CO_2 absorption band leads to a pressure corresponding to the radiometric top, the use of the solar O_2 absorption band indicates the middle of the cloud.
- The conversion among CT, CP and CZ requires ancillary information on the atmospheric temperature (and water vapour) profiles and introduces additional uncertainties (especially when the profiles do not resolve temperature inversions near the planetary boundary layer).

Cloud optical depth (COD) is usually retrieved from non-absorbing solar reflectances ($0.5 - 0.9$ μm). This optical method is most precise for COD values between 1 and 100.

Cloud emissivity (CEM) is retrieved at thermal wavelengths, leading to values between 0 and 1. Thermal wavelengths are more sensitive to optically thin cirrus than solar wavelengths. The conversion of CEM to COD (by the approximate formula $-2\,x\,\ln(1\text{-}CEM)$) depends on the spatial resolution, the heterogeneity of the scene, and the microphysics. However, one has to keep in mind that the converted COD is limited to a value ≤ 10.

Cloud effective particle radius (CRE) is inferred from spectral dependencies in absorption and scattering, by assuming particle shape and size distribution within the cloud. Whereas optical methods determine CRE for all clouds, in the case of optically thick clouds CRE only relates to the upper part of the cloud. This may introduce CRE biases (typically, overestimates for liquid clouds and underestimates for ice clouds). The different height contributions of CRE depend on the absorbing spectral band used in the retrieval: in general, absorption increases with increasing wavelength. IR Sounders provide estimates of CRE only for semi-transparent cirrus ($0.2 < CEM < 0.85$), but in this case CRE corresponds to an average over the whole cloud depth.

Cloud water path (CWP) can be estimated from COD if CRE is known. Whereas ISCCP assumes values for CRE, other methods retrieve CRE and COD together, the latter method providing a better estimate. As already indicated, the retrieved CRE is not representative for the entire cloud when the cloud is optically thick. This may introduce CWP biases (typically, overestimates for adiabatic liquid clouds and underestimates for ice clouds).

Table 1.1 summarizes the main characteristics of the cloud property retrievals (including spectral domain, spatial resolution, retrieval method as well as ancillary data) leading to the twelve data sets that participated in the GEWEX Cloud Assessment. Different instruments may need different retrieval techniques. The Cloud Assessment also includes cloud products obtained from the same satellite instruments, but by using different retrieval methods. The detailed retrieval descriptions are provided in Appendix 1.
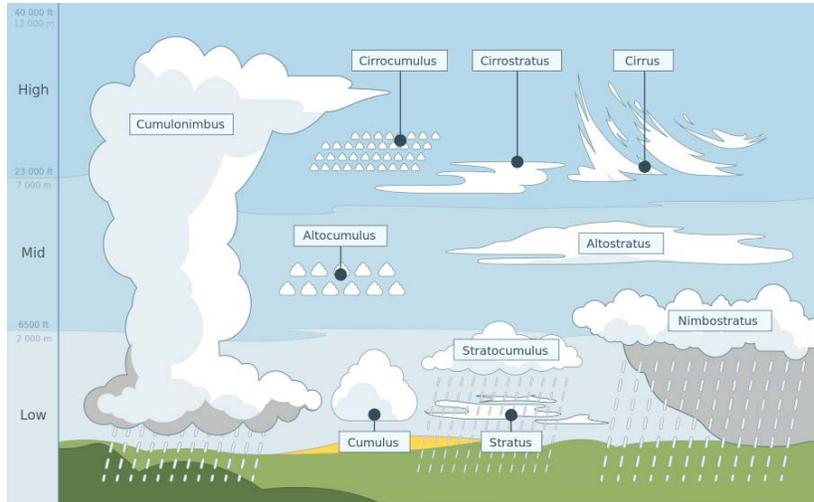
Figure 1.1: Illustration of cloud types distinguished by height and morphology, as initially classified by surface observers (Image credit: Valentin de Bruyn).

Figure 1.1 illustrates cloud types distinguished by height and shape, as initially classified by surface observers. ISCCP adapted this cloud type classification by using pressure and optical depth (Rossow and Schiffer, 1991; Rossow and Schiffer, 1999), leading to nine cloud types presented in Figure 1.2. This cloud type classification provides an approximate link between satellite-measured optical properties and the classical morphological cloud types (Hahn et al., 2001).

Figure 1.2: ISCCP cloud type classification according to cloud pressure and cloud optical depth.

1.2 Possible Retrieval Uncertainties and Biases

Cloud property uncertainties and biases depend on the cloud scene, identified by cloud type and cloud layering:

- **Low-level clouds underneath optically thick high-level or mid-level clouds are not detected by the instruments employed in this assessment.** Hence, the retrieved cloud properties correspond to those of the uppermost layer. Low-level clouds for these cases can only be detected by active radar (CloudSat, Stephens et al., 2002).
- **Low-level clouds underneath optically thin cirrus**: The retrieved cloud properties correspond to those of the *uppermost layer* when using *active lidar, CO_2 sounding* or *IR spectral differences*, to those of a *mid-level* cloud when using *simultaneous IR and VIS information* (radiative mean between high-level and low-level cloud) and to those of the *low-level* clouds when using *solar information alone*.
- **Midlevel clouds underneath optically thin cirrus**: The retrieved cloud properties correspond to those of the *uppermost layer*. However, cloud height might be underestimated.
- **Single-layer low-level clouds:** All data sets should provide the properties of the low-level clouds, barring heterogeneity effects, though with more noise when only IR measurements are used, because the contrast with the surface is low.

16

- **Single-layer thin cirrus:** The distinction between thin cirrus and clear sky depends on instrument sensitivity: *active lidar* and *CO_2 sounding* readily detect this kind of *cirrus.* An IR spectral signature may also help to detect it, but with more noise. Multi-angle imagers using only the solar spectrum will miss thin cirrus. During night and when the optical depth is larger than the detection sensitivity, ISCCP, using the IR atmospheric window channel alone, detects but misidentifies semi-transparent cirrus as mid-level cloud.

Further sources of uncertainties and biases in these products may be related to:
- Ancillary data used to isolate the cloud from surface and atmospheric contributions, although not all cloud detection methods depend on ancillary data
- Differences in methods between daytime and nighttime
- Oblique viewing angles, leading to larger samples or larger atmospheric path lengths which changes detection sensitivity
- Diurnal sampling
- Retrieval selection (sub-sampling)
- Effects of partly cloudy samples
- Misidentification of thermodynamical phase
- Assumptions on cloud particles (shape and size distribution)

Data sets using observations only from sun-synchroneous satellites cannot be used directly to study cloud dynamics because their time sampling (at lower latitudes) is too infrequent to see the evolution of cloud systems. The ISCCP products are based on the whole constellation of weather satellites, both polar orbiting and geostationary, providing global coverage every 3 hours. Therefore the ISCCP products could be used to sort the other data sets by "cloud age" allowing for a statistical composite of cloud evolution (at least for larger-scale weather systems). Such a synergy provides the opportunity for more advanced analyses of cloud properties and dynamics.

1.3 GEWEX Cloud Assessment

The GEWEX Radiation Panel (GRP, now the GEWEX Data and Assessment Panel) initiated the GEWEX Cloud Assessment in 2005 to compare available, global, long-term cloud data products with ISCCP. The focus was on the comparison of Level-3 (L3) cloud products (gridded monthly statistics). Because the primary purpose of this assessment is to evaluate the ISCCP product, while also providing assessments of other available products on a voluntary basis, the ISCCP product is used as the reference for comparisons. However, the results of these comparisons, together with the self-assessments described in Annex I, provide a state-of-the-art summary of cloud observation accuracy that should prove useful for climate studies and climate model evaluations. All data products described in this report are publically available; detailed descriptions of the retrieval methods and products are provided in Appendix I, including discussion of advantages and limitations. We present comparisons of climatological averages as well as regional, seasonal and inter-annual variations. Explanations for differences among the various data sets are offered and a summary of best estimates of cloud properties provided.

Table 1.1: Summary of Cloud Property Retrieval Characteristics of the Datasets Participating in the GEWEX Cloud Assessment

Dataset	Spatial Resolution	Cloud Detection	Variables	Retrieval Method	Ancillary Input
ISCCP	5 km, 30 km (sampled) 100 km clear sky estimation	1 VIS 1 IR window + 1 NIR over ice time – space variances	COD, CT -> CP, CZ Phase (W/I) CWP CRE	TB(11µm)-> CT, VIS->COD, CT correction for COD<5 ice: CT < 260 K fct(COD, phase, fixed CRE) VIS/NIR LUT approach (0.6, 3.7 µm)	TOVS profiles (operational) rad transfer+particle model surf properties rad.transfer + particle model
PATMOS-x	1 km x 5 km	6 Bayesian classifiers derived from CALIPSO	CEM, CT -> CP Phase (W/I) COD, CRE CWP	Optimal Estimation (11,12µm) spectral differences LUT approach (0.6, 3.7 µm) CLWP=fct(CODW, CREW); CIWP=fct(CODI)	NCEP reanalysis profiles (V1) MODIS snow mask rad. transfer + particle model (mixed habits for ice)
HIRS-NOAA	17 km	1 IR, time – space variances	CP, CEM -> CT	CO_2 slicing for CP<650 hPa, TB(11µm)	NCEP reanalysis profiles (V1)
TOVSB	17 km (detection) 100 km (retrieval)	multi-spectral IR + MW clear sky estimation	CEM, CP -> CT, COD Phase (W/I) CREIH -> CIWPH	weighted χ^2 method on CO_2 channels, COD = −2ln(1-CEM) ice: CT < 230 K fct(CEM(8µm),CEM(11µm)), fct(CREIH,CEM(11µm))	TOVS profiles (TOVS Path B) spectral surf. emissivities rad.transfer + ice crystal model (aggregates)
MODIS-ST	1 km (detection, COD, CRE, CWP, phase) 5 km (CP, CT, CEM)	multi-spectral IR/NIR/VIS (16 channels) + time-space variances	CP, CEM -> CT Phase (W/I) COD, CRE CWP	CO_2 slicing for CP<650 hPa, TB(11µm) VIS/NIR/IR spectral differences LUT approach (0.7, 0.9, 1.2, 1.6 µm), (1.6, 2.1, 3.7 µm) fct(COD,phase, CRE)	NCEP GDAS profiles, 16day spectral surf. albedo climatology rad. transfer+particle model (mixed particle habits for ice)
MODIS-CE	1 km, 4 km (sampled) 32 km clear sky estimation	multi-spectral IR/NIR/VIS (5 channels similar to VIRS)	CEM, CT -> CZ, CP Phase, COD, CRE CWP	IR split-window; lapse rate (7.1 K/km) + T profile CT + LUT approach (0.6, 2.1µm), (3.8 µm) CWP=fct(COD,CRE,phase)	GEOS profiles rad. transfer+particle model (mixed habits for ice)
AIRS-LMD	14 km	spectral emissivity coherence (a posteriori)	CEM, CP -> CT, CZ, COD Phase (W/I) CREIH, CIWPH	weighted χ^2 method, virt. T profile for CZ, COD=−2ln(1-CEM) ice: CT < 230 K LUT approach on 6 spectral emissivities (9-12µm)	AIRS profiles (NASA, V5) spectral surf. emissivities (AIRS,MODIS) rad. transfer+ice crystal model (hex. columns, aggregates)
CALIPSO-ST	0.06 km x 0.34 km	lidar VIS backscatter horizontal averaging	CZ -> CT Phase (W/I)	cloud top, uppermost cloud layer (for GEWEX) ice: 532 nm depolarization	GMAO profiles
CALIPSO-GOCCP	0.48 km x 0.34 km	lidar VIS backscatter vertical averaging	CZ -> CT	cloud mean altitude, uppermost cloud layer (for GEWEX)	GMAO profiles
POLDER	6 km (detection) 20 km (retrieval)	multi-spectral+ angle VIS/NIR threshold tests	Phase (W/I), COD CP	VIS/NIR polarization, LUT approach O_2-A band (763,765 nm), Rayleigh (490, 865 nm)	rad. transfer+ particle model (inhom. hex. columns for ice)
MISR	1 km	multi-specral+angle VIS/NIR	CZ	stereoscopic cloud top height	
ATSR-GRAPE	1 km (detection) 4 km (retrieval)	VIS/NIR/IR optimal estimation	COD, CP, CRE, Phase -> CT CWP	Optimal Estimation on VIS/NIR/IR (0.7,0.9,1.6,11,12 µm) fct(COD,CRE,phase)	ECMWF profiles (operational) rad. transfer + particle model

18

Four workshops were held to investigate these cloud products and to organize and prioritize future work: monthly averages of cloud amount (total and stratified by cloud height), seasonal cycles and interannual variabilities were compared in 2005 and 2006 in Madison (USA). The GEWEX Cloud Assessment website was then created (***http://climserv.ipsl.polytechnique.fr/ gewexca/***) to prepare for the third workshop in 2008 in New York (USA), where averages of cloud properties from twelve cloud data records were directly compared. To facilitate assessments, climate studies and evaluation of climate models, it was decided to prepare a common L3 database, including monthly averages, variabilities as well as histograms at a spatial resolution of 1° latitude x 1° longitude. All twelve participating teams provided their data in a common format. Results were presented at the fourth workshop in 2010 in Berlin (Germany). After detailed discussions, each data team revised the procedure to build averages and histograms for the L3 database with delivery by early 2011. The data were analyzed and corrected several times through February 2012. ***Every cloud team is responsible for the reliability of its own data set.*** This L3 database has already revealed its usefulness in the interpretation of cloud properties retrieved from different satellite instruments, as shown in the following report.

2. Data Inventory

The GEWEX Cloud Assessment focused on evaluating global Level 3 cloud products (gridded, monthly averages and statistics). During the project some effort was also spent on a strategy to build L3 products, because several of the cloud teams did not have yet much experience in creating L3 data. First results were presented in the fourth cloud assessment workshop and long discussions led to the L3 data products of the common GEWEX Cloud Assessment database described in this chapter. The analyses presented in Chapter 3 are based on these products. Details of the original products are given in Appendix 1.

The data sets are provided in netCDF format, with one file per cloud property, per individual year and observation time of day. The map grid corresponds to 1° latitude x 1° longitude.

The cloud teams produced the L3 data for the common GEWEX Cloud Assessment database by averaging the original L2 cloud products (given at instantaneous pixels) first over each grid cell (1° x 1°) for each time step (day) and then the averages of each grid cell over the month. Polar orbiting satellites provide measurements with one daytime (at a particular local time) and one nighttime overpass (12 hours later). At higher latitudes cross-track scanning instruments may measure the same location several times within 12 hours, whereas in the tropics each location is only measured once. Therefore, to keep track of the diurnal cycle of clouds, it is preferable to keep only one observation per half-day at every location, by choosing the observation with the smallest viewing angle at higher latitudes. Most of the data sets have followed this concept. Only the two MODIS teams started from daily L3 data, which kept the orbit overlap at higher latitudes (see description of Figure 2.2).

Each file contains monthly averages and statistics.

The following cloud properties (variables) are reported:
- Cloud amount (fractional cloud cover)   CA   (0-1)
- Cloud temperature at top   CT   (150-320 K)
- Cloud pressure at top   CP   (1013-100 hPa)
- Cloud height (above sea level)   CZ   (0-20 km)
- Cloud IR emissivity   CEM   (0-1)
- Effective Cloud amount (CA weighted by CEM)   CAE   (0-1)
- Cloud (visible) optical depth   COD   (0-400)
- Cloud water path (liquid, ice)   CLWP, CIWP   (0-3000 g/m^2)
- Cloud effective particle size (liquid, ice)   CREW, CREI   (0-200 μm)

Statistics are provided for these variables for all clouds and separately stratified by cloud top height category. The latter is defined by cloud top pressure as in ISCCP (Rossow and Schiffer 1999): high-level clouds (CP < 440 hPa), mid-level clouds (440 hPa ≤ CP < 680 hPa) and low-level clouds (680 hPa ≤ CP). ISCCP further classifies and names cloud types by COD range within each height category (Figure 1.2). The cloud distribution in these different categories is given by two-dimensional histograms of CP and COD.

In addition to CAH, CAM and CAL, we define relative height stratified cloud amounts which are scaled by the total cloud amount: CAHR = CAH/CA, CAMR = CAM/CA and CALR = CAL/CA (in %). The scaling by total cloud amount shows how the different height categories are divided among all clouds present.

Statistics are also distinguished by cloud phase (liquid, ice). Thermodynamical phase may be distinguished by CT (ISCCP, TOVS Path-B, AIRS-LMD), by polarization signature (POLDER, CALIPSO) or by spectral radiance differences (PATMOS-x, MODIS, ATSR-GRAPE).

In addition to monthly averages, intra-monthly standard deviations are reported, as well as histograms of some variables.

The files contain the following information for each map grid cell for each variable:
- nb of orbit passages   *n_tot*

- Percentage of retrieved pixels out of cloudy pixels   *f_var*
- Monthly average values   *a_var*
- Intra-monthly variability (standard deviation)   *s_var*
- Histograms with monthly statistics   *h_var*

where '*var*' stands for one of the cloud properties described above and is listed in Table 2.1.

Table 2.1: Variable names of the cloud properties with statistics also distinguished by altitude (H: CP < 440 hPa, M: 440 hPa < CP < 680 hPa, L: CP > 680 hPa) and by thermodynamical phase (W: water clouds, I: ice clouds, IH: ice clouds with CP < 440 hPa) available in the GEWEX Cloud Assessment database.

Total	H	M	L	W	I	IH
CA	CAH	CAM	CAL	CAW	CAI	CAIH
CAE	CAEH	CAEM	CAEL	CAEW	CAEI	CAEIH
	CAHR	CAMR	CALR	CAWR	CAIR	CAIHR
CT	CTH	CTM	CTL	CTW	CTI	CTIH
CP						
CZ						
CEM	CEMH	CEMM	CEML	CEMW	CEMI	CEMIH
COD	CODH	CODM	CODL	CODW	CODI	CODIH
				CLWP	CIWP	CIWPH
				CREW	CREI	

The GEWEX Cloud Assessment database includes cloud property statistics from twelve global cloud data products:

Using operational satellites:
- ISCCP (*Rossow and Schiffer, 1999*)   geostationary/polar imagers
- PATMOS-x (*Heidinger et al., 2012; Walther and Heidinger, 2012*)   polar imagers
- HIRS-NOAA (*Wylie et al., 2005*)   polar IR sounders
- TOVS Path-B (*Stubenrauchet al., 2006; Rädel et al., 2003*)   polar IR sounders

Using the NASA Earth Observing System:
- MODIS Science Team (*Menzel et al., 2008; Platnick et al., 2003*)   polar imager
- MODIS CERES Science Team (*Minnis et al., 2011*)   polar imager
- AIRS-LMD (*Stubenrauch et al., 2010; Guignard et al., 2012*)   polar IR sounder
- CALIPSO Science Team (*Winker et al., 2009*)   polar lidar
- CALIPSO GOCCP (*Chepfer et al., 2010*)   polar lidar
- POLDER (*Parol et al., 2004; Ferlay et al., 2010*)   polar multi-angle imager
- MISR (*Di Girolamo et al., 2010*)   polar multi-angle imager

Using European Remote Sensing Satellites:
- ATSR-GRAPE (*Sayer et al., 2011*)   polar multi-angle imager

Table 2.2: Variables and statistics (a = monthly average, s = intra-monthly variability, h = histogram) provided by the participating data sets (ISCCP, PATMOS-x, HIRS-NOAA, TOVS Path-B, AIRS-LMD, MODIS-ST, MODIS-CE, MISR, POLDER, ATSR-GRAPE, CALIPSO-ST, CALIPSO-GOCCP).

variable	ISCCP	PATMOSx	HIRS-NOAA	TOVSB	AIRS-LMD	MODIS-ST	MODIS-CE	MISR	POLDER	ATSR-GRAPE	CALIPSO-ST	CALIPSO-GOCCP
CA	ash	as	a	ash	ash	ash	ash	a	ash	ash	ah	ah
CAH	as	as	a	as	as	as	as	a	ash		a	a
CAM	as	as	a	as	as	as	as	a	ash		a	a
CAL	as	as	a	as	as	as	as	a	ash		a	a
CAW	as	as		as	as	as	as		ash		a	
CAI	as	as		as	as	as	as		ash		a	
CAIH	as	as		as	as		as		ash		a	
CAE	ash	as	a	ash	ash	ash	ash		ash			
CAEH	as	as	a	as	as		as					
CAEM	as	as	a	as	as		as					
CAEL	as	as	a	as	as		as					
CAEW	as	as		as	as		as					
CAEI	as	as		as	as		as					
CAEIH	as			as	as		as					
CAHR	as	a	a	as	as	a	as	a	ash	as	a	a
CAMR	as	a	a	as	as	a	as	a	ash	as	a	a
CALR	as	a	a	as	as	a	as	a	ash	as	a	a
CAWR	as	a		as	as	a			ash	as	a	
CAIR	as	a		as	as	a			ash	as	a	
CAIHR	as	a		as	as	a			ash		a	
CP	ash	ash	ah	ash	ash	ash	as		ash	ash		
CZ	ash				ash		ash	ah			ah	ah
CT	ash	ash	ah	ash	ash	ash	as			ash	ah	ah
CTH	ash	ash	a	ash	ash		as			ash	ah	ah
CTM	ash	ash	a	ash	ash		as			ash	ah	ah
CTL	ash	ash	a	ash	ash		as			ash	ah	ah
CTW	ash	ash		ash	ash	ash	as			ash	ah	
CTI	ash	ash		ash	ash	ash	as			ash	ah	
CTIH	ash	ash		ash	ash		as			ash	ah	
CEM	ash	ash	a	ash	ash	ash	as			ash		
CEMH	ash	ash	a	ash	ash		as			ash		
CEMM	ash	ash	a	ash	ash		as			ash		
CEML	ash	ash	a	ash	ash		as			ash		
CEMW	ash	ash		ash	ash		as					
CEMI	ash	ash		ash	ash		as					
CEMIH	ash	ash		ash	ash		as					
COD	ash	ash		ash	ash	ash	ash		ash	ash		
CODH	ash	ash		as	ash	ash	as		ash	ash		
CODM	ash	ash		as	ash	ash	as		ash	ash		
CODL	ash	ash		as	ash	ash	as		ash	ash		
CODW	ash	ash		as	ash	ash	ash		ash	ash		
CODI	ash	ash		as	ash	as	ash		ash	ash		
CODIH	ash	ash		as	ash	ash	as		ash	ash		
CLWP	ash	ash				ash	ash			ash		
CIWP	ash	ash				ash	as			ash		
CIWPH	ash	ash		ash	ash		as			ash		
CREW	ash	ash				ash	ash			ash		
CREI	ash	ash				ash	ash			ash		
CREIH	ash			ash	ash	ash	as			ash		
COD/CP	x	x		x	x				x	x		
CODW/CP						x						
CODI/CP				x	x	x						
CEM/CP	x	x		x	x	x						
CODW/CREW	x	x				x						
CODI/CREI	x	x		x	x	x						
CEM/CREI	x	x		x	x							

Table 2.3: Approximate local observation times and time periods covered by the individual data sets of the GEWEX Cloud Assessment database.

Data Set	1:30 AM	3:00 AM	7:30 AM	9:00 AM	10:30 AM	1:30 PM	3:00 PM	7:30 PM	9:00 PM	10:30 PM	Time period
ISCCP microphys.		x		x			x		x		**1984-2007** **1984-2000**
PATMOSx	x					x					**1982-2009**
			x					x			**1992-2009**
											histos: 1998-2009
HIRS-NOAA	x					x					**1986/87/89**
	x					x					**1991-2004,**
	x					x					**2006**
			x					x			**1987/89/90**
			x					x			**1992-1996**
			x					x			**1999**
			x					x			**2002-2006**
			x					x			**2008**
TOVSB microphys.			x					x			**1987-1994**
			x					x			**1987-1990**
	x					x					**1989-1994**
AIRS-LMD microphys.	x					x					**2003-2009** **2004-2009**
MODIS-ST					x					x	**2001-2009**
	x					x					**2003-2009**
MODIS-CE					x					x	**2001-2009** histos: >2006
	x					x					**2003-2008**
MISR					x						**2001-2009**
POLDER						x					**2006-2008**
ATSR-GRAPE					x						**1997-2002** **2003-2009**
CALIPSO	x					x					**2007-2008**

Table 2.2 summarizes which variables and statistics (average, intra-monthly variability and histogram) are available for each data product. Histograms contain monthly statistics within the cloud property boundaries per 1° latitude x 1° longitude, not normalized.

Table 2.3 presents the approximate local observation time of day and the time periods covered by each data product. For the ISCCP product, which has 3-hourly time intervals, the version provided in this database represents 6-hourly averages at local observation times around 3:00 AM, 9:00 AM, 3:00 PM and 9:00 PM to allow for better comparison to the polar orbiter-based products. Note however that the actual observation time of the operational polar orbiter-based products may vary with time as illustrated in Figure 2.1. This orbit drift is especially notable for the "afternoon" NOAA polar orbiters before NOAA-16.
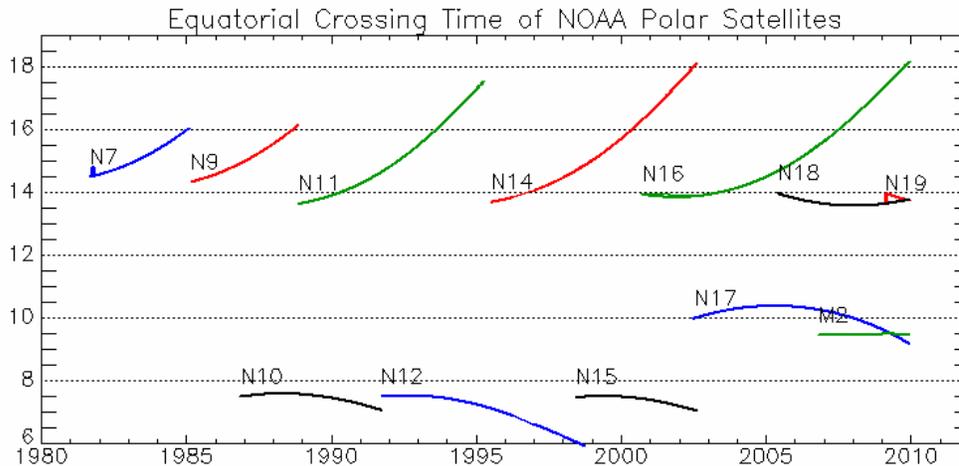
Figure 2.1: Local observation time at equator crossing of NOAA afternoon (top; NOAA-7, NOAA-9, NOAA-11, NOAA-14, NOAA-16, NOAA-18, NOAA-19) and morning (bottom; NOAA-10, NOAA-12, NOAA-15, NOAA-17) satellites, as well as of Metop (M2).

Instruments aboard satellites in sun-synchronous polar orbits provide global sampling but at the expense of time sampling: a single instrument in such an orbit generally samples a location only twice per day (depending on latitude and swath). The instruments that scan across the orbital track (AVHRR, MODIS, HIRS, AIRS) provide nearly complete global coverage in 12 hours (corresponding to a specific local observation time). Some of the imagers (MISR, POLDER, ATSR) have a much narrower scan swath so that their spatial coverage is not complete or only becomes complete after many days. The deployed radar and lidar instruments do not scan, so that 1° x 1° grid cells are sampled at most twice per month at low latitudes (Appendix 1.3.1.1.3).

For the study of global long-term anomalies in cloud properties it is important to sample a large proportion of the globe within 12 hours (corresponding to an instantaneous sampling fraction of the globe at a specific local observation time), so that all locations are observed with the same frequency during a month, and to have a constant coverage over time. The GEWEX Cloud Assessment database provides a number of orbit passages per month (n_tot) for each 1° x 1° grid cell, from which we can deduce the monthly average sampling fraction of the globe at a specific observation time (per day). It is determined as the area weighted average of n_tot divided by the number of days per month. This value may exceed 100% when multiple orbit passages per day are accumulated to determine the monthly cloud property averages, as for the two MODIS data sets at higher latitudes. Therefore the maximum of n_tot is set to the number of days per month in this calculation. Figure 2.2 presents the time series of these monthly mean 'instantaneous' sampling fractions of the globe at a specific local observation time for all participating data sets, separately for morning and afternoon orbits. The ISCCP sampling fraction is shown for local observation time at 9:00 AM and 3:00 PM, and it reaches almost 100%. PATMOS-x instantaneously samples about half the planet in the 1980s and 1990s, like HIRS-NOAA and TOVS Path-B. Around 2000, the PATMOS-x instantaneous sampling fraction increased to nearly 100% with some variations, depending on data availability and quality for processing. Compared to the operational sounders, AIRS-LMD provides about 80% sampling coverage. Note that the MODIS products provide instantaneous sampling coverage of nearly 100% because of orbit overlap at high latitudes. The sampling coverage in the tropics is about 90%. The narrow swaths of MISR and ATSR produce only 20 to 25% sampling coverage. The nadir-pointing lidar of CALIPSO samples only less than 5% of the earth at a specific local time. Therefore gridding CALIPSO data at 1° latitude x 1° longitude results in significant sampling noise, even for monthly averages.
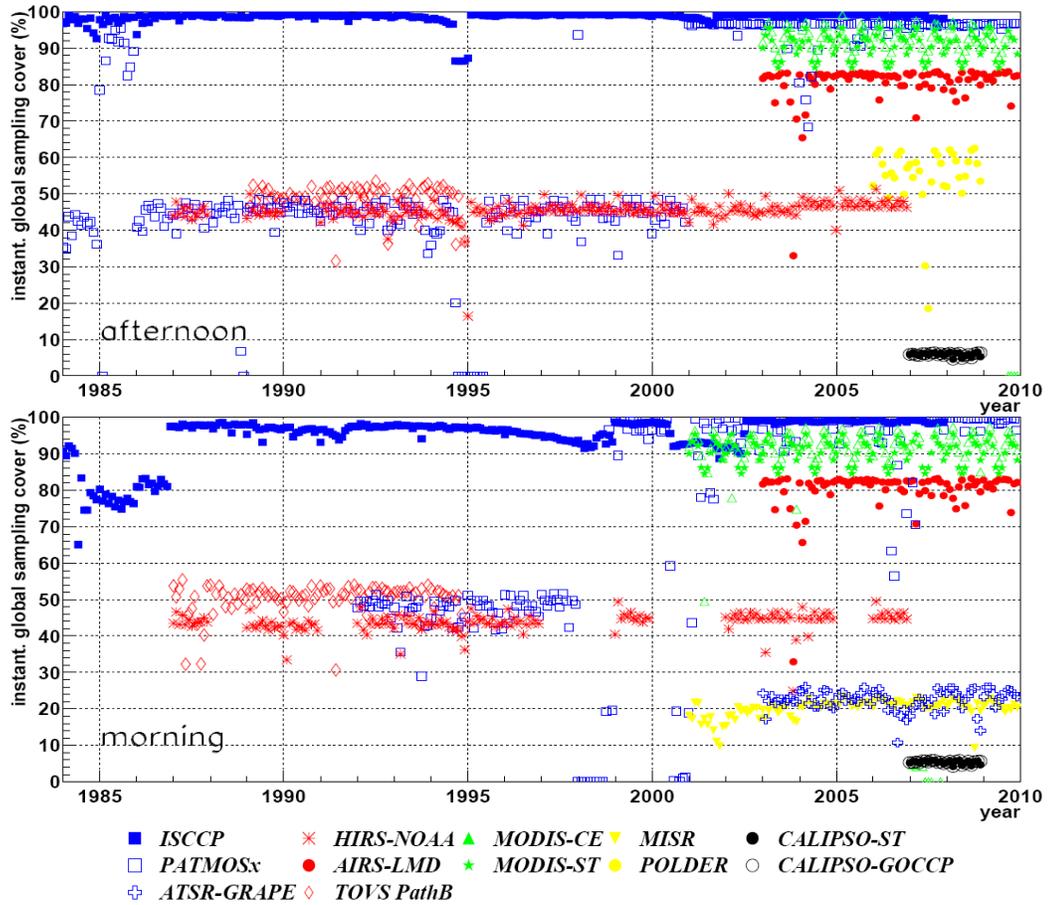
Figure 2.2: Time series of monthly mean instantaneous global sampling cover (at a specific observation time) of the participating cloud data sets. For each data set the period covered in the GEWEX database is shown, with local observation time at 1:30 PM (and 3:00PM for ISCCP) above and at 10:30 AM (TERRA satellite), 10:00 (ERS satellite), 7:30 (NOAA satellites) and 9:00 PM for ISCCP below.

3. Analyses Using the Cloud Assessment Database

This chapter presents average cloud properties and their variability, as observed from space. In synergy with more specific studies reported in the detailed data description in Annex I, the following comparison of cloud properties determined from different measurements (varying in spectral range, spatial resolution, viewing geometry) and using different retrieval methods allowed a better interpretation of the retrieved cloud properties, especially by evaluating biases, related to specific cloud scenes and to cloud diffusiveness. This leads to guidance about which data sets to use for which kind of studies.

The GEWEX Cloud Assessment database includes cloud properties retrieved from different satellite sensor measurements, undertaken at various local times and over various time periods, as presented in chapter 2. The GEWEX cloud climate record, ISCCP, is the data set with the best temporal resolution (eight observations per day) and therefore the only data set resolving a diurnal cycle. For a more consistent comparison with the other data sets in the assessment, ISCCP has provided L3 data at four specific local observation times 3:00 AM, 9:00 AM, 3:00 PM and 9:00 PM.

When not specifically mentioned in the text, climatological averages in this chapter are computed over the time intervals as follows:
- ISCCP, geostationary & NOAA satellites,   3:00 & 9:00 AM/PM,   1984-2007
- HIRS-NOAA, NOAA satellites,   7:30 AM/PM,   1987-2006
- TOVS Path-B, NOAA satellites,   7:30 AM/PM,   1987-1994
- AIRS-LMD, AQUA satellite,   1:30 AM/PM,   2003-2009
- PATMOS-x, AVHRR-NOAA,   1:30 & 7:30 AM/PM,   1996-2009
- MODIS-ST, AQUA satellite,   1:30 AM/PM,   2003-2009
- MODIS-CE, AQUA satellite,   1:30 AM/PM,   2003-2008
- CALIPSO-ST, A-Train,   1:30 AM/PM,   2007-2008
- CALIPSO-GOCCP, A-Train,   1:30 AM/PM,   2007-2008
- POLDER, A-Train, (only daytime),   1:30 PM,   2006-2008
- MISR, TERRA satellite, (only daytime),   10:30 AM,   2001-2009
- ATSR-GRAPE, Envisat, (only daytime),   10:00 AM,   2003-2009

For comparisons of cloud properties determined only in daytime, we present results at local observation time 1:30 PM (3:00 PM for ISCCP). For more detailed comparisons we limit the comparison to statistics at 1:30 PM (3:00 PM for ISCCP) in 2007 (leaving out differences due to different time periods), for which the following simultaneous data sets are available: ISCCP, PATMOS-x, MODIS-ST, MODIS-CE, AIRS-LMD, CALIPSO-ST, CALIPSO-GOCCP and POLDER.

3.1 Cloud Amount, Height, Temperature and Emissivity

This section presents cloud amount (fractional cloud cover), height, temperature, infrared emissivity as well as effective cloud amount (cloud amount weighted by cloud emissivity), as observed from space. These physical properties may be retrieved day and night. We also stratify statistics according to three cloud height categories (high-level, mid-level and low-level). For this separation cloud pressure is used, with CP interval limits at 440 hPa and 680 hPa. Cloud amount is often used to evaluate climate models (e.g. Zhang et al., 2005). Height-stratified cloud amount, temperature and emissivity averages provide a more detailed insight than averages over all clouds. After having compared global averages, we study latitudinal variation and seasonal cycles of these average properties and explore their probability density functions. Day – night differences and diurnal sampling differences are discussed in chapter 3.1.3 and geographical maps, often necessary for a better understanding of differences in the data sets, are

displayed in Annex 3.

In general, passive remote sensing provides cloud properties as observed from above. When stratifying into different height categories, cloud properties in category H correspond to all high-level cloud situations (single-layered and multi-layered), whereas those of category M only correspond to situations when mid-level clouds are the uppermost clouds (no high-level clouds above) and those of category L only to situations with single-layer low-level clouds (no high- or mid-level clouds above). CALIPSO data in the GEWEX Cloud Assessment database have been produced in a similar way for a better comparison (keeping only the uppermost cloud layer in the case of multi-layered clouds).

As discussed in the introduction, cloud scenes, which may lead to ambiguity in interpretation of disparate passive remote sensing techniques, fall into two categories:
1) Semi-transparent cirrus overlying clouds at lower levels (affecting the identification of high-level clouds and their average properties), and
2) Semi-transparent cirrus in a single layer (their non-detection also affects the total cloud amount).
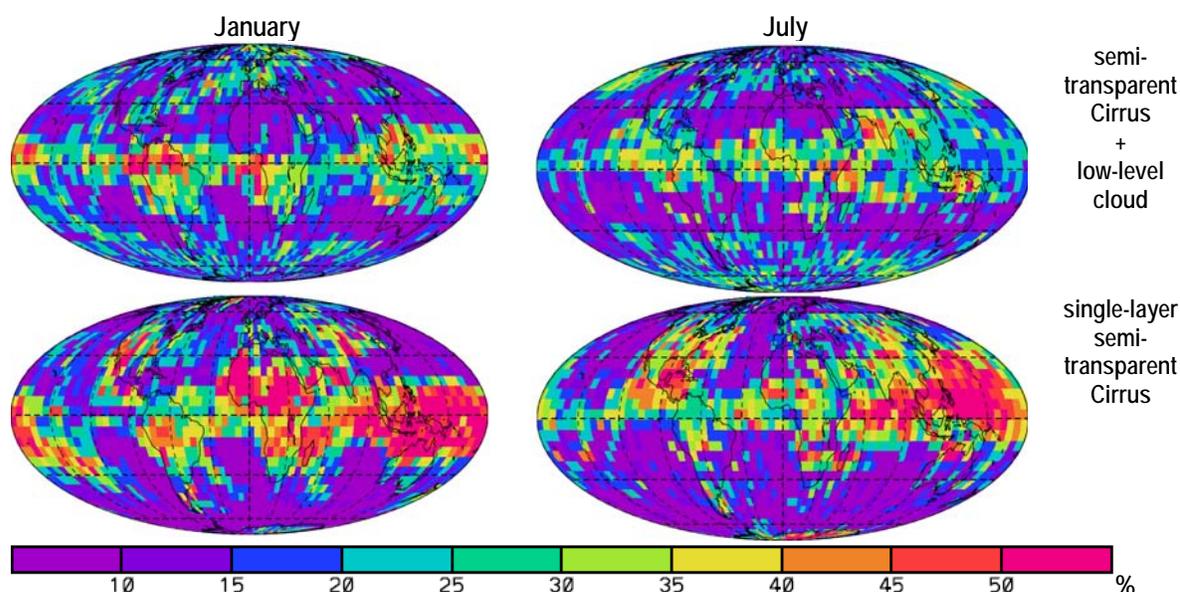
Figure 3.1.1: Geographical maps of occurrence of semi-transparent cirrus (COD < 3) overlying low-level clouds (top) and single-layer semi-transparent cirrus (bottom) relative to all clouds. Statistics averaged over 1:30 AM and 1:30 PM LT, from data prepared by CALIPSO-ST at a spatial resolution of 5° latitude x 5° longitude, separately in January (left) and July (right) 2008.

The overall frequency of occurrence of these two cases is estimated by the CALIPSO Science Team (CALIPSO-ST) results, which consider semi-transparent cirrus as high-level clouds with optical depth between 0.01 and 3. Geographical maps are presented in Figure 3.1.1, separately for January and for July. We have to keep in mind that these amounts only provide an ***upper limit of cases 1 and 2***, because ***ambiguity increases with decreasing optical depth*** so that at COD > 1 the effects are already much smaller. The upper limits of cases 1 and 2 correspond to *about 20% each of all clouds (or about 30% of all high-level clouds)*. There are slightly more cases of single semi-transparent cirrus over land (28%) than over ocean (20%), whereas the relative amount of semi-transparent cirrus overlying lower clouds is similar over ocean and over land. When comparing all high-level clouds in the midlatitudes, these appear more often as single semi-transparent cirrus in summer (34% / 24% in NH / SH, respectively) than in winter (29% / 20% in NH / SH, respectively).

CALIPSO-GOCCP (GCM-Oriented CALIPSO Cloud Product) also provides height-stratified cloud amounts including all cloud layers (Annex 1.1.3.1.2.3) underneath the uppermost layers, as long as these are not too opaque (optical depth < 3). When including all these cloud layers, the amount of all low-level

clouds relative to all clouds (3DCALR) is on average 57%. (3DCALR-CALR)/3DCALR gives a rough estimation of the overlap of low-level clouds by higher-level clouds: 26% of the coverage of all low-level clouds is overlapped by semi-transparent higher-level clouds (with optical depth < 3). This compares quite well to 31% determined by analyzing the cases of semi-transparent cirrus overlying clouds at lower levels provided by CALIPSO-ST. Overall, one fourth of overlap corresponds only to a total cover of about 0.15.

3.1.1 Global Averages

Table 3.1.1: Average cloud amount (CA), as well as partition of uppermost high-level, mid-level and single-layer low-level clouds over the globe, over ocean and over land. CAHR + CAMR + CALR = 100%. Discrepancies larger than rounding errors like for ATSR-GRAPE and MODIS-CE are linked to incoherent L3 data production. For comparison are also shown frequencies of cloud occurrence from SAGE.

	global				ocean				land			
	CA	CAHR (%)	CAMR (%)	CALR (%)	CA	CAHR	CAMR	CALR	CA	CAHR	CAMR	CALR
ISCCP	0.64	22	40	39	0.68	18	35	46	0.56	30	50	21
ISCCP 3PM	0.66	28	37	35	0.68	25	35	40	0.62	35	43	23
PATMOSX	0.68	39	20	41	0.72	37	16	48	0.57	45	29	26
ATSR-GRAPE	0.62	20	39	36	0.65	22	36	36	0.54	15	46	36
MODIS-ST	0.69	29	18	53	0.73	26	14	60	0.57	36	28	36
MODIS-CE	0.62	40	15	41	0.66	37	13	48	0.51	49	19	25
HIRS	0.74	55	19	26	0.82	51	20	30	0.54	65	17	17
TOVSB	0.70	41	16	42	0.74	38	13	49	0.60	49	24	27
AIRS-LMD	0.67	41	18	41	0.72	38	16	47	0.56	48	23	29
CALIPSO-ST	0.73	51	11	38	0.77	48	8	44	0.65	59	18	22
CAL-GOCCP	0.67	43	14	42	0.71	40	10	49	0.59	51	22	23
MISR	0.65	20	18	62	0.74	20	13	67	0.42	20	29	51
POLDER	0.56	12	43	45	0.61	12	36	52	0.45	14	59	28
SAGE	0.95	44	20	36	0.95	44	18	38	0.97	45	25	29

Table 3.1.1 and Figure 3.1.2 present global averages of total cloud amount, as well as of height stratified cloud amount scaled by total cloud amount. In addition, cloud amount differences between ocean and land are shown.

Total Cloud Amount

The global cloud amount (CA) of these data sets varies between 0.56 and 0.74. ***The spread is mainly explained by different instrument sensitivity***: The lowest CA provided by POLDER corresponds to clouds with optical depth > 2 (Annex 1.3.2.4). CA from MISR corresponds to clouds for which stereoscopic cloud height may be determined; since detection over land is more difficult, there is a low bias of up to 0.07 (Annex 1.3.3.5). Global CA is determined as 0.73 by CALIPSO-ST, the lidar having the greatest detection sensitivity to clouds down to VIS extinctions as small as 0.01 km^{-1} (Annex 1.3.1.1.1). Similar results are obtained (0.67 – 0.74) by infrared sounding instruments that use the CO_2 absorption band (MODIS-ST, AIRS-LMD, TOVSB, and HIRS-NOAA). It is interesting to note that the different spatial resolution of the instruments, varying from 300 m (lidar) to 15 km (HIRS, AIRS), does not seem to be a major influence on CA, in agreement with earlier studies (e.g., Wielicki and Parker, 1992). Global CA from multi-spectral imagers lies between 0.62 and 0.68, depending on the sensitivity of the cloud detection. The performance during daytime (with available VIS information) should be better than during

nighttime: Especially over land, where detection is more difficult, this may lead to low biases during nighttime of about 0.05 for ISCCP and MODIS-CE (section 3.1.3). Cloud properties from CALIPSO-GOCCP are inferred as in a GCM simulator, using a reduced vertical resolution, leading to a CA similar to the ones obtained from the multi-spectral imagers. Nearly-global cloud amount from surface observations amounts to 0.64 (Warren et al., 2007).

The cloud occurrence obtained from SAGE (P.-H. Wang, personal communication) is very high, because the limb-viewing sun occultation technique is sensitive to clouds down to an optical depth of about 0.03 and because any cloud appearing within the path length of 200 km is counted as 1. In synergy with other data sets the SAGE cloud occurrence can be transformed into a cloud amount by assuming a cloud size (Liao et al., 1995b; Wylie and Wang, 1997).

According to most data sets, there are about *10 - 15% more clouds over ocean than over land*. HIRS-NOAA shows 30% more clouds over ocean than over land. This may be explained by problems in low-level cloud detection over land (scenes with an IR window channel Brightness Temperature within 5 K of the NCEP "surface" temperature are discarded). MISR too detects ~30% more clouds over ocean than land. Diurnal sampling differences may also play a role: CA from MISR and ATSR are only sampled at ~10:30 AM LT, whereas most other instruments sample at multiple times of the day. Figure 3.1.11 shows a slightly smaller CA over land (about 0.04) and a slightly larger CA over ocean (about 0.02) in the morning than in the afternoon. However, then MISR and ATSR-GRAPE should show a similar ocean-land difference. Indeed, CA from MISR carries less sensitivity to thin cirrus detection over land compared to ocean, with a low bias of up to 0.07 (Annex 1.3.3.5). Accounting for this bias brings the MISR CA over land up to 0.49, which compares favourably to the MODIS-ST Terra morning-only CA over land of 0.50.

Height-Stratified Cloud Amount

Height-stratified cloud amount scaled by total cloud amount reflects how the different height categories are divided among all clouds present. It is less influenced by differences in cloud detection and should also be more useful for comparison with climate models. According to most data sets, about *40% of all clouds are single-layer low-level clouds* and only about *15% of all clouds* correspond to *mid-level clouds with no higher clouds above*.

CAHR, however, shows a spread from *12% to 55%*. This large *spread in CAHR is essentially explained by instrument performance for identifying thin cirrus, especially in cases of multi-layer cloud systems*. The highest value of CAHR should be determined by CALIPSO-ST, because the *active lidar is the most sensitive to thin cirrus (including sub-visible cirrus)*. Indeed, CAHR of CALIPSO-ST is 51%. For passive remote sensing the lower limit in cloud optical depth (COD) for identifying thin cirrus varies from about 0.1 (Menzel *et al.* 1989), for infrared sounding in the CO_2 absorption band (corresponding to CAHR of about 40%), to about 2 for multi-angle multi-spectral imagers using measurements in the solar spectrum (corresponding to CAHR of about 20%). *For thin cirrus identification, especially in cases of multi-layer clouds, IR spectral differences in the IR are powerful, whereas solar information is more important for the detection of low-level clouds (during day).*

The largest CAHR value of 55% from HIRS-NOAA has to be overestimated, because it is larger than the value from CALIPSO-ST. This can be explained by an underestimation of the partition of low-level clouds (CALR of 26% instead of 40%): The CO_2 slicing (comparing pairs of radiances, Annex 1.1.3.1) may only be used up to a pressure of 650 hPa. The height of low-level clouds, assumed to be opaque, is determined by one atmospheric window brightness temperature. The weighted χ^2 method used in the TOVS Path-B and AIRS-LMD retrievals does not introduce such a bias, even though the retrieval noise is larger for low-level clouds than for high-level clouds (Figure 1.2.4).
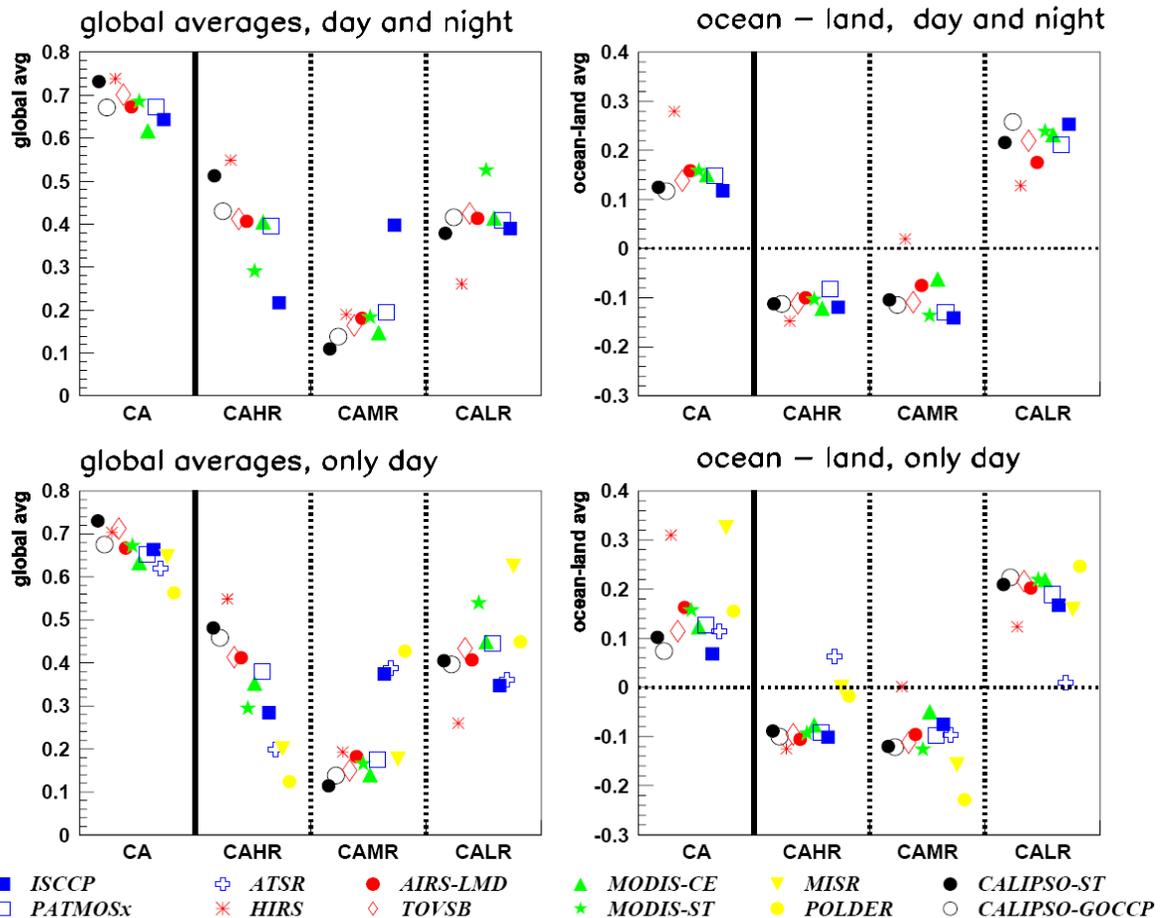
Figure 3.1.2: Global averages of total cloud amount (CA), and of amount of high-level, mid-level and low-level clouds relative to all clouds (CAHR, CAMR and CALR, respectively) (left). Statistics are averaged over day and night measurements (top) and averaged over day measurements only (1:30 PM LT, except for ISCCP (3:00 PM) and ATSR-GRAPE and MISR (10:30 AM), bottom). The panel on the right presents cloud amount differences between ocean and land.

PATMOS-x and MODIS-CE use an IR spectral difference to determine CEM and CT. Therefore height-stratified cloud amounts are similar to those obtained from AIRS-LMD and TOVS Path-B, as well as from CALIPSO-GOCCP (based on a retrieval adapted to be more consistent with comparisons at GCM resolution).

When the cloud height is determined by simultaneous use of VIS and IR measurements (like for ISCCP and ATSR-GRAPE), CAHR tends to be underestimated (with values of 33% and 20%, respectively) and CAMR to be overestimated (with values of 27% and 39%, respectively), because thin cirrus overlying low-level clouds are misidentified as mid-level clouds. When having only one IR window brightness temperature available during night, ISCCP also misidentifies single-layer semi-transparent cirrus as mid-level or even as low-level clouds (see also section 3.1.3). Therefore the global average partition of high-level clouds drops from 33% during day to 22% when including also night-time measurements. However, we want to remind the reader that the corrections applied for the distributed ISCCP products significantly reduces this effect (see Appendix 1.1.1).

One would expect for MODIS-ST an average CAHR around 40%, because CO_2 slicing is used to determine CEM and CP, but thin cirrus have been misidentified as low-level clouds, when the retrieval reverts to an IR window brightness temperature. Therefore CAHR is only 29% and CALR 53%. This problem will be resolved in Collection 6 of MODIS-ST.

The multi-viewing solar imager MISR underestimates high-level cloud partition by a factor of about 2 (with CAHR = 20%) and leads to an average **CALR** of about **60%**. The latter value corresponds to the *fraction of all low-level clouds*. This is due to MISR's stereoscopic ability to accurately retrieve the heights of low-level clouds under multi-layer cloud situations where thin cirrus clouds are present (Annex 1.3.3.5).

The lowest CAHR value of 12% from POLDER has two causes: 1) as for MISR the solar spectrum used by POLDER determines in the case of multi-layer clouds the high-level cloud properties only when COD > 2, and 2) cloud pressure (CP) determined by O_2-band absorption corresponds to a deeper level within the cloud than the radiative height determined by IR sounders and multi-spectral VIS-IR imagers. Because the distinction among cloud types uses fixed CP thresholds, these semi-transparent high-level clouds are then misidentified as mid-level clouds. To evaluate the effect of the second cause, POLDER also produced height-stratified cloud amounts by using CP determined from Rayleigh scattering. Global CAHR doubles to 24%. This data set is still experimental.

Height-stratified relative cloud occurrence from SAGE compares relatively well to that from IR sounders, except that SAGE does not observe any high-level cloud occurrence difference between ocean and land. One might explain this fact by a smaller horizontal extent of high-level clouds over land than over ocean.

Effective Cloud Amount and IR Cloud Emissivity

Figure 3.1.3 presents global averages of effective cloud amount (CAE), IR cloud emissivity (CEM) and cloud temperature (CT), as well as their height-stratified averages. In addition, differences between ocean and land are shown. These averages correspond to observations at 1:30 PM LT (3:00 PM for ISCCP). ATSR-GRAPE average cloud temperature is only available at 10:30 AM LT.

Global CAE (cloud amount weighted by IR cloud emissivity) is about 0.5 (varying from 0.46 to 0.61). For this comparison, ISCCP instantaneously retrieved VIS cloud optical depth (COD) was transformed into CEM by the approximate formula: *CEM = 1 – exp(-COD/2)*.

Global CEM is about 0.7. Average height-stratified CEM should increase from high-level to low-level clouds, because of the existence of semi-transparent cirrus. The large averages from ATSR-GRAPE (about 0.8 for all clouds and 0.9 for high-level clouds) are explained by the fact that the optimal estimation retrieval is on average only successful for 40% of all detected clouds (53% over land and 33% over ocean). For 60% of the clouds the retrieval is rejected because the uncertainty is too large. This sub-sampling leads to strong biases towards optically thick clouds (see also section 3.2.1.1). ISCCP reveals similar CEM averages for all height categories, because thin cirrus are missed or misidentified as optically thicker midlevel clouds (when overlying lower level clouds) which enhances average CEMH. Average CEML is the largest from HIRS-NOAA, because low-level clouds are assumed opaque. However CAEL agrees well with the other data sets, because CAL is underestimated. The lowest value of CEML is determined by TOVS Path-B due to the coarse spatial resolution of the retrieval (100 km) which is not adapted for low-level clouds which have smaller sizes.

Compared to CA, *CAE includes the radiative effect of the detected clouds*. Therefore, the **CAE of high-level clouds agrees much better between the different data sets than CAHR, because a smaller cloud amount due to missing thin clouds is compensated by a larger average IR cloud emissivity**.
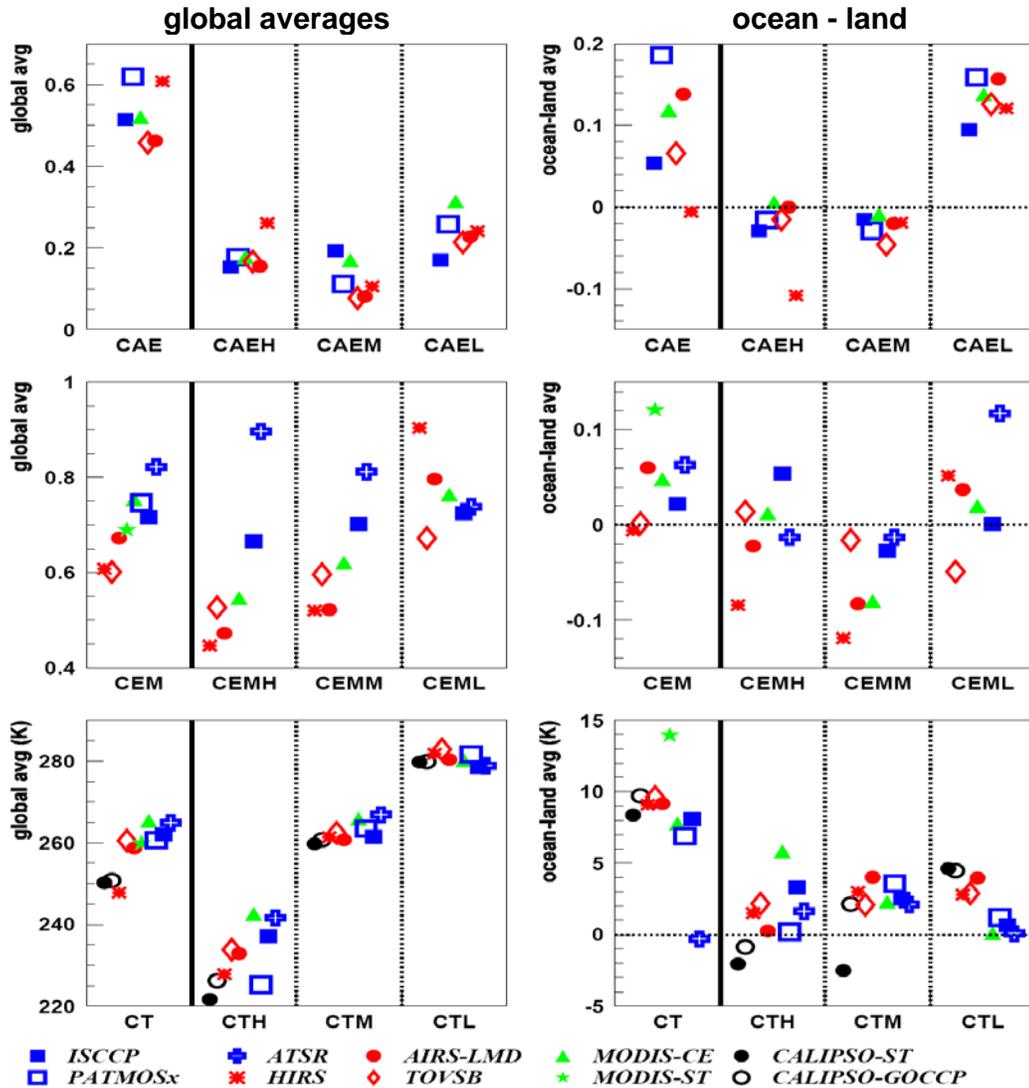
Figure 3.1.3: Global averages (left) and differences between ocean and land (right) of effective cloud amount (CAE, top), IR cloud emissivity (CEM, middle panels) and cloud temperature (CT, bottom), for all clouds as well as for high-level, mid-level and low-level clouds. Statistics for observations at 1:30 PM LT (3:00 PM for ISCCP, and 10:30 AM for ATSR-GRAPE).

From Table 3.1.1 and Figure 3.1.2 one deduces that of all clouds present there are about 10% more high-level and mid-level clouds over land than over ocean. On the other hand there are about 10% more clouds over ocean than over land, so that the average amount of high-level clouds is similar over land and ocean (about 0.30). CAEH and CAEM are also similar, as well as CEMH and CEMM (but with more spread among the data sets). CEM depends on the spatial resolution of the retrieval: CEM only corresponds to the IR cloud emissivity under the assumption that the samples are completely cloud covered. In the case of partly cloudy samples CEM corresponds to an effective cloud amount over the retrieved sample. The uncertainty should grow with the sample size and detection sensitivity noise.

Cloud Temperature

Global mean cloud temperature lies between 250 K and 265 K, the coldest value retrieved from CALIPSO, because the lidar has the highest sensitivity to thin cirrus. *CALIPSO* is also the only measurement providing *cloud top height*. *Passive remote sensing* (*except* when using multi-view to provide a *stereoscopic height* as in the MISR retrieval) provides a *'radiative height'* which may lie up to

1-2 kilometers below cloud top, depending on the strength of optical depth increase within the cloud (e.g. Liao et al., 1995a; Holz et al., 2008; Rossow and Zhang, 2010; Stubenrauch et al., 2010).

Whereas global averages of CTM and CTL agree well among all data sets, one observes a *spread of nearly 20 K in average CTH*. This is again *related to different sensitivity to thin cirrus* (since thin cirrus layers are often colder than thicker ones) as well as to *diffusive cloud tops of high-level clouds*.

Average CT is about 10 K warmer over ocean than over land, in agreement with more high-level and mid-level clouds over land and more low-level clouds over ocean. The ocean-land difference in height-stratified CT is reduced to less than 5 K, with a spread of the same order of magnitude among the different data sets for high-level and low-level clouds. Uncertainties may be linked to the use of different atmospheric temperature profiles to convert cloud height into cloud temperature. However, this uncertainty is probably more important on regional scale, because the differences between ISCCP, MODIS-CE and PATMOS-x are profile independent since these retrievals directly determine CT.

Synoptic Variability

Figure 3.1.4 presents global intra-monthly (synoptic) variability of CA, CAE, CEM and CT within the different data sets. Their global averages are around 0.28, 0.25, 0.18 and 18 K, respectively. A *spread* around these values may be interpreted as follows: *values larger than average indicate noise whereas values smaller than average indicate a lack of sensitivity*. Most data sets agree quite well, except slightly larger variability in CA for POLDER, smaller variability in CEM and CT for ATSR-GRAPE and in CAE and CEM for PATMOS-x as well as high CEM variability for TOVS Path-B. The latter may be explained by the coarse spatial resolution (100 km) of the retrieval. The optimal estimation retrieval of ATSR-GRAPE favors optically thick clouds, and this sub-sampling leads to less variability in CEM and CT.
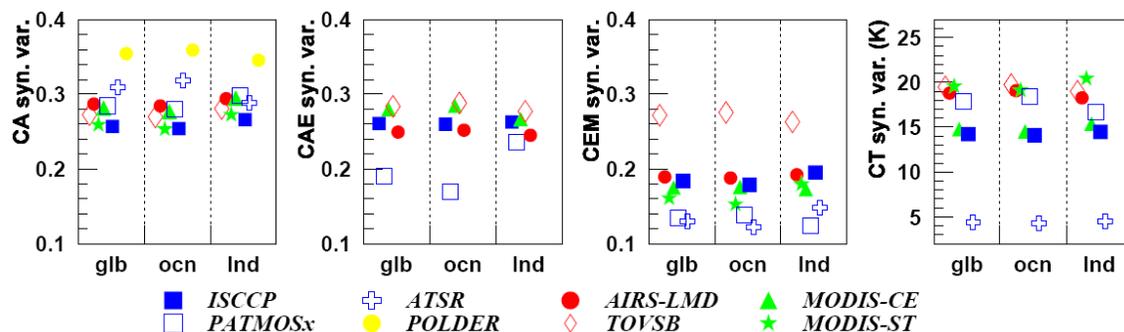
Figure 3.1.4: Average day-to-day (synoptic) variability (standard deviation) of cloud amount (CA), effective cloud amount (CAE), IR cloud emissivity (CEM) and cloud temperature (CT) over the globe, over ocean and over land. Statistics for observations at 1:30 PM LT (3:00 PM for ISCCP, and 10:30 AM for ATSR-GRAPE).

Correlations between Average ISCCP Cloud Pressures and Those of Other Data Sets

Because ISCCP is the GEWEX cloud data set and serves as a reference, we study in a next step correlations of the monthly mean cloud pressure (CP) between the different data sets and ISCCP. For this analysis monthly averages are compared for each 1° latitude x 1° longitude grid at 1:30 PM / 3:00 PM local time in 2007. Figure 3.1.5 presents these relationships over ocean: The lines correspond to the values with maximum population in scatterplots between ISCCP and the data set of comparison. In general monthly mean CP is well related with values similar to those of ISCCP (within 50 hPa). The agreement is better over ocean than over land (not shown), because cloud detection over land is more difficult.

Monthly mean CP values of AIRS-LMD and PATMOS-x are closest to those of ISCCP. CP of POLDER, using the O_2 absorption band, is always larger, because it sounds deeper into clouds. Larger mean values of MODIS-ST can be explained by a misidentification of thin cirrus as low-level clouds (Annex I). HIRS-NOAA average values are always lower than those of ISCCP, especially in regions with many low-level clouds (corresponding to average ISCCP cloud pressure around 700 hPa).
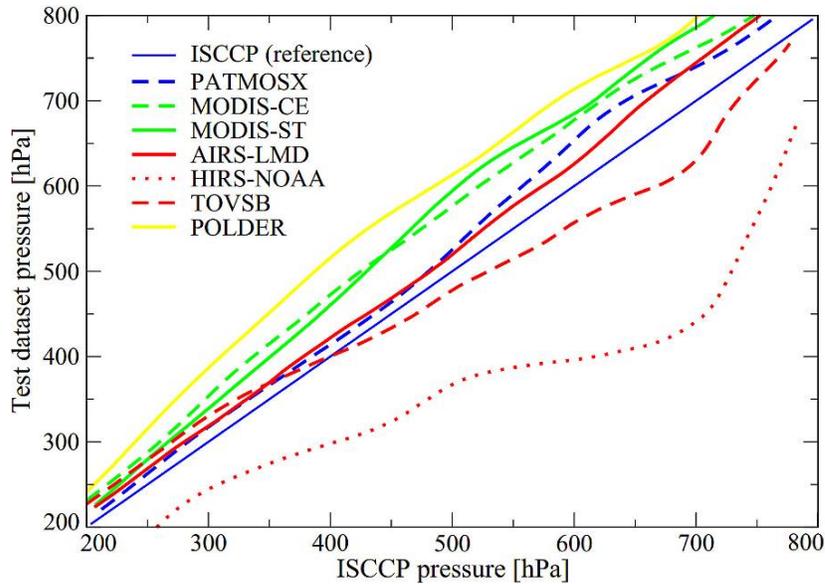
Figure 3.1.5: Average relations of monthly average CP between any cloud data set and ISCCP over ocean. Observations at 1:30 PM (3:00 PM) LT, 2007.

Summary

We have learned that differences in global averages are mainly related to instrument performance in identifying thin cirrus. This not only affects cloud amounts, but also the averages of the other quantities, because their sample populations differ. According to CALIPSO, semi-transparent cirrus (COD < 3) in a single layer and semi-transparent cirrus overlying lower level clouds (cases which may lead to confusion for passive remote sensing) each comprise about 20% of all clouds.

In the case of single-layer thin cirrus, this affects total cloud amount. In the case of cirrus overlying low-level clouds we essentially distinguish three categories of results:

1) Active lidar, IR sounders and multi-spectral imagers making use of IR spectal differences identify the presence of the cirrus.

2) Multi-spectral imagers using IR and VIS information are also sensitive to the clouds underneath and therefore identify these multi-layer cloud systems as mid-level clouds.

3) Multi-spectral VIS imagers are only sensitive to the low-level clouds.

In the case of thin cirrus overlying high-level clouds, CP and CT are only slightly larger for those data sets that are not sensitive to thin cirrus.

The next question one may ask is how a different performance for identifying thin cirrus may affect the geographical distributions and seasonal cycle of cloud properties.

3.1.2 Latitudinal Variation and Seasonal Cycle

Table 3.1.2 presents cloud amount and relative cloud amount stratified by height, separately for NH midlatitudes (30°N-60°N), tropics (15°S-15°N) and SH midlatitudes (30°S-60°S).

Table 3.1.2: Average cloud amount (CA), as well as partition of uppermost high-level, mid-level and single-layer low-level clouds over the globe, over NH midlatitudes (30°N-60°N), tropics (15°N-15°S) and SH midlatitudes (30°S-60°S), with CAHR + CAMR + CALR = 100%. Discrepancies larger than rounding errors like for ATSR-GRAPE and MODIS-CE are linked to incoherent L3 data production. For comparison, frequencies of cloud occurrence from SAGE are also shown.

	NH midlatitudes				tropics				SH midlatitudes			
	CA	CAHR	CAMR	CALR	CA	CAHR	CAMR	CALR	CA	CAHR	CAMR	CALR
ISCCP	0.67	23	45	33	0.60	31	34	37	0.78	15	39	46
ISCCP 3PM	0.72	27	42	31	0.61	44	29	27	0.79	18	40	42
PATMOSX	0.66	39	25	33	0.67	55	8	31	0.81	31	21	47
ATSR-GRAPE	0.68	19	39	39	0.60	28	38	27	0.76	18	35	44
MODIS-ST	0.68	31	23	46	0.70	38	7	55	0.82	24	19	57
MODIS-CE	0.61	41	18	37	0.59	54	10	33	0.77	31	17	51
HIRS	0.63	54	21	25	0.84	61	11	29	0.85	50	26	24
TOVSB	0.68	40	23	37	0.69	60	7	33	0.83	29	19	51
AIRS-LMD	0.69	40	22	38	0.67	59	11	30	0.80	28	21	51
CALIPSO-ST	0.70	53	14	34	0.79	66	5	29	0.81	42	11	47
CAL-GOCCP	0.66	46	17	35	0.66	54	9	36	0.79	36	12	51
MISR	0.59	22	22	56	0.65	22	16	62	0.82	20	15	65
POLDER	0.59	8	49	43	0.52	22	38	40	0.75	6	33	61
SAGE	0.99	46	28	26	0.97	56	13	31	0.95	42	25	33

Keeping in mind the different instrument performances for identifying thin cirrus, we deduce the following:

- The **SH midlatitudes** are covered by about 10% more clouds than the NH midlatitudes. We also find there the largest contribution of single-layer low-level clouds (about 50%), according to all data sets except HIRS-NOAA, which suffers from uncertain identification of low-level clouds with small thermal contrast.
- In the **tropics** we find the largest contribution of high-level clouds. Therefore CAHR varies the most between the different data sets: from 66% (CALISPO-ST), 60% (IR sounders), 55% (CALIPSO-GOCCP, SAGE, PATMOS-x, MODIS-CE), 45% (ISCCP-day), 40% (MODIS-ST), 30% (ISCCP day and night and ATSR-GRAPE) down to 22% (POLDER, MISR), with decreasing instrument or retrieval performance for identifying thin cirrus when low-level clouds are present. The relatively small difference in CAHR between CALIPSO-ST and IR sounders may be related to the fact that in the tropics thin cirrus at high altitudes are often related to the presence of denser clouds underneath (Wylie and Wang, 1997; Winker, 2002). According to CALIPSO, IR sounders, MODIS and PATMOS-x there are few situations in the tropics with uppermost mid-level clouds, a result already locally observed by Mace and Benson-Troth (2002) using ground-based radar and by Mace *et al.* (2009) using CloudSat.

Comparing the geographical patterns in the maps of Annex 3, ISCCP essentially underestimates CAHR in locations where there are many high-level clouds. One interesting feature is the Sahara, where

most data sets determine high-level clouds, whereas ISCCP identifes mostly low-level clouds (and also more clouds than the other data sets). This could probably be explained by missing thin cirrus and by detecting sand storms as low-level clouds.

CALR considers only single-layer low-level clouds, except MISR that identifies low-level clouds in the presence of overlying, undetected thin cirrus. Therefore MISR provides more low-level clouds than ISCCP. MODIS-ST is the other data set identifying so many low-level clouds. In Collection 5 of MODIS-ST, provided to the GEWEX Cloud Assessment database, thin cirrus are misidentified as low-level clouds, when the retrieval reverts to an IR window brightness temperature. This problem will be resolved in Collection 6 of MODIS-ST. It is interesting to note that in the SH stratocumulus regions both data sets using the CO_2 slicing retrieval method (MODIS-ST and HIRS-NOAA) identify more clouds as mid-level clouds than ISCCP. In general these regions have maximum CALR.

Figure 3.1.6 presents the latitudinal variation of CA, CAE, CEM and CT (total and height-stratified) as differences between their latitudinal averages and their global means. Statistics are compared for observations at 1:30 PM LT (3:00 PM for ISCCP) to minimize effects linked to diurnal variation. From this figure we deduce the following:

- *Most data sets show similar latitudinal variations*. Only in the polar latitudes is the spread among the different data sets larger, especially for CAMR, CALR and CEMH. Polar regions are the most difficult for a reliable retrieval of cloud properties, because the contrast between ice / snow and clouds is very small. CALIPSO should give the most realistic picture in these regions, even though polar stratospheric clouds have been removed in this version of the CALIPSO-ST results. Cloud properties of two polar regions are presented in more detail in chapter 3.3.

- The latitudinal variation in CA of all data sets (except HIRS-NOAA in the NH) indicates separations between the midlatitudes and the Inter-Tropical Convergence Zone (ITCZ). These correspond to the subtropical subsidence regions in which CA is lower than average. Maximum CA and CAE are detected by all data sets around 60° S. This region (roaring fifties and screaming sixties) has very strong westerly winds leading to frequent storms and probably also to thicker clouds than in the NH.

- The ITCZ is even more resolved in CAHR with an increase of 20%. The latitudinal variation of CT shows the ITCZ with the coldest clouds and the subtropical subsidence regions with the warmest clouds. Considering height-stratified averages, the latitudinal amplitude of CTH is largest for CALIPSO-ST and PATMOS-x. Indeed, CALIPSO-ST provides CT at cloud top and is most sensitive to thin cirrus. However, PATMOS-x, using a multi-spectral radiometer, should provide a 'radiative' cloud height, which is lower than the top, and therefore CTH should show a smaller amplitude. The result may be explained by the fact that the optimal estimation retrieval of PATMOS-x was trained with CALIPSO data, leading to a CT colder than that of the 'radiative' height. The latitudinal variations of CTM and CTL are very similar for all data sets and are linked to the latitudinal variation of lower air temperature. The amplitude attains 30 K for CTL.
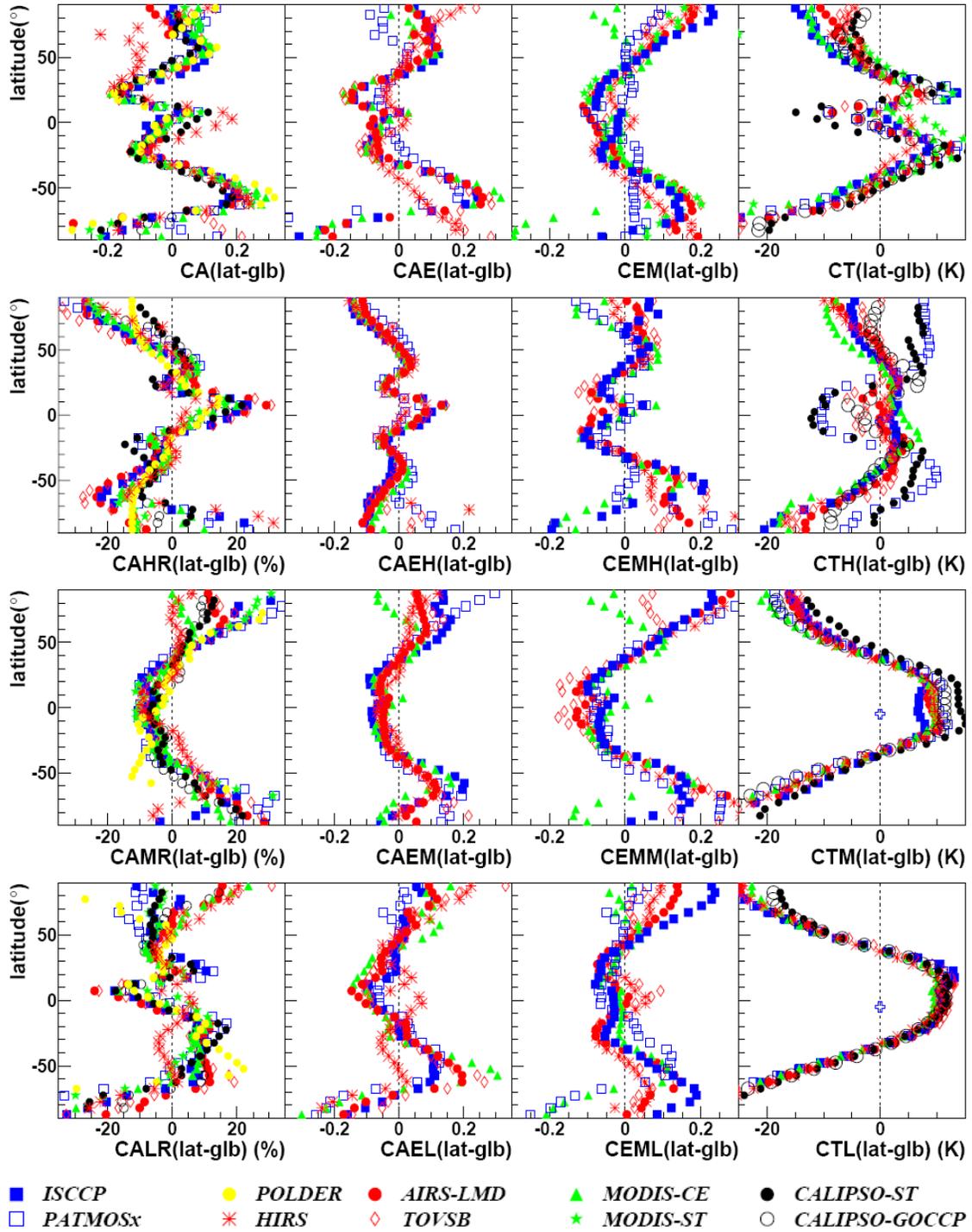
Figure 3.1.6: Latitudinal variation of annual mean cloud amount CA, effective cloud amount CAE, cloud emissivity CEM and cloud temperature CT, as well as of their height-stratified averages (relative to CA), presented as differences between latitudinal averages and global mean. Statistics at 1:30 PM LT (3:00 PM for ISCCP).
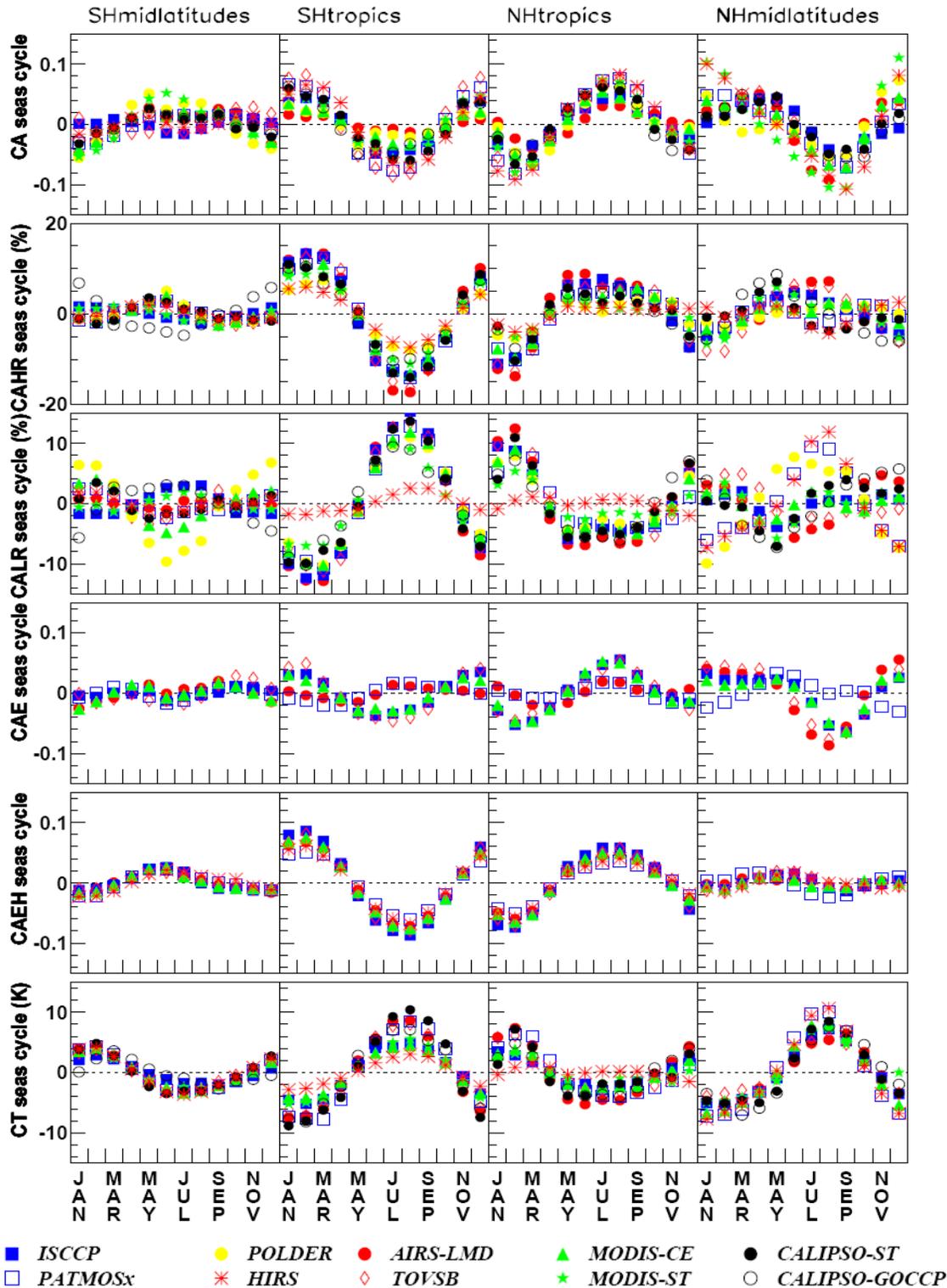
Figure 3.1.7: Seasonal variation of cloud amount CA, relative high-level cloud amount CAHR, relative low-level cloud amount CALR, effective cloud amount CAE, effective high-level cloud amount CAEH and cloud temperature CT in four latitude bands (60°S-30°S, 30°S-0°, 0°-30°N and 30°N-60°N), derived as the difference between monthly mean and annual mean. Statistics at 1:30 PM LT (3:00 PM for ISCCP).

Figure 3.1.7 presents seasonal cycles of CA, CAHR, CT, CAE and CAEH for four latitude bands of 30° from 60° S to 60° N, averaged over observations at similar afternoon local times.

38

- *Most data sets agree on the seasonal cycle* (except for CALR of HIRS-NOAA, linked to the use of the NCEP "surface" temperature for cloud detection which may be underestimated in summer and overestimated in winter over land). In general the seasonal variation seems to be smaller than the latitudinal variation, except for the transition of the ITCZ in the latitude bands 30°S - 0° and 0° - 30°N, with maximum amplitude of about 30% in CAHR. The seasonal cycle is generally larger over land than over ocean (Figures 3.24 and 3.25 in Annex 3).
- In the NH midlatitudes the seasonal cycles of CA and CAE have a minimum in August, whereas the seasonal cycle of CT has a maximum. This means at the end of summer there is less cloudiness, and when clouds are present they are low-level clouds. Over land, AIRS-LMD and TOVS Path-B identify slightly more thin cirrus than the other data sets (indicated also by a lower CT compared to other data sets, Figure 3.25 in Annex 3). However, this could also be explained by less sensitivity to low-level clouds over land.
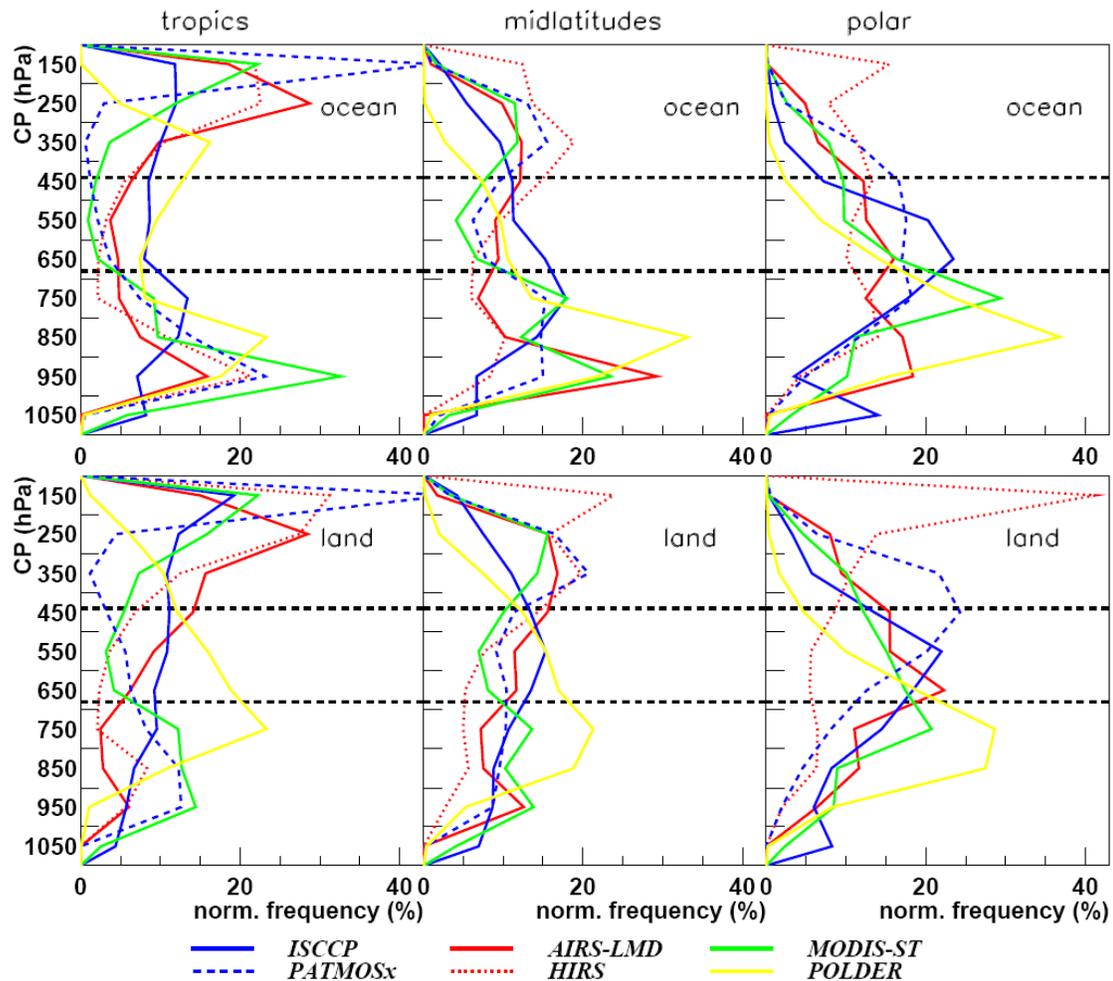
Figure 3.1.8: Probability density functions of cloud pressure CP in three latitude bands (tropics: 15°N-15°S; midlatitudes: 30°-60°; and polar: 60°-90°), separately over ocean and over land. Statistics for 2007 (2006 for HIRS), local observation time 1:30 PM (3:00 PM for ISCCP). The distributions are normalized by dividing the histograms by the number of cloudy samples (pixels).

After having compared monthly averages of various cloud properties, also stratified by height, we now explore the *probability density functions (PDFs) of cloud pressure and temperature*. These PDFs are computed by dividing the histograms available in the assessment database by the number of cloudy samples. Thus they reflect *how the detected clouds are vertically distributed within the atmosphere*. We only concentrate on quasi-simultaneous measurements in 2007 at 1:30 PM LT (and 3:00 PM for ISCCP) to avoid possible differences linked to different time periods and different diurnal sampling. Figures 3.1.8

39

and 3.1.9 compare PDFs of CP and of CT in tropics, midlatitudes and polar latitudes, separately over ocean and over land.
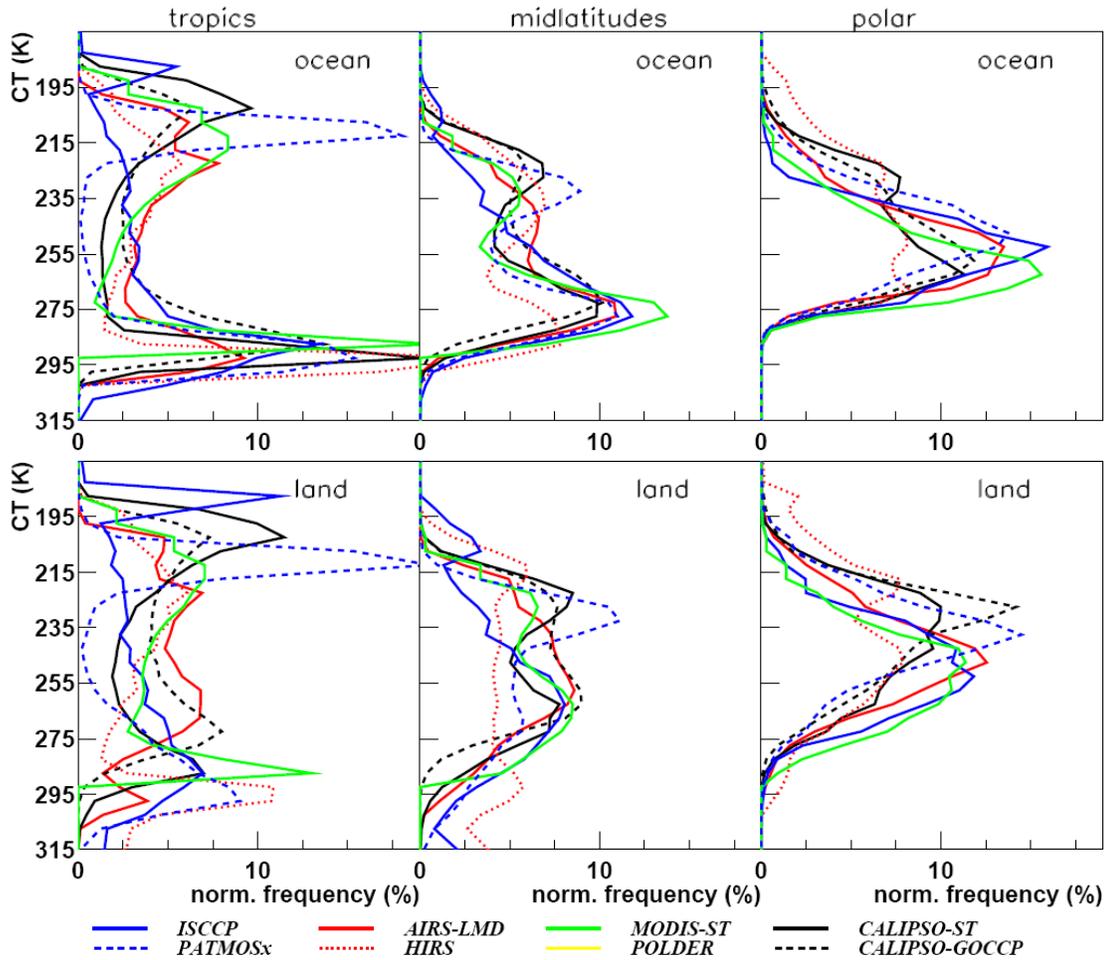
Figure 3.1.9: Probability density functions of cloud temperature CT in three latitude bands (tropics: 15°N-15°S; midlatitudes: 30°-60°; and polar: 60°-90°), separately over ocean and over land. Statistics for 2007 (2006 for HIRS), local observation time 1:30 PM (3:00 PM for ISCCP). The distributions are normalized by dividing the histograms by the number of cloudy samples.

The PDFs *show a bimodal structure, especially in the tropics*. This is the reason why average values of CP and CT may be ambiguous and why it is better to use, in addition to averages over all clouds, the height-stratified averages of the different cloud properties. The intervals for the height stratification are also indicated in Figure 3.1.8. The PDFs of CP confirm the results for height-stratified cloud amounts. The agreement in the shape of the PDFs is generally better over ocean than over land. *The bimodality and the spread in CP and CT decrease from tropics towards the poles, which is linked to the decrease of the tropopause and different cloud regimes*.

By comparing the shapes of the distributions in more detail, we note for *high-level clouds* in the tropics a *difference in the peak position*: near *150 hPa (around the tropopause)* from *MODIS-ST, PATMOS-x, HIRS-NOAA and ISCCP*, near *250 hPa* from *AIRS-LMD*, using a weighted c^2 method on spectral emissivities which leads to a 'radiative height' slightly lower than the one obtained from CO_2 slicing (see Annex I), and near *350 hPa* from *POLDER*, using the Oxygen A-band. Whereas *PATMOS-x* has a *very sharp peak at the tropopause*, the other distributions are broader. The peak positions for *low-level clouds* agree very well *over ocean* (*950 hPa*) among *MODIS-ST, PATMOS-x, HIRS-NOAA and AIRS-LMD*. POLDER produces a peak around 850 hPa, probably because partly cloudy low-level clouds

are not taken into account. The CP PDFs of ISCCP in the tropics are quite flat, whereas the CT PDFs of ISCCP show a similar bimodality as the other data sets. ISCCP first retrieves CT and then converts CT into CP by using retrieved operational TOVS atmospheric profiles (which may not always be simultaneous), thus adding uncertainty. Stubenrauch et al. (1999) show that the TOVS temperature profiles decreased the similarity of the CP distribution of ISCCP compared with the temperature profiles used in the TOVS Path B analysis. PATMOS-x also first determines CT. However, the bimodality in the tropics (which is the strongest for PATMOS-x with no contributions of middle-range temperatures) does not get lost. Whereas the ISCCP conversion of CT to CP and the AIRS-LMD conversion of CP to CT both used retrieved atmospheric temperature profiles, PATMOS-x, HIRS-NOAA and MODIS use NCEP reanalysis atmospheric profiles. It appears that in the tropics the NCEP profiles link warmer CT values (like the peak at 210 K) to smaller CP values (peak at 150 hPa), whereas by the use of the operational TOVS profiles in the ISCCP retrieval CT of about 190 K approximately leads to CP between 150 to 250 hPa.

Because CALIPSO-ST is the only data set providing CT at the top of the cloud, these PDFs should reach the lowest values. CALIPSO-ST first determines CZ and then transforms CZ to CT by using weather forecast atmospheric profiles, adding uncertainty to CT. Nevertheless, the peaks at low CT (corresponding to high-level clouds at least in the tropics) are at slightly lower temperature than those of PATMOS-x, MODIS-ST, HIRS-NOAA and AIRS-LMD. The peak at lower temperature for ISCCP in the tropics is explained by the fact that if the cloud is optically thin, the ISCCP retrieval sets the cloud height to just above the tropopause.

In general the PDFs of cloud temperature compare better than those of cloud pressure. The CP peaks around 150 hPa for HIRS-NOAA in the midlatitudes and polar latitudes, especially over land, seem to be outliers, wheras the differences in low CT are less striking. However, HIRS-NOAA first determines CP. Changes in the shape of distributions may occur when transforming one of the height correlated variables to another, because the relationship between pressure and temperature is not unique, but depends on latitude and season. *When using the different data sets, one has to consider which height variable was retrieved directly and which was deduced by atmospheric temperature profiles, adding additional uncertainties.*

3.1.3 Diurnal Variation

Clouds in contact with the surface, either directly embedded in the planetary boundary layer or via deep convection, exhibit systematic diurnal variations related to the daily cycle of surface solar heating (although some of the solar heat is directly deposited because of absorption by water vapor and aerosols concentrated near the surface). The ISCCP cloud products were designed to characterize basic cloud properties and their variations on all key time scales to elucidate cloud dynamical processes, including precipitation, and the effects of clouds on radiative fluxes. Therefore observations have been collected from the whole constellation of weather satellites, both polar orbiting and geostationary, providing global, 3-hourly coverage. Although many regional studies were done earlier, the first global analyses of diurnal cloud variations were based on the ISCCP products (Cairns 1995, Rossow and Cairns 1995).

Of all the cloud products considered here, the ISCCP products have the highest time resolution as all the others are based on observations from one or two sun-synchronous polar orbiting satellites. The scanning instruments provide samples with time intervals of 12 hr (6 hr if two polar orbiters are used), whereas the narrow-swath instruments provide sampling intervals of days to weeks.

In this report we are focusing on the averages and on the longer-term variations of cloud properties as represented by these data products but diurnal cloud variations can still affect these results in two ways: 1) Some instruments use a *different set of spectral channels for day and night retrievals*, hence the interaction of these differences with the intrinsic diurnal variations of clouds could introduce *systematic errors* in the results. 2) Some instruments have *different characteristics under day and night conditions or* are *limited to daylight conditions only*, which introduces a *sampling bias* in the results. The latter problem can affect all of the polar orbiter based products because of gradual changes in the time-of-day of orbit overpasses (orbit drift) or because

of changing numbers and/or mixtures of orbits included in the sample. Moreover, *because changes in the nature of the diurnal cloud variations may be one form of climate change*, the *limited sampling of polar orbiters may confuse such a change with other types of changes*.

Based on ISCCP results (Cairns 1995, Rossow and Cairns 1995, Rossow and Schiffer 1999), the most notable features of the diurnal cycle of clouds are significant differences between the phase of low-level cloud variations over ocean and land and between the phase of low-level and high-level cloud variations:

- Low-level clouds over ocean have maximum CA in early morning, while over land the maximum is in the early afternoon.
- High-level clouds have maximum CA in early to late evening.
- Mid-level clouds have maximum CA in late at night or early morning.

Because of the difficulty of ISCCP to detect all of the thinner cirrus at night, these results have been investigated using IR sounder (TOVS Path-B), exploiting the drifting afternoon polar orbiting satellites, in combination with the morning orbits (which do not drift much), to obtain another view of diurnal cloud variations (Stubenrauch et al*.,* 2006):

- Thicker cirrus over land in the tropics and midlatitude summertime have maximum CA in the evening.
- Cirrus increase during the afternoon and persist during the night.
- The varying proportions of thinner and thicker cirrus imply a gradual thickening of the cirrus clouds from late afternoon into the nighttime
- Mid-level CA exhibits a small increase during nighttime.

3.1.3.1 Day – Night Differences

Of the nine cloud data sets providing both daytime and nighttime results, three *change methods for cloud detection between day and night*: *ISCCP, PATMOS-x* and *MODIS-CE* use tests in the solar spectrum for cloud detection during daytime, in addition to tests in the thermal spectrum, but use either the same or different thermal radiance tests at night. Both ISCCP and MODIS-CE use the daytime IR tests without the visible channel tests at night; PATMOS-x uses a Bayesian training against CALIPSO but has fewer spectral channels at night. In polar regions MODIS-CE has a separate algorithm and ISCCP uses tests on an additional spectral channel. Because these algorithms determine cloud top height from CT, the absence of solar wavelength retrievals of COD at night also affects attempts to correct cloud height biases for IR-transparent clouds. The *IR sounders* (HIRS-NOAA, TOVS Path-B and AIRS-LMD) detect clouds and retrieve their properties by using the same IR channels day and night and retrieve CP from these measurements, so there should be *no artificial day-night differences* in CA and CP in these results. MODIS-ST also uses a similar IR cloud detection and cloud top retrieval procedure applied to its HIRS-like channels, so there should be no CA or CP differences between day and night. Note however, that these IR-only methods all use different procedures and *ancillary data* to obtain clear-scene radiances that have different treatments of the diurnal variations of land surface temperatures that can affect the results. *CALIPSO* uses the same measurements and algorithm day and night but may have a difference of detection sensitivity for the thinnest clouds because of *solar radiance noise during daytime* (see below).

Note that the original monthly mean ISCCP cloud products perform a correction for the day-night difference in algorithm by comparing the results from the two retrieval algorithms during daytime and extrapolating the differences into the nighttime; the version of ISCCP provided to the GEWEX Cloud Assessment database does not apply this correction in order to show the effects on cloud detection and cirrus cloud top heights more clearly.

Figures 3.1.10 shows differences between day and night among these nine products for CA, CAHR and CT, in three latitude zones, separately over ocean and over land. We only show data sets with measurements at 1:30 PM and 1:30 AM LT and compare with ISCCP at 3:00 PM and 3:00 AM LT. The day-night differences from HIRS-NOAA, TOVS Path-B, AIRS-LMD and MODIS-ST, as well as CALIPSO should in principle express only intrinsic day-night differences in CA, CAHR and CT. What is shown, particularly for CA, is that while these results differ by about the same amount as during daytime

(although differences over land areas approach 0.10), the relative positions of the points are not the same. In other words, the ***daytime differences and the day-night differences among the results*** with no algorithm changes do not show a consistent pattern reflecting the differences of instruments and retrieval methods, but rather ***show "random" differences of a few percent***. Ignoring the possibility of a detection sensitivity difference between day and night for CALIPSO, Figure 3.1.10 does not show a consistent association of CALIPSO results with the four IR sounder products particularly CAHR and CT over tropical land areas. This might, in fact, indicate a ***detection sensitivity difference in the CALIPSO results***, even though the IR sounder products also exhibit more scatter in this case, because the CALIPSO results differ by even more. The ISCCP and MODIS-CE results show a much larger positive day-night difference in CA over higher latitude land areas than the IR sounder and CALIPSO products, whereas the PATMOS-x exhibits smaller differences. Note that these differences do not track the CALIPSO results, even though the latter was used to train the algorithm.

Day-night differences in CAHR for ISCCP are large and positive, approaching 25% in the tropics over ocean and land and nearly 20% over higher latitude land areas; these differences are expected because this version of the ISCCP results (not the actual ISCCP D2 monthly product) does not correct for the lack of a COD-based adjustment of CT/CP and CAHR. In contrast the MODIS-CE shows somewhat smaller (10 – 20%) negative differences at all latitudes. These results are reflected in the CT differences. PATMOS-x results are similar to MODIS-CE, despite the tuning to CALIPSO.

day – night differences in CA, CAHR and CT
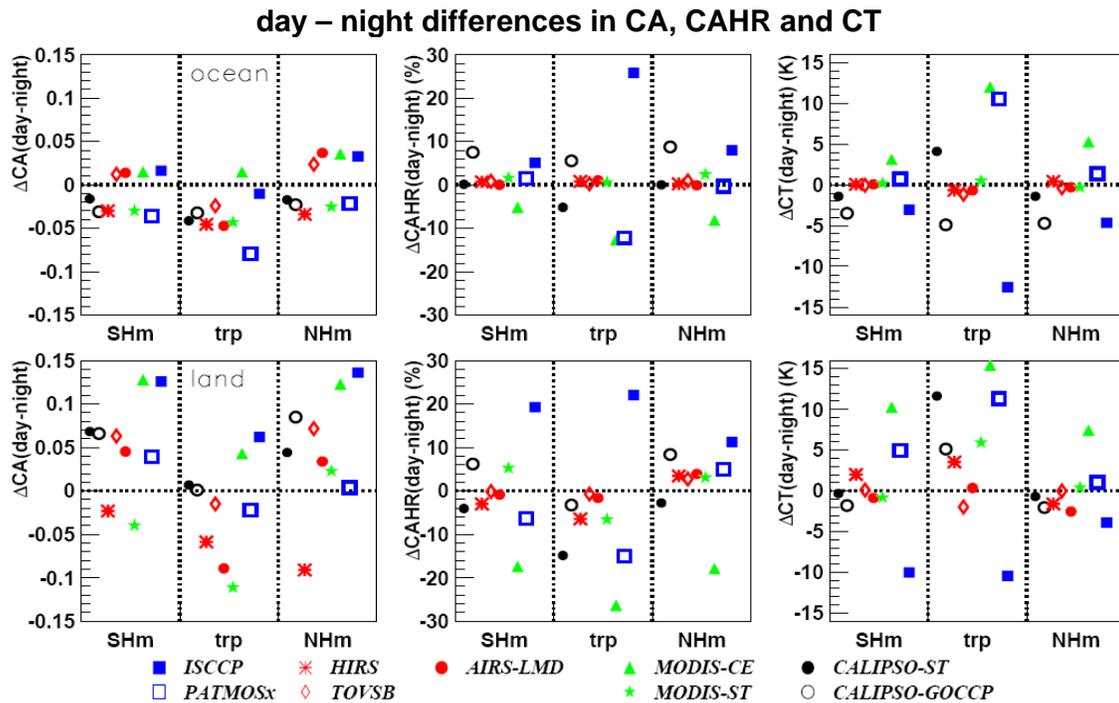
Figure 3.1.10: Day – night difference of cloud properties (cloud amount CA, high-level cloud amount, relative to CA, CAHR and cloud temperature CT, from left to right), separately over ocean (top) and over land (bottom) and for three latitude bands (30°S-60°S, 15°S-15°N, 30°N-60°N). Retrievals are compared between 1:30 PM and 1:30 AM LT (3:00 PM – 3:00 AM LT for ISCCP).

3.1.3.2. Diurnal Sampling Differences

Figure 3.1.11 presents differences between cloud properties (CA, CAHR and CT) retrieved in the afternoon and those retrieved in the morning, in three latitude zones, ocean and land separately. Retrievals are compared between 3:00 PM and 9:00 AM LT for ISCCP, 1:30 PM and 10:30 AM for MODIS (AQUA and TERRA satellite) and between 1:30 PM and 7:30 AM for PATMOS-x, HIRS and TOVS. These results provide an estimate of ***intrinsic cloud differences due to diurnal cycle*** since the algorithms are the same for both daylight times. The ***CA results over ocean exhibit a small average difference of about -0.02 to -0.01 for almost all products, consistent in sign with the known diurnal variations of low-level cloudiness*** (Cairns 1995) and no significant difference in CT. ***The differences in CAHR are slightly larger in magnitude (0.02 – 0.03) and generally positive consistent in sign with the known diurnal variations of cirrus*** (Cairns 1995). The situation over ***land areas*** shows a ***larger dispersion of results but still general agreement on the sign of the difference consistent with previous results***: positive CA difference of 0.04 – 0.08, nearly zero differences in CT (± 3 K) and small differences in CAHR with a tendency towards positive values. Notable outliers are HIRS-NOAA for CA over land, especially in the northern hemisphere – a disagreement as to sign, and PATMOS-x for CA and CAHR in the northern hemisphere – a disagreement as to magnitude and CT in the tropics, and ISCCP for CAHR over tropical land areas – a disagreement as to magnitude.

Afternoon – Morning Differences in CA, CAHR and CT
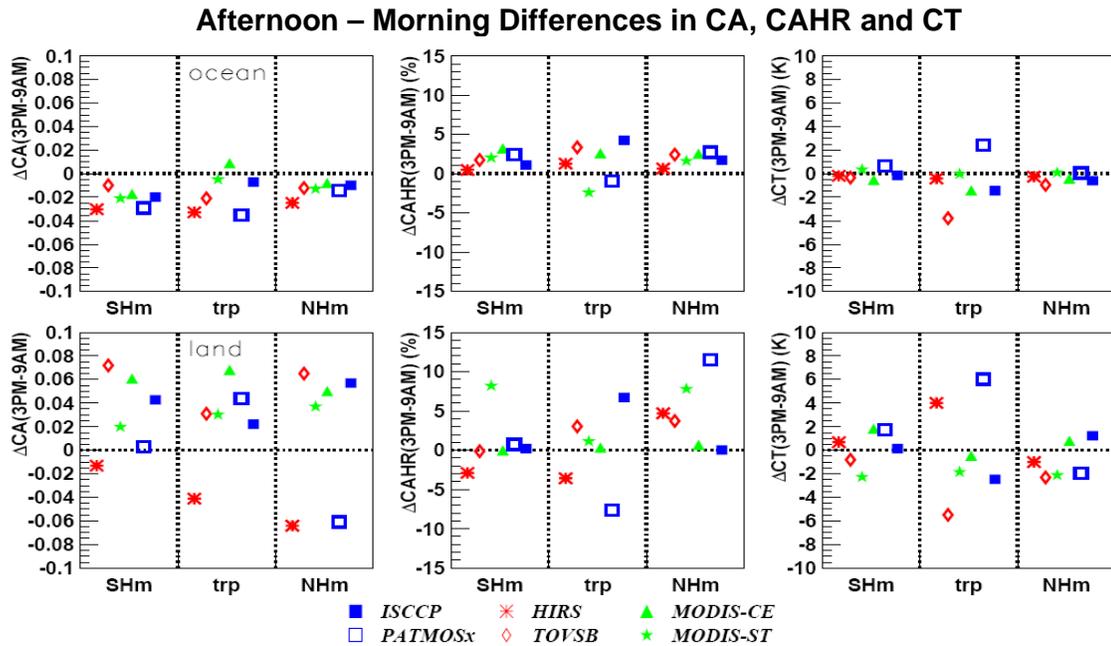
Figure 3.1.11: Afternoon – morning difference of cloud properties (CA, CAHR and CT, from left to right), separately over ocean (top) and over land (bottom) and for three latitude bands (30°S-60°S, 15°S-15°N, 30°N-60°N). Retrievals are compared between 3:00 PM and 9:00 AM LT for ISCCP, 1:30 PM and 10:30 AM LT for MODIS and between 1:30 PM and 7:30 AM LT for PATMOS-x, HIRS and TOVS.

Figure 3.1.12 shows the average differences between cloud properties when averaged over afternoon orbits (1:30 PM / 1:30 AM LT for NOAA satellites and AQUA) and those averaged over morning orbits (7:30 AM / 7:30 PM LT for the NOAA satellites and 10:30 AM / 10:30 PM for TERRA), where for some products the results are a mixture of the day and night algorithms. In general, the ocean differences are very small (< 0.02) for CA and even CAHR (< 0.02, except for MODIS-ST in the tropics) and CT (< 2 K). Over land differences are slightly larger, but also much smaller than the differences in Figures 3.1.10 and 3.1.11. Nevertheless, over land, one observes some disagreements among the products: for CA, most products show a negative difference of about 0.03 – 0.05 but HIRS-NOAA shows a positive difference and PATMOS-x results differ with latitude band. For CAHR the differences are distributed over ± 0.02 –

0.04 – there is not a consistent pattern, with a sign difference between HIRS-NOAA and TOVS Path-B in the NH midlatitudes (not seen in CT) over land areas.

All of the current cloud data products that report cloud optical and bulk microphysical properties from measurements in the solar spectrum are limited to daytime measurements. As there is some evidence for morning-afternoon differences in these properties of low-level clouds (Minnis et al., 1992; Han et al., 1995 and references therein), there is no reason to suppose that other cloud properties cannot vary diurnally. Hence our current knowledge of COD, CRE, CLWP and CIWP is biased to daytime results. The IR sounder products, which can determine emissivity for the optically thinner clouds, suggest more nighttime high-level clouds than daytime in the tropics (Stubenrauch et al., 2006), which also implies a decrease of CEM on average.

afternoon orbit – morning orbit differences of CA, CAHR and CT
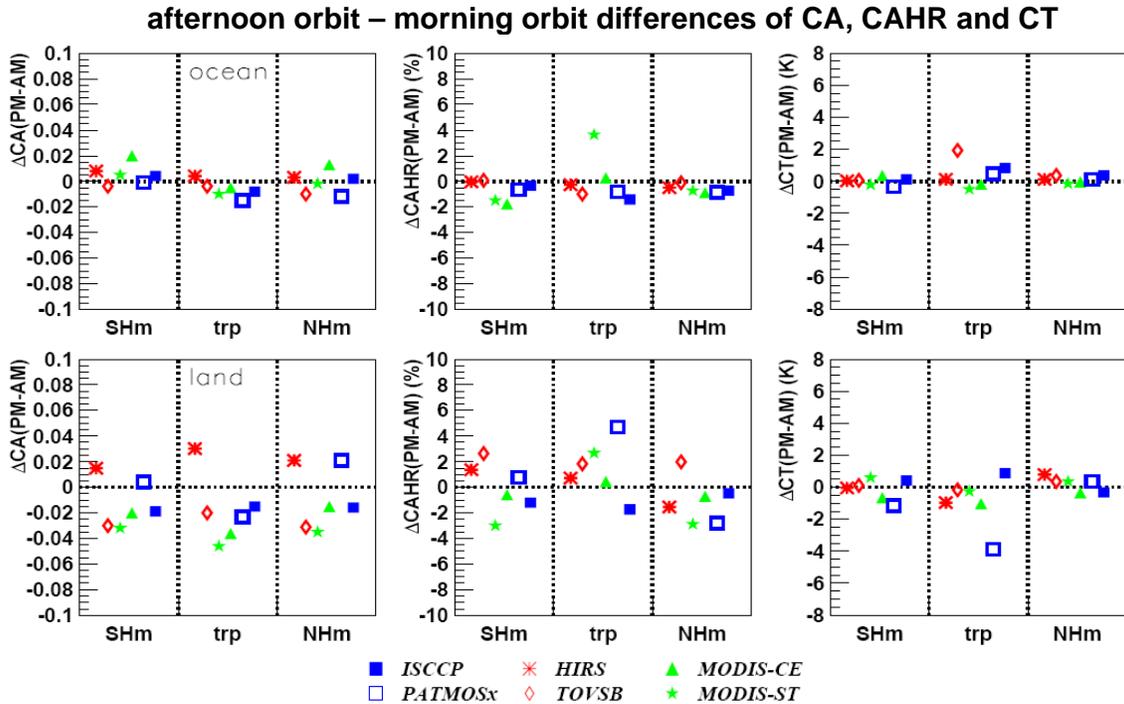
Figure 3.1.12: Afternoon orbit – morning orbit difference of cloud properties (CA, CAHR and CT, from left to right), separately over ocean (top) and over land (bottom) and for three latitude bands (30°S-60°S, 15°S-15°N, 30°N-60°N). Retrievals are compared between (3:00 PM + 3:00 AM) and (9:00 AM + 9:00 PM) LT for ISCCP, (1:30 PM + 1:30 AM) and (10:30 AM + 10:30 PM) LT for MODIS, AIRS and CALIPSO and between (1:30 PM + 1:30 AM) and (7:30 AM + 7:30 PM) LT for PATMOS-x, HIRS and TOVS.

Even without algorithm differences, diurnal sampling differences appear to cause some part of the differences in CA and CAHR shown in Figure 3.1.10, especially over land, of up to a few times 0.01. If these data products are to be used to study long-term variability, then any changes in the diurnal sampling can induce spurious interannual variability. The current versions of PATMOS-x and HIRS-NOAA are based on measurements from differing mixtures of morning and afternoon polar orbiting satellites, where the afternoon satellites exhibited strong drifts before NOAA-16 (Figure 2.1); when only using morning satellites, the drift effect is minimal for this product. The MODIS-ST, MODIS-CE, CALIPSO, MISR and POLDER are all onboard satellites with much better controlled orbits, so drift effects are also minimal for these products. The more complex diurnal sampling of the ISCCP product has been checked for anomalies in the ratio of day and night pixels: this ratio is on average 0.62 and varies slowly over the record from about 0.60 prior to 1995 to about 0.64 afterwards (see Appendix 2). As Figure 3.1.10 shows, the day-night differences in CA are < 0.04 so the spurious change in CA that could be induced by this change of diurnal sampling is < 0.005.

3.2 Cloud Optical and Bulk Microphysical Properties

Whereas cloud droplets in liquid clouds are spherical, ice crystals exist in a diversity of shapes. The refractive index of liquid and ice particles is also different but well-known. These facts mean that cloud optical depth and bulk microphysical property retrievals are dependent on distinguishing the cloud thermodynamical phase. Therefore we present statistics for cloud optical depth and bulk microphysical properties separately for liquid and for ice clouds.

Liquid and ice clouds are distinguished by polarization measurements (POLDER, CALIPSO), by cloud temperature (ISCCP: ice clouds CT < 260 K, AIRS-LMD, TOVS Path-B: ice clouds CT < 230 K, excluding mixed phase clouds) or by use of multi-spectral information (PATMOS-x, MODIS-ST, MODIS-CE and ATSR-GRAPE). Figure 3.2.1 presents global averages of fractions of liquid clouds and ice clouds relative to all detected clouds, as well as the differences between ocean and land. For all data sets the sum of CAWR and CAIR is 100%, except for AIRS-LMD and TOVS Path-B for which about 35% correspond to clouds of mixed phase (with temperature between 230 K and 260 K). Differences seem to depend much more on the sensitivity to the presence of thin cirrus than on the technique of distinguishing between liquid and ice clouds, as illustrated by the comparison of results from CALIPSO-ST and POLDER.

There are 10-20% more liquid clouds over ocean and about 5 to 15% more ice clouds over land. Only ATSR-GRAPE is an outlier (with less ice clouds over land than over ocean), probably linked to different retrieval success over land and over ocean.
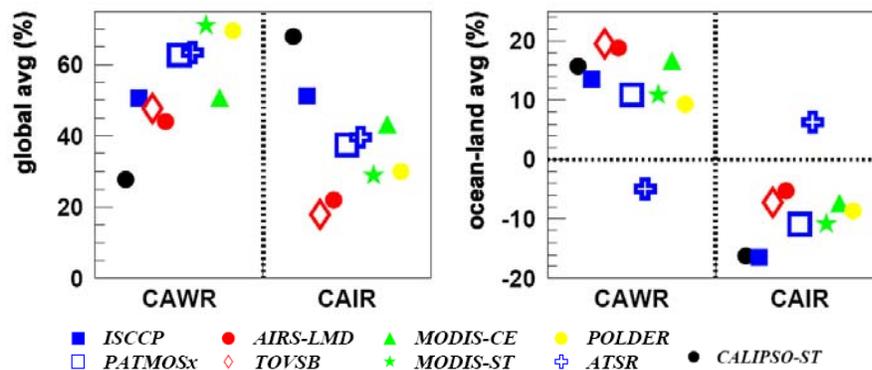
Figure 3.2.1: Left: Global averages of amount of liquid clouds (CAWR) and of ice clouds (CAIR) relative to total cloud amount. Their sum adds up to 100%, except for AIRS-LMD and TOVS Path-B which exclude mixed phase clouds. Right: Differences between ocean and land. Statistics at 1:30 PM LT (3:00 PM for ISCCP and 10:30 AM for ATSR-GRAPE).

Cloud optical depth (COD) is in general determined from VIS radiances and therefore only available during daytime. COD and CEM are functions of cloud water path (CWP) and effective particle radius (CRE). Whereas cloud water path strongly influences COD and CEM, the effective cloud particle size is distinguishable by spectral differences in the solar or thermal domain. Decreasing effective cloud particle size (averaged over a size distribution within the cloud) at a constant water path makes the solar albedo increase.

PATMOS-x, MODIS-ST, MODIS-CE and ATSR-GRAPE retrieve COD and CRE simultaneously. In a second step CWP is computed as a function of COD and CRE. (PATMOS-x, however, does not use the retrieved CRE for the computation of ice water path, but a parameterization based only on CODI.) ISCCP provides CWP directly from COD by assuming a value of CRE; here the ISCCP values of CRE are reported from a separate retrieval of CRE and COD from spectral reflectance differences. The TOVS Path-B and AIRS-LMD methods are based on spectral emissivity differences between 8 and 12 μm, making use of retrieved cloud pressure. IR methods are limited to semi-transparent ice clouds. Because

ice particles are in general not spherical, the retrieval of effective ice crystal radius (CREI) depends on assumptions on ice crystal shapes.

3.2.1 Cloud Optical Depth

3.2.1.1 Global Averages and Distributions

The monthly means of COD given in the cloud assessment database were created as radiative averages. Figure 3.2.2 presents global mean values of COD averaged over all clouds, as well as separately averaged over liquid clouds, ice clouds and high-level ice clouds. Differences between ocean and land are also shown.
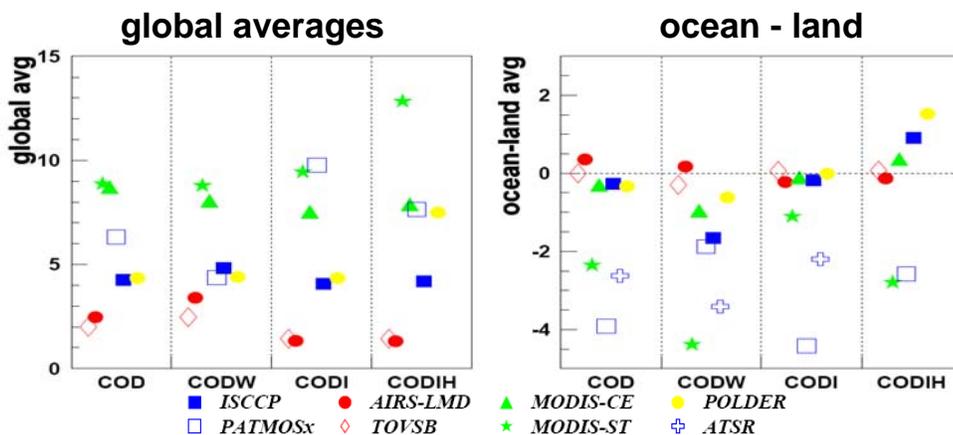
Figure 3.2.2: Left: Global averages of cloud optical depth (COD), separately for all clouds, for liquid clouds (W), for ice clouds (I), and for high ice clouds (IH). Right: Differences between ocean and land. Statistics at 1:30 PM LT (3:00 PM for ISCCP and 10:30 AM for ATSR-GRAPE).

Considering the Earth's planetary albedo and an average cloud amount larger 0.65, we know already that the average cloud optical depth has to be less than 5 (Zhang *et al.* 2004).

The data sets produce ***average COD between 4 and 9.*** Exceptions are ATSR-GRAPE with an average of 20 (off scale in Figure 3.2.2) and AIRS-LMD / TOVS Path-B with averages of 2.5 / 2.0. ***COD from IR sounders is given only as an indication*** for comparison. It is determined from CEM using the aproximate formula ***-2 x ln(1-CEM)***, and therefore is ***underestimated because CEM saturates at 1 for COD > 10***. Another source of underestimation is the ***coarse spatial resolution***. The ***ATSR-GRAPE*** averages are unrealistically large, most probably because the retrieval method rejects solutions with small COD (***successful retrieval only for 40% of all clouds***).

ISCCP provides a global average of about 4, with a slightly larger average for liquid clouds than for ice clouds. Note that this value produces about the right planetary albedo in radiative flux calculations (Zhang *et al.* 2004). Global averages from POLDER are similar, except for a larger CODI of high-level clouds of about 8, the latter linked to missed identifications of high-level clouds with COD < 2, when low-level clouds are underneath. COD from MODIS is on average about 9, again with similar averages for liquid and ice clouds. MODIS-ST eliminates about 20% of the clouds (assumed to be linked to partly cloudy FOV's and cloud edges, but also some optically thin cirrus) before determining COD, and therefore COD is biased high. A quantitative assessment of the impact of partly cloudy scene discrimination by the MODIS-ST relative to ISCCP COD is discussed by Pincus et al. (2012). Even though the MODIS-ST overall cloud fraction from the cloud mask is significantly larger than that from MODIS-CE, MODIS-CE performs retrievals on 7.5% more cloudy scenes (Minnis et al. 2011b). Additionally, MODIS-CE Ed2 limits the maximum COD retrieval to 128 compared to MODIS-ST, which has an upper limit of 100. These limits can result in differences (particularly for high-level ice clouds, among which are the thickest cumulonimbus clouds) and provide a compelling case for the use of

histograms in understanding differences in averages. Whereas the PATMOS-x COD average agrees with ISCCP for liquid clouds, COD for ice clouds is larger and similar to the values of MODIS. This could be linked to a difference in retrieval method: ISCCP assumes typical particles sizes for the retrieval of COD, whereas PATMOS-x determines COD in combination with CRE. The very low averages of AIRS-LMD and TOVS Path-B for ice clouds (of about 1.3) has four reasons: COD can not exceed 10 when obtained from CEM, ice clouds are defined as clouds with CT < 230 K (at these temperatures clouds are often optically thin), the coarse spatial resolution leads to a slight underestimation of COD (see liquid clouds) and a higher sensitivity to thin cirrus leads also to a lower average.

Ocean – land differences partly reflect cloud detection sensitivity differences: larger averages over land than over ocean could mean that optically thin clouds over land are more often missed. ATSR-GRAPE, PATMOS-x and MODIS-ST show the largest differences.
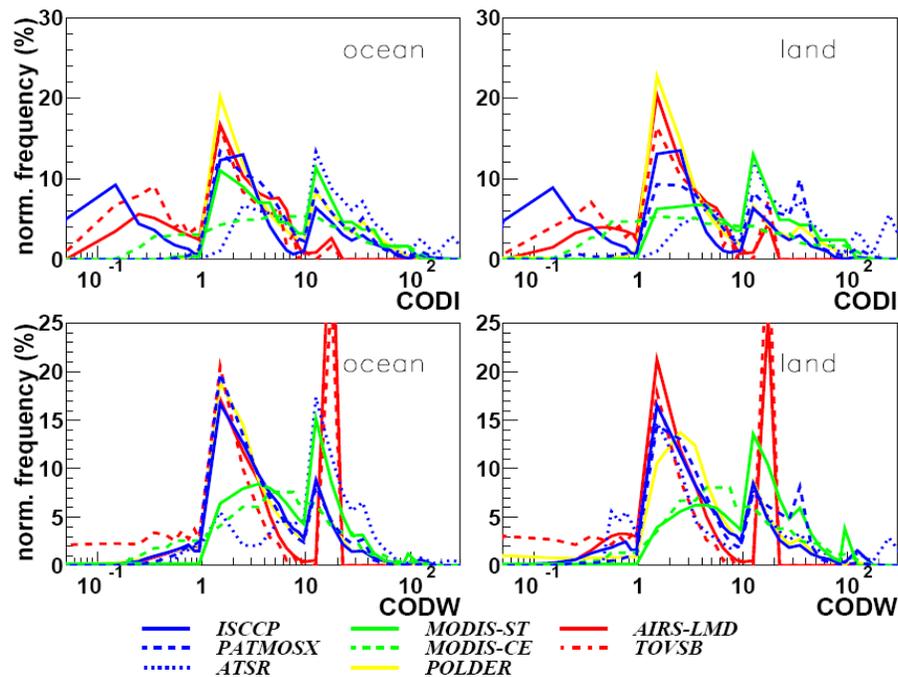
Figure 3.2.3: Normalized frequency distributions of cloud optical depth of liquid clouds (CODW) and of high-level ice clouds (CODI) over ocean (left) and over land (right). Statistics at 1:30 PM LT (3:00 PM for ISCCP and 10:30 AM for ATSR-GRAPE).

Figure 3.2.3 presents probability density functions of CODW and CODI, separately over ocean and over land. The distributions are again normalized in such a way that their integrals add to 100%. These distributions agree quite well, exhibiting the same multi-modal shape. One observes that the *contributions from optically thin clouds (COD < 1)* are *more important for ice clouds than for liquid clouds*, that the *main contributions* are *from clouds with COD between 1 and 10* and that a *third contribution* is *from clouds with COD > 10*. *The relative contributions of these partitions reflect the differences in the averages* in Figure 3.2.2. Compared to the other data sets the COD distributions, especially CODI, of ATSR-GRAPE are shifted towards much larger values, because successful retrieval is biased towards optically thick clouds. The narrow peak around 10 of AIRS-LMD /TOVS Path-B CODW can be explained by the transformation from CEM which leads to no sensitivity for values larger than 10.

3.2.1.2 Seasonal Variations

The seasonal cycles of CODW and CODI are indicated as relative differences (in %) in Figure 3.2.4, separately for the four latitude bands of 30° from 60°S to 60°N. ***The general behaviors of CODI are similar***, except for PATMOS-x, with a spread of about 20%. The ISCCP results show slightly larger amplitudes in midlatitudes than the other products. ***The seasonal cycle of CODI in the tropics has an amplitude of about 30 – 40%, linked to the transition of the ITCZ. In the midlatitudes CODI shows a maximum during winter, linked to winter storms. The general behavior of CODW is also similar among the data sets at low latitudes,*** except for ATSR-GRAPE, ***but exhibits more dispersion at midlatitudes.*** Notable outliers are MODIS-CE in the southern hemisphere winter and PATMOS-x in the northern hemisphere winter.
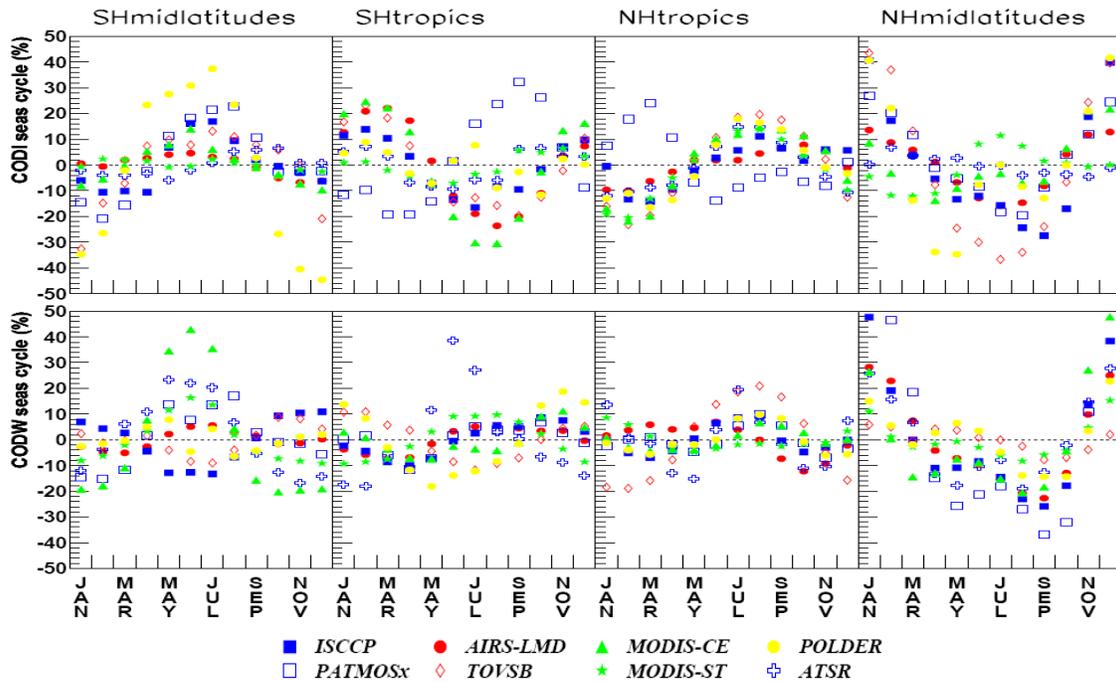
Figure 3.2.4: Seasonal variation of CODW and CODI in four latitude bands (60S-30S, 30S-0°, 0°-30N, 30N-60N), derived as the difference between monthly mean and annual mean, divided by annual mean (in %). Statistics at 1:30 PM LT (3:00 PM for ISCCP and 10:30 AM for ATSR-GRAPE).

3.2.1.3 Cloud Types
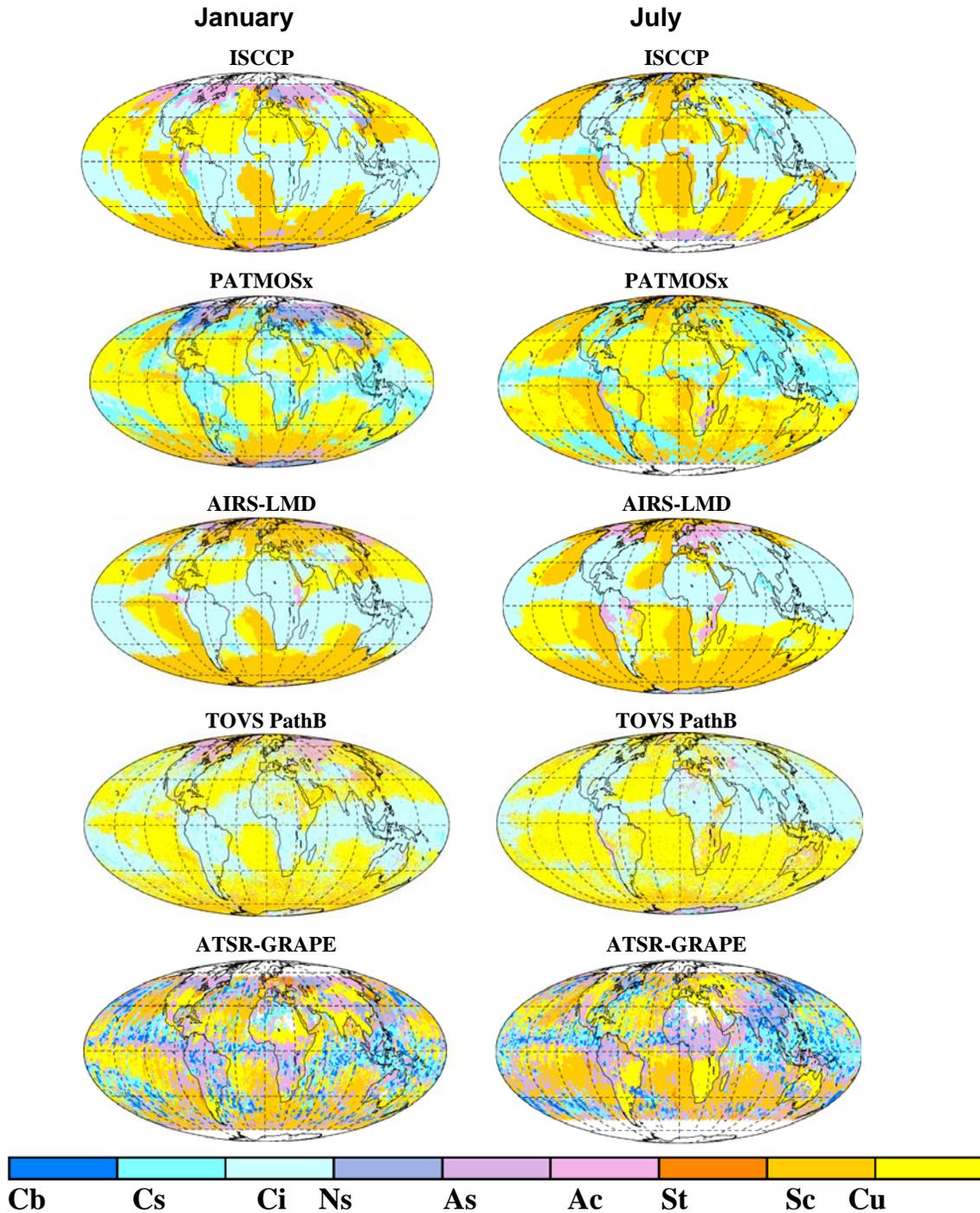
Figure 3.2.5: Geographical maps of most frequent cloud type (as defined in Figure 1.2) in January (left) and in July (right). Statistics at 3:00 PM LT for ISCCP, 1:30 PM LT for PATMOSx, AIRS-LMD and TOVS PathB, 10:00 AM LT for ATSR-GRAPE.

Several data sets also provide per 1° latitude x 1° longitude grid two-dimensional histograms of COD and CP, as defined by ISCCP and largely used for model evaluation (see also Figure 3.27). These two-

dimensional histograms give an impression how the retrieved clouds are distributed in the atmosphere. They do not add information to the intercomparison analyses using height stratification and PDFs, but they may be very useful for other studies. Cloud types have been defined from these two-dimensional histograms as in Figure 1.2. As an illustration, Figure 3.2.5 presents geographical maps of the most frequent of these cloud types, separately in January and in July. The geographical patterns agree quite well. However, the retrieval filtering by ATSR-GRAPE towards optcally thicker clouds is reflected by much less cirrus as most frequent cloud type, especially over land.

3.2.2 Bulk Microphysical Properties

3.2.2.1 Global Averages and Distributions

Figure 3.2.6 presents global averages of effective cloud particle radius and cloud water path, separately for liquid clouds and for ice clouds. Relative differences of these quantities between ocean and land are also shown.
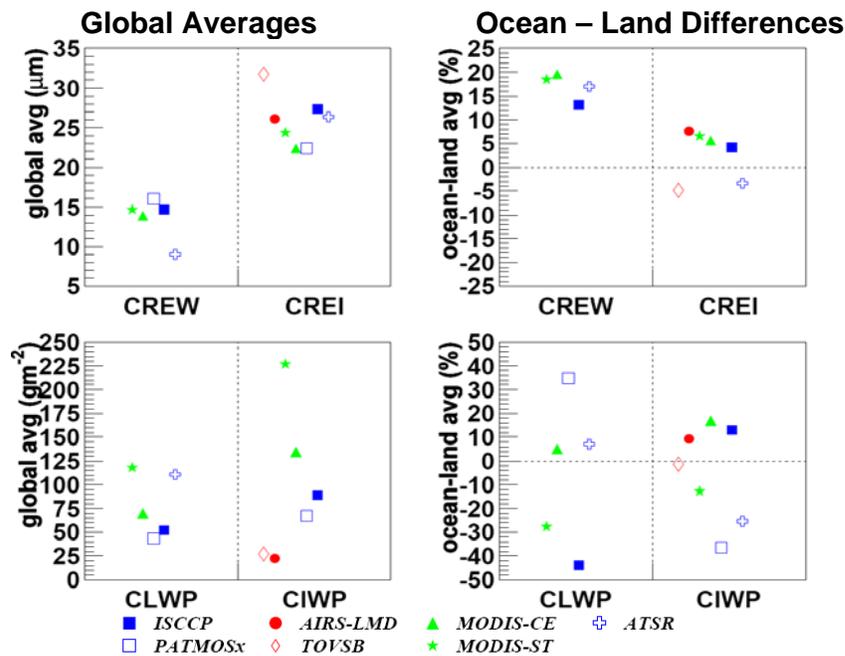
Figure 3.2.6: Left: Global averages of effective cloud particle radius (CRE, top) and cloud water path (CWP, bottom), separately for liquid clouds and for high-level ice clouds (ice clouds for MODIS-ST and PATMOSx). Right: Differences between ocean and land. Statistics at 1:30 PM LT (3:00 PM for ISCCP and 10:30 AM for ATSR-GRAPE).

Average day-to-day variabilities of CLWP, CIWP, CREW and CREI, are presented in Figure 3.2.7, also separately over ocean and land.
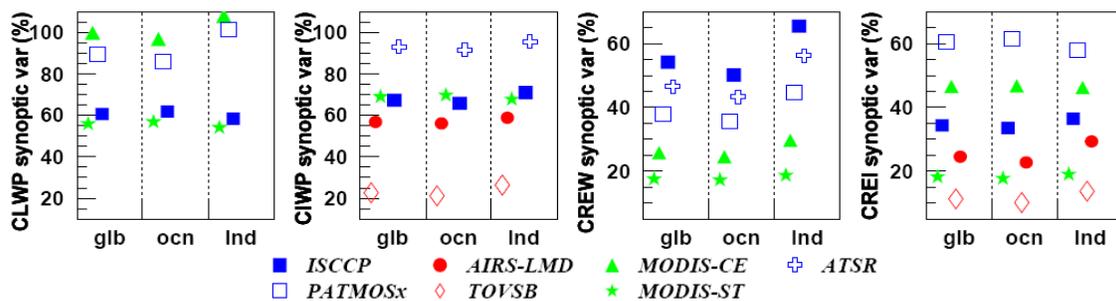
Figure 3.2.7: Global averages of synoptic variabilities of CWP and CRE (in %), separately for liquid clouds and for ice clouds.

Effective particle radii of liquid clouds and of high-level ice clouds agree quite well, with global averages of 14 μm (±1 μm) and 25 μm (±2 μm), respectively. Outliers are ATSR-GRAPE with average CREW of 9 μm and PATMOS-x and TOVS Path-B with average CREI of 10 μm and 32 μm, respectively.

Effective cloud droplet radius is on average about 15 – 20% larger over ocean than over land, whereas the difference in effective ice crystal radius is only about 5%.

Day-to-day variabilities in CRE vary between 20 and 60% for liquid clouds (slightly larger over land) and between 10 and 60% for ice clouds. This quantity provides some measure of sampling noise and of sensitivity. It is smaller for sub-sampled data sets (except ATSR-GRAPE), because the retrieval filtering leads to clouds with more similar properties (more opaque in the case of MODIS-ST and more semi-transparent for AIRS-LMD and TOVS Path-B).

The spread in cloud water path between the different data sets is large, especially for ice clouds. This is partly because this variable is determined from the others, apparently driven mostly by COD differences, and partly because the cloud selection for the retrieval of optical properties differs. ISCCP, PATMOS-x and MODIS-CE provide retrievals for all clouds which have been detected. MODIS-ST optical and bulk microphysical properties are retrieved of 80% of the detected clouds (Pincus *et al.* 2012), leaving out probable cloud edges and uncertain clouds. This leads to a positive bias in COD and CWP. The optimal estimation method applied in the ATSR-GRAPE retrieval also leads to a sub-sampling of clouds, leaving out thin cirrus and warm low-level clouds and leading to an even larger positive bias in COD and CWP compared to the other data sets, because the retrieval is only successful for 40% of all clouds. On the other end, IR sounders, with a coarse spatial resolution and a retrieval based on spectral absorption of ice crystals, values are only provided for semi-transparent ice clouds (CEM < 0.85). The lower CEM limit is reduced from 0.3 for TOVS to 0.2 for AIRS because of the better spatial resolution of the retrieval (15 km instead of 100 km).

Considering data sets with no cloud sub-sampling, global averages of cloud water path vary from 30 to 60 gm^{-2} for liquid clouds and from 60 to 120 gm^{-2} for ice clouds. The latter result may seem surprising, but the larger value can be explained by the inclusion of the very large WP values of relatively rare storm clouds in this category, which are treated as all ice even though they may be liquid in the lower levels. However, ocean – land differences in CWP are not consistent among the different data sets and average day-to-day variabilities are large. Figures 3.2.8 and 3.2.9 present probability density functions of effective droplet radius CREW, cloud liquid water path CLWP, effective ice crystal radius CREI and cloud ice water path CIWP, separately over ocean and over land. The distributions, normalized to an integral of 100%, are not Gaussian.

CREW PDFs of ISCCP, MODIS-ST, MODIS-CE and ATSR-GRAPE agree quite well over ocean, with a peak around 11 μm. The ISCCP PDFs have *two smaller peaks, one around 2 μm and another around 40 μm,* which are the limiting values of a retrieval using 3.7 μm radiances. The lack of these peaks in the MODIS-based results may be due to the subsetting criteria. The contribution of both cases is small, slightly larger over land. PDFs are similar over land, with maxima between 9 and 11 μm. Only the ATSR-GRAPE PDF is shifted towards too small values.

CLWP PDFs of all data sets have one peak around 70 gm^{-2}. A *second peak* around smaller values (1.5 gm^{-2} for PATMOS-x and ATSR-GRAPE and *8 gm^{-2} for ISCCP*) may partly stem from partly cloudy pixels or cloud edges, because CLWP of MODIS-ST (retrieving bulk microphysical properties only for well confirmed clouds) decreases smoothly towards smaller values. A very small peak around 700 gm^{-2}, slightly stronger over land than over ocean, is also present in all data sets.
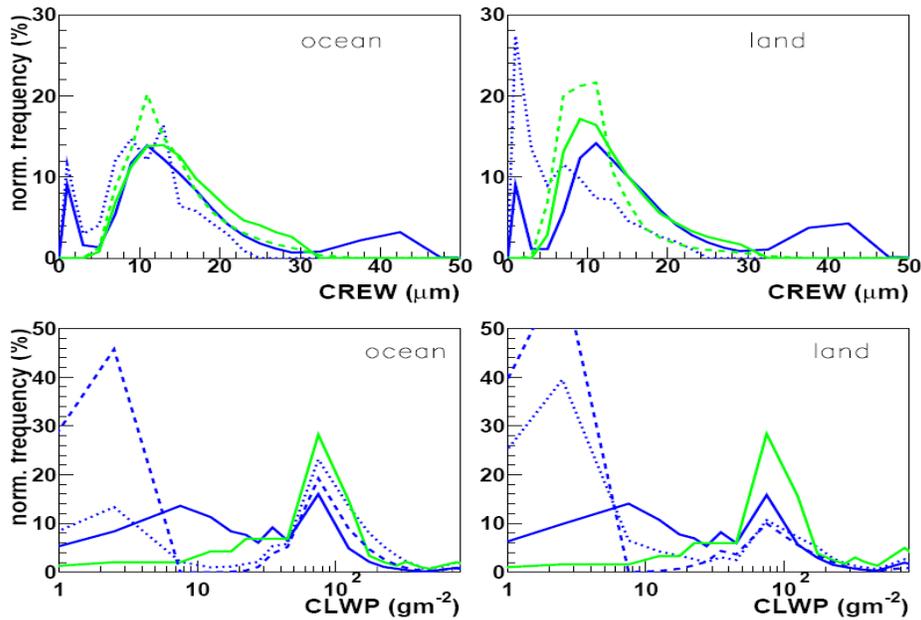
Figure 3.2.8: Normalized distributions of effective droplet radius (CREW, top) and cloud liquid water path (CLWP, bottom), separately over ocean (left) and over land (right). Statistics over the whole globe, daytime observations.

CREI PDFs of ISCCP, PATMOSx, AIRS-LMD and TOVS Path-B have a peak around 32 µm with a plateau down to 20 µm, whereas MODIS-ST produces a broader distribution with an average of about 25 µm. The spectral absorption increases slightly with wavelength from 1.6 µm (ATSR), 2.1 µm (MODIS-ST), 3.7 µm (ISCCP, PATMOSx, MODIS-CE) to 8.7 µm (AIRS, TOVS), so that by using shorter wavelengths one would expect to retrieve CREI slightly deeper in the cloud. This would lead to larger CREI (ice crystal size increases from cloud top to cloud base due to aggregation processes) for the same cloud statistics. When considering only semi-transparent cirrus, even IR channels get contributions from all levels within the cloud. Therefore, larger CREI values of ISCCP/PATMOSx/AIRS-LMD/TOVS Path-B compared to those of MODIS-ST may be again explained by sub-sampling of optically thicker clouds by MODIS-ST for which CREI would correspond only to the upper part of the clouds. The PDF of ***ATSR-GRAPE*** has a narrow peak around 25 µm, but does not appear to capture all of the natural variability. A second smaller peak around 18 µm produced by ISCCP can be probably explained by misidentified liquid clouds (or mixed phase clouds), because smaller values are more often linked to small COD (according to the CODI-CREI histograms). The CREI distribution of MODIS-CE is quite flat with a large amount of small values, especially over land: PATMOS-x also has a larger contribution of small values.

The CIWP PDFs depend strongly on sub-sampling: ISCCP provides a distribution with a large peak around 5 gm^{-2} corresponding to cirrus, a broad plateau between 10 and 100 gm^{-2} and a small peak at very large values, the latter corresponding to strong convective clouds. The PATMOS-x distributions are similar, with a larger peak at small values, linked to thin cirrus. Both data sets retrieve bulk microphysical properties of all detected clouds. The effect of retrieval filtering can be seen in the shift towards larger values in the distributions of MODIS-ST and ATSR-GRAPE which sub-sample optically thicker clouds, with peaks around 70 gm^{-2} and 700 gm^{-2}. The existence of these two peaks is in agreement with ISCCP and PATMOS-x. Sub-sampling of semi-transparent ice clouds (CEM < 0.85) by TOVS Path-B and AIRS-LMD leads to distributions in between, with CIWP not exceeding 100 gm^{-2}. Whereas the coarse spatial resolution of TOVS made it necessary to set a lower CEM limit at 0.3, this limit was reduced to 0.2 in the AIRS retrieval, leading to a peak at lower IWP, but at slightly larger value (10 gm^{-2}) as for ISCCP and PATMOS-x (5 gm^{-2}). The effect on the PDFs of CREI and CIWP when changing the limit for ice clouds from CT < 230 K to 260 K is negligible, probably because of the strong CEM limit.
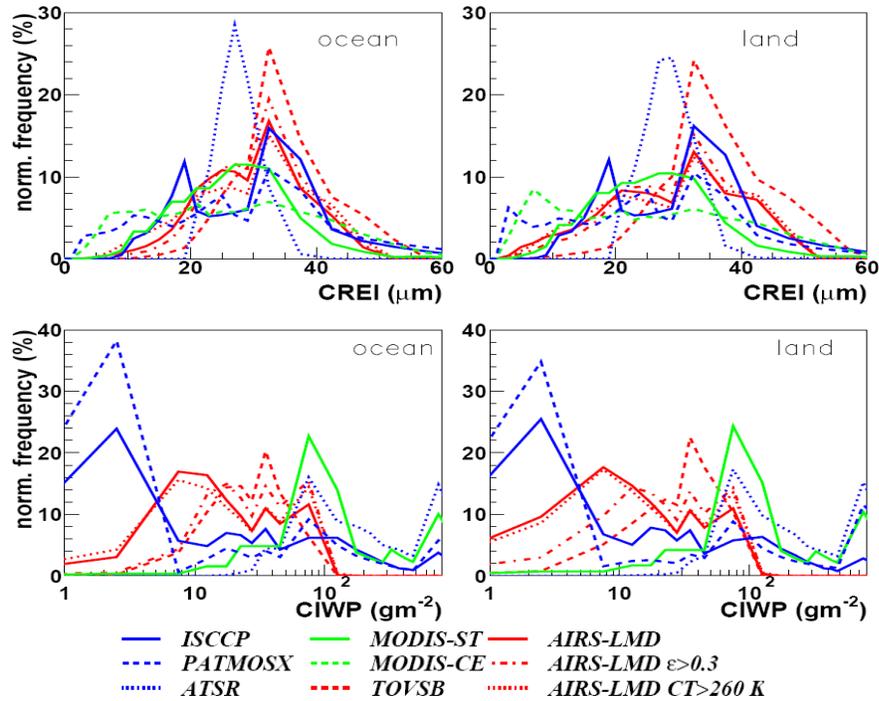
Figure 3.2.9: Normalized distributions of effective ice crystal radius (CREI, top) and cloud ice water path (CIWP, bottom), separately over ocean (left) and over land (right). Statistics over the whole globe, daytime observations. To study the sensitivity to limits in CEM (or COD) and in temperature (ice definition), distributions for AIRS-LMD (CEM>0.2 and CT>230K) are also shown for CEM > 0.3 (same limit as TOVS Path-B) and for CT > 260K (same limit as ISCCP).

3.2.2.2 Latitudinal and Seasonal Variations

Because the distributions are not Gaussian and their shapes also depend on sub-sampling, we illustrate latitudinal variations in Figure 3.2.10 by comparing CLWP, CREW, CIWP and CREI probability density functions between tropics, midlatitudes and polar latitudes.

The latitudinal variation of the retrieved bulk microphysical properties is essentially expressed by the relative height of the peaks at small and at large values. This means that the latitudinal variation of bulk microphysical properties, especially CWP, is directly linked to the change in occurrence of optically thin and thick clouds.

Geographical maps of annual mean cloud bulk microphysical properties (Annex 3) confirm the latitudinal distributions in Figure 3.2.10. According to ISCCP, largest annual averages of CLWP (> 100 gm^{-2}) appear in polar regions and over NH midlatitude land, whereas lowest annual averages appear over subtropical open ocean (< 20 gm^{-2}), regions with small annual averages of CA (Annex 3). PATMOS-x, MODIS-CE and ATSR-GRAPE show much smaller values in polar regions. The latter two however provide much larger values over SH midlatitude ocean. This is linked to the fact that ISCCP and PATMOS-x provide smaller values in the case of partly cloudy fields. CIWP from ISCCP seems to be the largest in convective regions over tropical land and in storm tracks over ocean in the midlatitudes. Smallest values appear in regions of large occurrence of broken low-level clouds. In general, ISCCP monthly averages are larger than those of TOVS Path-B and of AIRS-LMD, and even larger in the convective and storm tracks regions, which can be easily explained by the fact that the latter two data sets consider only semi-transparent cirrus. ATSR-GRAPE provides monthly averages much too large compared to the other data sets, again because of sub-sampling to only optically thick clouds.

54
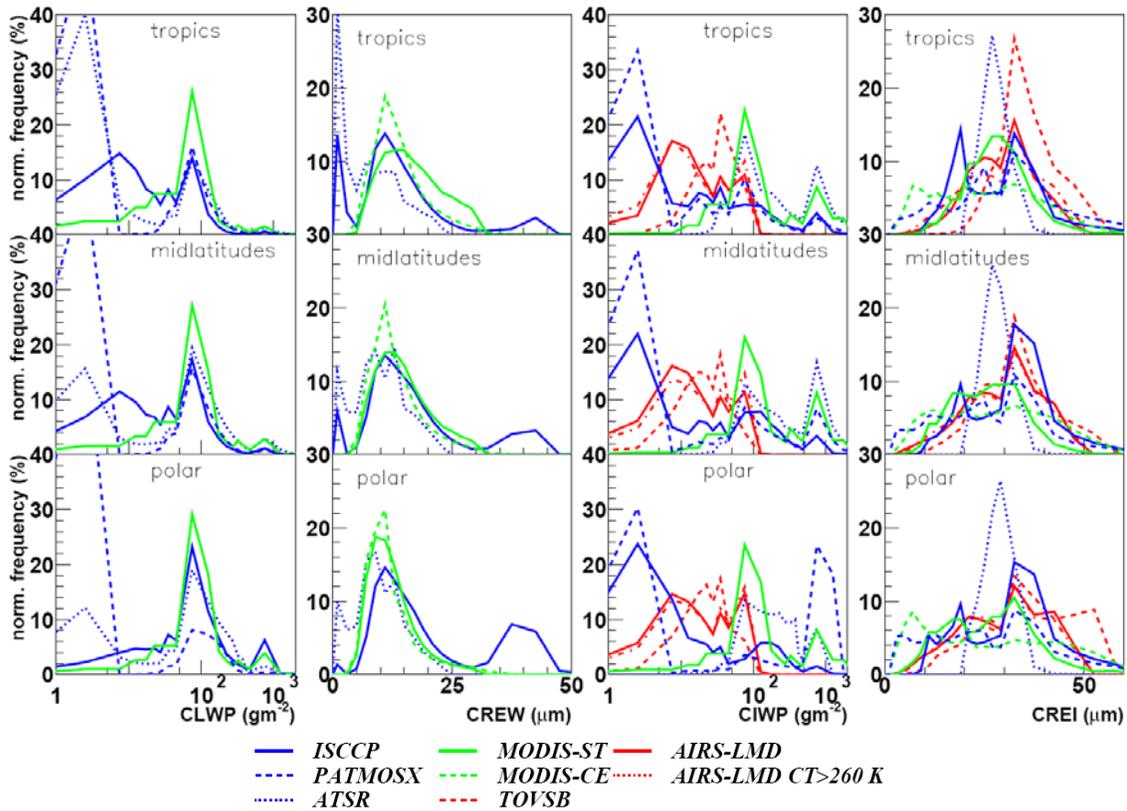
Figure 3.2.10: Normalized frequency distributions of CLWP, CREW, CIWP and CREI (from left to right) for three latitude bands: tropics (15°N-15°S), midlatitudes (30°-60° N/S) and polar latitudes (60°-90° N/S). Statistics at 1:30 PM LT (3:00 PM for ISCCP and 10:30 AM for ATSR-GRAPE).

CREW seems to be largest in the SH midlatitudes over ocean (except polar regions, for which probably CREW is overestimated because of falsely identified liquid clouds or mixed phase clouds). In the tropics MODIS-ST values are greater than ISCCP and MODIS-CE results, probably linked to sub-sampling, because when partly cloudy fields are examined CREW may be underestimated. The geographical variation of CREI from ISCCP is quite small.

To get an idea how much changes in the PDFs affect the mean values, we present in Figure 3.2.11 the seasonal cycle of the retrieved bulk microphysical properties as a relative change in mean values. As expected, *seasonal cycles of CLWP and CIWP are similar to those of CODW and CODI. The relative amplitudes are however smaller.*

A seasonal cycle of CREW is notable in the midlatitudes, with about 20% larger values in winter than in summer. The seasonal cycle of CREI is in general small (amplitude less than 10%). Outliers are PATMOS-x, and TOVS Path-B. The TOVS Path-B retrieval first determines CREIH by a spectral difference and then CIWPH as a function of CREIH and CEM, whereas AIRS-LMD determines both simultaneously, and the retrieval has a much better spatial resolution than the one of TOVS Path-B.
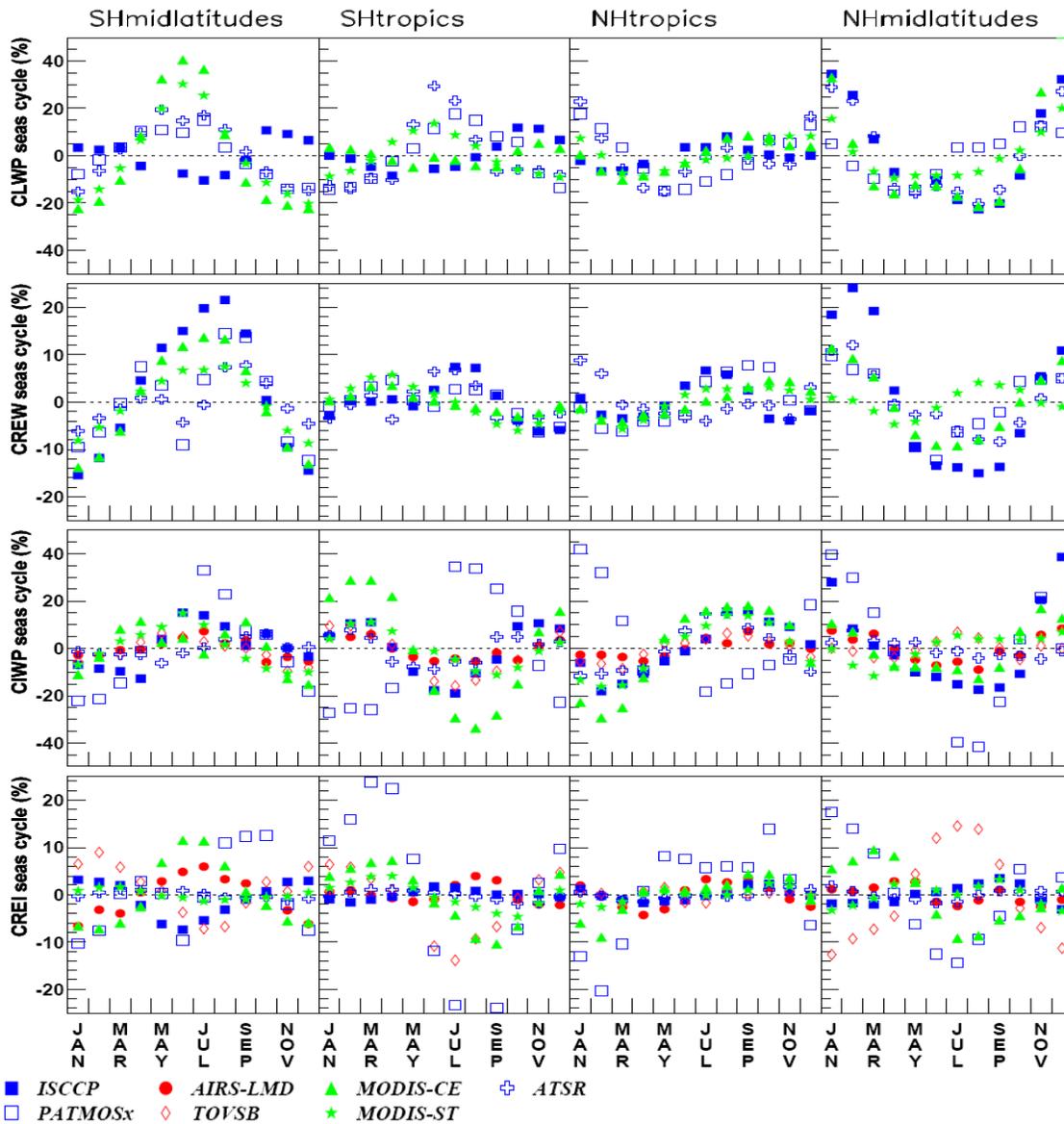
Figure 3.2.11: Seasonal variations (in %) of cloud liquid water path CLWP, effective droplet radius CREW, cloud ice water path CIWP and effective ice crystal radius CREI (from top to bottom) in four latitude bands (30S-60S,30S-0°,0°-30N and 30N-60N), derived as difference between monthly mean and annual mean relative to global mean. Statistics at 1:30 PM LT (3:00 PM for ISCCP and 10:30 AM for ATSR-GRAPE).

3.3 Cloud Properties in Specific Climate Regimes

The following comparisons give an idea how the different data sets agree in specific regions, corresponding to typical climate regimes. The ten regions of (Rossow et al., 2002), extended to 20° latitude x 20° longitude, are shown on the map in Figure 3.3.1. Regions 1 and 2 correspond to regions with marine boundary layer clouds of small spatial variability in COD; ocean storm tracks (with moderate spatial COD variability) can be found in regions 3, 4 and 5; regions 6 and 7 are regions with tropical cirrus with moderate to large spatial COD variability; regions 8 and 9 correspond to regions with active tropical convection with large spatial COD variability; and region 10 gives an example of midlatitude land with clouds of large spatial variability in COD. We have also added two polar regions, one in the North (11) and one in the South (12).
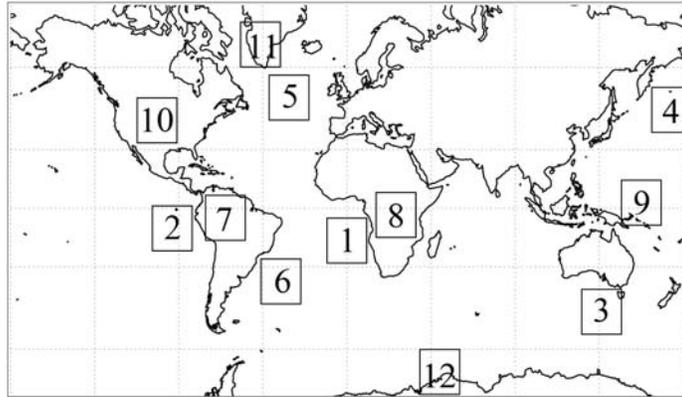
Figure 3.3.1: Geographical map of specific regions of typical cloud regimes with different spatial COD variability according to (Rossow et al., 2002):

1: SH Str Africa	2: SH Str America	
3: SH midlatitude storm	4: NH storm Eastern Pacific	5: NAtlantic storm
6: SH Ci off America	7: SH Ci Amazon	
8: SH Cb Africa	9: NH Cb Indonesia	
10: ARM Southern Great Plain	11: Greenland	12: Antarctica

Figure 3.3.2 presents differences between average cloud properties of these regions and their global averages. We note that all averages were determined as area weighted averages. Considered cloud properties are CA, CT, their day-to-day variability, CEM, CAE, CAHR, CALR, CTH, CTL, CEMH and CEML.

- ***Because differences to a reference (globe) are shown, the agreement between the data sets is quite good. The regional CA spread is less than 0.1. The spread in CAHR varies between 10% to 20%*** (the largest spread in polar regions and regions with frequent cirrus).

- The most cloudy regions are the storm regions 3 and 4 and Antarctica with CA about 0.15 larger than the global annual mean CA.

- The convective region over Africa has the largest CAHR, largest CAMR is situated in the North Atlantic (not shown) and largest CALR in the Stratocumulus regions.

- In the tropical convection regions, CALIPSO-ST CA / CAHR are larger and CT / CTH much lower, because of additional subvisible cirrus and of diffuse cloud tops (the other instruments provide a radiative height which is lower than the physical cloud top).

- Clouds are optically thickest in the polar regions and in the oceanic storm track regions. They are on average optically thinner in the cirrus regions, where horizontally extended cirrus surround the small convective areas in the tropical regions. CAE shows a similar pattern.

- Smallest day-to-day variability in CA is observed in the SH and NH storm track regions and in Antarctica. Largest day-to-day variability in CT is found in the convective areas in the ITCZ.

Figure 3.3.3 illustrates seasonal cycles of CA, CAHR, CALR, CAE and CT of these twelve regions. In general all data sets show a similar behavior, with some exceptions (as already discussed before).
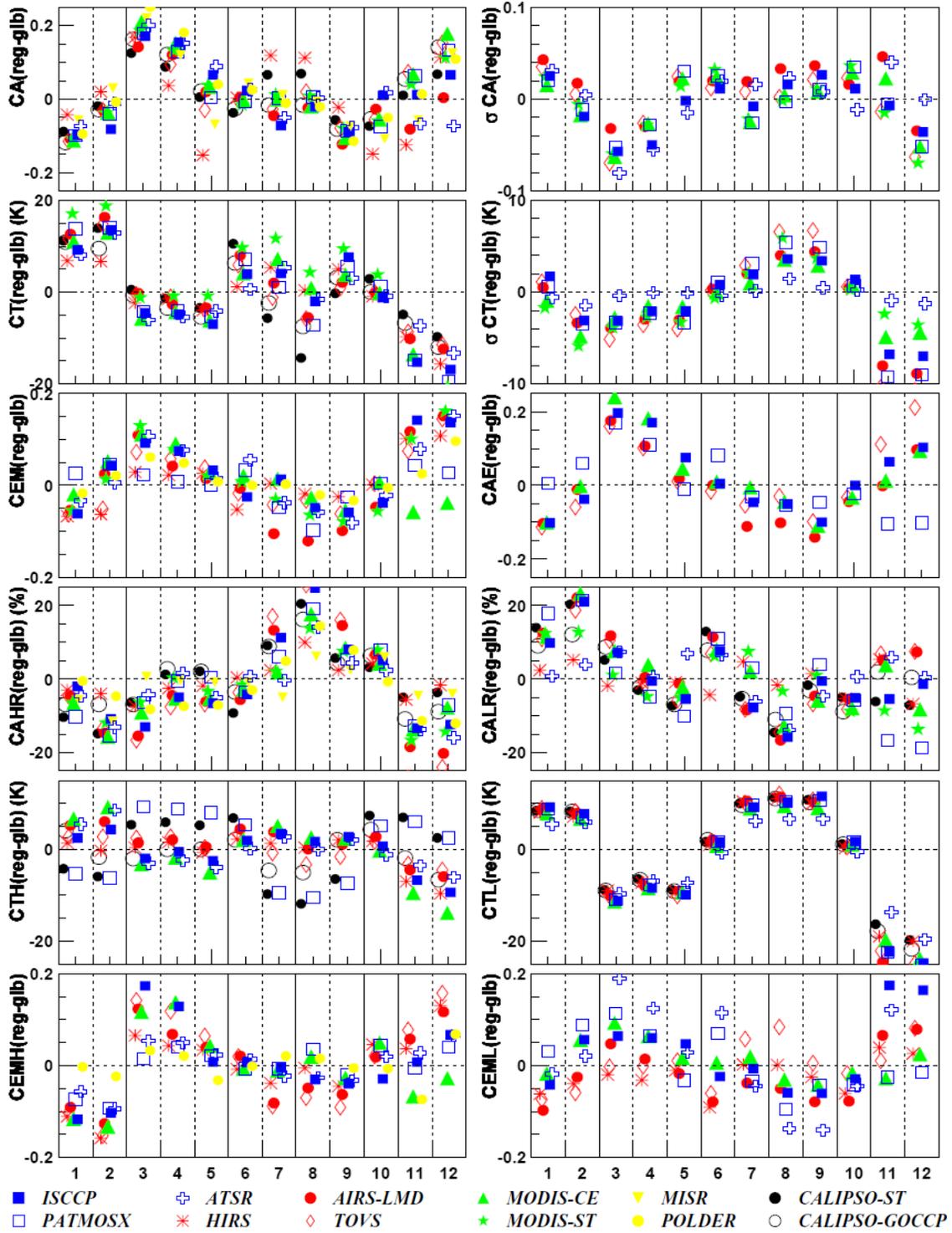
Figure 3.3.2: Differences of regional annual means and global annual mean of the different cloud properties for the following twelve regions: 1(SH Str Africa), 2 (SH Str America), 3 (SH midlatitude storm), 4 (NH storm Eastern Pacific), 5 (NAtlantic storm), 6 (SH Ci off America), 7 (SH Ci Amazon), 8 (SH Cb Africa), 9 (NH Cb Indonesia), 10 (ARM Southern Great Plain), 11 (Greenland) and 12 (Antarctica). Statistics at 1:30 PM LT (3:00 PM for ISCCP and 10:30 AM for ATSR-GRAPE).
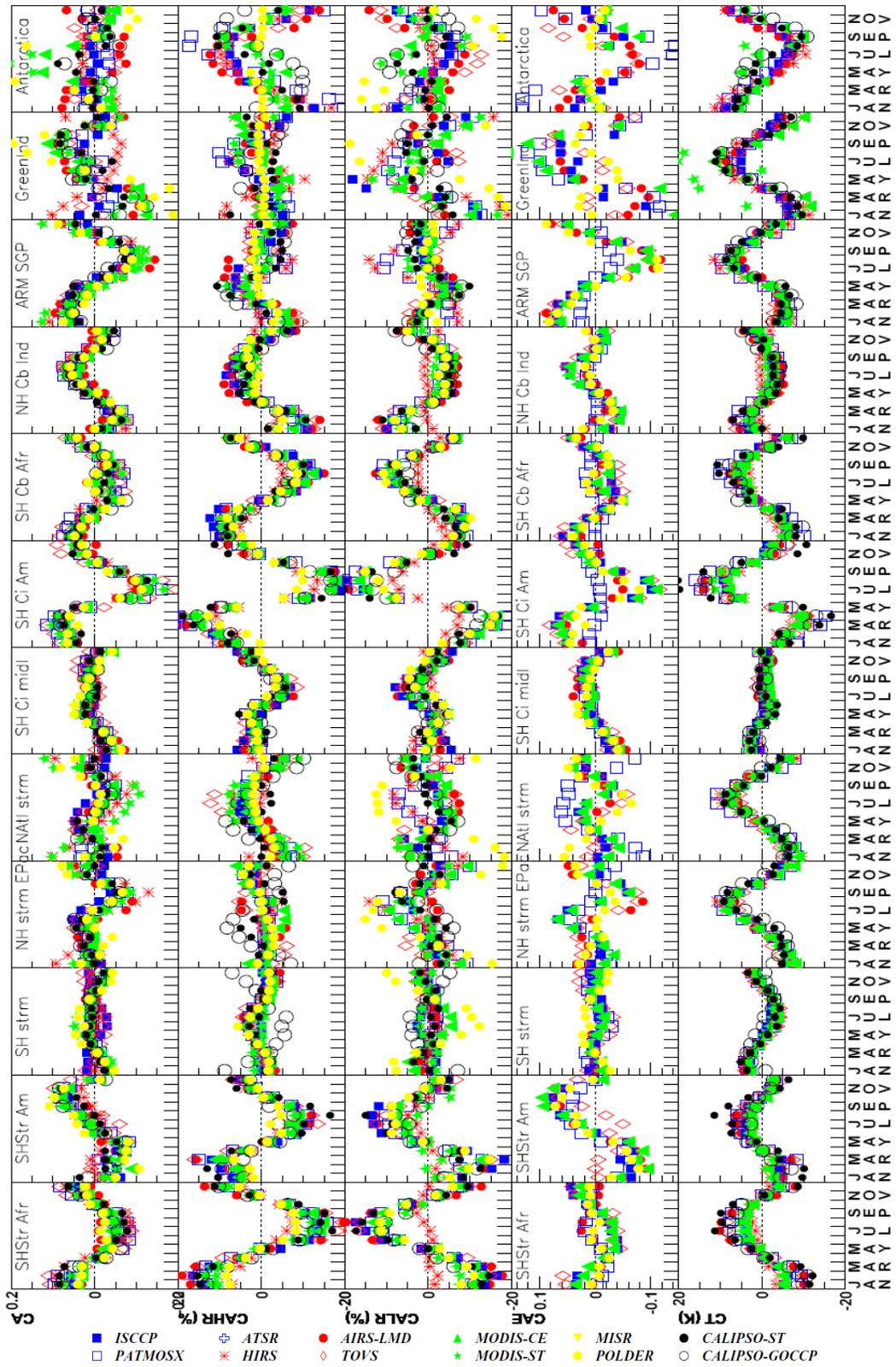
Figure 3.3.3: Seasonal cycles of CA, CAHR, CALR, CAE and CT for the twelve regions of Fig. 3.3.1.

3.4 Regional Cloud Property Range Due to Sensor Sensitivity and Retrieval Methodology

The previous sections have shown that derived cloud properties depend on instrument capabilities and retrieval performance. Figures 3.4.1 show geographical maps of the difference between maximum and minimum CA, CAHR, CAMR and CALR among six data sets (ISCCP, PATMOS-x, MODIS-ST, MODIS-CE, AIRS-LMD and TOVS Path-B).
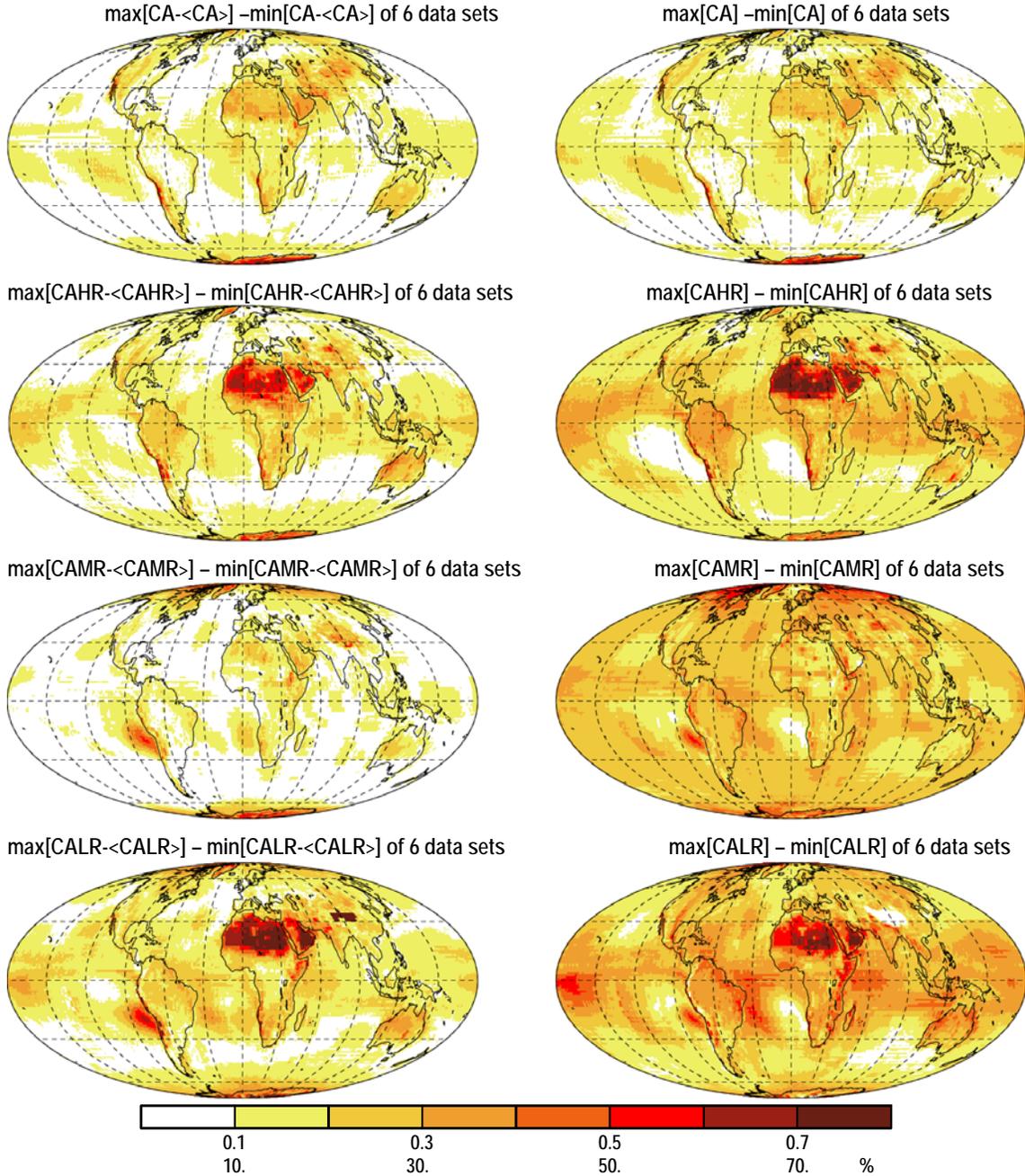
Figure 3.4.1: Regional maximum differences of CA, CAHR, CAMR and CALR within six cloud data sets (ISCCP, PATMOS-x, MODIS-ST, MODIS-CE, AIRS-LMD and TOVS Path-B), in a relative sense (variation, left) and absolute sense (right). Statistics are averaged over measurements at 1:30 PM LT (3:00 PM for ISCCP).

The six data sets have been chosen after eliminating data sets taking data at different observation times

(MISR and ATSR-GRAPE) and two outliers [HIRS-NOAA, with low sensitivity to low-level clouds, and POLDER, only providing information for clouds with optical depth > 2 (Zeng et al., 2011)].

max[CLWP-<CLWP>] – min[CLWP-<CLWP>] of 3 data sets   max[CLWP] – min[CLWP] of 3 data sets

max[CIWP-<CIWP>] – min[CIWP<CIWP>] of 3 data sets   max[CIWP] – min[CIWP] of 3 data sets

max[CREW-<CREW>] – min[CREW-<CREW>] of 3 data sets   max[CREW] – min[CREW] of 3 data sets

max[CREI-<CREI>] – min[CREI-<CREI>] of 3 data sets   max[CREI] – min[CREI] of 3 data sets
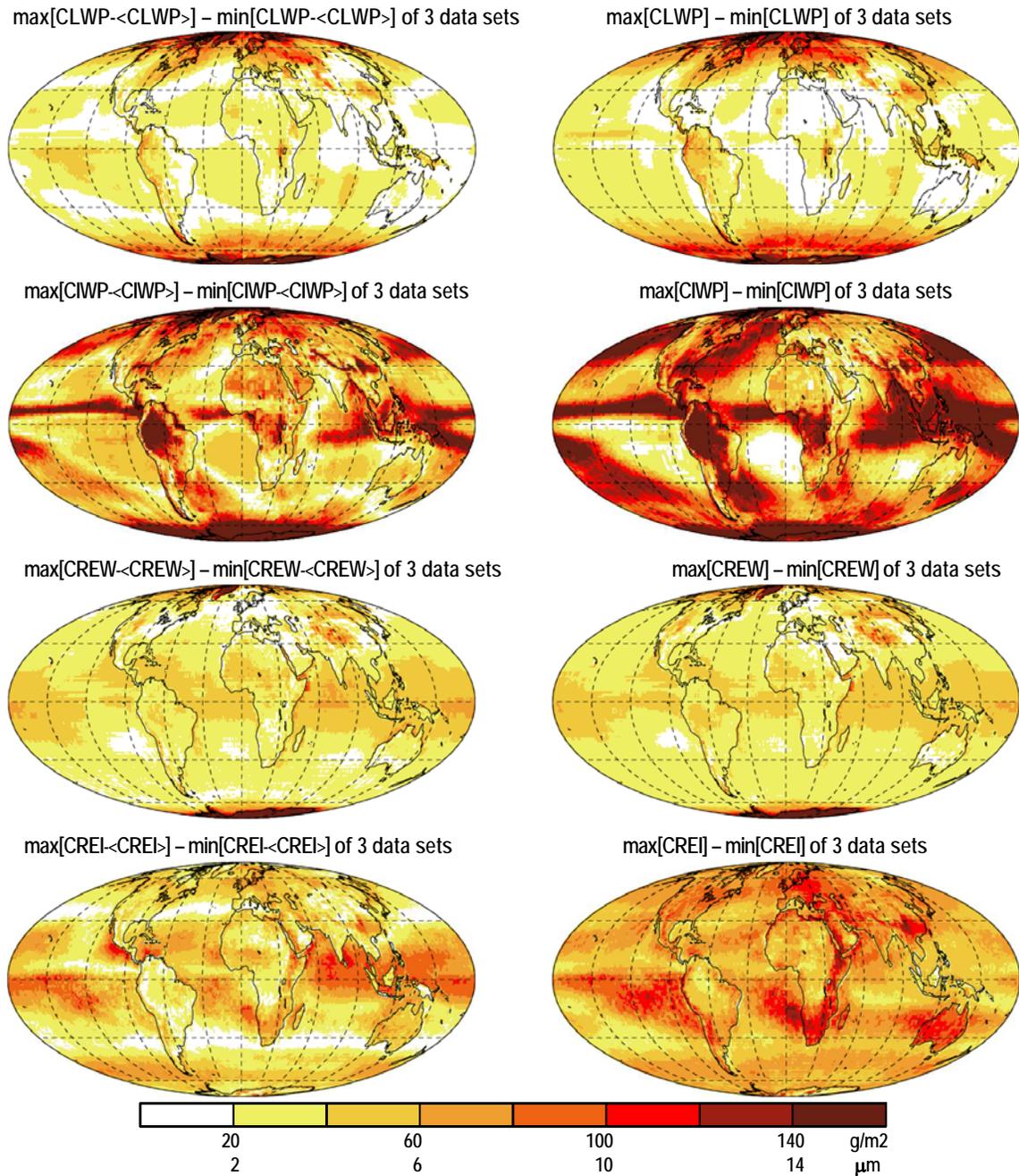
Figure 3.4.2: Regional maximum differences of CA, CAHR, CAMR and CALR within three cloud data sets (ISCCP, PATMOS-x and MODIS-CE), in a relative sense (variation, left) and absolute sense (right). Statistics are averaged over measurements at 1:30 PM LT (3:00 PM for ISCCP).

The CALIPSO data sets were eliminated because of their large sampling noise at 1° latitude x 1° longitude (Astin et al., 2001). The global maximum difference in CA of these six data sets corresponds to only 0.08 (Figure 3.1.2); however, locally, differences in detecting clouds within the data sets may reach 0.4 over deserts and high topography, especially Antarctica (Figure 3.4.1, right column). Another feature is the ITCZ where different sensitivities to thin cirrus lead to a spread of about 0.15 in CA. The

subtraction of the global annual means of the considered data sets leads to slightly improved difference patterns in CA, emphasizing the good agreement for latitudinal variation (Figure 3.4.1, left column).

Whereas the global range in CAHR and CALR of these data sets correspond to about 0.2 (Figure 3.1.2), local range of CAHR and CALR may reach even 0.4 (ITCZ and deserts). However, considering variations instead of absolute values (by subtracting global annual means of the considered data sets) leads to spreads mostly less than 0.2 (slightly smaller for CAHR than for CALR). Figure 3.4.2 shows geographical maps of the maximum difference in CLWP, CIWP, CREW and CREI among three data sets (ISCCP, PATMOS-x, and MODIS-CE) chosen after eliminating data sets with retrieval filtering (ATSR-GRAPE, MODIS-ST, TOVS Path-B and AIRS-LMD). The global maximum difference for bulk microphysical properties of liquid clouds is much smaller than for ice clouds except for the polar regions. IWP seems to differ strongly in regions with thin cirrus (up to 140 gm^{-2}) and CREI in regions which also have low-level clouds. This leads to the conclusion that CREI and IWP retrievals are the most difficult, because they may be influenced by underlying liquid clouds.

3.5 Long-Term Variations

3.5.1 Interannual Variability

Interannual variability should be *smaller than regional and seasonal variations* and *indicates natural variability,* which should be considered when analyzing trends. The natural variability may be enhanced by *retrieval noise or by reduced sampling, for example due to a narrower swath or daytime coverage only. On the other hand, less sensitivity to certain cloud types (for example cirrus) may reduce the natural variability.*

Table 3.5.1 Average inter-annual variabilities (seasonal cycle removed) of total cloud amount, height-stratified cloud amounts relative to total cloud amount and of cloud temperature over the globe, ocean and land.

	global					ocean					land				
	CA (%)	CAHR (%)	CAMR (%)	CALR (%)	CT (K)	CA (%)	CAHR (%)	CAMR (%)	CALR (%)	CT (K)	CA (%)	CAHR %)	CAMR %)	CALR (%)	CT (K)
ISCCP	2.2	2.3	2.5	2.9	1.1	2.1	2.2	2.4	3.2	1.1	2.2	2.5	2.6	2.2	1.1
ISCCP day	2.3	3.3	3.2	3.4	1.6	2.3	3.2	3.2	3.7	1.5	2.4	3.4	3.3	2.8	1.6
PATMOSX	2.9	3.4	1.7	3.3	1.9	2.8	3.3	1.6	3.5	1.9	3.2	3.5	2.1	2.9	1.8
ATSR-GRAPE	3.8	5.7	6.4	6.5	2.9	4.0	6.2	6.6	7.1		3.2	4.5	5.7	4.9	
MODIS-ST	2.6	3.4	1.8	3.4	1.9	2.5	3.2	1.5	3.4	1.8	2.8	3.8	2.6	3.3	2.1
MODIS-CE	2.8	3.4	1.5	3.3	1.5	2.7	3.4	1.4	3.6	1.5	3.1	3.4	1.8	2.7	1.6
HIRS	3.3	4.3	3.0	3.6	2.4	3.1	4.1	2.7	3.8	2.3	3.8	4.8	3.6	3.4	2.6
TOVSB	3.6	5.3	3.6	5.4	2.7	3.5	5.1	3.1	5.5	2.6	3.9	5.9	4.7	5.2	2.9
AIRS-LMD	2.6	3.6	2.1	3.5	1.9	2.5	3.4	1.8	3.6	1.9	2.8	3.8	2.7	3.2	2.0
MISR	4.1	5.6	4.8	6.7		4.0	5.3	4.1	6.4		4.3	6.3	6.6	7.6	

To filter out the seasonal cycle, the interannual variability has been computed for each month as the standard deviation of the monthly mean variable averaged over the whole period as

$$\sigma(\text{var}^m) = \frac{1}{N}\sqrt{\sum_{y=1}^{N}\left(\frac{\sum_{y=1}^{N}\text{var}^m{}_y}{N} - \text{var}^m{}_y\right)^2} \quad \text{for month } m$$

and then be averaged over all months. Measuring and studying the causes of interannual variations of cloudiness is another important use of these data products, especially those covering periods longer than a decade; but, because interannual variations are expected to be much smaller than diurnal or synoptic variations, the requirements on accuracy are more stringent. ***None of these products was originally intended for monitoring long-term variability; but given the importance of this topic and the growing length of some of these data records, their usefulness for this purpose needs to be evaluated.***

   Tables 3.5.1 and 3.5.2 show the deseasonalized average inter-annual variabilities for CA, CAHR, CAMR, CALR, and CT, globally and separately for ocean and land. As expected, global interannual variability is small; it is about 2 - 3% in CA and 2 K in CT. It is interesting to note that it is largest in the tropics, as the geographical maps in Appendix 3 also show, probably be linked to the El Niño Southern Oscillation (ENSO). One observes also a slightly higher interannual variability in NH midlatitudes than in SH midlatitudes, probably linked to a larger variability over land regions. MISR and ATSR-GRAPE exhibit systematically larger variations than any other product. This may be related to a smaller instantaneous Earth coverage (Figure 2.2). The larger values of TOVS Path-B may be linked to more noise in the retrieval because of its coarse spatial resolution (100 km).

Table 3.5.2: Average inter-annual variabilities (seasonal cycle removed) of cloud amounts and of cloud temperature, from the different satellite observations for NH midlatitudes (30°N-60°N), tropics (30°N-30°S) and SH midlatitudes (30°S-60°S).

	NH midlatitudes					tropics					SH midlatitudes				
	CA (%)	CAHR (%)	CAMR (%)	CALR (%)	CT (K)	CA (%)	CAHR (%)	CAMR (%)	CALR (%)		CA (%)	CAHR (%)	CAMR (%)	CALR (%)	CT (K)
ISCCP	1.9	2.4	2.4	2.6	0.9	2.5	2.6	2.5	3.2	1.4	1.4	1.9	2.1	2.8	0.8
ISCCP day	2.1	3.2	3.1	3.2	1.3	2.7	3.8	3.3	3.5	2.0	1.6	2.6	2.9	3.4	1.1
PATMOSX	2.8	3.3	2.0	2.9	1.4	3.1	3.7	1.3	3.8	2.6	2.1	3.0	1.7	3.1	1.2
ATSR-GRAPE	3.2	5.6	5.8	6.3	2.4	4.3	6.4	6.8	6.6	3.5	2.9	5.6	5.9	7.0	2.4
MODIS-ST	2.5	3.2	2.0	3.0	1.5	2.9	3.9	1.5	3.7	2.4	1.8	2.9	1.8	2.9	1.2
MODIS-CE	2.8	3.2	1.7	3.1	1.3	3.1	3.7	1.3	3.5	1.9	2.1	3.0	1.6	3.3	1.1
HIRS	3.7	4.4	3.2	3.6	2.2	3.6	4.8	3.0	4.2	3.0	2.7	3.6	2.9	2.9	1.6
TOVSB	3.4	5.4	4.3	5.2	2.3	4.1	5.8	2.8	5.5	3.5	2.7	4.8	3.8	5.2	1.9
AIRS-LMD	2.4	3.3	2.2	3.0	1.5	3.0	4.1	1.9	3.8	2.5	1.9	3.0	1.9	3.2	1.3
MISR	4.4	6.1	5.5	7.0		4.3	5.8	4.7	6.9		3.4	5.4	4.4	6.6	

3.5.2 Anomalies

   A number of factors can produce spurious interannual variations in the cloud products, because the size of the actual variations is small. All these factors are characteristics of the ***way in which the Earth is sampled by the satellite measurements*** used to produce the cloud product: any systematic or slow variations in the sampling of Earth can produce changes in the average values of cloud properties because these properties are not uniformly or randomly distributed over the globe or over time. In other words, ***because there are systematic variations of cloud properties with location on the globe, with time of day and season, variations of the sampling of the globe or of the time sampling can introduce changes in the results***. Moreover, even the weather-related variations of clouds exhibit significant auto-correlation so that the number of independent samples in a monthly mean is low enough to allow for some spurious statistical variations. ***Thus, until a cloud product has been examined to determine whether there have been any systematic changes in space-time sampling and what is the magnitude of change that these induce, its interannual variations have to be treated with caution. Appendix 2 illustrates the results of such investigations for the ISCCP product.***

   Figure 3.5.1 presents the time series of the ***deseasonalized anomalies in global monthly mean CA and***

CT over a 25 year period based on results from ISCCP, PATMOS-x, HIRS-NOAA, TOVS Path-B, AIRS-LMD, MODIS-ST, MODIS-CE and MISR. ***On average, the magnitude of the variations corresponds to the global mean interannual variability.*** ISCCP results including all daily observations are similar to the ones at 3:00 PM local observation time. Detailed investigations (Annex 2) on possible sources leading to spurious changes in the ISCCP CA time record show that, although they can change the magnitude of the slow CA variations by about one third, they cannot account for all of the variation.

Remember that all of the other products are based on diurnally-aliased sampling from sun-synchronous polar orbiting satellites, some of which drift in diurnal phase over time. Some of the products do not have very complete coverage of the globe on shorter time scales (Fig. 2.2) or are limited to daytime only.
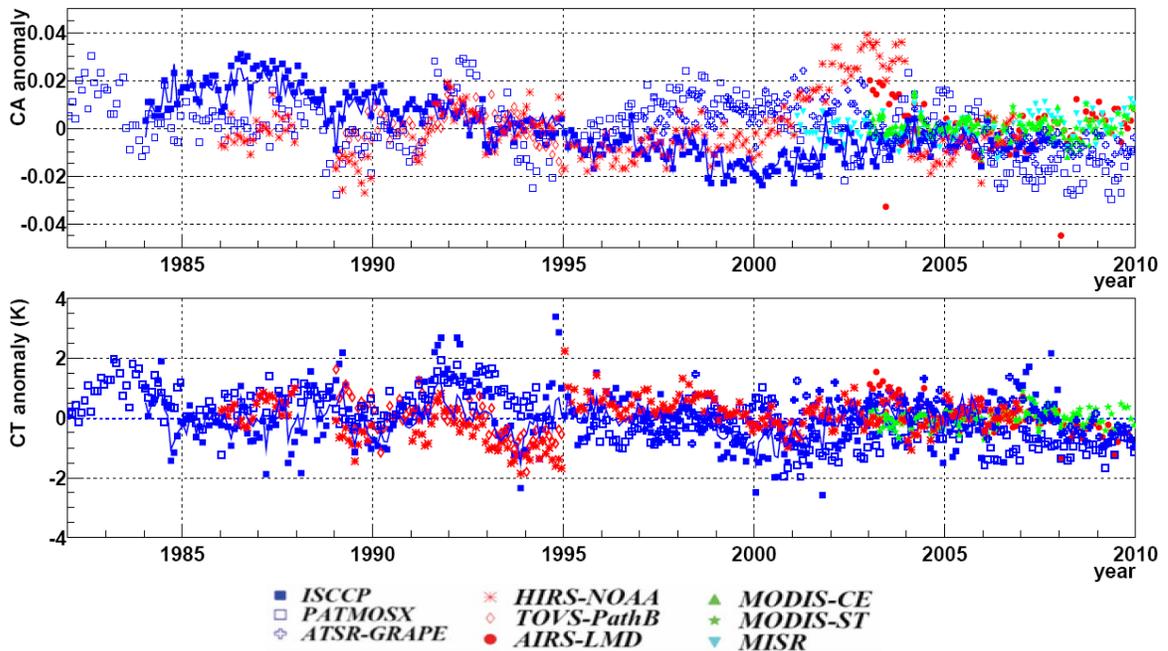
Figure 3.5.1: Time series of global cloud amount (CA) and cloud temperature (CT) anomalies. For each dataset the period covered in the GEWEX cloud assessment database is shown, with local observation time at 1:00 PM (3:00 PM for ISCCP, 10:00 AM for ATSR-GRAPE and 10:00 AM for MISR). ISCCP anomalies are also shown using the whole diurnal time statistics (blue line).

At this time, we have to say that this variation is still not confirmed. In any case, what can be concluded from the figure is that the global monthly mean CA is constant over this time period to within about 0.03, which can also be taken as a state-of-the-art estimate of the uncertainty in the variations of global monthly mean CA.

Figure 3.5.2 presents time series of deseasonalized anomalies in global monthly mean CAHR and CALR for five of the twelve regions shown in Figure 3.3.1: SH and North Atlantic storm regions, convective region over Africa, Southern Great Plains and a region in Antarctica. The slight decrease in CALR of ISCCP after 2000 is due to a change in ancillary atmospheric temperatures from NOAA. This figure illustrates the increase of natural interannual variability in smaller regions, of about 5% for CAHR and is slightly larger for CALR, and can reach even 10% when the region is affected by phenomena like ENSO, like the SH storm region. With larger regional variability on interannual time scales, it will be even more difficult to identify possible climate changes.
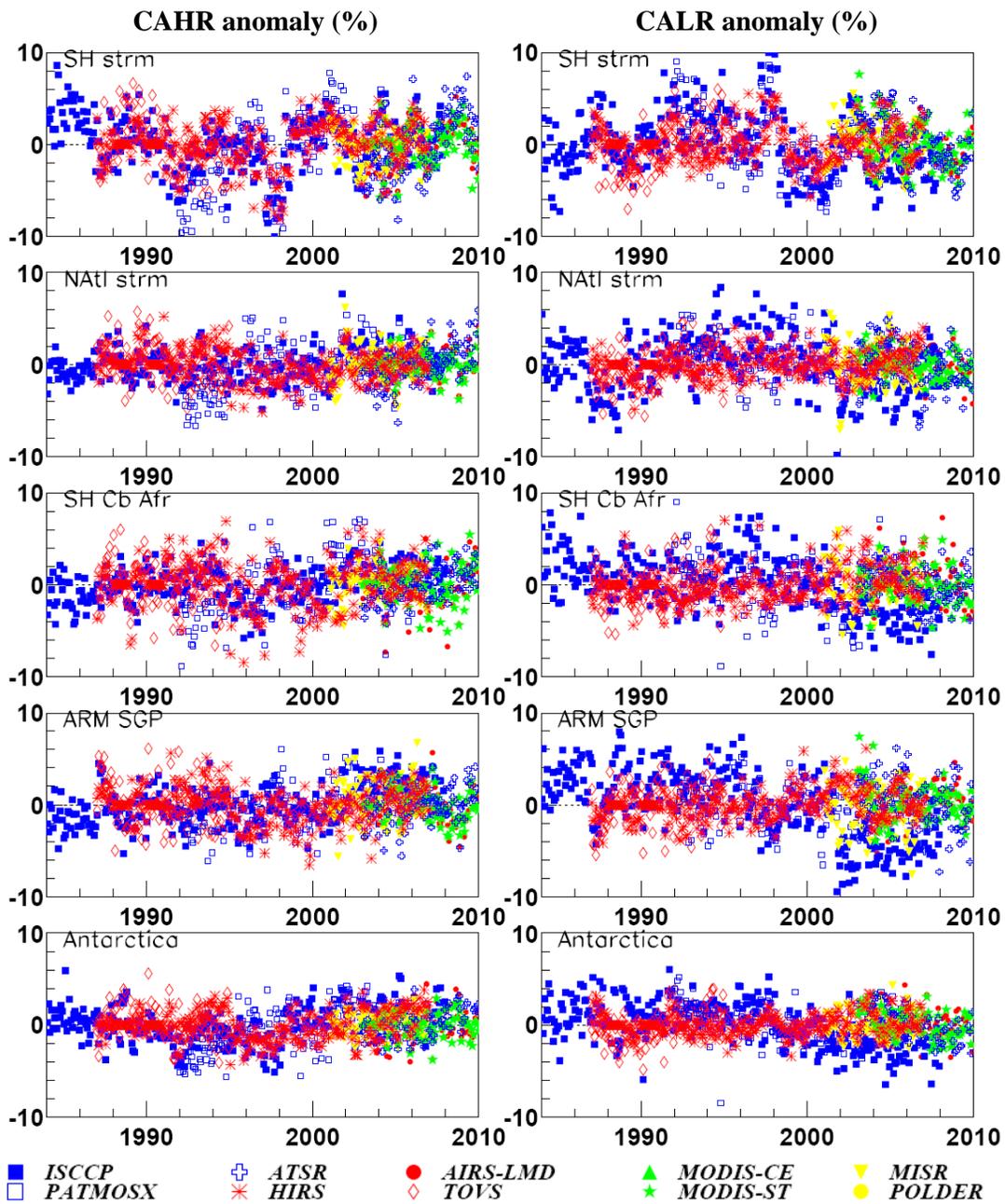
Figure 3.5.2: Time series of CAHR anomaly (left) and CALR anomaly (right) for ISCCP, PATMOS-x, HIRS-NOAA, TOVS-B, AIRS-LMD, MODIS-ST, MODIS-CE and MISR, over different regions (3, 5, 8, 10 and 12 of Figure 3.3.1).

3.5.3 Long-Term Variations and Radiative Flux Constraints

The Earth's radiation budget, a near balance of absorbed solar radiation and outgoing terrestrial radiation in the global annual average, places constraints on the average cloud properties: combinations of CA and COD should be (approximately) consistent with average reflected solar radiation and of CA and CT should be (approximately) consistent with average emitted terrestrial radiation.

If we (crudely) approximate the planetary albedo by the expression:

AP = CA x AC + (1 – CA) x AS

with planetary albedo 'AP' ($\cong 0.3$), clear sky albedo 'AS' ($\cong 0.16$), average cloudy sky albedo 'AC' and average cloud amount 'CA', then we can deduce the average cloudy sky albedo as:

CA x (AC – 0.16) = 0.14

or AC = 0.16 + 0.14 / CA

This is only an approximation both because the cloud and surface albedo do not add linearly to produce scene albedo and because the global mean AP depends on where the clouds are located (day-night, low-high latitude, ocean-land). Nevertheless, this expression provides some limits to combinations of CA and AC, which can be related to COD: Given 0.65 < CA < 0.70 as estimated from this assessment, then 0.375 > AC > 0.360, which is approximately given by clouds with 5.32 > COD > 4.95 (this relationship is based on the spherical albedo for a liquid cloud with 10 micron droplets). A more precise estimate is given by the ISCCP results: the global, annual average values are CA = 0.66 and COD = 3.9, which produce a planetary albedo of 0.31 (Zhang et al., 2004). The slightly lower COD results from the facts that a cloud over a reflective surface has a slightly larger albedo than a cloud over a black surface and that cloudiness is concentrated at higher latitudes, reducing their contribution to the total planetary albedo. This estimate that COD is about 5 for CA near 0.7 excludes the values of COD obtained from some of the data sets, but as explained before these larger values arise because some clouds have been excluded in their averages. This estimate also reinforces the conclusion that the larger values of CA from CALIPSO generally correspond to clouds with very small COD, which when added to the average would reduce COD further.

A similar exercise provides a rough limit for CT with the expression:

B(PT) = CA x B(CT) + (1 – CA) x B(AT)

and

CA x [B(CT) – B(AT)] = [B(AT) – B(PT)]

or B(CT) = B(AT) + [B(AT) – B(PT)] / CA

where B(T) is the flux for a blackbody at temperature T, PT is the effective planetary temperature, AT is the radiating temperature of the clear atmosphere (CA = 0) and CT is the average cloud top temperature taken to be the effective radiating temperature for cloudy sky (CA = 1). The outgoing longwave flux is measured to be about 235 Wm^{-2}, equivalent to a blackbody temperature of 254 K, and the global, annual mean clear sky flux is estimated to be about 260 Wm^{-2}, equivalent to a temperature of 260 K (much colder than the surface temperature because of the water vapor opacity of the atmosphere). Given 0.65 < CA < 0.70, then CT is about 250 K. A more precise estimate is given by the ISCCP results: global, annual average values are CA = 0.66 and CT = 262 K. The lower CT results from the fact that lower-level clouds included in the average are below much of the water vapor and contribute less effectively to the planetary emission.

Similar constraints can be placed on the variations of cloud properties (geographic, seasonal, synoptic, diurnal) using the observed variations of the TOA fluxes. Going further, comparing in detail the observed top-of-atmosphere and surface radiative fluxes and their variations to calculations of radiative that account not only for the cloud properties but also for the atmosphere and surface properties as well can provide an even stricter test of the accuracy of the cloud properties and their effects on Earth's radiation budget: This

exercise has been carried out for the ISCCP product, where the agreement between the ISCCP-based calculations (ISCCP FD product) and the long ERBS-based record of top-of-atmosphere radiative fluxes show excellent quantitative agreement (Zhang et al., 2004). This study also shows good agreement with another calculation that uses the ISCCP products in a different way and with the ERBE and CERES TOA flux products. Although the MODIS-CE product is employed to create a radiative flux product, like the ISCCP FD product, the radiative flux product is not a test of the reliability of this cloud product because adjustments are made to produce agreement with the direct CERES measurements. A parallel GEWEX assessment of radiative flux products has been completed (Raschke et al., 2012), which provides more detailed constraints on the cloud products used for some of the radiative flux products.

4. Conclusions and Recommendations

Satellite observations provide a continuous synoptic survey of cloud properties over the whole globe. ISCCP cloud products were designed to characterize essential cloud properties and their variations on all key time scales to elucidate cloud dynamical processes and cloud radiative effects. To resolve the diurnal cycle the observations were collected from imagers aboard geostationary and polar orbiting weather satellites. The ISCCP cloud products have been shown very valuable in many analyses, also in combination with other observations.

During the past decade, other global cloud data records have been established, using polar orbiting satellites. While these have many strengths, they lack the long-term, consistent nature of the ISCCP product that is so critical for climate studies. To be relevant for climate studies and for evaluation of general circulation models, the accuracy and error sources of all these cloud products (ISCCP included) must be determined. The GEWEX Cloud Assessment focused on the intercomparison of Level-3 cloud products of twelve participating global data sets. To facilitate the assessment a common database was created by the participating cloud teams. In addition to self-assessments of the different data sets (listed in Annex I), the analyses have shown how cloud properties are perceived by different instruments, measuring different parts of the electromagnetc spectrum, and how cloud property averages and distributions are affected by the different instrument choices.

- *Differences in average cloud properties, especially in high-level cloud amount, are mostly explained by instrument performance to detect and/or identify thin cirrus.* Active lidar measurements, IR sounding along the CO_2 absorption band and methods using IR spectral differences are powerful for thin cirrus identification (with decreasing sensitivity from the former to the latter). Visible information (during daytime) is more important for the detection of low-level clouds. Therefore the use of different spectral domains was identified as the main reason for discrepancies in retrieved cloud properties, and these can be understood as cloud scene dependent uncertainties and biases. The largest differences in retrieved cloud properties appear in the case of thin cirrus overlying low-level clouds: Whereas active lidar and IR methods determine the cloud properties of the cirrus (CALIPSO-ST, CALIPSO-GOCCP, HIRS-NOAA, TOVS Path-B, AIRS-LMD, MODIS-ST, MODIS-CE, PATMOS-x), IR − VIS methods (ISCCP, ATSR-GRAPE) provide the properties corresponding to a radiative mean from both clouds and VIS-only methods emphasize the clouds underneath (MISR, POLDER).

- Cloud top location can be indicated by height, pressure or temperature. *When the cloud top is diffuse*, meaning that optical depth increases slowly toward cloud base, *radiometric top does not coincide with the physical top.*

The GEWEX Cloud Assessment revealed how these biases may affect global averages, latitudinal variations, seasonal cycles and also probablilty density functions of various cloud properties such as cloud amount, effective cloud amount and cloud temperature (total and stratified by height) as well as cloud optical depth, water path and effective particle radius (separately for liquid and ice clouds).

Total and height stratified (using cloud top pressure) cloud amounts are often used to evaluate climate models. We consider height-stratified amounts relative to the total amount (CAHR, CAMR and CALR), because in comparisons these values should be less influenced by total cloud amount differences.

Global Averages

Cloud Amount

Global total cloud amount is about 0.70 (±0.03) when considering clouds with optical depth > 0.1. This value decreases to about 0.56 when only clouds with optical depth > 2 are considered.

According to most data sets there is about 0.10 to 0.15 more cloudiness over ocean than over land. Only HIRS-NOAA and MISR detect 0.30 more clouds over ocean than over land, which can most probably be attributed to uncertainties in cloud detection over land.

For the majority of data sets, about 40% (±3%) of all clouds are single-layered low-level clouds. Outliers are HIRS-NOAA with 26% (only one IR channel for low-level clouds), MODIS-ST with 53% (misidentification of very thin cirrus in collection 5) and MISR with 62% (good spatial resolution but only visible information). When taking into account clouds underneath semi-transparent high-level clouds, CALIPSO shows that the amount of all low-level clouds relative to all clouds reaches approximately 60%, compatible with the value obtained from MISR.

About 15% (±5%) of all clouds correspond to uppermost mid-level clouds. Values from ISCCP are 27% (day: IR and VIS) and 40% (day and night: night only one IR channel), respectively. These biases are due to semi-transparent cirrus overlying low-level clouds during day and in addition due to to semi-transparent cirrus during night. From CALIPSO we deduced that these cases constitute about 20% of all clouds, each contributing to an overestimation of about 10% in global CAMR and an underestimation in CAHR by ISCCP. This is in agreement with earlier, more detailed studies.

About 40 - 50% of all clouds are high-level clouds. The value decreases to 20% for identification of high-level clouds with optical depth > 2 (MISR). High-level clouds are most frequent in the tropics (15° N – 15° S), where their amount corresponds to about 60 - 65% of all clouds.

Global average effective cloud amount (cloud amount weighted by IR cloud emissivity) is about 0.50 (±0.05), and global values of effective cloud amount of high-level clouds agree much better among the different data sets than CAHR, because a smaller cloud amount due to missing thin cirrus is compensated by a larger average IR cloud emissivity.

Cloud Altitude

CALIPSO is the only mission providing accurate height for physical cloud tops. Passive remote sensing (except stereoscopic height by MISR) provides a 'radiative height' which may lie several hundred meters to a couple of kilometers below cloud top, depending on the vertical gradient of optical depth within the cloud. Such 'diffusive' cloud tops are especially prevalent in the tropics, which may bias cloud temperatures of high-level clouds by about +10 K. Compared to CALIPSO 'radiative height' lies near the middle between cloud top and 'apparent' cloud base (COD ≤ 3).

Cloud Optical Properties

- Cloud optical depth is in general determined from reflectances in the visible part of the solar spectrum. The thermodynamical phase is first estimated by cloud temperature, by polarization or by spectral radiance differences.

- ISCCP provides a global annual optical depth of about 4. This value is consistent with the planetary albedo constraint (for a cloud amount of 0.68 COD has to be slightly lower than ISCCP).

- *Since distributions are not Gaussian and averages depend on sub-sampling prior to retrieval, it is strongly recommended to consider probability density functions of cloud optical depth.* These agree quite well between the different data sets. One can distinguish three groupings in the distribution: clouds with optical depth smaller than 1, between 1 and 10 and larger than 10. The relative contributions of the upper and lower groups reflect sensitivities in sampling. The conversion of cloud emissivity (determined by IR sounding) to cloud optical depth limits values to less than 10. The ATSR-GRAPE retrieval is only successful for 40% of all clouds, with a bias towards optically thick clouds. For the retrieval of optical and microphysical properties the MODIS-ST retrieval filters clouds with optical depth > 1.

Cloud optical depth and emissivity are functions of bulk microphysical properties, especially of cloud water path. Effective cloud particle sizes influence more the spectral behaviour of cloud emitted or

reflected radiation, especially when particles are small. Cloud bulk microphysical properties are often retrieved after determination of cloud physical properties, under additional assumptions (for example on particle shape and size distribution within the cloud).

Cloud Microphysical Properties

Effective particle radii of liquid clouds and of high-level ice clouds agree quite well, with global averages of 14 μm (±1 μm) and 25 μm (±2 μm), respectively.

Effective cloud droplet radii are on average about 15 – 20% larger over ocean than over continents, whereas the difference in effective ice crystal radius is only about 5%.

Considering data sets with no cloud sub-sampling, global averages of cloud water path vary from 30 to 60 gm^{-2} for liquid clouds and from 60 to 120 gm^{-2} for clouds with ice tops. We stress that sub-sampling of ice clouds leads to smaller values (25 gm^{-2} for semi-transparent cirrus determined by AIRS-LMD, TOVS Path-B) and larger values (225 gm^{-2} for clouds with optical depth larger than 1.3 for MODIS-ST).

The examination of probablility density functions of bulk microphysical properties revealed differences which may be linked to thermodynamical phase misidentification (small partitions with larger droplet radii or smaller ice crystal radii), partly cloudy samples (leading to slightly smaller particle sizes and water path) and sub-sampling.

Latitudinal, Regional and Seasonal Variations

Whereas absolute values of relative high-level cloud amount depend on instrument performance to identify optically thin cirrus, all data sets show similar geographical distributions and latitudinal variations. Exceptions are polar regions (CAHR in South and CALR in North) and CALR from HIRS-NOAA (underestimation of low-level clouds with minimal thermal contrast).

The latitudinal variation of retrieved bulk microphysical properties (cloud water content and effective particle sizes) is essentially expressed by the relative contributions of small and large values.

When comparing regional averages relative to global averages, the agreement between the data sets is quite good. The spread in regional CA is less than 10% and in CAHR varies between 10 to 20% (polar regions and regions with frequent cirrus).

Most data sets also agree on the seasonal cycle. In general, seasonal variations are smaller than latitudinal variations, except for the transition of the InterTropical Convergence Zone (ITCZ), with maximal amplitude of 30% in CAHR. The seasonal cycle is generally larger over land than over ocean.

Seasonal cycle of optical depth agrees quite well for ice clouds (except for PATMOS-x): an amplitude of about 30 to 40% is linked to the transition of the ITCZ. At midlatitudes one observes a maximum in winter due to winter storms. Seasonal cycles of water path are similar to those of optical depth, with smaller relative amplitudes. Seasonal cycles of effective particle sizes are in general small and have to be considered with care, because they may be affected by misidentification of thermodynamical phase.

Diurnal Variation

Most notable features of the diurnal cycle of clouds, revealed by ISCCP, have been summarized in the report, but the Cloud Assessment was mainly focused on averages and longer-term variations. Diurnal variations can affect these results. Three of the twelve cloud data sets change their method in cloud detection between day and night (ISCCP, PATMOS-x and MODIS-CE) and three only sample daylight conditions (MISR, POLDER and ATSR-GRAPE). Day – night differences and daytime sampling differences among data sets with no change in method (IR sounders and lidar) reflect random differences of a few percent. CALIPSO seems to have a slightly smaller detection sensitivity of thin cirrus during day in this version (5 to 10% in CAHR over tropical land), linked to solar radiance noise. Day – night

differences of ISCCP are positive in CA over land (about 5% to 10%) and in CAHR (approaching 25% in the tropics). These differences are reduced in the actual monthly ISCCP products. The reasons for these differences are understood and presented above. One has to note that MODIS-CE shows similar differences in CA but differences of opposite sign in CAHR. PATMOS-x was trained by CALIPSO, but the behavior does not always follow CALIPSO, probably because of induced noise due to smaller information content.

Retrieval of cloud optical and bulk microphysical properties is limited to daytime measurements. Therefore our current knowledge is biased to daytime results. Only IR cloud emissivity and bulk microphysical properties of semi-transparent high-level (ice) clouds retrieved by IR sounders are available day and night, but the latter are only retrieved for a sub-sample of about 50% (25%) of all high-level clouds.

Longterm Variations

Interannual variability indicates natural noise, which should be considered when analyzing trends. Global interannual variability lies between 2% to 4% in CA, 2.5% - 3.5% in CAHR / CALR and 2 K in CT. Larger interannual variability (5%) is found for data sets with smaller instantaneous Earth coverage (ATSR and MISR) and for data sets characterized by larger retrieval noise due to coarse spatial resolution (100 km for TOVS Path-B). The most prominent feature in regional interannual variability seems to be linked to the El Niňo Southern Oscillation.

None of the data sets was originally intended for monitoring long-term variability. In addition, systematic or slow variations in the sampling of the Earth can produce spurious changes (like drifts in observation time by the NOAA afternoon satellites before NOAA-16), because cloud properties vary with location and time of day and season. After removal of seasonal variations, global cloud amount anomalies are reduced to 1% to 2%, within the range of interannual variability.

ISCCP exhibits a slow variation over the time period (1984 to 2008) that is not reflected in any other data set (with coarser time sampling). However, detailed investigations (Annex 2) show that spurious changes in calibration and sampling do affect the magnitude but do not eliminate this slow variation. At present one can only conclude that global monthly mean cloud amount is constant over the last 25 years to within 2.5%, within the range of interannual variability.

Since natural interannual variability increases when considering regions, one has to be careful to filter it out to identify possible climate changes in clouds.

Activities Initiated by the Assessment

The GEWEX Cloud Assessment database was created by the participating cloud teams to facilitate assessments, climate studies and evaluation of climate models. It includes monthly averages, day-to-day variability and histograms of various cloud properties at a spatial resolution of 1° latitude x 1° longitude. The analyses presented in this report have already revealed its usefulness. It is available at the GEWEX Cloud Assessment website: http://climserv.ipsl.polytechnique.fr/gewexca.

Four workshops offered an excellent forum for cloud researchers to investigate cloud retrievals and to organize and prioritize future work.

The GEWEX assessment efforts have already led to funding by space agencies for further assessments: EUMETSAT has initiated the Cloud Retrieval Evaluation Workshop (CREW, http://www.icare.univ-lille1.fr/crew/index.php/Welcome) focusing on detailed L2 data comparisons over limited areas and time periods. ESA included assessments of the Essential Climate Variables retrieved within the Climate Change Initiative.

Recommendations

These satellite cloud products are valuable for climate studies or model evaluation, because they show similar geographical patterns and seasonal cycles. Even if absolute values may differ due to different spectral domains used in the retrieval, one can explore relative changes in the different properties for this kind of studies.

When using a specific data set, one has to keep in mind specific limitations and biases:

ISCCP is the only data set to resolve the diurnal cycle. However, high-level clouds may be misidentified as mid-level clouds in the case of thin cirrus during night and thin cirrus overlying low-level clouds during day. So far only ISCCP cloud properties have been tested by comparing resulting radiative fluxes to those determined from Earth Radiation Budget instruments, revealing excellent quantitative agreement (GEWEX Radiative Flux Assessment). Effective cloud particle sizes are retrieved for all clouds, but by using AVHRR data alone. Biases may appear due to partly cloudy samples and to ice-water misidentification.

The **PATMOS-x** data set shows improvement in the identification of cirrus, by using AVHRR data alone. However, diurnal variation in cloud physical properties and seasonal variation of optical and microphysical properties show still some inconsistencies.

The active lidar of the **CALIPSO** mission is the most sensitive to thin cirrus (including subvisible cirrus) and also gives information on all cloud layers within the atmosphere up to an optical depth of 3. To complement this information a coupling with the radar of the CloudSat mission is necessary, but still their instantaneous Earth coverage is small (5%).

IR sounding methods are sensitive to thin cirrus with optical depth larger than about 0.1, providing reliable cirrus properties day and night. The CO_2 slicing retrieval method employed by **HIRS-NOAA** is not applicable to low-level clouds, whereas a weighted χ^2 method used in the retrieval of **TOVS Path-B** and **AIRS-LMD** may be applied to all clouds. However, the noise for low-level clouds is larger than for the other clouds because of low radiative contrast and of coarse spatial resolution of these instruments (15 km). The noise is largest for TOVS Path-B due to 100 km retrieval spatial resolution. Bulk microphysical properties can be only determined for semi-transparent cirrus.

The spatial resolution of **MODIS-ST**, also using the CO_2 slicing method for retrieval of cloud pressure and emissivity, is much better (1 km). However the retrieval method employed in Collection 5 led to some misidentification of very thin cirrus as low-level clouds. The retrieval has been improved for Collection 6. Optical and bulk microphysical properties are only determined for a sub-sample corresponding to clouds with optical depth > 1, and therefore their ice water path is biased high.

The retrieval method of **ATSR-GRAPE** has been recently developed, and is still being improved. At present the method is only successful for 40% of all clouds, leading to a bias towards optically thick clouds.

An important application of these data sets is the study of cloud processes, by using the synergy of different variables and data sets. For this kind of study one needs instantaneous data with a good temporal resolution, distributed by the different data processing centers.

Monitoring long-term variations is very difficult with these data sets. ISCCP, the GEWEX cloud data set, is the data set with the best Earth coverage and the best sampling of the diurnal cycle. Since there are systematic variations of cloud properties with location on the globe, time of day and season, variations in sampling can introduce changes. Before attributing cloud amount and cloud property changes to climate change, one has to investigate sampling changes and the consistency of the applied ancillary data of the particular data set used.

The ISCCP data record will be reprocessed in 2012. This kind of assessment should be regularly repeated, in a cycle of eight to ten years. However, for a better effectiveness, future assessments should be supported by funding.

APPENDICES

1. Description of Cloud Products and Their Retrieval Methods

1.1 Cloud Products from Operational Satellites

1.1.1 International Satellite Cloud Climatology Project (ISCCP)
W.B. Rossow

To resolve the diurnal cycle of clouds, ISCCP emphases temporal and spatial resolution, rather than spectral resolution. To achieve this goal, the only possibility at the time the project started in 1982 was to use VIS (day only) and IR atmospheric window radiance measurements from imagers on the suite of geostationary and polar orbiting weather satellites. Today, using the available satellite constellation to obtain uniform global coverage with diurnal time resolution still limits the spectral information to the same two wavelengths. Time sampling is three hourly and the initial spatial resolution of about 5 km is sampled at about 30 km (a new version of the ISCCP products will be released in 2012 based on a spatial sampling at about 10 km). The ISCCP data set is the GEWEX cloud data set and covers at present July 1983 through December 2009.

1.1.1.1 Measurements

The basic measurements analyzed to produce the ISCCP Cloud Products are the visible (VIS) and "window" infrared (IR) radiances (wavelengths 0.6 and 11 μm, augmented by 3.7 μm radiances over snow-ice covered locations) measured by the international constellation of meteorological satellite imaging radiometers. The VIS radiances are cross-calibrated to an absolute standard defined by the post-launch calibration of the NOAA-9 AVHRR channels by six NASA ER2 under-flights with a laboratory-calibrated (NIST traceable standard) spectrometer. The IR radiance calibration is anchored to the on-board calibration of the NOAA-9 AVHRR. The calibration procedure has three additional steps: (1) all geostationary radiances are normalized to the "afternoon" AVHRR operating at the same time, (2) all AVHRRs are normalized to NOAA-9 using a globally complete distribution of land surface targets for VIS and percentile values from global, 2-week histograms of IR radiances over oceans, and (3) coincident retrievals of cloud top and surface temperatures and cloud and surface reflectances from each geostationary satellite and the afternoon polar orbiter are used for a final adjustment of the IR and VIS calibrations, respectively. The radiances are subsequently treated as spectrally the same as the NOAA-9 measurements: VIS radiances are ratioed to the corresponding effective solar constant for each satellite before normalization and IR radiances are reported as brightness temperatures to reduce the effects of spectral differences. Estimated relative (absolute) calibration uncertainties are 3% (7%) for VIS and 1% (2%) for IR (Brest et al., 1997).

All image pixels are Earth-located to an accuracy better than 30 km.

1.1.1.2 Cloud Detection

The ISCCP cloud detection procedure analyzes VIS and IR radiances separately; the results at night are from IR-only, whereas daytime results are reported for both the IR-only analysis and from the combination of VIS and IR (VIS-IR) results. The latter reports cloud present if it is detected at **either** wavelength. In the gridded cloud products, the difference between the daytime VIS-IR and IR-only results is interpolated over the nighttime at each location to improve nighttime cloud detections of low-level clouds. The basic cloud-clear decision (at each wavelength) is made by testing whether the observed radiance at each pixel location-time differs from an estimated clear-sky value for each location-time by more than a threshold amount. The threshold amounts are wavelength and location-dependent as determined by the characteristics of the surface (land, open water, topography, snow and ice cover) at that location-time and have magnitudes that are estimates of the uncertainty of the clear sky radiance values. The complex part of the detection method uses

four (two) different estimates of clear-sky radiances for IR (VIS) obtained from a series of tests of the spatial and temporal contrasts of the radiances. The theory behind these tests is that clear-sky radiance contrasts are much smaller than cloudy-sky contrasts, especially in time, and that clear-sky radiances are warmer (darker) than cloudy-sky radiances in IR (VIS). The relative weight given to these two assumptions varies with surface type: the latter is given more weight over open water and less weight over land and snow-ice. Because all tests are performed for each month, the clear-sky estimate is guaranteed to lie within the actually observed range of radiance values for that month. Because these tests are all relative comparisons, the ISCCP cloud detection is nearly independent of radiance calibration (a weak dependence over oceans occurs because the clear-sky VIS radiance is constrained by an ocean reflectivity model). Comparisons of ISCCP cloud detections (Rossow and Schiffer, 1999) against other measurements (satellite and surface) have been used to estimate an instantaneous random uncertainty at mesoscale of about "10 - 15% due to a combination of resolution effects (about 5%) and spatial sampling effects (about 10%). Cloud amount precision for a particular location-time ranges from 0.8 - 5%. Monthly mean random uncertainty at mesoscale is estimated to be about "3 - 5%; global mean random uncertainty may be as small as "1 - 2%. Systematic errors that have been discovered so far concern primarily spatial resolution effects ("3% – the effect is systematic for specific cloud types, it may be an overestimate for low-level broken clouds and an underestimate for cirrus) and the missed detection of optically very thin cirrus and cumulus (about 10% underestimate).

1.1.1.3 Retrieval

Once all image pixels are separated into clear or cloudy categories, look-up tables, based on radiative transfer model simulations of the IR and VIS radiances (assuming NOAA-9 spectral response functions) employing atmospheric properties (temperature, water vapor, ozone, surface pressure) specified for each location-time from external data sets, are used to retrieve surface temperature and visible reflectance from the clear-sky estimates of radiances in the first pass through the data set. Then these surface properties are used to retrieve CT (CP is determined from the atmospheric temperature profile) and COD for cloudy pixels in a second pass. Also, surface properties are retrieved again for clear pixels and monitored relative to the clear-sky estimates. No aerosol effects are accounted for. Clouds are represented as plane-parallel (typical pixel size is 5 km), single-layer clouds composed of an assumed distribution of particle sizes: for liquid clouds ($CT \geq 260$ K) the particles are spheres with an effective radius of 10 μm (and an effective variance of 0.15) and for ice clouds ($CT < 260$ K) the particles are fractal shapes with an effective radius of 30 μm (and a variance of 0.1 and an aspect ratio of unity). Gas effects are considered above and below the cloud layer but not within the cloud layer. The surface is assumed to have an effective IR emissivity of unity and a reflectivity that is angle dependent over oceans (based on Fresnel reflection from a surface with a detailed wave-slope model) and isotropic over land and ice. Estimated relative (absolute) uncertainties of the retrieved cloud properties depend on the cloud type but appear to be about 1 K (3 K) for CT and 10% (15%) for COD (estimated uncertainties for cirrus clouds are about 3 K for CT and 25% for COD) (Rossow and Schiffer, 1999). Known systematic errors are underestimation of cirrus cloud top heights by several kilometers when they overlie low-level clouds and overestimates of COD at low sun angles and over snow-ice surfaces. Estimated relative (absolute) uncertainties of retrieved surface properties are 2 K (4 K) for surface temperature and 3% (5%) for visible reflectances.

1.1.1.4 Products and Characteristics

The complete ISCCP data set is comprised of 11 products: the re-formatted, calibrated, navigated radiances (B3, about 1 Gbytes per month), the final radiance calibration coefficients (BT, about 70 Mbytes per month), the atmospheric properties (TV, about 6 Mbytes per month), the merged sea ice and snow cover (IS, about 0.25 Mbytes per month), the pixel-level cloud product (DX, equivalent to Level 2, about 5 Gbytes per month), the gridded, 3-hr cloud product (D1, equivalent to Level 3, about 320 Mbytes per month), the gridded monthly mean cloud product (D2, about 8 Mbytes per month), the twice-daily cloud particle sizes (RE, about 200 Mbytes per month), the mesoscale convection tracking survey (CT, about 60 Mbytes per month), the midlatitude cyclone survey (CY, 5 Mbyes per month), and the radiative flux profiles (FD). The latter product is actually 5 products: the full input data set (INP, about 205 Mbytes per month), the full radiative flux profiles (PRF, about 205 Mbytes per month), the surface flux subset (SRF, about 70 Mbytes per month), the top-of-

atmosphere subset (TOA, about 60 Mbytes per month) and the monthly mean fluxes (MPF, about 0.8 Mbytes per month). More details can be found on the ISCCP website: **http://isccp.giss.nasa.gov**.

The basic satellite IR and VIS images analyzed by ISCCP are composed of individual pixels, with matched IR and VIS sizes of about 5 km, sampled at 25 - 30 km and 3 hr intervals (polar orbiter data are not time sampled). The combination of satellites provides global coverage that directly resolves the diurnal cycle everywhere. The optimum constellation of satellites is 5 geostationaries and 2 polar orbiters; for a little more than half of the time record, coverage was obtained by only four geostationaries and two polar orbiters. Since mid-1998, the coverage has been provided by five geostationary and two polar orbiters. The time period covered by the ISCCP data products currently is July 1983 – December 2009. A new version, based on 10 km sampled radiances, will be released in 2012 and will continue as the whole ISCCP becomes operational.

High-level, midlevel and low-level clouds are defined by CP values within three intervals (separated at 440 and 680 hPa). During daytime, clouds are further classified into nine types by separating each of the three cloud height categories into thin, medium and thick clouds according to three COD intervals (separated at 3.6 and 23). The ISCCP D1 and D2 data sets give daily and monthly three-hourly statistics on cloud amount CA (fraction of cloudy pixels) and cloud type amount at spatial intervals of 2.5°.

Using only the AVHRR instruments on the NOAA polar orbiters, which have an additional measurement at 3.7 μm, mean cloud-top effective radii of liquid and ice cloud particles (separated by CT = 260 K) have been retrieved for the period 1983 through 2001, based on the method developed by Han et al. (1994, 1999). Although these results are not included in the standard ISCCP products, they are included here will be released as a separate product.

1.1.1.5 Uncertainty Estimates

The ISCCP data set has been thoroughly evaluated. Uncertainty in retrieved cloud properties depend essentially on the cloud type (Rossow and Schiffer, 1999). For CT there are four situations:

1) Low clouds with distinct tops and moderate-to-large optical thicknesses (COD > 5),
2) High-level, diffuse-topped clouds with moderate-to-large COD,
3) Isolated high-level, optically thin clouds and
4) High-level, optically thin clouds above lower thicker clouds.

When the COD is large, the observed IR radiance is emitted mostly from the upper part of the cloud, with no significant contribution (< 10% for COD = 5) from below the cloud and hence the CT retrieval does not depend on COD. For a cloud with a distinct top (optical thickness increases from the cloud top downward over a very small vertical extent), CT is most accurate. In this case, the main error sources in CT are from radiometer calibration (< 1.5 K, Brest et al., 1997), radiative transfer calculations and uncertainties in the atmospheric temperature-humidity profiles (the latter two factors are only important for low-level clouds). Careful comparison of marine stratus cloud tops with collocated measurements from FIRE and ASTEX shows agreement of CT within 1.0 to 1.5 K. However, the ISCCP values of CP are too low by 50 to 80 hPa (Wang et al., 1999) because of systematic errors in the operational TOVS temperature profiles used to convert CT to CP. Comparison of CP for all low- and midlevel clouds with cloud-top pressure inferred from rawinsonde humidity profiles (Wang et al., 2000) shows agreement within 25 to 50 hPa.

When the cloud top is diffuse (COD is slowly increasing from the top downward over a considerable vertical extent), the emission arises from within the cloud and therefore CT represents the temperature of the radiative cloud-top height (Holz et al., 2007). In this case, CT is larger than the temperature at the precise physical top. According to an analysis of limb-viewing SAGE observations (Liao et al., 1995a), almost 70% of the high clouds in the tropics have a diffuse cloud top, leading to an average CP discrepancy with the precise physical cloud-top of about 150 hPa. At higher latitudes, however, only 30 to 40% of the high clouds are in this category, leading to an average CP discrepancy of about 50 hPa [see also the comparison with Calipso by Rossow and Zhang (2010)].

The main source of bias in the retrieved COD during day comes from differences between the actual

and model-specified cloud microphysical properties. An increase of a factor of two in effective droplet radii leads to a decrease of retrieved COD by about 15% (Nakajima and King, 1990). During night, cloud-top location can only be estimated from the IR radiance, leading to an average positive bias in CP of about 75 hPa, as has been shown in comparison with IR sounder measurements (Stubenrauch et al., 1999a). Table 1.1.1 summarizes uncertainty estimates for the different cloud properties, determined from detailed intercomparisons with different data sets and published in more than 42 scientific articles.

Table 1.1.1: ISCCP Uncertainty Estimates

	CA	CT	CP	COD	CWP
Mesoscale & Instantaneous:	0.10	2 - 6 K	50 - 200 hPa	15 - 25%	10 - 30%
Regional Monthly Mean:	0.05	2 K	100 hPa	10%	10 - 30%
Global Annual Mean:	0.03	1 K	100 hPa	5%	10 - 30%
Accuracy:	0.10	1 - 2 K	100 hPa	5%	30%

1.1.2 AVHRR Pathfinder Atmospheres Extended: PATMOS-x
A. Heidinger, A. Walther, M. Foster

The Pathfinder Atmospheres Extended (PATMOS-x) is a cloud data product developed by NOAA. The PATMOS-x data submitted to GEWEX is based on the Advanced Very High Resolution Radiometer (AVHRR) flown on the NOAA and EUMETSAT polar orbiting sensors, though the PATMOS-x analysis software is also capable of processing MODIS and GOES Imager measurements. In contrast to ISCCP, PATMOS-x provides data over the entire globe from one sensor, although the monthly averages may be composed of data from more than one polar orbiter. The AVHRR sensors also provide more spectral information that allows for more complex and more day/night consistent algorithms than possible with ISCCP. However, the AVHRR platform does not provide the consistent diurnal sampling offered by the geostationary imagers. For most of the time period, AVHRR data are available four times per day though the observation times vary as the polar orbiting satellites slowly drift from their original orbits. No accounting for the diurnal cycle and orbit drift was done in the GEWEX submission, but the PATMOS-x team is developing diurnally adjusted data sets. The observation times are included in the original PATMOS-x data set.

1.1.2.1 Measurements

The GEWEX submission of PATMOS-x is based on the AVHRR Global Area Coverage (GAC) data. Each GAC pixel is the average of four 1.1 km AVHRR pixels along the scan line and sampling of every third scan line. The geographic area represented by one GAC pixel is approximately 1 km by 5 km. PATMOS-x currently includes data from the AVHRR/2 and AVHRR/3 series. AVHRR/2 provides measurements with central wavelengths of 0.63, 0.86, 3.75, 10.8 and 12.0 microns. AVHRR/3 data may include 1.6-micron observations in place of the 3.75-micron observations during daytime. In general, the AVHRR/3 data flown in the afternoon orbits (NOAA-16, 18 & 19) never utilized the 1.6 micron channel, while those flown in the mid-morning orbits (NOAA-17, METOP-A) always utilized the 1.6 micron channel during the day. The exception to this rule is data from NOAA-16 prior to May 2003, where the 1.6 micron channel was on during the day.

The AVHRR data used in PATMOS-x is provided by the NOAA CLASS system. The processing starts with the L1b data stored in the original 10-bit format. The thermal calibration is accomplished using the method outlined in (Rao, 1993). The solar reflectance channels are calibrated using the method of (Heidinger et al., 2010), which used MODIS as the calibration standard. The AVHRR clock error impact on the geolocation was accounted for using a routine provided by Fred Nagle of the University of Wisconsin/SSEC. The clock error values came from the University of Miami.

In addition to calibration and geolocation, the PATMOS-x L1b processing system also ingests and incorporates ancillary data to each pixel. These ancillary data sets include white-sky surface reflectances, infrared surface emissivity, land/sea information, coast masks and land cover classifications. Temperature and moisture profiles and surface temperatures, surface pressures and snow cover over land are provided by the NCEP Reanalysis Version 1 with output generated four times daily. The radiative transfer for the thermal channels is performed using the PFAAST model provided by Hal Woolf of University of Wisconsin /SSEC. The RTM coefficients were computed for each AVHRR sensor using the nominal AVHRR spectral response functions.

The Level-1b data is processed into a series of L2 files. All L2 files for each satellite for each day are collected and processed further to generate L2b files. L2b files provide global fields with a spatial resolution of 0.1 degree. The creation of the L2b data is accomplished by sampling the L2 data using a nearest-neighbor approach. Each point in the L2b is the data from one pixel with no averaging done. At higher latitudes where orbits overlap, the data with the most nadir view is selected. L2b data are computed for each node (ascending and descending). The 1° x 1° L3 data submitted to the GEWEX project was generated from the L2b product.

1.1.2.2 Cloud Detection

(Heidinger et al., 2012) describes the cloud detection scheme employed in PATMOS-x. The PATMOS-x technique is a naïve Bayesian methodology. An analysis of co-located NOAA-18/AVHRR and CALIPSO/CALIOP observations was used to automatically derive the Bayesian classifiers globally. The resulting algorithm used 6 Bayesian classifiers computed for 7 separate surface types. Relative to CALIPSO, the final results show a probability of correct detection of roughly 90% over water, deserts and snow-free land, 75% over the Arctic and below 70% over the Antarctic. Comparisons of the PATMOS-x results to those from ISCCP and MODIS GEWEX submissions indicate close agreement with zonal mean differences in cloud amount, being less than 5% over most zones. Most areas of difference coincide with regions where the Bayesian cloud mask reported elevated uncertainties. The ability to report uncertainties is a critical component of this approach though this information is not reported in the GEWEX data set.

1.1.2.3 Retrieval

1.1.2.3.1 Cloud Phase and Type Estimation

The cloud typing routine classifies each pixel into one of seven categories (0-clear, 1-fog, 2-liquid water cloud, 3-supercooled water cloud, 4-opaque ice, 5-cirrus, 6 – multilayer cirrus). These were chosen because they represent a minimum set of types evident in the spectral signatures provided by the AVHRR. The multi-layer cirrus type is restricted to semi-transparent cirrus that overlies a warmer and lower-level cloud. The actual technique is described in (Pavolonis et al., 2005). The multi-layer detection is described in (Pavolonis and Heidinger, 2004) and global results are shown and compared to other estimates in (Heidinger and Pavolonis, 2005).

1.1.2.3.2 Cloud Height and Emissivity Estimation

Cloud temperature CT and emissivity CEM are retrieved by an optimal estimation approach based on split window observations (11 and 12 μm). This algorithm is described and evaluated in (Heidinger and Pavolonis, 2009). The relation between brightness temperatures at 11 and 12 μm for a single layer cloud depend on CT, CEM and the cloud microphysics. We assume the cloud microphysics and estimate CT and CEM. Our choice for the assumed microphysical parameter has been guided by comparisons to MODIS CO_2 slicing results. The a priori constraints are based on the cloud type classification and MODIS CO_2 slicing results. For high thin cirrus, we have found CT to be highly sensitive to the a priori constraint as well as CEM. Our analysis has also demonstrated that the CT accuracy allows for proper placement of ice clouds into the high cloud category. For low level cloud or optically thick high cloud, the method performs similar to a single channel 11 μm approach. Like TOVS Path-B this approach allows for simultaneous estimation of CT and CEM day and night. This algorithm is one reason that PATMOS-x

high cloud amounts show realistic day-night differences. CP and CZ are estimated from CT using the co-located NCEP Reanalysis profile.

1.1.2.3.3 Daytime Cloud Optical and Microphysical Properties (DCOMP)

The COD and effective cloud particle radius (CRE) are retrieved for daytime observations by an optimal estimation approach using the 0.63 and 3.75 micron channels (Walther and Heidinger 2012). The forward operator is based on Mie theory and an adding/doubling radiative transfer model. For ice phase functions we use ice crystal habit distributions as described by (Baum et al., 2005). The forward simulation output is stored in look-up-tables to speed up the retrieval.

The surface reflectance over land for 0.63 µm is taken from white-sky albedo maps generated by the MODIS-ST group. The 3.75 µm surface reflectance and emissivity over land is provided by the SEEBOR emissivity database (Seemann et al., 2008). Over ocean, fixed values of surface reflectance and emissivity are assumed.

Atmospheric correction is done in a two-level scheme separated into above cloud and below cloud corrections. The first part computes the reflectance observable at the top of the cloud level. Atmospheric transmission below the cloud is incorporated by adjusting the surface albedo to an effective value. Simplified algorithms based on forward simulations are used to compute atmospheric transmission values for ozone and for water vapor. MODTRAN v4 code is used to compute regression coefficients as a function of absorber amount, which is provided by NCEP. In a similar manner for the 3.75 µm channel, atmospheric transmission is provided by PFAAST – a fast infrared radiative transfer model that uses the NCEP profiles.

Based on Optimal Estimation, DCOMP makes use of the uncertainty estimates of input parameters and the forward model and then propagates these into uncertainty estimates for the retrieved parameters.

We derive liquid water path and ice water path using COD and CRE by LWP = 5/9 *COD*CRE for liquid cloud phase (Wood; Hartmann 2006) and IWP = [COD**(1/0.84)]/0.065 for ice water path (Figure 7 in Heymsfield et al. 2003). The Heymsfield relationship was derived empirically from aircraft measurements. The motivation for this choice is that the cloud-top effective radius for thick ice clouds has little correlation with the effective radius deeper into the cloud. Our analysis indicates that this empirical relationship based solely on COD gives values higher than those predicted by the method employed for water clouds.

1.1.2.4 Products and Characteristics

This section summarizes the procedures to obtain the cloud properties and indicates the necessary tools and ancillary data, as well as specific processing for the statistics provided in the GEWEX Cloud Assessment database.

Table 1.1.2: Characteristics of PATMOS-x Data Set for the GEWEX Cloud Assessment Database

Method and ancillary data:
- **Cloud detection**: 6 Bayesian classifiers, depending on 7 surface types (Heidinger et al., 2012)
- **CT, CEM:** from T(11µm) and T(12µm) (Optimal Estimation) (Heidinger; Pavolonis, 2009)
  Radiative transfer model: PFAAST
  Assumptions: cloud type from MODIS and microphysics:
- **CP:** from CT, use atmospheric profiles: NCEP Reanalysis Version 1
- **COD, CRE:** from 0.6µm, 3.8µm (Optimal Estimation) (Walther and Heidinger, 2012)
  Radiative transfer model: Successive Order of Interaction (SOI) model (essentially an adding/doubling model) used to compute cloud scattering tables. (Heidinger et al., 2005) PFAAST used for clear-sky IR computations. Single scattering and a multiple scattering approximation employed for clear-sky 0.6µm radiative transfer.
  Surface reflectance: MODIS-ST, surface emissivity: SEEBOR database
  Single Scattering Properties: Mie (water) and mixture of ice crystal habits (ice)

- **CWP:** from COD and CRE: (CLWP = 5/9 COD x CREL; CIWP = $COD^{1/0.84}/0.065$)

Characteristics:
- **Strengths:** CT, CP, CEM same retrieval method during day and night,
- **Limitations:** Optical and bulk microphysical properties are available only during day

Specifics for GEWEX Statistics:
- Re-normalize by the IR-only total cloud amount to mitigate day/night cloud masking differences on the layered cloud amounts.
- AMPM files only exists for periods and products for which all four overpass types are available (morning and afternoon satellites and ascending and descending).

1.1.2.5 Uncertainty Estimates

Table 1.1.3: PATMOS-x Uncertainty Estimates

	Ocean	Snow-free Land	Snow-covered Land	Desert	Arctic	Antarctic
Probability of Correct Cloud Detection	0.93	0.86	0.77	0.91	0.74	0.71

Probability of Correct Cloud Detection for PATMOS-x determined through a comparison with the CALIPSO/CALIOP cloud layer product. Data used consisted of multiple days of collocated NOAA-18 and CALIPSO/CALIOP measurements.

Cloud type	CZ bias (km)	CZ Std. Dev. (km)	CT bias (K)	CT Std. Dev. (K)	CEM bias	CEM Std. Dev.
Low -Level	-0.80	2.45	2.79	14.2	0.08	0.27
Mid-Level	-0.09	2.53	1.86	17.0	0.01	0.23
High Thick	0.26	0.86	-0.94	4.0	0.00	0.02
High Thin	0.57	2.43	-2.85	16.9	-0.06	0.15
All Clouds	-0.1	2.5	0.36	16	0.01	0.2

Performance metrics of the PATMOS-x IR cloud height algorithm (ACHA) generated by the comparison of pixel-level results to those from CALIPSO/CALIOP during periods of simultaneity. Bias is computed as PATMOS-x – CALIPSO. Because these results are computed from pixel-level results, the standard deviations (Std. Dev.) of the differences are likely over-estimates of the values for the L3 data submitted here.

	COD	CRE	CWP
Liquid Phase	20%	2 μm	30%
Ice Phase	30%	5 μm	50%

Performance metrics for the PATMOS-x Daytime Cloud Optical and Microphysical Properties (DCOMP) algorithm. The estimates are based on comparisons of PATMOS-x run on MODIS and compared to AMSRe and the MODIS Science Team (MYD06) Collection 5 products.

1.1.3 Cloud Properties from HIRS/TOVS

The TOVS instruments aboard the NOAA Polar Orbiting Environmental Satellites have measured radiation emitted and scattered from different levels of the atmosphere since 1979. The TOVS system consists of two sounders for the troposphere: the High resolution Infrared Radiation Sounder (HIRS) with 19 IR spectral channels between 3.7 and 15 μm and one VIS channel (0.7 μm) and the Microwave Sounding Unit (MSU) with four microwave channels around the O_2 absorption band centered at 5 μm. (There is also a Stratospheric Sounding Unit.) The IR channels are clustered near absorption bands of CO_2, centered at 4.3 and 15 μm, a water vapor absorption band centered at 6.7 μm and an Ozone absorption band around 9.3 μm. By assuming that CO_2 is uniformly mixed in the atmosphere, absorption and emission due to CO_2 can be used to sense the temperature and the uppermost cloud level in the atmosphere: measured radiances from near the center of a CO_2 absorption band are sensitive only to the upper atmosphere while radiances from the wings of the band (away from the band centre) see successively lower levels of the atmosphere. HIRS provides measurements at a spatial resolution of about

17 km (at nadir). Table 1.1.4 presents the HIRS spectral bands used for the retrieval of CP and CEM, and Figure 1.1.4 illustrates the weighting functions of the CO_2 absorption band channels. MSU provides measurements at a spatial resolution of about 100 km (at nadir). Microwave radiation passes through aerosols and most clouds. Therefore MSU can be used to predict HIRS clear sky radiances: differences between HIRS and MSU radiances can be taken to indicate the presence of clouds. In 2001, MSU was replaced by AMSU with water vapor sounding capability and a smaller footprint of 45 km at nadir.

Table 1.1.4: HIRS spectral bands used in the cloud top pressure and effective cloud amount algorithm, including bandcenters, principal absorbing components, and approximate pressure level corresponding to the peak in the individual band weighting functions.

HIRS Band Number	HIRS Bandcenter	Principal Absorbing Components	Approx. Peak in Weighting Function (hPa)
8	11.1	H_2O, CO_2	Surface
7	13.3	H_2O, CO_2, O_3	900
6	13.6	H_2O, CO_2, O_3	700
5	13.9	H_2O, CO_2, O_3	500
4	14.2	H_2O, CO_2, O_3, N_2O	300

Within the NOAA/NASA Pathfinder Program, two retrieval algorithms had been chosen to convert these measurements into physical properties of the atmosphere and surface: TOVS Path-A (Susskind et al., 1997), making use of a weather forecast model and a priori data, and TOVS Path-B (Scott et al., 1999; Stubenrauch et al., 2006), using only a priori data. These data sets provide atmospheric temperature and water vapor profiles as well as cloud and surface properties.

NOAA is also establishing a cloud climate record from HIRS, using the CO_2 slicing method (see below). The CO_2 slicing approach has a long history, having been applied to data from both HIRS (Wylie et al., 1999; 2005) and the Geostationary Operational Environmental Satellite (GOES) sounder (Menzel et al., 1998). More recently it has been applied to the data from the Moderate resolution Imaging Spectro-radiometer (Menzel et al., 2008).

1.1.3.1 HIRS-NOAA
P. Menzel, D. Wylie, E. Olson, B. Baum

1.1.3.1.1 Measurements

The calibrated and navigated HIRS data are processed at single pixel resolution for FOVs with satellite viewing angle of $\leq 32°$; global coverage is realized every two days with one satellite. The accuracy of the cloud retrieval depends on good calibration, knowledge of spectral response functions, and accurate computationally fast radiative transfer models to simulate top-of-atmosphere radiances. For the NOAA-14 HIRS and following, the knowledge of spectral response functions (SRF) has been improved through comparison with AIRS spectra (using the approach of Tobin et al, 2001). For sensors before NOAA-14, sensor to sensor radiance calibration differences must be reduced using simultaneous nadir overpasses (Shi et al., 2009) and making the implied spectral adjustments (this work is underway). The difference between calculated and observed clear-sky radiances for the CO_2 slicing spectral bands relies on a radiance bias adjustment.
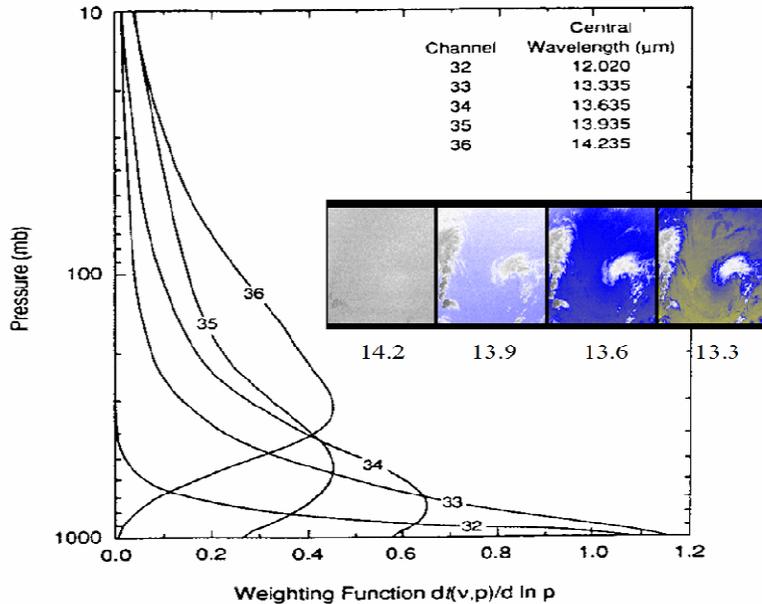
Figure 1.1.1. Weighting functions for the four HIRS channels in the CO_2 absorption band where HIRS channels 4, 5, 6, 7, and 10 are equivalent to these MODIS channel 36, 35, 34, 33, and 32.

1.1.3.1.2 Cloud Detection

Determination of the cloud mask used to separate clear from cloudy HIRS fields of view (FOV) is based on spatial and temporal variances in the 11-μm window channel following Jackson and Bates (2001). Clear FOVs are identified by low variances between neighboring FOVs and the warmest data at each location over 5 days are reported. This method of clear FOV identification is similar to that used in the ISCCP. The radiances are also corrected for zenith effects (limb darkening) and the observations viewing zenith angles limited to less than 32°. After establishing the cloud mask, the clear sky measurements from the past 35 days are composited and compared to forward model calculations of clear channel radiances using NCEP–National Center for Atmospheric Research (NCAR) reanalysis project temperature and moisture soundings. This is done to establish the biases in the clear radiance calculations with respect to the clear sky measurements. In a second iteration, a screening for thin cirrus using the CO_2 channels is applied and the biases are recalculated for the remaining clear HIRS pixels. No external temperature information is used for the cloud mask. The biases in the clear radiance calculation are averaged over 30 days in a uniform grid (with cell sizes of 2.5° latitude by 2.5° longitude). Separate bias grids are used for the ascending and descending orbits on each satellite to accommodate different aspects of the diurnal cycle. The biases are applied in the radiative transfer equation solution for cloud height.

1.1.3.1.3 Retrieval

CP and CEM are determined using radiances measured in spectral bands located within the broad 15 μm CO_2 absorption region. The CO_2 slicing technique is based on the atmosphere becoming more opaque due to CO_2 absorption as the wavelength increases from 13.3 to 15 μm, thereby causing radiances obtained from these spectral bands to be sensitive to different layers in the atmosphere. CO_2 slicing corrects for cloud semi-transparency and thus is well suited for detecting high thin cirrus. CO_2 slicing works best for clouds located above 650 hPa where the weighting functions are largest and the clear and cloudy fields of view offer larger thermal contrast. For clouds below 650 hPa, the cloud is assumed to be opaque and the infrared window brightness temperature is compared to the NCAR/NCEP Reanalysis temperature profile; this works best over oceans where the surface temperature is reasonably well characterized but often suggests low clouds incorrectly over land.

CP is converted to CZ and CT through the use of gridded meteorological products that provide temperature profiles at 25 hPa intervals from 1000-900 hPa, 50 hPa intervals from 900-100 hPa, and at 70,

50, 30, 20, and 10 hPa every 6 hours. The product used for this purpose is provided by the NCEP/NCAR Reanalysis (Kalnay et al., 1996). Differences between model-derived and measured clear-sky radiances are reduced with a radiance bias adjustment to avoid height assignment errors. Cloud properties are derived similarly for both daytime and nighttime data as the IR method is independent of solar illumination. CO_2 slicing is most effective for the analysis of midlevel to high-level clouds, especially semi-transparent high clouds such as cirrus. One constraint to the use of the 15 μm bands is that the cloud signal (change in radiance caused by the presence of cloud) becomes comparable to instrument noise for optically thin clouds and for clouds occurring in the lowest 3 km of the atmosphere. When low clouds are present, the 11 μm data are used to infer cloud top temperature and then pressure and height via model analysis.

The CO_2 slicing technique is founded in the calculation of radiative transfer in an atmosphere assuming that only a single cloud layer is present. For a given FOV the observed radiance can be assumed to very good accuracy to be the linear combination of the clear radiance and the radiance from the cloud layer. Then following Chahine (1974) and Smith and Platt (1978), the inference of CP for a given cloud element is derived from radiance ratios between two nearby spectral bands written as

$$\frac{R(\lambda_1) - R_{clr}(\lambda_1)}{R(\lambda_2) - R_{clr}(\lambda_2)} = \frac{CEM_1 \int_{pi}^{pj} \tau(\lambda_1, p) \frac{dB[\lambda_1, T(p)]}{dp} dp}{CEM_2 \int_{pi}^{pj} \tau(\lambda_2, p) \frac{dB[\lambda_2, T(p)]}{dp} dp} \quad (1.1.1)$$

For frequencies that are spaced closely in wavenumber, the assumption is made that CEM_1 is approximately CEM_2, and this allows the pressure of the cloud within the FOV to be determined. If CEM is overestimated, then CP is also overestimated. The atmospheric temperature and transmittance profiles for the two spectral bands must be known or estimated.

Once a cloud top pressure has been determined, the effective cloud emissivity (by assuming a cloud covering the whole FOV) can be evaluated from the IR atmospheric window band data using the relation

$$CEM = \frac{R(\lambda_{aw}) - R_{clr}(\lambda_{aw})}{B[\lambda_{aw}, T(p)] - R_{clr}(\lambda_{aw})} \quad (1.1.2)$$

Here CEM is the cloud emissivity, λ_{aw} represents the window band wavelength, and $B[\lambda_{aw}, T(CP)]$ is the opaque cloud radiance. CEM cannot be calculated without an estimate of the window band clear sky radiance. In the case of a partly covered cloud field within the FOV, CEM will be underestimated. Therefore, when *CEM* is less than unity, HIRS may be observing broken cloud, overcast transmissive cloud or broken transmissive cloud. With an observational FOV of roughly twenty kilometers across, the semi-transparency for a given field of view is more often due to cloud emissivity being less than one than due to the cloud not completely covering the field of view. For most synoptic regimes, especially in the tropics and subtropics, this is found to be true (Wylie et al., 1994).

Equation (1.1.1) is used to determine the mean cloud properties from a 20 km FOV (all pixels are treated as the same size, roughly the average over the scan angle range used). On the left side of Equation (1.1.1), cloud radiances are measured by HIRS. Clear radiances are determined in a radiative transfer calculation of the HIRS spectral band radiances using a transmittance model called Pressure layer Fast Algorithm for Atmospheric Transmittances (PFAAST) (Hannon et al., 1996; Strow et al., 2006); this model has 101 pressure level vertical coordinates from 0.05 to 1100 hPa and accounts for variations in satellite zenith angle, absorption by well-mixed gases (including nitrogen, oxygen, and carbon dioxide), water vapor (including the water vapor continuum), and ozone. The global analyses of temperature and moisture fields from the National Center of Environmental Prediction (NCEP) Reanalysis and the Reynolds blended sea surface temperatures (Reynolds and Smith 1994) are used to define the fields of temperature and moisture used in the forward calculation. The calculation of radiances also includes a

sinuoidal varying, globally uniform CO_2 concentration that increases 1.5 ppm per year from 337.5 in January 1980 to 381 ppm in January 2009 with a seasonal amplitude change of $\pm$ 3 ppm.

The right side of Equation (1.1.1) is calculated from a temperature and moisture profile and the profiles of atmospheric transmittance for the spectral bands as a function of p, the cloud top pressure (the integration through the atmosphere is accomplished at 101 discrete levels. Again, the NCEP Global Reanalysis of temperature and moisture fields are used. A radiance bias adjustment of measured versus calculated clear sky radiances is based on the previous 35 day clear sky radiance composite; this adjustment is used to assure that the right and left sides of Equation (1.1.1) are balanced.

The cloud top pressure is selected with a "top-down" approach. If the most opaque bands (14.2 μm /14.0 μm) detect cloud so that $(R - R_{clr})$ for both bands is greater than the instrument noise (estimated at 0.5 mW/m²/ster/cm⁻¹) and Equation (1.1.1) produces a solution high in the troposphere, this is taken as the cloud top pressure solution (no other band ratios are investigated). This ratio is most sensitive to the highest clouds. If the most opaque bands do not produce a solution, a ratio of less opaque bands (14.0 μm /13.6 μm) is investigated for a solution in the upper part of the troposphere; if found this is taken as the cloud top pressure solution (no other bands are investigated). This ratio is generally more sensitive to middle-level clouds and cloud edges where information from the atmosphere below is important. If the less opaque bands do not produce a solution, a ratio of even less opaque bands (13.6 μm /13.3 μm) is investigated. This would yield the cloud top pressure for the lowest level clouds. Additionally, stratospheric clouds are identified when the water vapor sensitive band 12 at 6.7 μm is warmer than the infrared window band 8 at 11 μm.

If a radiance ratio for cloudy FOVs cannot be calculated reliably for any of the possible band pairs because $(R - R_{clr})$ is less than 0.5 mW/m2/ster/cm⁻¹ (approximately the instrument noise level) or none of the cloud top pressure solutions were in the appropriate range for that band pair, then a cloud top pressure is calculated directly from the infrared window band assuming that the cloud layer is opaque and that it has a brightness temperature colder than the surface physical temperature by 3 K over ocean and 5 K over land where Tsfc is time interpolated from the NCEP Reanalysis – if the latter condition is not met, the FOV is labeled "uncertain" instead of "cloudy." This procedure is not actually used over land; all FOVs that fail in the CO_2 slicing retrieval are labeled "uncertain." The HIRS observed 11.1 μm IR window band brightness temperature is compared with a corresponding brightness temperature profile derived from the gridded model product to infer a cloud top pressure and the effective cloud amount is assumed to be unity. In this way, all clouds are assigned a cloud top pressure either by CO_2 or infrared window calculations. It should be noted that low clouds below 950 hPa or over barren land are assumed to be uncertain and designated as such; below 950 hPa the thermal contrast is not reliable and over barren land (as identified in the IGBP ecosystem maps - Defries et al., 1995) where the surface temperature is not tracked well in the NCEP Reanalysis. In the current form of the algorithm, very thin high clouds (likely ice clouds) are sometimes mistaken for low level opaque clouds; Wylie and Menzel (1989) found that this occurred for about half of the very thin clouds with CEM less than 0.1.

1.1.3.1.4 Products and Characteristics

Characteristics of the HIRS-NOAA data set for the GEWEX Cloud Assessment database are found in Table 1.1.5.

Table 1.1.5: Characteristics of HIRS-NOAA Data Set for the GEWEX Cloud Assessment database

Method and ancillary data:

- **Spectral bands used:** 5 CO_2 channels + IRW band : IR only, day and night
- **Cloud detection:** Spatial and temporal variances of window channel data plus CO2 channel screening of thin cirrus, giving CA
- **Clear radiance estimate:** Explicit forward radiance calculation (based on NCEP/NCAR) Reanalysis) with calculated minus measured radiance bias adjustment

- **Cloud parameters processed:** CP, CEM, CT
- **Method:** CO_2 slicing, T(IRW) for CP > 650 hPa

Characteristics

- **Strengths:** good detection of high thin clouds even in partly cloudy FOVs
- **Limitations:** thermal contrast for low clouds is suspect (low cloud with CTP> 950 hPa or with 3 (5) deg C of SST (LST) or over barren land is assumed to be clear sky); polar clouds

1.1.3.1.5 Uncertainty Estimates

Error analyses for the method are provided in Menzel et al. (1992) and Baum and Wielicki (1994). HIRS CO_2 spectral bands (Figure 1.1.1) are similar to those on VAS and MODIS. VAS CO_2 channels (14.25, 14.01, and 13.33 μm) are similar to three of the four on HIRS. MODIS spectral bands were specified to be the same as those on HIRS. Thus, studies of cloud top property errors associated with VAS and MODIS are assumed to indicate the errors associated with HIRS (ignoring the effect of fov size where HIRS has a 20 km footprint, VAS 14 km, and MODIS 1 km aggregated to 5 km).

In the following we summarize uncertainties of the CO_2 slicing method.

- Errors associated with the assumption of constant emissivity for the CO_2 channels are negligible.
- The CO_2 slicing algorithm determines the height of the radiative center of the cloud; for optically thick clouds this is near the cloud top while for optically thin clouds it is near the cloud middle.
- Multi-layer cloud situations where an opaque cloud underlies a transmissive cloud cause errors in the height of the transmissive cloud of about 100 hPa for most cases (the cloud is determined to be too low in the atmosphere). The error in transmissive cloud height is largest when the underlying opaque layer is in the middle troposphere (400 - 700 hPa) and small to negligible when the opaque layer is near the surface or close to the transmissive layer.
- When the surface temperature guess doesn't track surface warming (cooling), then the cloud layer is calculated to be too low (high). Nominal diurnal changes in the ground temperature are typically tracked to better than 5 C in the CO_2 slicing algorithm, so that they have little effect on the ability to detect transmissive clouds or to determine their heights.
- The CO_2 solution is largely insensitive to errors in the temperature sounding in the lower troposphere. There are often compensating effects in the integration of the atmospheric column. The errors in the CO_2 slicing cloud top pressure estimate caused by sounding errors in layers where the CO_2 spectral channels have sensitivity are roughly inversely proportional to the lapse rate at the level of the cloud.
- Instrument noise causes the CO_2 slicing algorithm to miss roughly half of the thin cirrus with effective cloud amount less than 0.10; this represents about 5% of all observations.

Table 1.1.6: HIRS-NOAA Cloud Parameter Uncertainty Estimates
- Cloud detection: uncertain over ocean 15-20% of observations, uncertain over land 15-20% of observations in pm orbit, 20-30% of observations in am orbit
- CP: +/- 50 hPa
- CEM: +/- .05 for CEM> 0.50, +/- 0.15 for CEM<0.50
- CT: +/- 5 deg C

1.1.3.2 TOVS Path-B
C.J. Stubenrauch

1.1.3.2.1 Measurements

The Improved Initialization Inversion (3I) algorithm (Chédin et al., 1985; Scott et al., 1999) is based on a fast line-by-line radiative transfer model (4A, Scott and Chédin, 1981; ***http://www.noveltis.net/4AOP***) and a data set for the initial guess of the atmospheric temperature profile retrieval (TIGR, Chédin et al., 1985; Chevallier et al., 1998). The latter consists of brightness temperatures of the HIRS and MSU channels that have been simulated by the 4A radiative transfer model from clear sky radiosonde measurements of about 2000 atmospheric temperature and humidity profiles, classified into five air masses (tropical to polar). Systematic biases between observed and simulated brightness temperatures (T_B) due to the radiative transfer model, to instrument calibration (satellite-to-satellite consistency) or to unexpected events (such as the Mt. Pinatubo eruption) are removed by applying corrections to the measured HIRS brightness temperatures (Scott et al., 1999). This method also takes care of changes in the CO_2 concentration over time (Chédin et al., 2003). These bias adjustment corrections were obtained from a collocated radiosonde-satellite data set (DSD5 data set; Uddstrom and McMillin, 1993), provided by the National Satellite Data and Information Service (NESDIS) of NOAA for the period between 1987 and 1995.

1.1.3.2.2 Cloud Detection

Clouds are detected at HIRS spatial resolution (~17 km at nadir) by a succession of threshold tests. An important part of the cloud detection is the use of simultaneous MSU radiance measurements in channels 2 and 3, assuming there is no cloud or precipitation contamination of the MSU measurements. Because the latter probe through the clouds, they are used to predict clear sky IR brightness temperatures, which are compared to those of the HIRS instrument for all individual pixels to decide if they are cloudy. Other tests use surface estimates of the atmospheric window channel brightness temperatures at 3.7, 4 and 11 µm, in which contributions from water vapour and surface emissivity are removed by a regression from different HIRS brightness temperature channels. Regression coefficients depend on airmass and have been obtained using least square fits to the TIGR data set. Surface estimates of the brightness temperatures at 3.7 and 4 µm are compared, and the surface estimate of the brightness temperature at 11 µm is tested for spatial heterogeneity. Studies concerning the temporal evolution of cloud properties after the eruption of Mt Pinatubo in June 1991 (Stubenrauch and Eddounia, 2001; Luo et al., 2002) revealed that high-level clouds were not affected globally by the huge amount of aerosols released into the stratosphere. However, the original cloud detection (Chédin et al., 1985; Stubenrauch et al., 1999a) had to be slightly modified, because these aerosols were falsely detected as low-level clouds by the TOVS instrument. The revised cloud detection is documented in (Stubenrauch et al., 2006).

1.1.3.2.3 Retrieval

1.1.3.2.3.1 CP, CEM, CT

To insure more coherence with the MSU spatial resolution (~100 km at nadir), the HIRS radiances are averaged separately over clear pixels and over cloudy pixels within 100 km x 100 km regions. Cloud properties are determined from the averaged cloudy pixel radiances assuming that all cloudy pixels are covered by a single homogeneous cloud layer.

CP and CEM are obtained from four radiances along the 15 µm CO_2-absorption band (with peak responses from 400 to 900 hPa levels in the atmosphere) and one in the 11 µm IR atmospheric window by a method based on the coherence of CEM (Eq. 1.1.3), obtained from the five channels sensitive to the pressure level of the real cloud.

$$\mathbf{CEM}(\mathbf{p}_k, \lambda_i) = \frac{\mathbf{R}_m(\lambda_i) - \mathbf{R}_{clr}(\lambda_i)}{\mathbf{R}_{cld}(\mathbf{p}_k, \lambda_i) - \mathbf{R}_{clr}(\lambda_i)} \qquad \text{for i = 4,8} \qquad (1.1.3)$$

where λ_i is the wavelength of HIRS channel i, p_k is the pressure level k out of 30 levels, R_m is the measured radiance, R_{clr} is the retrieved clear sky radiance and R_{cld} is the calculated radiance emitted by a homogeneous opaque single cloud layer.

$$\chi_w^{\,2}(\boldsymbol{p_k}) = \sum_{i=1}^{N} \left[(\boldsymbol{R_{cld}}(\boldsymbol{p_k}, \lambda_i) - \boldsymbol{R_{clr}}(\lambda_i)) \cdot \boldsymbol{CEM}(\boldsymbol{p_k}) - (\boldsymbol{R_m}(\lambda_i) - \boldsymbol{R_{clr}}(\lambda_i)) \right]^2 * \boldsymbol{W}^2(\boldsymbol{p_k}, \lambda_i) \quad (1.1.4)$$

Minimizing χ_w^2 in Eq. 1.1.4 leads to consistent values of CEM and the corresponding pressure of the cloud, CP. Empirical weights $W^2(p_k, \lambda_i)$ reflect the effect of the brightness temperature uncertainty on the cloudy and clear radiances at each cloud level within the air mass class closest to the observation (Stubenrauch et al., 1999b). It is important to allow values larger than 1 for CEM, because at larger pressure levels R_{clr} and R_{cld} become very similar and their uncertainties can lead to large values of CEM (We allow values up to 2, but for further analyses the maximum value is set to 1). When the χ_w^2 method leads to a non-acceptable value of CEM (larger than 2, this threshold includes noise for low-level clouds), the scene is set to clear sky.

CT is obtained from CP using the retrieved atmospheric temperature profiles. In case the retrieval of the atmospheric profiles failed (in general for situations with opaque clouds), the first guess profile of the TIGR data set is used. The cloud amount is the fraction of cloudy HIRS pixels in each 1° longitude x 1° latitude grid. The effective cloud amount CAE over a 1° grid is the product of cloud amount CA and CEM.

1.1.3.2.3.2 Bulk Microphysical Properties of Semi-Transparent Cirrus

The retrieval of mean effective ice crystal radii of semi-transparent cirrus (CREIH) is based on spectral cirrus emissivity differences between 11 and 8 μm. The difference increases with decreasing mean effective ice crystal size: it is largest for small ice crystals (about 0.3 for effective ice crystal radius of 2.5 μm) and it becomes negligible for CREIH of about 40 μm. Cirrus effective emissivities at 8.3 and 11.1 μm are retrieved from the measured radiances, cloudy radiance at cloud pressure CP and clear sky radiances as in Eq. 1.1.3. Atmospheric water vapor contributions are taken into account by using cirrus emissivities instead of brightness temperatures, and therefore the retrieval is independent of atmospheric conditions (Rädel et al., 2003). CREIH is obtained from the retrieved cirrus effective emissivities by comparing to look-up tables. These have been constructed from radiative transfer computations (Streamer, Key and Schweiger, 1998), after having included single scattering properties of planar polycrystals distributed according a bimodal Γ-size distribution (Mitchell et al., 1996, 2002). To reduce the contribution of partly cloud-covered pixels, the ice crystal size retrieval is only performed for high-level clouds of large horizontal extension (1° x 1°), corresponding to about 90% of all high-level clouds. CT of these clouds is smaller than 260 K. Because the retrieval in the IR is mainly based on spectral absorption difference, it performs well only for semi-transparent cirrus clouds (CEM between 0.3 and 0.85, or COD between 0.7 and 3.8), about 60% of all high-level clouds. The CREIH retrieval is influenced by the increase of pixel size and path of the emitted radiation received by the HIRS radiometer with viewing zenith angle. Therefore, the CREIH retrieval has been applied only to viewing zenith angles less than 30°. In a second step, the ice water path CIWPH of thin cirrus is determined from CREIH and the cirrus emissivity at 11 μm, again using a look-up table approach (Stubenrauch et al., 2004).

1.1.3.2.4 Standard Products and Characteristics of GEWEX-Archived Version

This section summarizes the procedures used to obtain the cloud properties and indicates the necessary tools and ancillary data, as well as data availability and specific processing for the statistics of the GEWEX Cloud Assessment database.

Table 1.1.7: Characteristics of TOVS Path-B Data Set for the GEWEX Cloud Assessment database

Method and Ancillary Data:

- **Cloud detection:** multi-spectral, including MSU to predict clear sky snow/ice flag from MSU
- **CP, CEM:** from CO_2 band + IRW (weighted χ^2): 6 channels
  - o Clear sky estimate: 4A radiative transfer, TIGR spectral transmissivities,
  - o Bias adjustment from collocated radiosonde-TOVS (DSD5, NOAA-NESDIS),

- o Atmospheric profiles: retrieved (3I) or first guess (TIGR)
- o No assumptions on microphysics
- **CT:** from atmospheric profiles
- **CREIH, IWPH:** from cirrus emissivities at 8.3μm, 11.1μm (LUT)
  - o Surface emissivity: CERES/SARB database, regrouped to 8 types
  - o Radiative transfer model: Streamer
  - o Single Scattering Properties: planar polycrystals, bimodal size distribution
  - o CT < 260 K, 0.3 < CEM < 0.85, θv < 30°

Characteristics:

- CT, CP, CEM same retrieval method during day and night
- COD is determined from CEM as COD = -2 x ln(1-CEM)
- CREIH, CIWPH during day and night, but only for (CP < 440 hPa, 0.3 < CEM < 0.85, CT > 260 K) and for zenith viewing angles < 30°
- **Strengths:** good sensitivity to thin cirrus, reliable cirrus properties also in case of multi-layer clouds, day and night, no bias in low cloud properties
- **Limitations:** larger noise in low cloud properties, polar clouds

Specifics for GEWEX Statistics:

- CT is used to distinguish between ice clouds (CT <230 K) and liquid clouds (CT > 260 K); mixed phase clouds are not considered separately.
- Data are stored separately for AM and PM observations. In the case of several AM or PM observations within the same 1° latitude x 1° longitude only the observation with the smallest viewing zenith angle is kept.
- NOAA10, NOAA12 and NOA11 data were processed for physical cloud properties (local observation times 7h30 and 1h30); for bulk microphysical properties of semi-transparent high ice clouds only NOAA10 data could be used (valid 8.3μm channel).

Data Availability:
At present, L3 data (in netCDF, like for GEWEX Cloud Assessment) gridded at 1° latitude x 1° longitude are available at **http://ara.lmd.polytechnique.fr**, from NOAA10 and NOAA12 observations (local observation time: 7h30 AM and 7h30 PM).

1.1.3.2.5 Uncertainty Estimates

The accuracy in CP is limited to the pressure level step of about 35 hPa. The CP uncertainty can be estimated by the difference in CP between the solution of the minimized χ^2 and CP of the second smallest χ^2. Over ocean, this uncertainty is about 25 hPa, smallest in the southern hemisphere (20 hPa) and largest in the northern hemisphere subtropics (30 hPa). Over land, the uncertainty is on average 40 hPa, with a minimum in the tropics (30 hPa) and maximum in the northern hemisphere subtropics (50 hPa). Cloud-top height has been further evaluated using simultaneous LITE data (Stubenrauch et al. 2005). The cloud height determined by TOVS corresponds well in general to the height of the 'apparent middle' of the cloud system: with coincidences for 53% of TOVS Path-B low-level clouds within 1 km and for 49% of TOVS Path-B high-level clouds within 1.5 km, respectively. For low clouds this height is close to the real cloud-top (about 600 m), whereas in the case of high clouds with diffuse cloud-tops, especially in the tropics, the difference between cloud top and radiative height can be as large as 2 km. 22.5% of TOVS Path-B low-level clouds are covered by an additional very thin high cloud layer not detectable by TOVS. Comparing for these cases the TOVS cloud height with the second LITE cloud layer increases the overall agreement for low-level clouds to about 64%. Figure 1.2.4 presents zonal means of the uncertainty estimates of TOVS Path-B and AIRS-LMD retrievals, and global mean uncertainties are presented in Table 1.2.7.

Sensitivity studies of CREIH, linked to different assumptions in the retrieval, are described in (Rädel et al. 2003). Uncertainties due to assumption of the cloud physical properties (height, vertical extent) and to surface temperature and lapse rate are small (less than 5%). Over desert CREIH may be underestimated by 10%. Partial cloud cover may lead to an overestimation of about 10% (for thick cirrus), and in the case of low clouds underneath the cirrus CREIH may be overestimated by up to 25% (for thin cirrus). Assumptions on ice crystal habit and on the shape of the size distribution within the cloud may reach 25%.

1.2 Cloud Data Products from the NASA Earth Observing System

1.2.1 MODIS

The Moderate Resolution Imaging Spectroradiometer (MODIS) is a 36 channel instrument flying on the NASA TERRA satellite ("10:30am" orbit) since 2000 and the NASA AQUA satellite ("1:30pm" orbit) since 2002. The channels cover the main part of the solar spectrum from about 0.4 to 2.2 μm and the thermal infrared from about 3.7 to 14.4 μm (see figure 1.1.1). The solar channels have field of views (FOVs) at nadir ranging from 250 m to 1 km and the thermal IR channels have FOVs of 1 km. The scan swath is 2330 km wide providing complete global coverage every two days. MODIS data have been analysed by two teams to produce cloud data products.

1.2.1.1 MODIS Science Team
S. Ackerman, S. Platnick, B. Maddux, R. Pincus

1.2.1.1.1 Cloud Detection (MOD35)
The MODIS Cloud Mask algorithm discriminates cloud from clear sky at 1 km resolution (and 250 m) by exploiting information from fourteen IR and near-IR radiance bands, and two VIS/NIR reflectance bands (Ackerman et al., 1998; Frey et al., 2008; Ackerman et al., 2008). Separate data sets are produced for day and night because of the increased ability of the Cloud Mask to detect clouds during daytime scenes (Liu et al., 2010). Tests depend on surface characteristics and solar illumination (e.g. ocean, land, snow/ice, desert, coast, sunglint, etc.). A series of threshold tests (Table 1.2.1) attempt to detect the presence of clouds or optically thick aerosol within the instrument FOV. Each test is assigned a value between 0 and 1, representing increasing confidence in clear-sky conditions, which is a linear function between two thresholds a and g. These high confidence cloud and clear thresholds, a and γ respectively, are determined from observations and/or theoretical simulations. Tests capable of detecting similar cloud conditions are grouped together (Table 1.2.1). While these groups are arranged so that independence between them is maximized, few, if any, spectral tests are completely independent. As described by Ackerman et al. (1998), a minimum confidence is determined for each group as the minimum of the confidence levels of all individual spectral tests within each group. The final cloud mask confidence is then determined from the product of results for each group. The approach is clear-sky conservative in the sense that if any test is highly confident that the FOV is obstructed by cloud elements, the final clear sky confidence is 0. The mask assigns each pixel to one of four categories (confident clear, probably clear, uncertain/probably not clear, and confident not clear) based on clear sky confidence boundaries of 0.99, 0.95, and 0.66. For the GEWEX Cloud Assessment, the MODIS-ST cloud amount (CA) for confident clear and probably clear pixels is considered zero and for pixels flagged with one of the two "not clear" categories is considered one.

1.2.1.1.2 Retrieval (MOD06)

Cloud Top Properties

Cloud pressure (CP) is derived using six thermal infrared bands (both day and night), at 5 km spatial resolution by applying the CO_2 slicing technique in combination with the 11 μm window band (Menzel et al., 1983; Menzel, 2008; see also section 1.1.3.1). The CO_2 slicing technique retrieves cloud pressure and effective cloud amount (same as effective emissivity which is the product of cloud fraction and emissivity) for opaque or non-opaque mid- to high-level clouds. The method takes advantage of differing partial absorption in several of the MODIS infrared bands located within the broad 15 μm CO_2 spectral absorption region. Retrievals are derived from ratios of differences in radiances between cloudy and clear-sky regions at two nearby bands. In MODIS operational processing, cloud pressures are calculated for the following ratio pairs: 14.2 μm/13.9 μm; 13.9 μm/13.6 μm, 13.6 μm/13.3 μm, 13.9 μm/13.3 μm, and 13.3 μm/11 μm. The emission and absorption of the cloud are assumed to be identical in the spectral band pairs. The most representative cloud pressure is chosen by minimizing the difference between the observed cloud signal and the cloud signal calculated from a forward radiative transfer model. The

fundamental CO2 slicing retrieved quantities are pressure and effective emissivity applied to a 5 x 5 pixel scene (5 km spatial scale at nadir). CO_2 slicing works best for clouds with CP > 650 hPa where the weighting functions are largest and the clear and cloudy FOV offer larger thermal contrast. For clouds with tops greater than 650 hPa, the cloud is assumed to be opaque and the infrared window brightness temperature is compared to the Global Forecast System temperature profile (GFS; Derber et al., 1991). Of the 25 pixels, at least 4 must be flagged as *probably cloudy* or *cloudy* by the cloud mask (i.e., cloud fraction $\geq$ 16%). The algorithm uses analyses from the GDAS gridded meteorological profile product (1° spatial and 6 hour temporal resolution), and the NCEP Reynolds Blended Sea Surface Temperature (SST) product to calculate the required clear-sky radiances. Once CP is determined for a given 5 x 5 scene, cloud temperature (CT) is derived through the National Center for Environmental Prediction (NCEP) GFS. The latter provides gridded temperature profiles at 25 hPa intervals from 1000-900 hPa, 50 hPa intervals from 900-100 hPa, and at 70, 50, 30, 20, and 10 hPa every 6 hours. Differences between model-derived and measured clear-sky radiances are reduced with a radiance bias adjustment to avoid height assignment errors (Menzel et al., 2007).

Table 1.2.1: MODIS-ST cloud mask tests.

Non-cloud obstruction (heavy aerosol)
Thin Cirrus Detected (solar)
Shadow Found
Thin Cirrus Detected (IR)
Cloud adjacency
simple IR Threshold Test (group I)
High Cloud: CO_2 Threshold Test (group I)
High Cloud : 6.7 μm Test (group I)
High Cloud: 1.38 μm Test (group IV)
High Cloud: 3.7-12 μm Test (group II)
IR Temperature Difference
3.9-11 μm Test (group II)
Visible Reflectance Test (group III)
Visible Ratio Test (group III)
Near-IR Reflect. Ratio Test (group III)
3.7-3.9 μm Test
Temporal Consistency
Spatial Variability: 16 spots of 250 m
VIS FOV(1,1) - FOV(1,2) ….
VIS FOV(1,1) - FOV(4,4)

Cloud Thermodynamic Phase and Optical Properties

The thermodynamic phase of each pixel is required because the retrievals must use separate forward calculations, i.e., lookup tables (LUTs), for liquid and ice clouds. For optical property retrievals, this determination is made using on a variety of tests in the VIS/NIR, SWIR, and IR portions of the spectrum (King et al., 2004; Riedi et al., 2010); when these tests disagree or are otherwise ambiguous, the pixel phase is labeled "unknown" and liquid water cloud libraries are used in the retrieval.

Cloud optical depth and effective particle radius (COD and CRE) are simultaneously retrieved by minimizing the difference between the observed and modelled reflectances in a band with negligible water absorption (e.g., 0.67, 0.86, and 1.2 μm) and one with appreciable absorption (e.g., 1.6, 2.1, and 3.7 μm), with the band combination depending on the surface type. MOD06 also includes an absorbing band retrieval combination (1.6 and 2.1μm) for ocean and snow/ice surfaces. All MOD06 optical retrievals use the MODIS 1 km aggregation L1B file. Forward calculations are tabulated across the COD, CRE, and satellite-view geometric space (Platnick et al., 2003). Land and snow/ice surface spectral albedo is provided from a gap-filled version of the MODIS land team albedo product (Moody et al., 2005). The ocean diffuse incidence albedo is specified as 0.05 globally.

Information from four different CRE are included in the pixel-level (L2) data file, derived separately from band combinations that use the 1.6, 2.1, and 3.7 μm band, as well as the 1.6/2.1 μm combination. However, only the CRE retrievals corresponding to the 2.1 μm and the 1.6/2.1 μm combination are

aggregated in the L3 file (MOD08). When the simultaneous retrieval of COD and CRE fails (i.e. the observations cannot be fit to the forward calculations) the pixel is not included in L3 aggregated statistical summaries that include joint histograms of COD and CRE. For these so-called "failed" retrievals, a retrieval of COD alone is attempted using the same fixed particle sizes assumed by ISCCP (10 and 30 μm, respectively, for liquid water and ice phase clouds) and if successful, is reported in the L2) file but is not aggregated to L3. Despite being retrieved as having liquid water phase, pixels flagged as "unknown" phase are aggregated separately in MOD08 and therefore do not impact liquid phase statistics.

1.2.1.1.3 Products and Characteristics

MODIS pixel-scale observations are aggregated on a 1° equal-angle grid (King et al., 2003) in the MOD08 L3 file. Observations from the Terra and Aqua MODIS instruments are aggregated separately. All retrievals from a given platform within a day are included, so the frequency of observations increases with distance from the equator due to overlapping swaths (2330 km for MODIS); therefore, observations from overpasses at different times (with potentially very different viewing and illumination geometries) may be included in the statistics. Monthly L3 statistics obtained from the public archive site (ladsweb.nascom.nasa.gov) are derived from daily aggregations that are weighted by the number of retrievals (i.e., pixel-count weighted); for cloud-related variables, this means that cloudier days count more than less-cloudy days. However, for the GEWEX cloud assessment the CA data sets (excluding CA_op, see below for details), are not weighted by daily pixel counts, i.e., each daily mean is weighted equally into the month. This was done solely to be consistent with CA data sets from other teams. Some GEWEX histogram data sets had to be re-binned from MOD08 histograms because the agreed upon GEWEX statistic had different bin resolution than those available directly from MOD08. Cloud optical properties are summarized separately for ice- and liquid-phase clouds, as well as for all phases (including "uncertain," see previous section).

The optical retrieval algorithm filters out pixels designated as "not clear" by the cloud mask but which are unlikely to be completely cloud-covered as required by the forward model. This removal algorithm is referred to as "clear-sky restoral". The algorithm is based on tests for spectral and spatial uniformity to further discriminate dust, heavy smoke, snow/ice, and sunglint. In addition, pixels containing cloud edges and partly cloudy pixels identified from 250 m cloud mask tests are removed. Retrievals are not performed for pixels identified by this "clear-sky restoral" algorithm. (Note: the GEWEX data set provided may differ significantly from future Collections of MODIS Level-3 data due to the treatment and aggregation of these pixels. Collection 6 will aggregate the successful retrievals into Level-3.) Cloud edge detection is the most frequent source of pixel removal in broken liquid water cloud regimes. Consistent with being partly cloudy, these edge pixels have a statistically smaller COD than their non-edge neighbors. For Terra MODIS, the edge pixels also have larger 2.1 μm CRE retrievals (also consitstent), though Aqua MODIS shows no significant change in CRE for this population of pixels for reasons that are not yet understood. An example of the impact of the restoral algorithm on tropical low clouds performed during Collection 6 testing is given in Table 1.2.2. In general, for tropical low clouds, about 25-50% of the time attempts to retrieve cloud edge pixels "fail" in the sense that simultaneous COD and CRE retrievals are not consistent with the LUTs (see previous section), and so would not have been aggregated to MOD08 anyway.

Cloud Amount Difference (%)
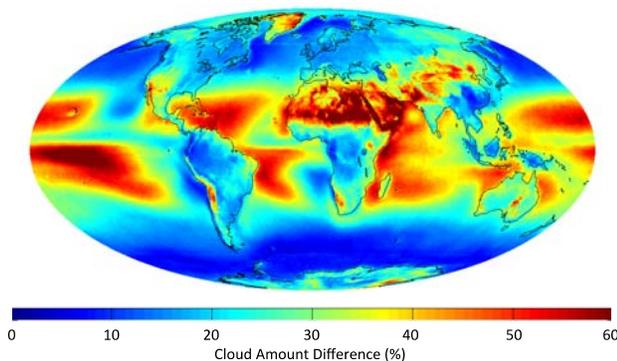
Figure 1.2.1: Difference between MOD35 cloud amount (CA) and MOD06 retrieval CA, relative to MOD35 CA. The MOD35 is the product that CA, CT, CP are derived from and MOD06 is the product that COD, CRE, CWP are derived from.

Note that only one estimate of CA provided in this assessment is intended to be used for comparison with other GEWEX CA data sets: the one derived from MOD35 which gives the proportion of pixels deemed by the cloud mask to be cloudy or probably cloudy (i.e., "not clear"). However, there is another data set that gives the proportion of available pixels for which cloud optical properties are attempted and both COD and CRE are successfully retrieved. Differences between these two estimates are typically dominated by pixels removed by the clear-sky restoration algorithm though the proportion of unsuccessful retrievals can be significant, see Figure 1.2.1.

Table 1.2.2. Mean cloud optical retrievals of different populations of pixels for Terra MODIS, 1 April 2005, ±30° latitude, ocean only, and liquid water clouds with CP ≥ 680 mb. The total cloud amount from the cloud mask (MOD35) for the region is 62%; numbers in parenthesis give the population number relative to the MOD35 cloud amount in percent. About 8.6% of MOD35 pixels were removed due to glint and heavy dust/smoke detection; there were no possible COD or CRE retrievals for another 3%.

Pixel Population	Successful COD & 2.1 µm CRE retrievals		Successful COD retrievals only (CRE retrieval not possible)
	COD	CRE (µm)	
Pixels remaining after removal algorithm is applied	7.1 (46.3%)	16.0	4.6 (7.3%)
Pixel identified as cloud edge	2.0 (23.2%)	18.1	1.2 (8.6%)
Pixels identified as partly cloudy by 250m tests	0.8 (5.7%)	19.4	0.5 (6.4%)
All pixels	5.1 (75.2%)	16.9	2.1 (22.3%)

Averages for COD are reported as linear and its base-10 logarithm in the MOD08 Level-3 data set. Because the latter approximates the radiative mean COD (reported by ISCCP) we have only included it in the assessment data set. Liquid and ice water path are computed from the COD and CRE retrievals for each 1 km pixel, assuming that clouds are vertically homogeneous, then averaged separately for liquid and ice clouds.

1.2.1.1.4 Uncertainty Estimates

The performance and characteristics of the MODIS cloud mask has been addressed in several recent papers (e.g. Liu et al., 2004; Li et al.,1993; Platnick et al., 2003; King et al., 2003; Lee et al., 2004; Naud et al., 2005; Ackerman et al., 2008; Liu et al., 2010; Maddux et al., 2010). Holz et al. (2008) compared MODIS cloud retrievals with collocated CALIOP retrievals. The nearly instantaneous comparisons were compiled regionally and globally. Globally, 88% of the time the MODIS 1 km cloud mask pixels and the CALIOP 1 km averaged layer product agree for cloudy conditions during August 2006 and February 2007. For clear-sky conditions the agreement is about 85%. The best agreement is found for non-polar daytime and the poorest agreement in the polar regions. These results are consistent with the comparisons between MODIS and CloudSat/Calipso over polar daytime and nighttime scenes found in Lui et al., 2010. Liu et al. (2010) found that the nighttime polar biases, associated with sea ice fractal coverage, had significant implciations on trends in decadal cloud cover in the Arctic nighttime. Results from regional comparisons are found in the following table.

Table 1.2.3. The global fractional agreement of cloud detection between MODIS and CALIOP for August 2006 and February 2007. The results are separated by CALIOP averaging amount, with the 1 km averaging results listed first and the 5 km averaging results presented in parenthesis, as well as day, night and surface type (from Holz et al., 2008).

	August 2006 Clear	August 2006 Cloudy	February 2006 Clear	February 2006 Cloudy
Global Day/Night CALIOP 1-km (5-km)	0.84 (0.73)	0.88 (0.87)	0.85 (0.75)	0.88 (0.87)
Non-Polar Day/Night CALIOP 1-km (5-km)	0.87 (0.76)	0.91 (0.88)	0.85 (0.76)	0.90 (0.89)
Non-Polar Day CALIOP 1-km (5-km)	0.89 (0.85)	0.90 (0.88)	0.87 (0.78)	0.91 (0.89)
Non-Polar Night CALIOP 1-km (5-km)	0.85 (0.76)	0.91 (0.88)	0.84 (0.74)	0.90 (0.88)
Non-Polar Land CALIOP 1-km (5-km)	0.90 (0.85)	0.84 (0.80)	0.82 (0.74)	0.85 (0.84)
Non-Polar Ocean CALIOP 1-km (5-km)	0.86 (0.78)	0.93 (0.91)	0.86 (0.79)	0.93 (0.90)
Arctic > 60° lat	0.74 (0.62)	0.90 (0.93)	0.82 (0.62)	0.73 (0.79)
Antarctic<-60° lat	0.77 (0.55)	0.73 (0.76)	0.91 (0.85)	0.88 (0.88)

Uncertainty estimates are computed for each retrieval of COD, CRE, and water path. This pixel-level estimate includes the effect of uncertainties in instrument calibration and nominal plane-parallel forward models, surface spectral albedo, and spectral atmospheric correction (primarily due to above-cloud atmospheric moisture uncertainty). Other error terms can be important on a pixel-level basis (e.g., vertical and/or horizontal inhomogeneity) so the uncertainty estimates provided are a lower bound on the true uncertainty (Platnick et al., 2004). Uncertainties are calculated from the cloud reflectance look-up tables used in the retrievals and therefore depend on viewing and illumination geometry, as well as surface characteristics (snow-free spectral albedo and/or the presence of snow/ice).

We estimate the uncertainty in the mean of aggregated pixels by assuming that pixel-level errors are perfectly correlated within each each grid cell on a given day but that day-to-day errors are perfectly uncorrelated. This has the effect of greatly reducing the uncertainty in the mean of monthly aggregations (by a factor of about √30 if the same number of cloudy pixels is present during a month and cloud properties are reasonably consistent over the month). True errors sources are almost certainly not uncorrelated from day to day - calibration and modeling errors, in particular, are probably not well represented as random errors. At the same time, error sources are unlikely to be perfectly correlated for a given daily aggregation. Uncertainties are a strong function of COD, CRE, solar-view geometry, and surface type; simple summary statements are not possible. Global browse imagery of MOD08 optical retrieval statistics, including means and uncertainty in the mean are available at ***modis-atmos.gsfc.nasa.gov/IMAGES/mod08d_menu_c5.html*** (daily aggregations) and ***modis-atmos.gsfc.nasa.gov/IMAGES/mod08m_menu_c5.html*** (monthly). Representative MOD06 pixel-level retrieval uncertainty examples are shown in Figs. 1.2.2. Uncertainty estimates are still the subject of active development and are intended as rough guidance rather than definitive estimates.
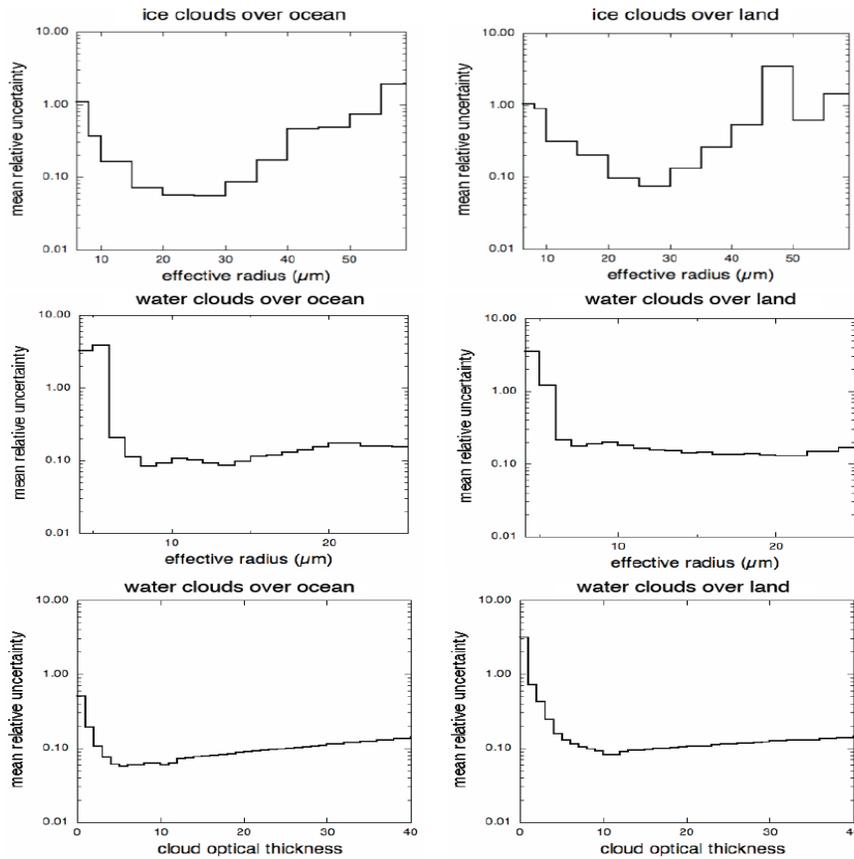
Figure 1.2.2. Example distribution of pixel-level uncertainty estimates for COD and CRE from MOD06 for a subtropical data granule. Note that a value of 1.0 represents a 100% relative uncertainty.

Holz et al. (2008) also compared MODIS derived cloud top heights to CALIOP derived heights. Globally, MODIS underestimates the CZ relative to CALIOP by 1.5 km for both August 2006 and February 2007. This value of 1.5 km is obtained using the CALIOP 1 km layer products. When compared to the CALIOP 5-km products, the differences increase to 2.5 km as a result of CALIOP's increased sensitivity to optically thin cirrus. When only high clouds above 5 km are considered, the differences are found to be greater than 4 km with individual comparison having differences larger than 15 km. The large MODIS underestimates for optical thin cirrus occur for cases when MODIS reverts to a window brightness temperature retrieval instead of CO_2 slicing (when either the spectral radiance contrast is too small or the retrieved CP is not in the range for the specific channel pair). A systematic bias is found for marine low-level stratus clouds, with MODIS overestimating the CZ by 1-2 km, this will be corrected for in future data collections.

Table 1.2.4: The cloud top height global statistics of the mean differences between MODIS and CALIOP. A mean less than zero occurs if the MODIS cloud top height is on average lower then CALIOP. The results are separated by month, global, and non-polar with non-polar including all regions except those above 60 deg N and below 60 deg S and Polar Regions. The results are also separated by 1-km and 5-km CALIOP cloud top heights with the 5 km differences within the parentheses. Results from Holz et al. (2008).

	August 2006 Mean (km)	August 2006 STD (km)	February 2007 Mean (km)	February 2007 STD (km)
Global 5km 1 km (5km)				
All Clouds	-1.5 (-2.5)	2.9 (3.8)	-1.5(-2.4)	2.9 (3.8)
High (>5km)	-2.8 (-4.2)	3.5 (4.3)	-2.8 (-4.1)	3.5 (4.4)
Low (<5km)	-0.2 (-0.3)	1.3 (1.3)	-0.3 (-0.4)	1.3 (1.3)
Non-Polar				
All Clouds	-1.5 (-2.6)	3.0 (4.0)	-1.6 (-2.7)	3.0 (4.1)
High (>5km)	-2.8 (-4.4)	3.8 (4.6)	-2.7 (-4.3)	3.7 (4.7)
Low (<5km)	-0.3 (-0.5)	1.2 (1.3)	-0.3 (-0.5)	1.3 (1.3)
Arctic > 60 deg Latitude				
All Clouds	-0.8 (-1.4)	2.1 (2.6)	-1.8 (-2.3)	2.6 (2.9)
High (>4 km)	-1.6 (-2.5)	2.4 (2.7)	-3.4 (-3.8)	2.4 (2.6)
Low (<4 km)	0.2 (0.1)	1.1 (1.1)	0 (0)	1.6 (1.7)
Antarctic < -60 deg Latitude				
All Clouds	-2.1 (-3.4)	2.8 (3.9)	-0.8 (-1.2)	1.7 (2.1)
High (> 4 km)	-3.2 (-4.6)	2.6 (3.7)	-1.7 (-2.3)	1.9 (2.2)
Low (< 4 km	0.4 (0.3)	1.4 (1.4)	0 (0)	1.0 (1.0)

1.2.1.2 MODIS - CERES Science Team
P. Minnis

The MODIS data are also analyzed with a different set of algorithms for the Clouds and the Earth's Radiant Energy System (CERES) Project (Wielicki et al., 1998). The motivation for operating a different analysis system is based on the need for consistency among the results from different satellites, retrieval of cloud properties for all identified clouds, a fixed algorithm for long time periods, and close collaboration with the complete CERES data analysis team. The CERES algorithms were originally designed for use with the 5-channel Tropical Rainfall Monitoring Mission (TRMM) Visible and Infrared Scanner (VIRS) as well as MODIS to provide a consistent cloud database across platforms. The CERES Project has scanners measuring broadband shortwave and longwave radiative fluxes on the TRMM, TERRA and AQUA satellites and required stable cloud properties to consistently interpret the measurements. The CERES Edition-2 (Ed2) cloud algorithms were used to generate the cloud properties presented in this document. These algorithms and their uncertainties are discussed in detail by Minnis et al. (2008a, 2011).

1.2.1.2.1 Measurements

CERES analyzes pixels on a "tile" basis; each tile consists of an array of pixels corresponding to roughly 32 km x 32 km. Radiances taken at 0.64, 1.6 or 2.1, 3.8, 10.8, and 12.0 μm are used in the analysis of each pixel. The full resolution VIRS 2-km data are analyzed by CERES, while 1-km MODIS data are first sampled every other scan line and every fourth pixel element. The clear-sky and surface radiance characteristics are estimated for each tile and used to analyze each pixel. Surface skin temperature and atmospheric profiles of temperature and humidity are taken from the Global Modeling Assimilation Office GEOS 4.03 analyses (Bloom et al., 2005). Surface emissivities and albedos are based on VIRS and MODIS data as described by Minnis et al. (2008a). Those input parameters are used to predict the clear-sky radiances and determine atmospheric attenuation of the spectral radiances. Calibration differences (e.g., 2008a, b) among the various imagers were not reconciled in the Ed2 analyses. The algorithms used for Ed2 are applicable to many other satellites and are being used to analyze all of the geostationary satellite imagery in near-real time for input to weather forecast models.

1.2.1.2.2 Cloud Detection

The CERES Ed2 system uses two separate cloud detection algorithms for polar and non-polar regions. The latter is described in detail by Minnis et al. (2008a) and can be applied to both MODIS and VIRS data because it primarily relies only on the 5 channels common to both instruments: 0.64, 1.6, 3.8, 10.8, and 12.0 μm. For AQUA, CERES Ed2 used the 2.1-μm channel in place of 1.6 μm. The mask consists of a set of cascading thresholds that first classify high-altitude, thick ice clouds using a crude IR threshold that depends on the surface type and local sounding. This simple test accounts for ~43% of the cloudy pixels. The next step uses IR, VIS, and brightness temperature difference (BTD) thresholds set relative to their expected clear-sky values to determine the likelihood of being cloudy. If the radiances for a given pixel fail or pass all three thresholds, the pixel is classified as clear or cloudy. This process classifies another 40% of the pixels. The remaining pixels are then scrutinized with a more complicated set of thresholds eventually resulting in a final classification for the remaining 17% of the pixels. The polar cloud mask (Trepte et al., 2002) follows a similar procedure using a different set of thresholds and tests. There are some differences in the polar masks used for TERRA and AQUA.

1.2.1.2.3 Retrieval

CERES Edition-2 uses three separate cloud retrieval algorithms (Minnis et al., 2011a). The Visible Infrared Shortwave-infrared Split-window Technique (VISST) and Shortwave-infrared Infrared Near-infrared Technique (SINT) are used during the day (solar zenith angle < 82°) over snow-free and snow-covered surfaces, respectively. The Shortwave-infrared Infrared Split-window Technique (SIST) is used over all surfaces at night and near the terminator in daylight. In all 3 methods, the shortwave infrared channel (3.8 μm) is used to estimate cloud particle size and effective cloud temperature is primarily determined by the infrared (10.8 μm) channel. The VISST and SINT use the visible (0.64 μm) and near-infrared (1.62 or 2.13 μm) channels, respectively, to determine optical depth. Calculations using a set of reflectance and emittance models based on distributions of various sizes of water droplets and smooth hexagonal ice crystals (Minnis et al., 1998) are used to iteratively match the observed radiances in the selected channels to derive cloud particle size (CRE), optical depth (COD) and emissivity (CEM), and effective temperature (CT). Phase is determined by CT and the model results that best match the radiances. Other tests (e.g., using the 12-μm channel model results for VISST) are used to assist the phase selection when the primary tests are ambiguous. At night, the optical depths are only expected to be valid for values less than about 3 or 4. The COD retrievals are primarily used to account for semi-transparency in the retrieval of the effective cloud temperature. Default values of CRE and COD are used when optical depth exceeds 4. In general, there is little skill in the nighttime retrieval of particle sizes except over the ocean.

Additional parameters are derived from the three primary parameters. Effective cloud height (CZ) and pressure (CP) are determined using a combined lapse-rate-sounding method that matches effective temperature (CT) with altitude. A lapse rate of 7.1 K km^{-1} anchored to the 24-hour running surface temperature defines the vertical profile of temperature from the surface to 700 hPa. Between 750 and 500 hPa, the lapse rate is blended with the local temperature profile from the GEOS analysis and for pressures less than 500 hPa, only the GEOS profile is used to define the change of temperature with altitude. Cloud layer thickness and cloud-top pressure are estimated using empirical formulas based on the phase, effective cloud height and temperature, and COD. The cloud base pressure is computed as the difference between the cloud-top pressure and cloud thickness. For liquid water clouds and optically thick ice clouds, it is assumed that the effective and top heights are essentially equal. Cloud ice (CIWP) and liquid water path (CLWP) are derived from the product of optical depth and particle size. Because of a coding error in the *AQUA* Ed2 algorithm, the optical depths and, hence, the water paths, derived using the SINT over snow surfaces are underestimated by a factor of 2-3, on average.

1.2.2.1.4 Products and Characteristics

CERES determines first, for each pixel, whether it is clear or cloudy along with a descriptor of the scene identification quality (e.g., weak or strong, dust, smoke, glint). Next, for clear pixels, the surface skin temperature is estimated, and for cloudy pixels retrievals are performed to obtain cloud phase, effective emissivity, temperature, height, and pressure, cloud-top and base pressure, optical depth, particle

effective size (radius for liquid and diameter for ice), and ice or liquid water path. If the primary observed spectral radiances cannot be matched to any of the models, then the pixel is reclassified as clear if the VIS-IR radiances are darker-warmer than clear sky predictions, reclassified as cloudy with the parameters filled with the results of a simple VIS-IR retrieval method assuming a particle size, or reclassified as a no-retrieval pixel if the simple VIS-IR retrieval fails. For Ed2, this last category occurs less than 4% and 0.5% of the time in non-polar regions during day and night, respectively. Over polar regions, the no-retrieval percentage increases to almost 9%. These numbers are reduced substantially in CERES Edition 4.

The CERES Ed2 products are officially available as averages within the CERES Single-Scanner Footprint (SSF), which, for TERRA and AQUA, roughly correspond to a 20-km pixel at nadir. The averages are computed by weighting each pixel value by the CERES scanner point spread function, which includes areas outside the nominal 20-km radius. Before averaging, the cloudy pixels are assigned to one of two atmospheric layers. Thus, the cloud height/pressure information is compressed into one or two layer averages.

The CERES Ed2 processing system also archives pixel-level results for areas surrounding selected locations for quality control and validation efforts. Averages of each cloud parameter are computed from pixel-level results each month on the CERES 1° latitude-longitude grid for quality control purposes. These regional averages are used to produce the CERES results (MODIS-CE) presented in this document.

1.2.2.1.5 Uncertainty Estimates

The CERES global cloud amounts are generally less than those from many other satellite cloud climatologies, but agree well with the surface-based climatology (Minnis et al. 2008). The CERES results were also compared with those from the Cloud-Aerosol Lidar and Infrared Pathfinder Satellite Observations (CALIPSO) lidar. Subsequent analysis revealed that of the 0.18 fraction of the total pixels classified as clouds by the CALIPSO Version-2 algorithms and as clear by CERES, 76% were low water clouds and only 24% were ice clouds. It was found that all of the missed ice clouds had optical depths less than 0.3, while 65% (84%) of the missed liquid water clouds had optical depths less than 0.3 (0.5) suggesting that many of those missed clouds may have been aerosols misclassified as clouds. The missed clouds from AQUA were primarily found in the trade cumulus areas and in the polar night. The TERRA polar mask appears to have worked better in the polar regions than that for AQUA in that monthly mean CERES TERRA cloud amounts over an instrumented ground site in Barrow, Alaska all fell between the radar- and lidar-detected CAs during all seasons (Kato et al. 2006). This finding is consistent with CERES missing only the optically thinnest clouds in polar regions year round. CERES Edition 4 (called Edition 3) detects and retrieves more clouds than CERES Edition 2.

Inherent uncertainties in the retrieved cloud properties due to the algorithms and assumptions are similar to those reported by Han et al. (1994). The main assumption that the clouds can be represented as single-layer plane parallel clouds is not taken into account in such estimates. It is more effective to estimate the uncertainties by comparing the retrievals with different measurements of the same properties. Cloud optical depths and effective particle sizes derived with these algorithms have been compared with in situ and active sensor (lidar and radar) measurements with generally favorable agreement for single-layer clouds. Table 1.2.5 summarizes the comparisons to date using the CERES algorithms applied to data from MODIS and from the Geostationary Operational Environmental Satellite (GOES). It is an expanded version of Table II from Minnis et al. (2011). ARSCL refers to the ARM Active Remote Sensing of Clouds cloud boundary product (Clothiaux et al., 2000) applied to data taken at the Southern Great Plains Central Facility (SCF). Microwave radiometer data were used to retrieve cloud liquid water path at the SCF and for the ARM Mobile Facility (AMF) located at Pt. Reyes, California (see Minnis et al., 2011). No comparisons have yet been performed for clouds that were identified as multilayered by the independent measurement systems.

On average, the CERES low-cloud heights range from 0.5 km lower to 0.5 km greater than those from radar and lidar measurements, independent of time of day. There is a tendency to overestimate low-cloud

height over land (Dong et al., 2008). Midlevel cloud heights are typically underestimated by -0.2 to -1.5 km. Optical thick high-cloud heights are generally underestimated by -0.6 to -1.6 km.

During daytime, the cirrus cloud heights tend be too low compared to the lidar measurements (e.g., Mace et al., 2005; Smith et al., 2008), but, at night, the SIST-derived cirrus CZ values are very close to those determined from lidar and radar data (Smith et al., 2008). From Table 1.2.5, it is seen that the average differences between CZ from CERES and the reference instruments for thin cirrus vary from -1.9 and -2.6 km during daytime and between -0.1 and -1.6 km during the night. Based on the CALIPSO comparisons, the larger value for thin cirrus during the day is probably more representative. The differences are expected to be negative because cloud-top height is compared with CZ, which for CERES, is the radiating height. The value of CERES CZ corresponds to a height located ~1.1 optical depths below cloud top for clouds having COD > 3 (e.g., Minnis et al., 2008) and to a smaller optical depth below the physical top for thinner clouds. For the thicker clouds, the actual top-radiating height difference is often between 1 and 2 km (Minnis et al., 2008). It can be as large or greater for thin cirrus clouds depending on the vertical distribution of ice water content, but is probably not greater than 2 km, on average. Thus, the daytime CERES thin cirrus cloud heights are probably biased low. The nocturnal values, though, are closer to the true values. The day-night difference appears to be due to a discrepancy between the IR and VIS optical depths and/or the ice crystal models used in the CERES and other retrieval methods (e.g., Yang et al., 2008).

Retrievals of CODI using the CERES algorithms for thin cirrus clouds tend to be greater those from radar, lidar, and radiometer retrievals (Min et al., 2004; Mace et al., 2005; Chiriaco et al., 2007) and from in situ data (Young et al., 1998) by 13 – 44% for average optical depths less than ~ 1.5. These overestimates of COD contribute to the thin cirrus height bias discussed above. Part of the bias is due to an error in the CERES removal of ozone absorption in the retrieval (Minnis et al., 2011). Correction of the error would reduce the bias some, especially at higher latitudes. Further reduction of the bias would require employment of an ice crystal scattering model having a smaller asymmetry factor than used by CERES.

Retrievals of CREI are 2.8 to 4.0 μm smaller than the radar retrievals for thin cirrus clouds. These underestimates balance the overestimates of CODI for the thin ice clouds resulting in very close agreement in CIWP between CERES and the radar measurements. Few microphysical comparisons exist for thick ice clouds because of the difficulty of measuring the overall content of a thick ice cloud with aircraft. However, the mean CERES AQUA retrievals of CIWP in all conditions appear to agree very well with those from CloudSat, except over the Arctic (Waliser et al., 2009).

Liquid water cloud microphysical properties have only been compared to other measurements for stratus clouds but reveal that stratus CODW from MODIS TERRA and AQUA over the SCF are, respectively, 4% less and 8% greater than those measured at the surface. Similar comparisons using GOES and VIRS data indicate that CODW is underestimated by 4 to 6%. CREW from VIRS and MODIS is typically within 0.5 μm of that retrieved from surface radar-radiometer measurements over the ARM SCF site (Dong et al., 2008; Minnis et al., 2011). A 1.4-μm average underestimate in CREW over the SCF was found using GOES data (Dong et al., 2002). The CERES CLWP retrievals vary from being 8 gm^{-2} less than to 11 gm^{-2} greater than CLWP retrievals using ground based microwave radiometers. Compared to microwave radiometer-based retrievals of CLWP from the AQUA Advanced Microwave Sounding Radiometer-EOS (AMSR-E) over oceans, the CERES CLWP values are 9% too low, on average.

Differences in bulk microphysical properties of ice clouds between the MODIS-ST and MODIS-CE retrieved microphysical properties are primarily due to differences in cloud sampling (MODIS-ST uses a sub-sample by removing cloud edges), retrieval wavelengths (2.1 μm sounds deeper into the cloud than 3.8 μm), and ice crystal scattering models.

Table 1.2.5: Summary of comparisons of retrievals using VISST/SIST with independent measurements

Parameter	Independent measurement, X	VISST – X	σ	Number of samples	Satellite
single-layer cloud heights		*(km)*	*(km)*		
low, day & night	radar, SFC	-0.6	0.6	178	MODIS[*]
low, day	ARSCL, SFC	-0.1	0.7	458	GOES[#]
low, night	ARSCL, SFC	-0.2	1.5	108	GOES[#]
low, day & night	CALIPSO, global	-0.5 to 0.5	NA	> 10^6	MODIS[†]
midlevel, day	ARSCL, SFC	-0.8	0.9	242	GOES[#]
midlevel, night	ARSCL, SFC	-1.1	1.2	207	GOES[#]
midlevel, day & night	CALIPSO, global	-0.2 to -1.5	NA	> 10^6	MODIS[ɛ]
high, day, COD < 3	radar, SFC	-2.6	NA	19	[∞]MODIS[¥]
high, day, COD < 3	radar, SFC	-2.5	1.1	9	MODIS[¥]
high, day, COD < 3	ARSCL, SFC	-1.9	1.7	173	GOES[#]
high, day, COD ≥ 3	ARSCL, SFC	-1.1	1.1	539	GOES[#]
high, night, COD < 3	radar, SFC	-0.4	NA	29	[∞]MODIS[¥]
high, night, COD < 3	ARSCL, SFC	-0.1	1.2	301	GOES[#]
high, night, COD ≥ 3	ARSCL, SFC	-0.6	0.9	584	GOES[#]
high, day & night, COD > 8	CALIPSO, global	-1.6	1.3	15,367	MODIS[†]
high, day & night	CALIPSO, global	-2.0 to –3.0	NA	> 10^6	MODIS[ɛ]
all, day, COD < 5	radar, SFC	-1.4	1.6	140	[∞]VIRS
all, day, COD > 5	radar, SFC	-0.3	1.2	145	[∞]VIRS
all, night, COD < 5	radar, SFC	-0.2	1.3	158	[∞]VIRS
all, night, COD > 5	radar, SFC	-0.2	1.0	147	[∞]VIRS
daytime optical depth		*%*	*%*		
CODW, stratus	radar/radiometer, SFC	-5.8	40	72	GOES[Δ]
CODW, stratus	radar/radiometer, SFC	0.2	25	54	MODIS[*]
CODW, stratus	radar/radiometer, SFC	-4.0	NA	60	VIRS[∞]
CODI,,cirrus	radiometer, SFC	29	58	47	GOES[«], [49]
CODI,,cirrus	radar/radiometer, SFC	13	47	6	GOES[a]
CODI,,cirrus	radar, SFC	15	49	9	MODIS[¥]
CODI,,cirrus	radar, SFC	44	NA	49	VIRS[∞]
daytime particle effective size		*μm*	*μm*		
CREW, stratus	radar/radiometer, SFC	1.4	2.7	72	GOES[Δ]
CREW, stratus	radar/radiometer, SFC	0.1	1.9	54	MODIS,[*]
CREW, stratus	radar/radiometer, SFC	-0.2	NA	49	VIRS[∞]
CREI, cirrus	radar, SFC	-2.8	3.4	9	MODIS[¥]
CREI, cirrus	radar, SFC	-4.0	NA	49	VIRS[∞]
daytime water path		*gm^{-2}*	*%*		
CLWP, stratus	microwave radiometer, SFC	10.7	32	72	GOES[Δ]
CLWP, stratus	microwave radiometer, SFC	11.3	29	54	MODIS[*]
CLWP, stratus	microwave radiometer, SFC	-8 (-6%)	NA	60	VIRS[∞]
CLWP, stratus	microwave radiometer, AMF	7.8	40	40	MODIS[∞]
CLWP, marine stratus	AMSR-E	-12 (-9%)	NA	>10^4	MODIS[∞]
CIWP, cirrus	radar/radiometer, SFC	1.7	22	6	GOES[a]
CIWP, cirrus	radar, SFC	0.2	50	9	MODIS[¥]
CIWP, cirrus	radar, SFC	4 (21%)	NA	49	VIRS[∞]

NA – not available

[*]Dong et al. (2008), [#]Smith et al. (2008), [¥]Mace et al. (2005), [†]Minnis et al. (2008), [ɛ]Sun-Mack et al. (2007), [Δ]Dong et al. (2002), [a]Mace et al. (1998), [«]Min et al. (2004), [∞]Minnis et al. (2011)

The independent measurements of the various cloud properties have their own biases and uncertainties that must be considered when comparing with any other data set such the CERES cloud parameter values. Thus, until all of those uncertainties are also known, the absolute errors in the CERES cloud properties cannot be fully assessed from the comparisons. However, it is clear that, except for the thin cirrus cloud heights and the corresponding optical depths that the biases are likely small, on average.

1.2.2 AIRS-LMD

C.J. Stubenrauch, A. Guignard

1.2.2.1 Measurements

Launched in May 2002 onboard the NASA EOS platform AQUA, the AIRS instrument (Aumann et al., 2003; Chahine et al., 2006) provides very high spectral resolution measurements of Earth emitted radiation in three spectral bands (3.74-4.61 μm, 6.20-8.22 μm and 8.80-15.40 μm) using 2378 channels with a spectral resolution given by $\Delta\lambda/\lambda = 0.0008$. The polar orbiting AQUA satellite provides observations at 1h30 and 13h30 local time (LT). The spatial resolution of these measurements is 13.5 km at nadir. Nine AIRS measurements (3 x 3) correspond to one footprint of the Advanced Microwave Sounder Unit (AMSU). Atmospheric profiles are retrieved (Susskind et al., 2003, 2006) from cloud-cleared AIRS radiances (Chahine et al., 2006) at the spatial resolution of an AMSU footprint by comparing AIRS and AMSU radiances to remove cloud-contaminated scenes. NASA AIRS L2 standard products include temperature at 28 pressure levels from 0.1 hPa to the surface and water vapour mixing ratios in 14 pressure layers from 50 hPa to the surface. Validations with radiosonde data from the NOAA–NESDIS operational meteorological database archive (Divakarla et al., 2006) and with Atmospheric Radiation Measurement (ARM) data (Tobin et al., 2006) have shown that the accuracy is close to 1 K in 1 km layers for temperature and better than 15% in 2 km layers for water vapour. For the cloud property retrieval we have collocated the NASA AIRS L2 standard products (version 5) with a subset of AIRS L1B radiance measurements, which have been downloaded from the NASA data pool (***http://mirador.gsfc.nasa.gov***); the AIRS L2 products are used to select the most similar temperature profile and associated spectral transmissivities from the TIGR database. CA for this product is determined post-facto after applying the spectral analysis to all scenes (see Section 1.2.2.3).

1.2.2.2 Retrieval

1.2.2.2.1 CP, CEM, CT, CZ

The methodology of cloud property retrieval is similar to the method developed for TOVS Path-B. It is based on a weighted χ^2 method using channels around the 15 μm CO_2 absorption band (Stubenrauch et al. 1999b), providing CP and CEM of a single cloud layer (of the uppermost cloud layer in the case of multi-layer clouds). χ^2 is computed by summation over seven wavelengths λ_i across the CO_2 absorption band around 15 μm and one at 11 μm (IR window), as in Eq. (1.2.1).

$$\chi^2(\boldsymbol{p_k}) = \sum_{i=1}^{8} \left[(\boldsymbol{R_{cld}}(\boldsymbol{p_k}, \lambda_i) - \boldsymbol{R_{clr}}(\lambda_i)) \cdot \boldsymbol{CEM}(\boldsymbol{p_k}) - (\boldsymbol{R_m}(\lambda_i) - \boldsymbol{R_{clr}}(\lambda_i)) \right]^2 * \boldsymbol{W}^2(\boldsymbol{p_k}, \lambda_i) \quad (1.2.1)$$

The measured radiance R_m is obtained from the AIRS L1B data. From the eight AIRS channels five closely correspond to those used in the TOVS Path-B cloud retrieval (section 1.1.3.2), at wavelengths of 14.190, 14.002, 13.928, 13.279 with 10.901 μm, and three are additional channels at 14.298, 14.094 and 13.239 μm (AIRS channels 174, 193, 210, 226, 239, 355, 362 and 787). The weighting functions of these channels are shown in Figure 1.2.3 as the derivatives of the transmission function with respect to pressure. For this illustration, they have been simulated by the 4A radiative transfer model (Scott and Chédin, 1981; operational version available at ***http://www.noveltis.net/4AOP***) for an average tropical atmosphere, taken from the TIGR database (Chédin et al., 1985; Chevallier et al., 1998; Chédin et al., 2003).
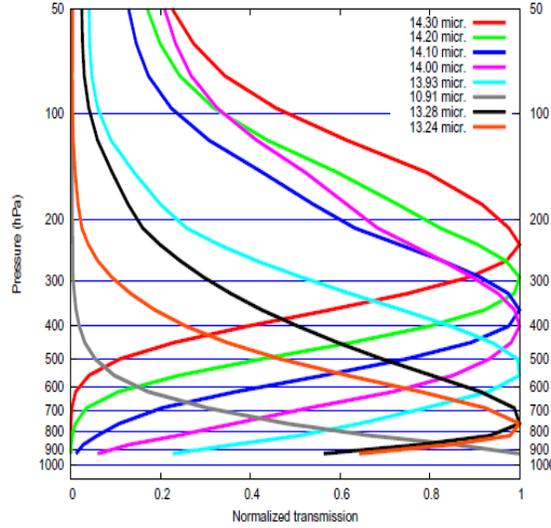
Figure 1.2.3: Weighting functions of eight AIRS channels, from near the centre towards the wing of the CO_2 absorption band around 15 μm, used in the LMD cloud property retrieval.

R_{clr} is the radiance which would be measured by AIRS in the case of clear sky, and R_{cld} is the radiance emitted by a homogenous opaque single cloud layer, pre-calculated for 39 assumed cloud pressure levels p_k above surface (984 hPa to 106 hPa). For this computation we need the NASA AIRS L2 temperature profiles as well as spectral atmospheric transmissivity profiles for an atmospheric situation similar to the retrieved atmospheric temperature and water vapour profiles. These atmospheric spectral transmissivity profiles have been simulated by the 4A radiative transfer model, separately for each satellite viewing zenith angle (up to 50°) and for about 2000 representative clear sky atmospheric temperature and humidity profiles of the TIGR database. The proximity recognition between the NASA AIRS L2 atmospheric profiles and the TIGR atmospheric profiles is described in detail in (Stubenrauch et al., 2008). If no simultaneous NASA AIRS L2 atmospheric profile of good quality is available (which may occur if the situation is too cloudy), a running average of atmospheric profiles with good quality (Tobin et al., 2006) over one week, at a spatial resolution of 1° latitude x 1° longitude, is used. The third choice is a monthly mean of atmospheric profiles with good quality, at 1° latitude x 1° longitude. For the computation of R_{clr} we also need spectral surface emissivities. These are provided for the latitude band 30°N – 30°S as climatological monthly averages from three years of AIRS data (Péquignot et al. 2008), at a spatial resolution of 1° latitude x 1° longitude. For the rest of the globe we use climatological monthly averages from six years of MODIS data (Seemann et al., 2008), at a spatial resolution of 0.5° latitude x 0.5° longitude, which have then been spectrally interpolated to the AIRS channels.

By introducing empirical weights $W(p_k, l_i)$, the method takes into account 1) the vertical contribution functions of the different channels, 2) the growing uncertainty in the computation of CEM with increasing p_k and 3) uncertainties in atmospheric profiles. These weights are determined for each of the five TIGR airmass classes (tropical, midlatitude summer and winter, polar summer and winter) as in Eqs. 8 and 10 of (Stubenrauch et al., 1999b). Minimizing χ^2 in Eq. 1.2.1 is equivalent to $d\chi^2/dCEM = 0$, from which one can extract CEM and CP as:

$$CEM(CP) = \frac{\sum_{i=1}^{8}[R_m(\lambda_i) - R_{clr}(\lambda_i)] \cdot [R_{cld}(CP,\lambda_i) - R_{clr}(\lambda_i)] \cdot W^2(CP,\lambda_i)}{\sum_{i=1}^{8}[R_{cld}(CP,\lambda_i) - R_{clr}(\lambda_i)]^2 \cdot W^2(CP,\lambda_i)} \qquad (1.2.2)$$

It is important to allow values larger than 1, because at larger pressure levels R_{clr} and R_{cld} become very similar and their uncertainties can lead to large values (Stubenrauch et al., 1999b). When the c^2 method leads to an un-acceptable value of CEM (larger than 1.5), the scene is set to clear sky.

CT is determined from CP, using the NASA AIRS L2 temperature profile. The transformation of CP into CZ makes use of the virtual temperature profile determined from the NASA AIRS L2 temperature and water vapour profiles. In case the retrieval of the atmospheric profiles has failed (in general for situations with opaque clouds), a running mean of atmospheric profiles of good quality is used (over one week up to one month). CA is the fraction of cloudy AIRS footprints per 1° longitude x 1° latitude grid. CAE is the product CEM, averaged over cloudy AIRS footprints per 1° longitude x 1° latitude grid, and CA.

1.2.2.2.2 Bulk Microphysical Properties of Semi-Transparent Cirrus

The retrieval is applied to all AIRS footprints regardless of whether they contain cloud or not later. A test based on the spectral coherence of retrieved cloud emissivities (see next section) decides whether the AIRS footprint is cloudy (overcast or mostly cloudy) or clear (or not cloudy enough to determine reliably the cloud properties). Thresholds have been established by comparing clear and cloudy scenes within the AIRS footprints, distinguished by coincident CALIOP measurements (Stubenrauch et al., 2010).

Cloud bulk microphysical properties, effective ice crystal radius (CREIH) and cloud ice water path (CIWPH), are determined from six spectral emissivities (between 8 and 12 μm) of high-level semi-transparent ice clouds (CP < 440 hPa, CT < 260 K and 0.2 < CEM < 0.85). For the retrieval look up tables have been calculated, using the radiative transfer model 4A (Scott and Chédin, 1981), coupled (Pierangelo et al., 2005) with the multiple scattering code DISORT (Stamnes et al. 1988). The cirrus emissivity depends on CIWP, CREI and on the dominant shape of the ice crystals. Single scattering properties calculated by Baran (2003), separately for ice crystals with the shape of pristine columns and of aggregated columns, have been integrated over a bimodal size distribution (Mitchell et al., 1996) and then be included into the code 4A-DISORT, as function of CREI. The spectral emissivity ε is determined from the radiances as:

$$\varepsilon(\lambda, \theta_v, De, IWP) = \frac{R^m(\lambda, \theta_v, De, IWP) - R^{clr}(\lambda, \theta_v)}{R^{cld}(p_{cld}, \lambda, \theta_v) - R^{clr}(\lambda, \theta_v)} \quad (1.2.3)$$

For each viewing zenith angle θ_v, each wavelength λ, spectral emissivities $\varepsilon(\lambda, \theta_v, \boldsymbol{De}, \boldsymbol{IWP})$ have been simulated by varying CREI between 3.5 and 45 μm and CIWP between 1 and 120 gm^{-2}, respectively. CREI and CIWP are retrieved as the couple for which the calculations fit the data best. Retrievals are limited to a viewing zenith angle of 40°. The retrieval method, sensitivity studies and results are described in (Guignard et al., 2012).

1.2.2.3 A Posteriori Cloud Detection

To distinguish cloudy from clear sky scenes in a way which does not depend on regionally and seasonally varying cloud detection thresholds, we have developed a method which is applied *after* the retrieval of CEM, CP and CT. It is based on the spectral coherence of retrieved cloud emissivities. For each AIRS footprint spectral cloud emissivities e are determined at six wavelengths λ_i = 11.85, 10.90, 10.69, 10.40, 10.16, 9.12 μm as:

$$\varepsilon(\lambda_i) = \frac{R_m(\lambda_i) - R_{clr}(\lambda_i)}{R_{cld}(CP, \lambda_i) - R_{clr}(\lambda_i)} \quad (1.2.4)$$

where R_{cld} is now determined for CP which has been retrieved by the χ^2 method (see above). When CP is well determined, the cloud emissivities should differ only slightly between 9 and 12 μm. The variability should be larger, when the footprint is partly cloudy or clear and hence the cloud pressure can not be well determined. In this case, the footprint is declared to be clear. In the following, we summarize the tests for the AIRS-LMD cloud detection. The AIRS footprint is cloudy if the following conditions are fulfilled:

CEM > 0.05

no snow or sea ice:	snow or sea ice:
$\sigma(\varepsilon_i)$ / CEM < 0.2 if p_{cld} < 440 hPa or p_{cld} > 680 hPa	$\sigma(\varepsilon_i)$ / CEM < 0.3
$\sigma(\varepsilon_i)$ / CEM < 0.1 if 440 hPa < p_{cld} < 680 hPa	$TB(11\mu m) - TB(7\mu m)$ > -5 K

and over land or snow:

$CT - T_{surf}(air) < -3 \text{ K}$

1.2.2.4 Standard Products and Characteristics of GEWEX-Archived Version

We summarize the method, necessary tools and ancillary data, as well as data availability and specific processing for the statistics of the GEWEX cloud assessment database.

Table 1.2.6: Characteristics of AIRS-LMD Data Set for the GEWEX Cloud Assessment Database

Method and Ancillary Data:

- **Cloud detection:** a posteriori, based on spectral coherence of cloud emissivities (9-12μm), snow/ice flag from AMSU (NASA L2)
- **CP, CEM:** from CO2 band + IRW (weighted χ^2): 8 channels
    - Clear sky estimate: 4A radiative transfer, TIGR spectral transmissivities,
    - Atmospheric profiles: retrieved (NASA): simultaneous or averages
    - No assumptions on microphysics
- **CT:** from retrieved atmospheric profiles (NASA)
- **CREIH, IWPH:** from cirrus emissivities at 6 wavelength between 8.5μm, 12μm (LUT)
    - Surface emissivity: 30N-30S AIRS (LMD retrieval), > 30°: MODIS
    - Radiative transfer model: 4A-DISORT
    - Single Scattering Properties: pristine and aggregated columns (ice), bimodal size distribution
    - CT < 260 K, 0.2 < CEM < 0.85, θv < 40°

Characteristics:

- CT, CP, CEM same retrieval method during day and night, spatial resolution 14 km
- COD at IR wavelengths is determined from CEM as COD = -2 x ln(1-CEM)
- CREIH, CIWPH during day and night, but only for (CP < 440 hPa, 0.2 < CEM < 0.85, CT > 260 K) and for zenith viewing angles < 40°
- **Strengths:** good sensitivity to thin cirrus, reliable cirrus properties also in case of multi-layer clouds, day and night, no bias in low cloud properties
- **Limitations:** larger noise in low cloud properties, over land no clouds with CT-Tsurf > -3 K; polar clouds

Specifics for GEWEX Statistics:

- CT is used to distinguish between ice clouds (CT <230 K) and water clouds (CT > 260 K); mixed phase clouds (230 K < CT < 260 K) are not considered separately.
- Data are separately stored for AM and PM observations. In the case of several AM or PM observations within the same 1° latitude x 1° longitude only the observation with the smallest viewing zenith angle is kept.
- AQUA data from 2003 to 2009 were processed for physical cloud properties (local observation times 1h30 AM / PM); from 2004 to 2009 for bulk microphysical properties of semi-transparent high ice clouds.

Data Availability:
At present, L3 data (in netCDF, like for GEWEX Cloud Assessment) gridded at 1° latitude x 1° longitude are available at ***http://ara.lmd.polytechnique.fr***, from NOAA10 and NOAA12 observations (local observation time: 7h30 AM and 7h30 PM). L2 data (in netCDF) are distributed by the ICARE Thematic Center created by CNES (***http://www-icare.univ-lille1.fr/***).

1.2.2.5 Uncertainty Estimates

Because we use a χ^2 method for the retrieval of CEM and CP, an estimate of the retrieval uncertainy can be given by the difference between the solution, corresponding to the minimum χ^2, and the next best solution. Average CP uncertainty lies around 40 hPa; with CT uncertainty of high clouds between 3 and 5 K and of low clouds between 2 and 6 K, the largest values in the tropics. CEM is better determined for high clouds, with an average uncertainty of 0.05, whereas for low clouds the uncertainty lies between 0.10 (in the Southern hemisphere midlatitudes) and 0.25 (in the tropics). The uncertainty of cloud amount can be roughly estimated by comparing cloud amount including and excluding clouds with CEM < 0.05. It

varies between 0.05 and 0.15 (over desert and Antarctica). Figure 1.2.4 presents zonal means of these uncertainty estimates, for AIRS-LMD as well as for TOVS Path-B (see section 2.3.2). Uncertainty estimates for CA and CEML are smaller for TOVS Path-B, probably because of the coincident use of MSU in cloud detection, whereas uncertainty estimates for CP and CEMH are slightly smaller for AIRS-LMD, probably because of the better spectral and spatial resolution.

Cloud height and cloud detection have been evaluated using two years of collocated CALIPSO data (Stubenrauch et al., 2008, 2010).

The 'a posteriori' cloud detection leads to an agreement with the CALIPSO cloud detection (at a horizontal averaging of 5 km or less) of about 82.7% / 90.3% / 93.8% over ocean and 76.2% / 73.4% / 84.2% over land, respectively in tropical latitudes, midlatitudes and polar latitudes and of about 83.0% / 78.8% over sea ice and 71.8% / 69.4% over snow, respectively in midlatitudes and polar latitudes for observations at 1:30 LT and of about 69.2% / 87.1% / 93.2% over ocean and 84.3% / 82.4% / 83.3% over land, respectively in tropical latitudes, midlatitudes and polar latitudes and of about 84.9% / 84.7% over sea ice and 77.4% / 66.3% over snow, respectively in midlatitudes and polar latitudes for observations at 13:30 LT. In general this agreement is quite good, especially if we consider that CALIPSO only samples the AIRS footprint. Agreement is slightly better over ocean than over land.
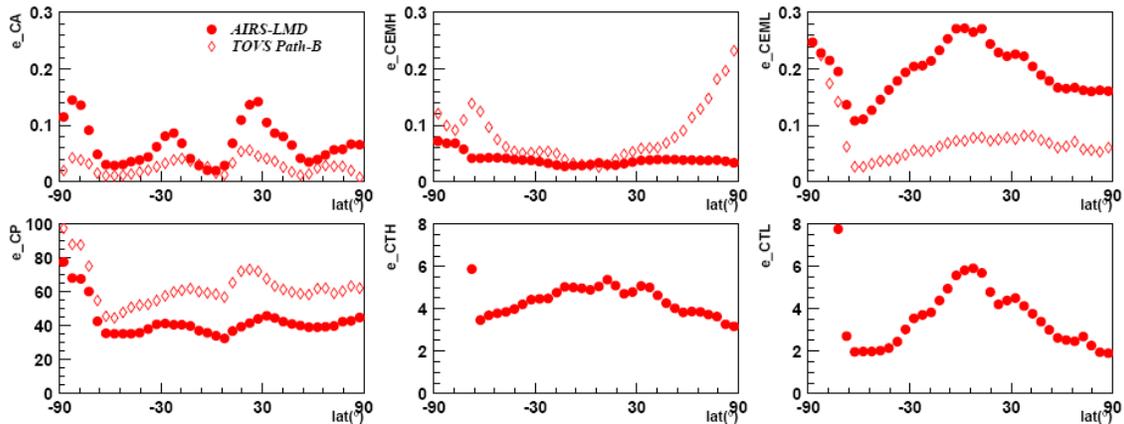
Figure 1.2.4: Zonal mean uncertainty estimates (from first and second c2 solution) of CA, CEMH, CEML, CP (in hPa), CTH (in K) and CTL (in K) for TOVS Path-B (except for CT) and AIRS-LMD.
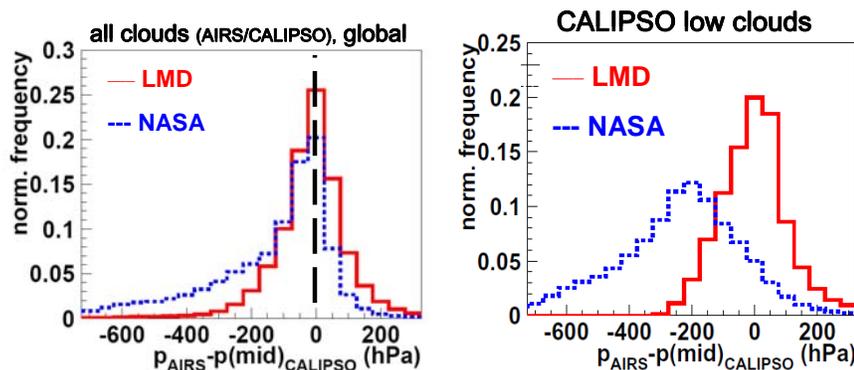
Figure 1.2.5. Normalized frequency distributions of the difference between AIRS cloud pressure and pressure of the 'apparent middle' of the uppermost cloud layer detected by CALIPSO at horizontal averaging over 5 km or less. Observations at 1:30 LT. AIRS cloud retrievals from LMD are compared to those of NASA L2 products (Version 5), left for all clouds and right for CALIPSO low clouds.

Cloud height from the AIRS LMD cloud retrieval has been evaluated using the height of the maximum backscatter signal and of the 'apparent middle' of the highest cloud layer detected by CALIPSO, at

horizontal averaging over 5 km or less, corresponding to a sensitivity in terms of minimum detectable particle backscatter coefficient of about 0.0008 $km^{-1}sr^{-1}$ at night and about 0.0015 $km^{-1}sr^{-1}$ during day, for a cirrus with an altitude of about 12 km (Winker et al., 2009). This corresponds to clouds with optical depth larger than about 0.05 to 0.1 (Winker et al., 2008). All difference distributions (for high and low clouds as well as in the tropics, midlatitudes and polar latitudes, Stubenrauch et al. 2010) are Gaussian with a strong peak around 0, whereas the AIRS L2 cloud height provided by NASA exhibits a strong underestimation of cloud pressure for CALIPSO low clouds, in agreement with a study of Kahn et al. (2008). Figure 1.2.5 presents these distributions over the whole globe, separately for all clouds and only for low-level clouds. The retrieved cloud height of about 66% (80%) of AIRS high-level (low-level) clouds lies within 1.5 km of the 'apparent middle' of the CALIPSO cloud layers. Comparing cloud pressures shows an agreement in cloud height of 72% (59%) for high-level (low-level) clouds within 75 hPa. For high-level clouds the agreement is slightly better when comparing to the 'apparent middle' of the cloud instead of to the height of the maximum backscatter signal. This is because the maximum backscatter signal can be as much as 1 km above the 'apparent middle' of the cloud, especially in the case of optically thick clouds. High-level clouds are also geometrically thicker and more heterogeneous than low-level clouds. The cloud height is determined with less uncertainty in the case of thicker clouds and of single layer clouds, however, the height differences between AIRS and CALIPSO always peak around 0, indicating no bias, with the exception of some AIRS thin midlevel and low clouds which are probably falsely identified as thicker low clouds. This could be caused by the broken edges of thin high-level clouds overlying low-level clouds. Table 1.2.7 summarizes average uncertainty estimates from TOVS Path-B and AIRS-LMD.

Table 1.2.7: Average uncertainty estimates for TOVS Path-B and AIRS-LMD cloud properties

ECV's:	CA	CT	CP	CEM	CREI
	0.05-0.15	2-4 K	40-50 hPa	0.05-0.15	5μm

1.3 Complementary Cloud Products

1.3.1 CALIPSO

The CALIPSO satellite carries three instruments: the Cloud-Aerosol LIdar with Orthogonal Polarization (CALIOP), a three-channel IR radiometer and a single channel visible imager. CALIOP is a nadir-viewing two-wavelength, polarization-sensitive lidar (Winker et al., 2007; Hunt et al., 2009). The two passive instruments image a 60 km swath centered on the lidar footprint. CALIPSO flies as part of the A-train constellation, acquiring observations since June 2006. The A-train satellites fly in a 705-km, sun-synchronous, 1:30 PM orbit with a 16-day repeat cycle. The nadir-viewing CALIOP provides global sampling with very sparse coverage between 82°N and 82°S. The CALIPSO satellite is controlled to fly within 2 minutes of the AQUA satellite to provide near-simultaneous measurements with the MODIS and AIRS instruments on AQUA. The CALIPSO orbit is slightly inclined relative to AQUA. To keep the CALIOP footprint out of MODIS sunglint, CALIPSO maintains an ascending node crossing bias relative to AQUA of 215 km to the east.

The CALIOP laser transmitter produces simultaneous, co-aligned, pulses at 1064 nm and 532 nm. The outgoing laser beam is linearly polarized. Two separate receiver channels measure the components of the 532 nm backscatter return polarized parallel and perpendicular to the outgoing beam. Backscatter signals from the 20 nsec laser pulses are sampled at a rate of 10 MHz. Samples are averaged on-board the satellite to provide a range resolution of 30 meters below an altitude of 8 km and 60 meters between 8 and 20 km. The diameter of the laser footprint is 70 meters at the Earth's surface with a spacing of 335 meters between footprint centers. The instrument operates continuously, providing observations during both day and night portions of the orbit.

Nighttime profiles from the 532 nm parallel channel are calibrated by the standard lidar technique of normalizing return signals to a molecular model (Russell et al., 1979; Powell et al., 2009). Gridded GMAO GEOS-5 meteorological data are interpolated to CALIOP measurement locations and the

measured 532 nm parallel backscatter signal is calibrated by normalizing the observed signal to the predicted molecular signal in the region between 30 km and 34 km. The daytime solar background prevents this technique from being applied to sunlit portions side of the orbit. Therefore, daytime calibrations are interpolated from adjacent nighttime calibrations. Calibration uncertainties for the 532 nm channel are on the order of 5% (Rogers et al., 2011). Cloud temperatures, T_{cld}, are obtained by relating measured height to temperature from the GEOS-5 product. In Version 2 data, only mid-cloud temperature is reported.

Two CALIPSO cloud products have been produced for the GEWEX cloud assessment. Both rely on the same CALIOP Version 2 Level 1 profile data. The CALIPSO-ST product is produced from cloud occurrence data reported in the standard CALIPSO Version 2 Level 2 lidar cloud layer product, and thus relies on the standard CALIOP cloud detection algorithm. The CALIPSO-GOCCP product is produced directly from CALIPSO Version 2 Level 1 data by applying an alternate, simplified cloud detection algorithm. The GOCCP algorithm has been developed to produce an observation-based product consistent with that produced by the CALIPSO cloud simulator developed for the CFMIP project (Chepfer et al., 2008; Bodas-Salcedo et al., 2011). A comparison of the CALIPSO-ST and CALIPSO-GOCCP products can be found in Chepfer et al. (2012).

1.3.1.1 CALIPSO Science Team
D. Winker

1.3.1.1.1 Cloud Detection
CALIOP directly observes cloud height from laser pulse time-of-flight measurements. Because the cloud altitudes can be referenced to sea level via the pulse time of flight, the long term stability of the altitude measurement is very high. Multiple aerosol and cloud layers can be detected in a column, to the point where the accumulated optical depth is larger than 3 to 4.

Cloud and aerosol layers are detected by comparing the measured 532 nm signal return with the return expected from a molecular atmosphere. An adaptive threshold test is used (Vaughan et al., 2009) and the height of the physical top height, rather than the effective radiative height, is reported. Clouds with visible extinction as small as about 0.01 km^{-1} can be detected, resulting in much larger high cloud cover than other sensors due to the prevalence of optically thin ice clouds, particularly in the tropical upper troposphere. Aerosols and clouds are then discriminated by comparing the magnitude of the 532 nm return signals and the ratio of the 532 nm and 1064 nm backscatter return strength (Liu et al., 2004; Liu et al., 2009). Layers are assigned a cloud-aerosol discrimination score (CAD_Score), indicating the degree of confidence in classifying a layer as cloud or aerosol. Score values range from -100 for aerosols, to +100 for clouds, with larger absolute values indicating higher confidence. Values A few specific values. Values larger than 100 are used to indicate special conditions (see Data Quality Summaries posted on the CALIPSO website.) Because cloud signals are much larger than molecular signals, calibration errors have minor impact on the accuracy of cloud detection. The same detection algorithm is used during the daytime and nighttime portions of the orbit, except that different detection thresholds are used. This results in artificial day-night differences in the fraction of optically thin cloud.

2.3.1.1.2 Retrieval
Cloud ice-water phase. In CALIOP Version 2 data, clouds are classified as liquid or ice. Analysis of the parallel and perpendicular polarization of 532 nm backscatter signals provides vertically-resolved identification of cloud water phase according to the algorithm of Hu et al. (2007). In the single-scattering approximation, the backscatter return from liquid spherical cloud droplets retains the incident polarization, while returns from ice crystals are depolarized. Multiple scattering in dense liquid clouds produces depolarization of the lidar returns, but the relation between backscatter magnitude and depolarization is different than for ice clouds.

1.3.1.1.3 Standard Products and Characteristics of GEWEX-Archived Version

Several aerosol and cloud data products are available from the NASA LaRC Atmospheric Sciences Data Center (*http://eosweb.larc.nasa.gov*). Level 2 cloud data includes: cloud base and top heights; cloud water phase; and extinction profiles and layer optical depth for optically thin ice clouds (COD ≤ 3). IWC and IWP are provided for the first time in Version 3 data products. Because signal averaging is required to detect and retrieve weak clouds, Level 2 cloud parameters are retrieved and reported at horizontal resolutions ranging from 1/3 km (single shots) to 80 km. The 1/3-km cloud layer product is based on Level 1 single-shot data, which is only available from the surface to 8 km. The 5-km cloud layer product contains clouds from the surface to 20 km, detected with horizontal averaging of 5, 20, or 80 km. Daytime and nighttime data are contained in separate files.

The CALIOP cloud statistics and the descriptions of the cloud detection and retrieval algorithms below are based on Version 2 products. Version 2 algorithms are described in Winker et al. (2009) and references cited therein. The global gridded cloud statistics produced for the GEWEX cloud assessment will be made available at *http://eosweb.larc.nasa.gov*. Version 3 products are released since 2010, making use of improved cloud-aerosol discrimination and cloud ice-water phase algorithms.

Construction of Level 3 GEWEX statistics. Although CALIOP is able to detect multiple cloud layers in a column, to be more compatible with passive cloud retrieval statistics for the GEWEX cloud assessment were computed using only the highest cloud in each column. CALIOP is able to detect tenuous clouds that are missed by most passive sensors resulting in larger cloud fractions, particularly for high clouds.

To properly represent both broken boundary layer cloud and tenuous ice clouds, cloud statistics are computed from a data set constructed by merging clouds in the 1/3-km cloud layer product with ice clouds in the 5-km cloud layer product. A cloud layer detected after horizontal averaging over 5 km or more is considered to be overcast over that interval. Because 1/3-km data detection of water cloud is already very sensitive, only ice clouds are used from the 5-km product. Several screening steps are applied:

1) Cloud-Aerosol Discrimination: The CAD_Score is used to screen out low confidence cloud layers. Only layers with 70 < CAD_Score < 103 are used.
2) Optically thin ice clouds occurring above the Greenland and Antarctic plateaus are often misclassified as aerosol. Because aerosol almost never occurs over these plateaus at concentrations large enough for CALIOP to detect, any aerosol layers above the plateaus are assumed to be misclassified and have been reclassified as cloud. This increases the cloud fraction over the Antarctic plateau by about 5%.
3) Polar stratospheric clouds are screened out. The reported statistics are based only on tropospheric clouds.

1.3.1.1.4 Uncertainty Estimates

Detection thresholds applied to single-shot (1/3 km) profiles provide detection of optically thin water clouds with mid-visible extinction of about 0.2 km^{-1} or larger. Since these optically thin water clouds are typically a few hundred meters thick, the detection limit corresponds to an optical depth on the order of 0.04. Figure X shows detection thresholds, in terms of extinction, used to detect ice clouds in profiles averaged to 5 km and to 80 km. Thresholds are adjusted according to background lighting levels. "Low" refers to low background lighting and indicates a threshold that would be used for optically thin cloud over ocean. "High" refers to high background illumination and represents thresholds used for optically thick, bright clouds or optically thin clouds over deserts or snow. Because different thresholds are used for day and night, cloud occurrence exhibits a diurnal bias due reduced sensitivity during daytime to optically thin clouds having optical depths on the order of 0.01 or less. A number of studies evaluating CALIOP cloud detection are consistent with these detection limits (McGill et al., 2007; Davis et al., 2010; Yorks et al., 2011; Thorsen et al., 2011).
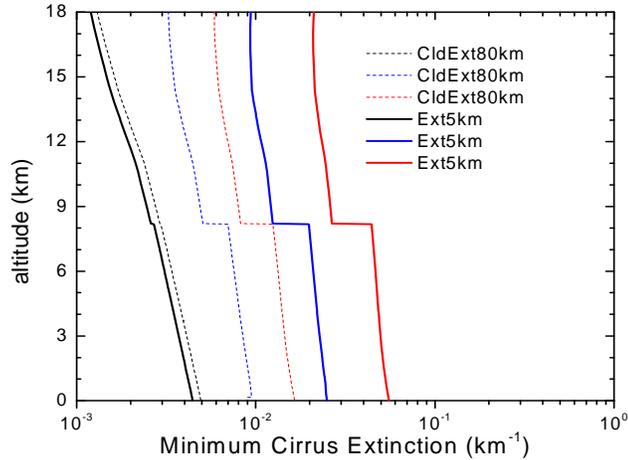
Figure 1.3.1. CALIOP cirrus detection limits in terms of mid-visible extinction coefficient.

One challenge in developing a climatology from satellite lidar is the sparse sampling provided by a nadir-viewing zero-swath instrument. Observations must be averaged on sufficiently large space and time scales to be statistically meaningful and representative. Monthly CALIOP cloud statistics are being made available on a 1° equal-angle grid. Sampling statistics at this resolution are very poor, as indicated by the left panel of Figure 1.3.2. At low latitudes, 1° latitude x 1° longitude grid cells are sampled at most twice during a month and some 1° x 1° grid cells are never sampled. Cloud statistics are only meaningful when accumulated to larger spatial-temporal scales, such as monthly zonal or seasonal 5° x 5°.
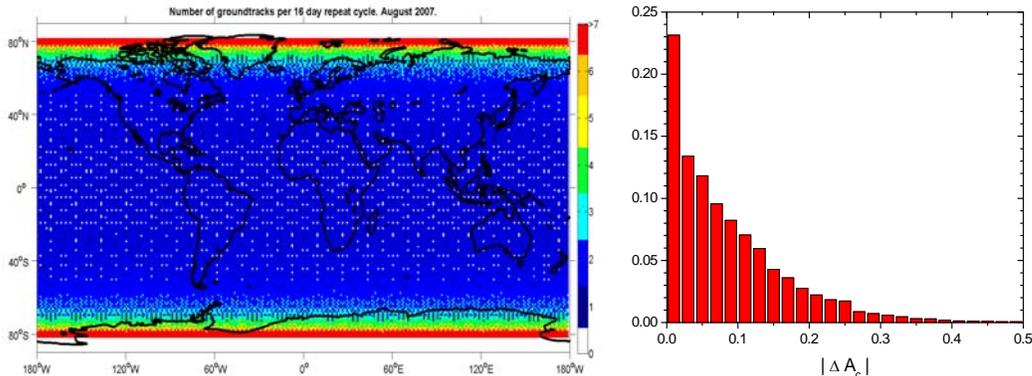
Figure 1.3.2: Geographical map showing the number of 1° x 1° grid cells sampled by CALIPSO during one 16-day orbit cycle (left) and distribution of absolute differences between odd-day and even-day grid-cell cloud fraction for 1° x 1° grid cells (right), computed for July-August 2007.

To estimate uncertainties in cloud statistics reported on the 1° x 1° spatial grid, two 1° x 1° gridded averages of mean total cloud cover were computed by averaging only even days and only odd days over a 60 day period. Due to the interleaved sampling, the differences in the two 30-day averages should be due primarily to sampling noise. The right panel of Figure 1.3.2 shows the frequency distribution of the cloud cover differences between the 59,040 even and odd 1° x 1° grid-cell averages.

Due to a coding error in the CALIOP Version 2 algorithms, clouds with tops below 4 km altitude detected in single shot profiles were not properly cleared from 5-km averages causing cloud fraction to be exaggerated in regions dominated by broken low altitude clouds. To mitigate this error, and because even optically thin water clouds can be detected in 1/3 km profiles, CALIPSO-ST is constructed using water clouds only from the 1/3 km product, while ice clouds from both the 1/3-km and 5-km cloud layer products are included. This reduced the impact of the coding error, but poor performance of the Version 2 ice-water phase classification algorithm caused some low water clouds in the 5-km product to be

erroneously classified as ice and these clouds were then merged into CALIPSO-ST. (The cloud-clearing error was corrected in CALIOP Version 3 data. Version 3 also uses a new ice-water classification algorithm with improved performance.)

The net effect of these various errors on cloud cover has been evaluated by comparing one month of the CALIPSO-ST product used in the GEWEX comparison study with results from the CALIPSO-ST algorithm applied to CALIOP Version 3 data. The comparison showed no significant differences in cloud fraction for high and middle clouds, but use of Version 3 data gave a global-mean low-cloud fraction about 5% less than Version 2. Figure 1.3.3 shows the differences in low cloud fraction between CALIPSO-ST computed with CALIOP Version 2 data and with Version 3 data. Most of the differences occur at low latitudes. Over tropical and subtropical oceans, Version 2 low cloud amount is greater than Version 3 by 20% - 30% in regions dominated by small-scale clouds.
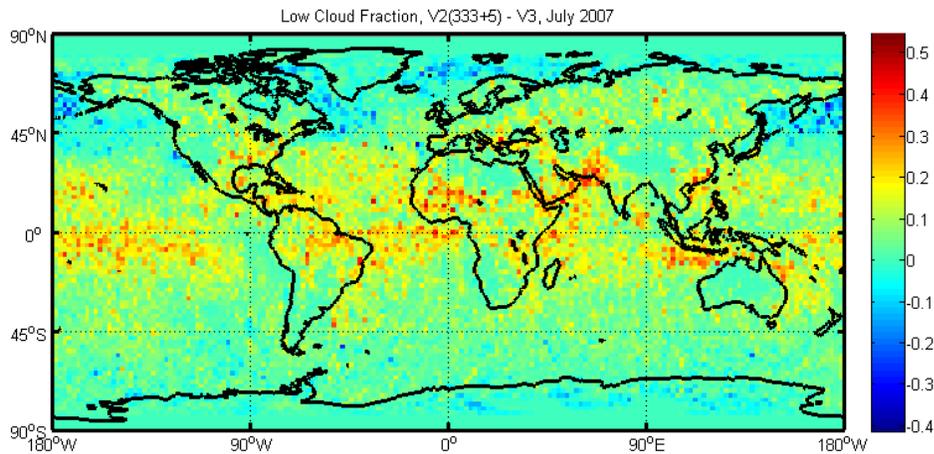
Figure 1.3.3. Differences in low cloud fraction from CALIPSO-ST computed using CALIOP Version 2 and Version 3 data (Version 2 minus Version 3) for July 2007.

1.3.1.2 CALIPSO GOCCP
H. Chepfer, G. Cesana

The GCM-Oriented CALIPSO Cloud Product (CALIPSO-GOCCP, Chepfer et al., 2010) is designed to evaluate the cloudiness simulated by General Circulation Models (GCMs). For this purpose, CALIOP L1 data (collection V2. 01) are processed following the same steps as in a lidar simulator used to diagnose the model cloud cover that CALIPSO would observe from space if the satellite was flying above an atmosphere similar to that predicted by the GCM. The cloud properties are inferred from CALIPSO observations exactly in the same way as in the simulator (similar spatial resolution, same criteria used for cloud detection, same statistical cloud diagnostics). This ensures that discrepancies between model and observations reveal biases in the model's cloudiness rather than differences in the definition of clouds or of diagnostics (Chepfer et al., 2008). CALIPSO-GOCCP is used for the Cloud Feedback Model Intercomparison Program (CFMIP-2 experiment, ***www.cfmip.net/***).

1.3.1.2.1 Measurements

In CFMIP-2, the CALIPSO simulator results are computed on a vertical grid of 40 equidistant levels (height interval, $\Delta z = 480$ m) distributed from the sea level to 19.2 km. We used the Attenuated Backscattered profile at 532nm (ATB, 583 vertical levels, collection V2.01) and the Molecular Density (MD) profile (33 vertical levels) that are part of the CALIOP lidar Level 1 data set. Each profile is independently averaged or interpolated onto the 40-level vertical grid, leading to the ATB_{vert} and MD_{vert} profiles. This averaging significantly increases the ATB signal-to-noise ratio. To convert the MD profile into molecular ATB, ATB_{vert} and MD_{vert} profiles are analyzed and averaged in cloud-free portions of the

stratosphere: 22 < z < 25 km for night time data (20 < z < 25 km for day time), and 28.5 < z < 35km in the Southern Hemisphere (60°s to 90°S) during winter (June to October) to avoid Polar Stratospheric Clouds. At these altitudes z, ATB_{vert} and MD_{vert} profiles are each averaged horizontally over +/-33 profiles (+/-10 km) on both sides of a given profile. The ratio between these two values (R = <ATB_{vert}> / <MD_{vert}>) in the cloud-free stratosphere is then used to scale the MD_{vert} profile into an ATtenuated Backscatter Molecular signal profile ($ATB_{vert,mol}$). This latter represents the ATB profile that would be measured in the absence of clouds and aerosols in the atmosphere. The lidar scattering ratio (SR) vertical profile is then computed by dividing the ATB_{vert} profile by the $ATB_{vert,mol}$ profile.

The horizontal resolution of the SR profile is 335 m and the vertical resolution (40 levels -480m) is close to that of GCMs within the CFMIP-2 experiment.

Despite the vertical averaging, the signal-to-noise ratio remains low during daytime in clear-sky regions because of the large number of solar photons reaching the lidar's telescope. However, the solar reflection of optically thick clouds decreases the signal-to-noise ratio in the stratosphere, giving anomalous R values. Therefore, daytime profiles with R values significantly different from those associated with nighttime profiles (R > 0.95 or R < 0.14) are rejected. They represent about 30% of the total number of Level 1 V2.01 daytime profiles. Moreover, above highly reflecting boundary layer clouds (SR> 30, z<2.4km), the cloud detection threshold is increased, in order to get a constant signal-to-noise ratio in the upper and lower troposphere despite the different spatial resolutions of CALIOP Level 1 data above and below 8km of altitude.

1.3.1.2.2 Cloud Detection

Several simple diagnostics are derived from the SR profile. The atmospheric layer is labeled as cloudy when SR > 5 and $ATB-ATB_{mol} < 2.5.10^{-3}$ $km^{-1}.sr^{-1}$ (this latter is to avoid false cloud detection in the upper troposphere / lower stratosphere, where the ATB_{mol} is very low). We then determine if the profile contains at least one cloud layer within the low-level (P > 680 hPa), middle-level (440 < P < 680 hPa) and upper-level (P < 440 hPa) atmospheric layers, and in the whole column. To keep detailed information about the distribution of the lidar signal intensity, we also record the occurrence frequency of different SR values (we use 15 intervals of SR values, ranging from 0 to 100) as a function of height (y-axis) to build the histograms of SR values (referred to as SR CFAD532 in the GOCCP data set).

1.3.1.2.3 Standard Products and Characteristics of GEWEX-Archived Version

CALIPSO-GOCCP contains four different cloud files for the period 2006-2010. The entire data set is available on the CFMIP-OBS database ***http://climserv.ispl.polytechnique.fr/cfmip-obs/*** and a subset is available on ***http://www.icare.univ-lille1.fr***.

1) ***instant_SR_CR_DR***: is an orbit file which contains the Scattering Ratio (and the Color Ratio, and the Depolarization Ratio) over 40 vertical levels at 335 m intervalsalong the satellite flight track. Each file corresponds to half an orbit and contains the longitude, latitude, altitude, time, ground base elevation and the three ratios.
2) ***SR_histo***: contains the number of occurrence of the Scattering Ratio within a given bin (19 different bins are considered for a given altitude level in a given latitude-longitude grid box, accumulated over a month. The vertical resolution is 480m and the horizontal resolution is 2°x2°.
3) ***3D_CloudFraction***: contains the monthly mean cloud fraction over a 2°x2° latitude- longitude grid box and 40 vertical levels between the ground and 19.2 km.
4) ***MapLowMidHigh***: contains the total monthly mean cloud fraction maps, and the monthly mean cloud fractions map at three different vertical levels following the ISCCP definition (Low level for CP<680 hPa, Mid level for 680<CP<440hPa, High for CP<440hPa) over a 2° x 2° latitude-longitude grid box. Monthly cloud fractions in the main files are computed by dividing, for each longitude-latitude-altitude grid box (e.g. 2° x 2°), the number of cloudy profiles encountered during one month by the total number of instantaneous SR profiles measured during that month, whereas the cloud fractions in the 3D files are calculated with respect to the number of SR profiles that are not fully attenuated.

Each of these diagnostics has its counterpart included in the lidar simulator outputs of COSP (CFMIP Observation Simulator Package, ***http://code.google.com/p/cfmip-obs-sim/***).

Processing for GEWEX-CA Database

The GEWEX-CA database contains two types of CALIPSO-GOCCP files:

- The main files which contain only information on uppermost cloud layer in order to mimic passive remote sensing,
- The "3D" named-files which include all clouds, consistently with the standard CALIPSO-GOCCP product ("MapLowMidHigh") presented in the previous section.

The main files contain the cloud altitude CZ corresponding to the mean altitude of the upper cloud layer at the vertical resolution of CALIPSO-GOCCP (480m). The "3D" files contain the mean altitudes of all the cloud layers identified as cloudy within the vertical profile.

The cloud temperature CT is computed similarly to the cloud altitude. The cloud temperature CT is computed from GMAO GEOS-5 meteorological data (initially given over 583 vertical levels) averaged over the 40 levels of 480 m.

The CALIPSO-GOCCP included in the GEWEX-CA data set is gridded over 1° x 1° latitude-longitude boxes for each month, in contrast to the standard CALIPSO-GOCCP data set which is gridded over 2° x 2° and averaged over seasons (3 months) and several years.

1.3.1.2.4 Uncertainty Estimates

The main limitations of CALIPSO-GOCCP products are the following:

- The spatial sampling: the gridded data set cannot be used for a single month of a single year over a 1x1° lat-lon box because the number of samples is too low. It can be used for a single month, but over a 5° x 5° latitude-longitude grid box. It can be used over a 2 x 2° latitude-longitude grid when data are accumulated over a season (3 months) during several years (at least 2).
- The clouds located below a higher altitude cloud with COD larger than 3 cannot be detected because the laser is fully attenuated. It means that the amount of low-level clouds is likely underestimated in the deep convective-region of the Inter Tropical Convergence Zone and in mid-latitudes in the storm tracks.
- Due to the contamination by solar photons during day time, the signal-to-noise ratio is not the same during day and night time, consequently the differences between day and night cloud covers can not be directly interpreted as a diurnal variation.

An evaluation of CALIPSO-GOCCP against others satellite clouds climatologies is reported in (Chepfer et al., 2010).

1.3.2 POLDER
J. Riedi, S. Zeng, F. Parol

1.3.2.1 Measurements

The PARASOL mission was launched on December 18, 2004 and has been providing science data from the POLDER3 (Polarization and Directionality of the Earth's Reflectances) instrument since March 2005. PARASOL has been orbiting in conjunction with other platforms of the A-Train at an altitude of 705 km in a sun-synchronous ascending orbit with a 13:30 equatorial crossing local time. The orbit had been adjusted so that targets simultaneously observed by the active instruments of the A-Train (Caliop and CloudSat) can be observed by POLDER in geometries corresponding to the backscatter direction.

For the first time, more than 5 years of continuous data are available from a POLDER type instrument. This unique data set provides information useful for both climate modelling and more fundamental

atmospheric research. POLDER is a multispectral imaging radiometer-polarimeter with a wide field-of-view, a moderate spatial resolution, and a multi-angle viewing capability. The instrument design and capabilities have been described by a number of authors (Deschamps et al. 1994) and we only indicate here specific details relevant to the Parasol mission.

POLDER3/Parasol has a slightly different design compared to previous POLDER instruments. Namely, a 1020 nm channel was added and polarization measurement capability was moved from the 443 nm to the 490 nm channel to account for difficulties in radiometric calibration of previous instruments. Also, the rectangular CCD array of detectors has been oriented with its longer dimension along track to provide more viewing directions. This results in a narrower ground swath width of 1440 km but still enables complete global coverage every two days.

When the satellite passes over a target, POLDER3/Parasol observes it at up to 16 different viewing directions and in several narrow spectral bands of the visible and near-infrared spectrum (443 to 1020 nm).

Thanks to its unique capabilities in terms of multiangle and polarization measurements, POLDER is able to provide information that can help understand relations between cloud macrophysical, microphysical and radiative properties with a particular handle on problems linked to cloud 3D effects and general cloud cover heterogeneity (Parol et al., 2004). With respect to the problem of cloud heterogeneity, the Parasol mission also takes advantage of the potential synergy with the MODIS instrument to fill in the gaps of POLDER limited spatial resolution and spectral coverage. However we focus here on single instrument retrievals and operational products.

POLDER Level 1 calibrated and georeferenced data are produced and provided on a fixed integerized sinusoidal grid with a ground resolution of 6 km x 6 km. The POLDER Level 2 and Level 3 products "Earth Radiation Budget, water vapor and clouds" (hereafter "ERB & Clouds") are provided on a fixed sinusoidal grid of 18.5 km x 18.5 km (corresponding to 3x3 Level 1 pixels). These are routinely processed and distributed by the ICARE data and services center (***http://www.icare.univ-lille1.fr***).

Although no onboard calibration system is available on PARASOL, vicarious calibration methods have been developed specifically for POLDER to guarantee a stable and accurate calibration of the instrument (Fougnie et al., 2007).

The main "ERB & Clouds" products routinely available from POLDER3/PARASOL are the cloud mask, cloud thermodynamic phase, cloud top height (2 methods), cloud optical thickness and shortwave scene albedo products. It is worth noting that the different retrieval algorithms use, when necessary, the 15 day averaged surface properties derived directly from the POLDER land surface products. This approach reduces the biases and errors due to inaccurate representation of surface BRDF.

1.3.2.2 Cloud Detection

The cloud detection algorithm, detailed in Buriez et al. (1997), is based on a series of sequential threshold tests applied to each individual pixel (6 km) and for every viewing direction. Four tests aim at detecting clouds and three additional tests are applied to confirm clear pixels. POLDER cloud detection aims thus to identify the confident clouds pixels which are used then to derive the cloud optical properties. The four "cloudy" tests are on the apparent pressure that is obtained from the estimate of oxygen absorption around 763nm (Vanbauce et al., 1998), on the solar reflectance at 865nm (490nm) over ocean (land), on the 865nm-polarized reflectance (Goloub et al., 2000) and on the 490nm-polarized reflectance (Goloub et al., 1997). Three additional "clear" tests with particular clear thresholds are applied to indicate confident cloud free surface if a pixel fails to pass the four cloudy tests above: a low reflectance test, a spectral reflectance variability test (between 865nm and 443nm) and an apparent pressure test. If a pixel fails to pass all these seven tests, and remains unclassified, angular and spatial variability tests will be used. Afterwards, when all of elementary pixels are identified as either clear-sky or cloudy, the cloud fraction is computed at super-pixel scale (3x3 pixels), direction by direction. The final cloud fraction is then averaged over all the 16 directions.

Clearly, the multidirectional capability of PARASOL is very useful for discriminating between clear and cloudy pixels. As an example, over ocean a simple reflectance threshold test can always be applied since some PARASOL pixels can be observed with angular configuration outside the glint region.

In addition, a cloud cover confidence index is defined from the intermediate results of the cloud detection algorithm. This parameter takes advantage of the multidirectional capability of PARASOL and allows tidentification of pixels for which cloud detection may be suspicious or of high confidence depending on the total number of available directions and tests that have been applied.

1.3.2.3 Retrieval

The interesting and unique feature about Parasol retrievals for clouds is its ability to drive the inversion process by a proper discrimination of cloud phase and cloud microphysical model thanks to the directional polarization measurements. Moreover, the consistency check of the retrieved parameters direction by direction is an indicator of the performance of the retrieval algorithms.

POLDER cloud phase is unique and based on polarization signatures (Goloub et al., 2000; Riedi et al., 2000, 2001, 2007). As such, it does not require assumptions about the atmospheric temperature profile and may be considered as unbiased with respect to temperature because the information content carried by polarization is linked solely to particle. Therefore it provides complementary information to evaluate phase information from other cloud climatologies or cloud phase representation in models (Doutriaux and Quaas, 2004; Weidle and Wernli, 2007). The method provides a phase index (clear, ice, liquid, mixed, undetermined) along with a confidence level. The usefulness of POLDER observations to detect aerosol layers over underlying liquid clouds also has been demonstrated (Waquet et al., 2008).

To derive the albedo from bidirectional reflectance observations, or equivalently, the hemispherical flux from radiance observations, several approaches are possible. Ours is based on radiative transfer modelling. In a first step, the narrowband albedo is derived from bidirectional reflectances using a radiative transfer model. This retrieval is performed at 490, 670, and 865nm. Spectral cloud optical thickness and narrowband albedo are derived using a look-up table (LUT) technique as described in Buriez et al. (2006). LUTs are calculated using a plane-parallel radiative transfer model applied to two cloud types (ice and liquid water) depending on the cloud thermodynamical phase index derived from PARASOL polarized reflectances.

A single ice cloud model based on the Inhomogeneous Hexagonal Model (Labonnote et al., 2000, 2001; Baran and Labonnote 2006, 2007) is used to retrieve ice cloud properties. This ice cloud model has proved to minimize angular biases of retrieved optical thickness (Buriez et al., 2001; Zhang et al., 2009) and provide consistent interpretation of both total and polarized bidirectional reflectances.

In a second step of the analysis, all three narrowband albedo products are used to estimate the broadband shortwave albedo as described in Buriez et al. (2007).

PARASOL provides two different products related to cloud top pressure. The so-called "Rayleigh pressure" uses polarized measurements at 490 and 865 nm to estimate above cloud Rayleigh optical thickness and to derive cloud top altitude. On the other hand, the "oxygen" pressure relies on radiances at 763 and 765 nm and uses the differential absorption in the O_2-A band to evaluate the transmission along the average photon path-length from which an equivalent pressure can be derived (Vanbauce et al., 1998). It is important to note that cloud top pressure is reported in the official POLDER products only for clouds having an hemispherical albedo greater than 0.3, corresponding roughly to an optical thickness of 2. Therefore, the POLDER cloud top pressure information provided for the GEWEX assessment do not include results for optically thinner clouds. This explains significant differences in high cloud statistics (amount and optical thickness) as observed from POLDER and other climatologies.

As a general rule, it is considered that the Rayleigh pressure is sensitive to the cloud top and the Oxygen pressure is more related to the pressure level at the geometrical middle of the cloud (Vanbauce et

al., 2003; Sneep et al., 2007). Evaluation against CALIPSO observations showed that the Rayleigh pressure provides more accurate information for high clouds than for low clouds, whereas the Oxygen pressure is better suited for evaluation of low cloud top pressures, which have a limited vertical extent. Eventually, a merged product will be created to take advantage of each method and provide an accurate determination of cloud top pressure for all clouds.

1.3.2.4 Standard Products and Characteristics of GEWEX-Archived Version

Cloud statistics provided for the GEWEX cloud assessment exercise have been computed directly from the official level 2 POLDER3/PARASOL products available through ICARE center (*http://www.icare.univ-lille1.fr*). No specific selection or filtering of data has been made in the process but three important points should be considered in the interpretation of POLDER products provided here.

First, cloud detection is attempted for all pixels only under daylight conditions including those for which snow covered surface or sea ice is indicated by the ECMWF reanalysis ancillary data. However, for the latter pixels, only cloud phase is determined whereas other properties are not retrieved (cloud optical thickness, albedo). This introduces a first difference between the sample consisting of detectable clouds and the subset of clouds with associated retrieved properties.

Second, the Rayleigh cloud top pressure can only be retrieved when observations conditions allow access scattering angles between 80° and 120°. Therefore, only about two thirds of all clouds have a Rayleigh cloud top pressure reported. This is one of the main reasons for providing POLDER statistics based on the Oxygen A-Band cloud top pressure retrievals.

The third point is related to the restriction imposed on the minimum cloud hemispherical albedo necessary to attempt cloud top pressure retrievals. As a consequence and as stated earlier, clouds having a COD less than about 2 are not present in the POLDER statistics when cloud top pressure is required to classify between low, middle and high clouds. This explains why POLDER statistics of high clouds are significantly different from other climatologies because this level is where most of the thin clouds (especially thin cirrus) occur. Generally, it is expected that POLDER data set will exhibit fewer high clouds with an average optical thickness slightly higher than other data sets.

1.3.2.5 Uncertainty Estimates

Evaluation of the algorithm performance is provided in publications related to each product as summarized hereafter.

Cloud detection has been evaluated through comparisons against synoptic ground observations (Riedi et al., 1999), ground based lidar (Chepfer et al., 2000), other sensors or climatologies (Seze et al., 1999; Riedi et al., 2000; S. Zeng, PhD thesis 2011).

Cloud phase has been validated against ground-based measurements (Riedi et al., 2001), comparison with other climatologies (Riedi et al., 2000), in depth comparison with MODIS (Riedi et al., 2007) and CALIOP (Zeng et al., 2010) phase products.

Cloud top pressures have been evaluated against active sensor information from ground based sites (Vanbauce et al., 2004) and by direct comparison with CALIPSO/CLOUDSAT products (Ferlay et al., 2010).

Cloud optical thickness and albedo have been evaluated mostly through analysis of self consistency and identification of systematic angular retrieval biases (Loeb et al., 2000; Buriez et al., 2001, 2005), comparison with MODIS (Zhang et al., 2009; Zeng S., PhD thesis, 2011) and CERES (Viollier et al., 2002).

Overall, it has been established that POLDER's strongest limitation is its rather coarse spatial resolution and limited capabilities to detect thin clouds. The main advantages of the POLDER data set reside in a unique and temperature-independent cloud phase retrieval technique, much improved capabilities to derived unbiased cloud optical thickness and albedo compared to single view instruments

and the two cloud top pressures derived without assumptions on atmospheric temperature profiles. It is however important to keep in mind that global statistics of cloud cover properties derived from POLDER can not account for clouds with an optical thickness smaller than 2, except for cloud phase which is currently retrieved for all detected clouds.

1.3.3 MISR
L. Di Girolamo, G. Zhao, A. Menzies

1.3.3.1 Measurements

MISR is the first high-resolution imager to make global, near-simultaneous, multi-spectral, and multi-angle radiometric measurements of the Earth. Details of the MISR instrument and performance can be found in Diner et al. (1998). In brief, nine separate cameras provide viewing zenith angles relative to the surface reference ellipsoid of 0°, 26.1°, 45.6°, 60.0°, and 70.5°, with one camera (designated AN) pointing toward the nadir, one bank of four cameras (designated AF, BF, CF, and DF in order of increasing off-nadir angle) pointing forward in the along-track orbital direction, and one bank of four cameras (designated AA, BA, CA and DA) pointing in the backward direction. It takes approximately 7 minutes to view a given scene from all nine cameras. Each camera has four narrow spectral bands centered at 446, 558, 672 and 866 nm. From its 705 km orbit, the AN camera has a spatial resolution of 250 m and a swath width of 376 km. All other cameras are designed to give a cross-track resolution of 275 m with a swath width of 413 km.

MISR is on board the EOS-TERRA satellite, which is sun-synchronized and crosses the equator at a local time ~10:30 AM from north to south. Given its swath width, it takes nine days to achieve complete coverage at latitudes equatorward of 60°; polar region coverage is achieved in two days except for a small region at the poles. MISR has a 14-bit radiometric resolution and does not saturate over bright surfaces such as snow and thick clouds. MISR also has high radiometric stability with an absolute calibration uncertainty of better than 4% (Bruegge et al., 2007). Since launch, MISR has kept the radiometric drift to nearly undetectable levels and angle-to-angle image co-registration to sub-pixel accuracies (Diner et al., 2007).

1.3.3.2. Cloud Detection

MISR has three cloud detection algorithms, each of which is optimized for certain underlying surfaces. Their cloud detection results are stored in three cloud masks, the Radiometric Camera-by-camera Cloud Mask (RCCM), the Angular Signature Cloud Mask (ASCM), and the Stereo-Derived Cloud Mask (SDCM). They are reported at 1.1 km resolution. Detailed algorithm descriptions the RCCM, ASCM and SDCM can be found in Diner et al. [1999(a)], Di Girolamo and Wilson (2003), Zhao and Di Girolamo (2004), Yang et al. (2007), and Di Girolamo et al. (2010b). In brief, the RCCM is generated for each of the nine cameras using radiometric information collected within each camera; hence, each region on Earth has nine RCCMs. The RCCM algorithm is divided into land and ocean algorithms. Over ocean, the observables used to generate the RCCM are the bidirectional reflectance factor (BRF) in the near-IR band at 1.1-km resolution, and the standard deviation of the 4×4 array of the 275-m red band BRF (σ_{672}) within a 1.1-km area. The near-infrared BRF and σ for each pixel are each tested against three thresholds to classify a pixel as high-confidence cloudy, low-confidence cloudy, low-confidence clear, or high-confidence clear. The two tests may return different results, and the final cloud mask is determined from the logical combination of the results of two tests. Fully taking into account the fact that the thresholds are a function of sun/viewing geometry, the RCCM algorithm breaks the ranges of solar zenith angle, viewing zenith angle, and relative azimuth angle into 10, 5, and 12 bins, respectively. Three thresholds are set for each bin for each observable. Over land, the RCCM uses two different observed quantities: a parameter D derived from the normalized difference vegetation index and red-band BRF, and σ_{672}. The thresholds used to test the first observable are dynamically derived and updated seasonally for each of the 1579 land surface regions that are defined in its Cloud Screening Surface Classification data set.

Both the ASCM and SDCM make use of information from multiple cameras to achieve a single ASCM and SDCM product for each region on Earth. The ASCM uses only a single threshold test over the entire globe. The test is the band-differenced (blue and near-infrared bands) angular signature (BDAS). Three cloud detection thresholds are applied to each BDAS observation to assign confidence levels for the final ASCM, using the same designation as the RCCM. The BDAS thresholds are binned by sun/view geometry using the same bin division as in the RCCM. The SDCM also uses a single threshold test over the entire globe. The test is based on the stereo heights derived during MISR standard processing. The stereo height of the feature is compared to the surface height. If the feature height is greater than the mean surface height by 562 m plus the standard deviation of the surface heights within the 1.1 km resolution MISR stereo height retrieval, then the SDCM outcome is "Cloud"; otherwise, it is "Near Surface."

The performances of all three cloud masks have been evaluated against visual inspection, field campaigns and other satellite-derived cloud masks [Di Girolamo et al., 2010(b)]. In summary, the RCCM performs well over ice-free ocean and snow-free land surfaces. As anticipated, the ASCM performs well primarily over snow-ice covered surfaces. In general, the SDCM is good over both land and ocean, but may not detect clouds close to the surface. In addition, unlike the RCCM and ASCM, the SDCM contains a large amount of "no retrieval." This typically occurs whenever the stereo algorithm is unable to match any features viewed by MISR. A more detailed description of the quality of these masks relative to the determination of cloud fraction is given below in Section 1.3.3.5.

1.3.3.3 Retrieval of Cloud Top Height and Cloud Fraction by Altitude

The multi-angle design of the MISR instrument produces nine views of the same scene on Earth within 7 minutes. This allows for the simultaneous retrieval of cloud motion and cloud height using stereo photogrametric techniques. The detailed description of the MISR retrieval algorithm of cloud top height (CZ) can be found in Diner et al (1999(b)), Horvath and Davies [2001 (a) and (b)], Morney et al. [2002 (a) and (b)], and Davies et al. (2007). Unlike conventional retrieval techniques using IR or CO_2 absorption bands, the accuracy of MISR height retrievals does not rely on the validity of atmospheric temperature profile and/or radiometric calibration. CZ values are reported relative to the sea level at 1.1 km resolution. Based on the comparison with in situ and ground-based active measurements, the MISR CZ RMS error is ~560 m (Muller et al., 2002; Naud et al., 2002, 2004, 2005; Marchand et al., 2007; Genkova et al., 2007; Garay et al., 2008; Harshvardhan et al., 2009) with no detectable bias. Cloud top heights are also corrected for cloud-motion effects caused by winds, which are derived using a triplet set of cameras. CZ values are reported in different wind categories, based on the quality of wind retrievals. Only cloud top heights with best wind retrieval are used to produce the GEWEX data set.

The joint distribution of cloud fraction and cloud top height is summarized in a Multi-angle Imaging SpectroRadiometer (MISR) climatological product, called the Cloud Fraction By Altitude (CFBA) (Di Girolamo et al. 2010(a)). CFBA provides monthly global cloud top fractions binned at every 500 m altitude (up to 20 km above the sea surface level) with a horizontal resolution of 0.5°×0.5° latitude/longitude degree.

The CFBA production involves two-stage processing. In stage 1 processing, three steps are taken to produce CFBA on a per orbit basis. The first step is to divide the swath of a whole orbit into 17.6 km × 17.6 km regions and calculate cloud fraction for each region from the RCCM. The cloud fraction of each 17.6 km region is calculated as the ratio of the number of 1.1 km cloudy pixels to the total number of cloudy and cloud-free pixels within the region. A 1.1 km pixel is cloudy if the AN-RCCM flags it as either high-confidence cloudy or low-confidence cloudy. However, if the AN-RCCM for the pixel is contaminated with sunglint, the RCCM of the nearest camera without sunglint contamination will be used. Sunglint is conservatively set to exist within a 40° scattering-angle about the specular direction. If no glint free camera can be found, the 1.1 km pixel is treated as "no retrieval". Over the snow/ice covered grid cells, as classified in the MISR ancillary data set, the combined ASCM and SDCM are used to determine if a 1.1 km pixel is cloudy. The ancillary sea ice masks at 1 degree resolution is labeled snow/ice if > 5% of the region has snow/ice for more than 4 days of the month based on satellite microwave data.

The second step of processing involves assigning cloud top height to each 17.6 km × 17.6 km region. The heights are directly read from the MISR L2 Cloud Classifiers product (Diner et al., 1999), which reports the median of the 1.1 resolution MISR stereo heights within 17.6 km × 17.6 km region. These median heights are corrected with best wind retrievals and are recorded relative to the sea surface level. Both the cloud fraction and heights of each region for each orbit are stored as an intermediate data set for further processing. Because of the nature of the MISR stereo technique, some regions may not have valid height retrievals. The stereo algorithm requires high quality wind measurements to correct cloud height and will fail when such measurements are not available, such as over large homogenous cloud fields that lack the contrast necessary for accurate wind retrieval. When height retrievals are not available, a nearest-neighbor search of valid height retrievals within 200 km from the center location of a region will be conducted. The first returned nearest neighbor valid height at 17.6 km resolution is assigned to the region. If no valid height retrieval is returned, the region will be flagged as "no retrieval." Two fields for the CFBA outputs are stored in the intermediate product; one set is generated using the nearest-neighbor algorithm and the other without. The third step of processing includes projecting cloud fraction and heights at 17.6 km resolution from steps 1 and 2 processing into 0.5°×0.5° latitude/longitude degree grids and binning clouds fractions by cloud heights. The grids are defined to break latitude and longitude into half-degree increments ranging from 90° N to 90° S and -180° W to 180° E, respectively. A region belongs to a grid box if its center is within the boundaries of the grid box. For each half-degree box, cloud fractions are further binned by their heights. Height is broken up into 500 m increments and ranges from -500 m to 20,000 m. There are 4 additional height bins that represent: values less than -500 m, values above 20,000 m, negative infinity to infinity representing total cloud fraction, and no height retrieval. The mean, standard deviation, and number of cloud fractions of the regions sampled in each bin are calculated and reported at each grid box.

The second and final stage is to aggregate the intermediate product from stage 1 processing to generate the publicly available monthly, quarterly, and annual CFBA products. Due to the nature of the MISR Level 2 products, some orbits are poorly registered and contained no valid value from the *MedianPrelimCloudHeight* field in the Cloud Classifiers product. The first step in stage 2 processing is to generate a set of daily summaries by aggregating the orbital CFBA files from stage 1 processing. Before the aggregation is performed, cloud fractions of each orbit file are normalized so that the sum across all height bins (excluding the total cloud fraction bin for any 0.5°×0.5° degree grid box is equal to the total cloud fraction of the grid box. This is done by multiplying each bin by the number of values it contains to obtain the sum of the cloud fractions in that bin, and then dividing each bin by the total number of samples across all heights for a given grid box. The second and final step in generating the daily summary is to average all the normalized orbital CFBA files for a single day. Each orbit is given equal weight. The number of samples for each grid box and height bin will now represent the number of orbits that went into each average as opposed to the number of 17.6 km×17.6 km regions that went into the intermediate orbit file. Likewise, the standard deviation will now represent the variance among orbits instead of 17.6 km samples. The process for generating a monthly summary is the same as for a daily summary, except that no normalization, mixing of fields or value reassignment is performed. To generate a monthly summary, all the daily summaries for the month are read and averaged together with equal weight assigned to each day.

More detailed algorithm description of CFBA can be found in Di Girolamo et al. (2010a). The CFBA was specifically designed for studies concerning the climatological characteristics of the joint distribution of cloud fraction and cloud top height at local, regional, and global scales. For example, Figure 1.3.4 presents an analysis of the change in cloud height along the GEWEX Cloud System Study Pacific Cross Section. The good vertical resolution allows one to observe, for example, the increase in cloud height of boundary layer clouds as we move away from the Californian coast.

The strength of the CFBA product for the GEWEX cloud assessment lies in its stereoscopic derived cloud top altitudes, which is completely independent of other instrument techniques, does not use ancillary temperature profiles, are unbiased relative to the many in situ and ground based active

measurements referenced in the first paragraph of 1.3.3.3, and carry an rms uncertainty at the pixel-scale of ~560 m.
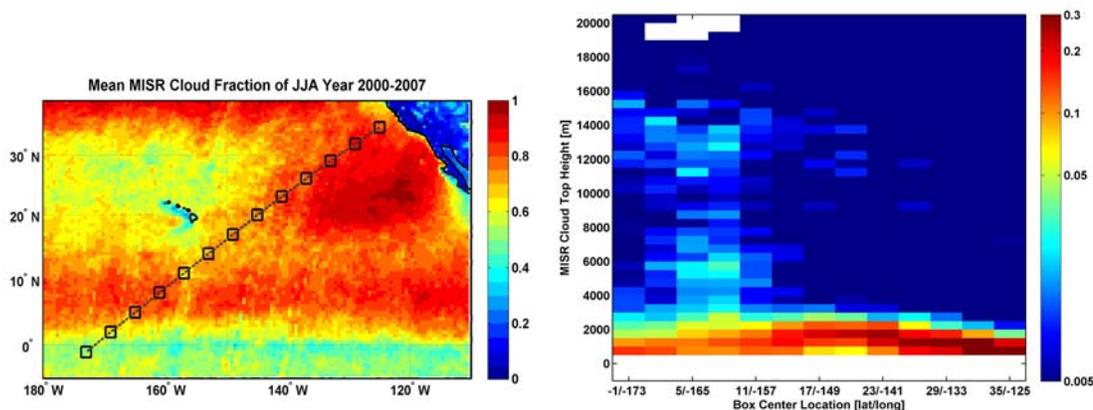
Figure 1.3.4: The left image shows the total cloud fraction, along with a line defined as the GCSS Pacific Cross Section, averaged for June, July, and August from 2000-2007. The right image shows the averaged cloud fraction vs. altitude at the locations defined by the squares in the left image.

1.3.3.4. Processing for GEWEX-Archived Database

The CFBA monthly product has been reprocessed to meet the GEWEX cloud assessment data requirement. Note that this step degrades the horizontal and vertical resolution of the original public CFBA product; it is done only for the purpose of meeting the GEWEX cloud assessment intercomparison requirements. The horizontal spatial resolution of the monthly CFBA product has been downgraded into $1° \times 1°$ grid box, and the 41 height bins (from < -500 m to 20 km) are regrouped into low (< 680 hPa), middle ([440, 680]), and high (< 440 hPa) pressure bins. Before the height bins are regrouped, cloud fractions in the first (<-500 m), second height bin (-500~0 m), and the 45th height bin (the no-retrieval bin) are added up and the sum is redistributed amongst the other height bins proportionally. The proportion of the redistributed cloud fraction for each bin equals to the ratio of the cloud fraction of the bin to the total cloud fraction (the 44th height bin). The heights of 680 and 440 hPa pressure levels are determined for each month for each 1° latitude band using the ancillary pressure data set generated from GEOS 5 data, which provides a list of height and pressure pairs for each 1-degree latitude band on a daily basis. The daily values of the altitudes of 680hPa and 440hPa are calculated from this daily data set and then averaged together with equal weight to form averages for each month and each latitude band. Only GEO 5 data of year 2007 is used to create the ancillary pressure data set, with an assumption that annual variation in pressure level for each latitude band is negligible. The reprocessed cloud fractions of low, middle, and high pressure bins are further packed into individual files in the GEWEX file format.

1.3.3.5 Uncertainty Estimates

The CFBA algorithm accounts for the strengths and weaknesses of the MISR cloud products, as well as sampling characteristics of the instrument and its products, so as to provide the best estimate of monthly cloud fraction by altitude that can be derived from the MISR Level 2 cloud products. The CFBA uses input data from the Level 2 cloud products. Therefore, all of the Level 2 cloud quality statements apply, which can be found at **http://eosweb.larc.nasa.gov/PRODOCS/misr/Quality_Summaries/L2_Cloud_Products.html** and Di Girolamo et al. [2010(b)]. The unique characteristics of the MISR cloud detection and cloud height retrieval should be kept in mind when the MISR GEWEX products are used in scientific analyses. These features are emphasized as follows:

1) MISR retrieves cloud top heights based on the altitude of greatest spatial contrast as viewed by multiple cameras. The COD threshold at which the stereo algorithm identifies thin clouds depends,

117

in part, on the contrast of the underlying surface. As a result, the heights of thinner single-layered clouds can be retrieved over ocean compared to over land.

2) In the case of thin high-altitude clouds over thicker and lower altitude clouds, MISR-stereo may retrieve the altitude of the lower cloud without degradation in the quality of the retrieved height for the lower cloud, since it may be the lower cloud that offers greater spatial contrast as viewed by MISR. This has the advantage over conventional IR-based techniques that may place the cloud at an altitude that is between the high thin cloud and low thick cloud, where clouds may not exist. Therefore, when comparing MISR cloud heights with those derived from conventional IR, MISR may report a smaller fraction of high cloud and larger fraction of low cloud, but the total cloud fraction remains comparable if the data sets have the same cloud detection sensitivities.

3) MISR does not report cloud heights for all pixels detected as cloud by the MISR cloud masks. For example, a thick cloud that has no spatial contrast over some horizontal scale will have no retrieved heights over that scale. A nearest-neighbor-search for heights, combined with the MISR cloud masks, is used to minimize the sampling artifacts that may arise from these "no-retrieved-heights". Where the search is unsuccessful, the no-retrieved-heights cloud fraction is recorded in the CFBA product and accounted for in the total cloud fraction as reported in the product.

4) The total cloud fraction is the fraction of pixels detected as containing "some" cloud. Over snow- and ice-free regions, the MISR cloud mask performs well at detecting sub-pixel clouds. Since sub-pixel clouds (by definition) do not fully cover a pixel, the true cloud fractions (as would be defined by a perfect cloud detector using pixels that are near infinitesimal in size) will be overestimated in regions populated by small clouds (e.g., trade wind cumulus regions). A full discussion on this issue is given in Zhao and Di Girolamo (2006). An algorithm to correct the overestimation of cloud fraction, based on Di Girolamo and Davies (1997), is anticipated to be complete in the near future by Jones et al. (2010).

5) Since land surfaces provide greater underlying spatial contrast compared to ocean, the MISR cloud detection and cloud top retrieval algorithms will miss a greater fraction of optically thin clouds over land. It has been determined that total cloud fraction over snow-free land and ice-free ocean is biased low by ~7% and ~2%, respectively (Di Girolamo et al., 2010b). This is relative to supervised support vector machine classification on a large number of randomly selected scenes applied to the RCCM.

6) The snow and ice mask used in the CFBA product is a monthly mask at 1-degree resolution. A 1-degree grid is labeled snow/ice if > 5% of the region has snow/ice for more than 4 days of the month based on SSM/I data. Where labeled snow/ice covered, snow/ice thresholds for the ASCM are used. When these thresholds are applied to 1.1 km pixels that are, in truth, not covered by snow/ice within the snow/ice-labeled 1-degree region, an underestimation of cloud occurs. As a result, cloud fraction may be underestimated in polar regions, particularly near the snow/ice – snow/ice-free boundaries. The MISR team is currently considering updating the monthly sea/ice mask to a daily mask at higher spatial resolution.

7) Because only daylight data are collected by MISR, a monthly grid-cell in the high-latitude summer hemisphere will contain data that have been sampled from two ranges of solar zenith angles: one from the ascending branch of the orbit, the other from the descending branch of the orbit. Any diurnal cycle in cloud cover that exists in the high-latitude summer hemisphere, or unknown solar zenith angle bias in cloud detection and cloud-height retrievals, gets folded into the mean values of cloud. For all other regions and times, the data that goes into the CFBA is sampled solely from the local mid-morning time that is characterized by the orbit's mid-morning equator-crossing-time of the descending branch (~10:30 A.M.).

8) Stereo processing requires high-quality image navigation of the orbit. Where the quality is deemed poor due to lack of ground control points within the orbital swath needed for proper navigation, the entire orbit is removed from the statistics. As a result, not all longitudes along a given latitude line are sampled equally.

9) Reprocessing CFBA for the GEWEX database involves height-to-pressure conversion, calculated from the pressure data set of GEOS 5. Therefore, any error in the pressure retrieval may propagate into the MISR GEWEX product. In addition, the longitudinal variation in the heights of pressure levels is not provided in the GEOS 5 data set. Since only the GOES 5 data of year 2007 is used in

processing the MISR GEWEX product, the annual variation in the heights of pressure levels is not considered. Uncertainties in this conversion have not been assessed.

The above nine points summarize the quality of the CFBA, which are important to track in the scientific analysis of the product. These translate directly to the GEWEX Cloud Assessment. For this assessment effort, the average standard error in the mean in CA for a 1°x1° monthly grid point is estimated to be 0.03 – 0.07, with a low bias of 0.02 – 0.07, depending on the underlying surface and ones definition of "cloud". The average standard error in the mean CZ for a 1°x1° monthly grid point is estimated to be 100 – 250 m, with no bias. This precision and accuracy is conditional upon the heights that are retrieved by MISR's stereoscopic technique, which have been validated against in situ and ground-based active measurments of same-cloud samples (Section 1.3.3.3). Of course, points 1 and 2 above may lead to a different subset of cloud sampled between MISR-retrieved heights and those from other sensors (even for other sensors viewing within the MISR swath). This would produce a relative bias in mean CZ between MISR and other sensors. In comparing Low, Middle and High cloud amounts with other GEWEX Cloud Assessment data sets, point (2) and (9) above are expected to explain much of the descrepencies, along with sampling differences tied to orbital configuration and the diurnal cycle of cloud cover.

1.4 Cloud Products from the European Remote Sensing Satellites

1.4.1 ATSR-GRAPE
C. Poulsen, A. Sayer

The ATSR have flown on ERS-2 (Mutlow et al., 1999) in a 10:30 orbit and ENVISAT (Llewellyn et al., 2001) in a 10:00 orbit, providing a long time-series (from 1995-present) with continuation guaranteed with the launch of SLSTR (Sea Land Surface temperature radiometer) on board Sentinel-3 in 2013. The ATSR analysis method (called ORAC, Oxford RAL retrieval of Aerosol and Cloud) has been applied to ATSR-2 and AATSR measurements; the results included in the GEWEX archive cover 1997-2009.

ATSR results have already been used to analyse ship tracks (Campmany et al., 2009; Sayer et al., 2010b) and to study cloud-aerosol interactions (Bulgin et al., 2009). The ATSR analysis method could in fact be applied to many different passive visible and infrared remote sensing instruments. Indeed, the theoretical basis for the algorithm was established through a EUMETSAT study to derive cloud properties for the Meteosat Second Generation (Watts et al., 1998) SEVIRI instrument. A version of the algorithm for SEVIRI is under development at EUMETSAT.

The ATSR level-2 data set and additional level-3 GEWEX files from partial years, as well as more information on the data set are freely available from the British Atmospheric Data Centre at ***http://badc.nerc.ac.uk/browse/badc/cwvc/data/grape/arc/v3***.

1.4.1.1 Measurements

The ATSRs are dual-viewing instruments measuring visible and infrared radiances (at 0.55, 0.67, 0.87, 1.6, 3.7, 11 and 12µm) with 1 km pixel size at nadir. The initial ATSR-1 instrument (without the visible channels) operated from 1991-2000. The area sampled by AATSR consists of two curved swathes approximately 550 km wide: a nadir view, looking down at zenith angles from 0º-22º, and a forward view inclined between 53º-55º to the normal to the surface. The Level 1b product used here has collocated and regridded the forward-view measurements with the nadir-view measurements. The two views image the same scene with a time difference of about 150 seconds.

The revisit time interval is 3-6 days, dependent on latitude. The ATSR-2 instrument on ERS-2 has a similar sampling to AATSR however the swath over sea for the visible channels is reduced to 312 km because of restricted telemetry to ground.

The ATSR instruments are designed to have exceptional sensitivity and long term calibration stability. Thermal channels are calibrated using two on-board black bodies at known temperatures, which are observed during each across-track scan of the instrument. This makes it possible to determine single channel equivalent brightness temperatures to ± 0.05 K (Smith et al., 2001). The instrument also has an on-board visible/near-IR calibration system enabling the visible channels to be calibrated to an accuracy better than 4% (Smith et al., 2009), which is subsequently improved via vicarious calibration using scenes of known stable surface BRDF (certain deserts and ice caps). Unfortunately while the stability of the channels for GEWEX processing is good, there exists an offset between ATSR-2 and AATSR visible channels. This has been identified and corrected in subsequent versions of the data product.

1.4.1.2 Cloud Property Retrieval

The ORAC algorithm (Poulsen et al., 2010; Watts et al., 1998) is an optimal estimation retrieval that can be used to determine both aerosol and cloud properties from visible/infrared satellite radiometers. In the case of cloud retrievals the algorithm fits radiances computed from LUTs created from DIScrete Ordinates Radiative Transfer (DISORT) (Stamnes et al., 1998) to the TOA signal measured by the satellite by varying the COD, CRE, CP, phase and surface temperature simultaneously. The result is a radiatively consistent set of cloud properties. The cloud retrieval has thus far been applied to ATSR-2 and AATSR, as well as to SEVIRI and AVHRR measurements. Currently the retrieval does not make use of the 0.55 or 3.7 μm channel.

The optimal estimation (OE) framework of ORAC provides key advantages:

- The ORAC algorithm currently assumes a single layer model and retrieves COD, CP, CRE, CA and sea surface temperature. Each retrieval has an associated cost and error. From these retrieved products we can subsequently derive CLWP and CIWP.
- The ability to include prior knowledge of the retrieved quantities is inbuilt into the method. This is particularly valuable for constraining the retrieval of surface temperature.
- The retrieval provides comprehensive error propagation, allowing measurement error, forward model error (due to approximations and assumptions which must be made in the modelling of TOA radiance) and uncertainties in a priori knowledge to be combined to give a rigorous estimate of the uncertainty on retrieved values on a pixel by pixel basis.
- SW/LW radiative effects of cloud can be readily computed from the fitted cloud model and is ensured to be consistent with the observed radiances.
- ORAC uses real-time radiative transfer, the method relies on fitting the measurements, to within expected error limits, to the predicted values. Since exact methods are far too slow the strategy adopted then is to utilise 'fast', non-exact, radiative transfer models with analytical gradients. This is achieved by decoupling the cloud and atmospheric ('cloud free atmosphere') parts of the system.
- ORAC then uses precalculated multiple scattering cloud radiative properties stored in look-up tables (LUTs), and clear atmosphere radiance and transmission calculations (MODTRAN for the visible channels and RTTOV for the Infrared)
- These two components and surface properties are merged into a three-layer (below cloud, cloud and above cloud) system by relatively straightforward and computationally efficient equations.
- ORAC uses MIE scattering for water droplets and optical properties from Baran for ice crystal.
- ECMWF temperature humidity and surface properties, i.e., wind speed and surface temperature, at 6 hourly intervals are used as a priori information for the retrievals.

The data were processed for all pixels that passed an initial cloud flag. Over sea the cloud flag is one based on the cloud tests described in (Zavody et al., 2000). Over land the cloud flag is that described in (Birks, 2009), which uses a Normalised Difference Vegetation Index (NDVI) technique. The optimal estimation method also gives an indication of whether a scene is cloud or not via cost and retrieval errors, and this information is used in addition to the cloud flags to determine if a scene is really cloudy. There is evidence that the cloud mask procedure produces more false positives and false negatives over land than over ocean.

1.4.1.3 Evaluation

A recent paper by A. Sayer et al. (2011) gives a detailed evaluation of the ATSR cloud properties.

Each of the Level 2 ATSR cloud products has an associated error derived from the Optimal estimation algorithm that provides a detailed estimation of the errors in the retrieved quantities, and quantification of the 'goodness of fit' of the observations to the cloud forward model. The error of the product and the 'cost' are used to derive the Level 3 products and allow for a detailed evaluation in addition to the comparison with other products summarised in the previous sections. The following extra points should be noted.

1. The values in the Level 3 file have been sub-sampled using thresholds on the maximum allowed error on each retrieved variable and a maximum cost threshold (i.e., cost < 10).
2. The model used is a single layer cloud model hence not unexpectedly the model performs poorly for multi-layered cloud.
3. Cloud identification and retrievals are difficult over snow and ice and the cost may not be a good indicator of quality. Retrievals over this region should be treated cautiously.

The ATSR data record is a relatively new time series. It provides a complementary data set to the existing passive visible and IR sensors. The data presented here is the first complete run through of the data. The authors have not utilised the full potential of the instrument and the algorithm has advanced considerably since this data was produced, however the data set is already providing useful information. It is hoped that in the context of the ESA cloud climate change initiative the algorithm and ATSR can be further exploited.

1.5 Other Cloud Products

1.5.1 SAGE II
P. Minnis, P.-H. Wang

1.5.1.1 Measurements

The Stratospheric Aerosol and Gas Experiment (SAGE) II aboard the Earth Radiation Budget Satellite (ERBS) uses the solar occultation technique to measure atmospheric aerosols and gases in the stratosphere (McCormick, 1987) from October 1984 to August 2005. The self-calibrating limb transmission measurements centered at seven wavelengths between 385 nm and 1020 nm are used to retrieve concentration profiles of ozone, water vapor, nitrogen dioxide, and vertical distributions of aerosol extinction coefficient at 385-, 453-, 525-, and 1020-nm wavelengths (Chu et al., 1989). Due to the microphysical relationship between aerosols and cloud, SAGE II extinction measurements also contain some information on aerosol-cloud interaction (Wang et al., 1994). In addition, the presence of optically thick (in occultation geometry this may be a much thinner cloud when viewed from nadir) clouds along the viewing path of SAGE II terminates the profile. Thus, data from SAGE II also contain information on cloud top height of optically thick clouds (Wang et al., 2001).

The instrument has a field of view (FOV) that is 0.5 arc-min in the vertical and 2.5 arc-min in the horizontal at the tangent to the limb. Using an "onion-peeling" data retrieval scheme with a 1 km vertical increment, the FOV defines a sampling volume that is about 1 km in the vertical, 2.5 km in the horizontal (perpendicular to the viewing path), and 200 km along the viewing path at a tangent height of 20 km. Optically, the aerosol extinction coefficient measurement covers a dynamic range from 2.e-6 to 2.e-2 km^{-1}, corresponding to optical depth of 0.0004 to 4 for the 200 km path length of the tangent shell. For a 1 km thick layer, the corresponding optical depth is about 2.e-6 to 2.e-2 in the vertical. Thus, clouds with an extinction greater than about 0.02 km^{-1} terminate SAGE II profiling. They are referred to as opaque clouds (OCs).

Under normal conditions, i.e., when the atmosphere is not disturbed by volcanic aerosols, the upper limit of the aerosol extinction is about 0.0002 km^{-1} at 1020 nm. As a result, the measurements with extinction coefficients between 0.0002 and 0.02 km^{-1} correspond to subvisible cirrus clouds (SVCs) (Sassen and Cho, 1992). In the case of OCs in the troposphere, they are most likely to be cirrus clouds (Ci).

The ERBS orbital characteristics are such that SAGE II sunrise/sunset measurements provide a latitudinal coverage of about 135° within one month. Poleward of 55° latitude, there are no measurements during winter. The eruption of Mount Pinatubo (15.14°N, 120.35°E) in June 1991 produced the largest stratospheric aerosol loading ever observed by satellite (McCormick et al., 1995), and therefore prevented SAGE from sensing below an altitude of about 20 km during the months after the eruption. Hence, the period from June 1991 until November 1993 has to be excluded for the cloud analysis.

1.5.1.2 Cloud Detection and Retrieval

As indicated in the previous section, SAGE II measurements contain information on SVCs and OCs. In the case of a single SAGE II event, the measurement can reveal the vertical location of aerosols, and possible presence of SVCs and OC top height. The OC top height is simply determined by the lowest height of the SAGE II profile measurement. The determination of the presence of SVCs from aerosols is not so straight-forward. An elaborate two-wavelength method has been developed by Kent et al. (1993) to identify SVC from SAGE II data, based on the extinction coefficients at 525 nm and 1020 nm on a seasonal and latitudinal basis. Thus, SAGE II provides the SVCs' extinction coefficients at these two wavelengths in addition to their altitudes. The corresponding uncertainty of the SVC extinction coefficients is estimated according to the spread of the transmission data in the 1 km vertical bin used in the data retrieval.

The associated OC height uncertainty is estimated by the vertical resolution of the SAGE II measurement, i.e., 1 km. This is also the case for SVCs. It should be mentioned that the above argument is based on the assumption that the SVC/OC is located within the tangent shell of the corresponding limb viewing path. Unfortunately, there is no information on the precise location of the cloud along the viewing path or on the shape of the SAGE II cloud observation. As a result, SAGE II can only provide the lower limit of the cloud height.

When the SAGE II profile data collected over a certain period and over a geographic area are used all together, it is possible to derive a meaningful occurrence frequency for SVC and OC as a function of altitude (Wang et al., 1996, 2001). In the case of SAGE II OCs, the vertical distribution of the frequency of the cumulative OCs (COC) and the uppermost OCs (UOC) can also be determined (Wang et al., 2001). It has been shown that the COCs are related to large-scale circulation (Wang et al., 1998), and that the UOCs are related to cloud outgoing longwave radiation (COLR) (Wang et al., 2002). As to the uncertainty estimate of the derived cloud occurrence frequency, the SAGE II cloud count is equivalent to a binomial experiment with the cloud frequency as the binomial parameter (Wang et al., 2001). Therefore, the 95% confidence interval can be determined by using a standard statistic method (e.g., Johnson and Kotz, 1969).

1.5.1.3 Uncertainty Estimates

Due to the path length of 200 km cloud occurrence frequency is greater than the cloud amount determined by instruments with a better spatial resolution. However, optimum effective cloud sizes can be determined by comparison with ISCCP (Liao et al. 1995a) and HIRS (Wylie and Wang 1997): High level cloud amounts from SAGE II and ISCCP agree to within 5% if the SAGE II data are analysed with a threshold extinction coefficient of 0.008 km^{-1} (since ISCCP misses subvisible clouds) and an effective cloud horizontal size of 75 km. Systematic regional differences indicate variations of the effective cloud sizes over a range of at least 50 – 125 km. The 12 to 22% differences in high cloud frequency between HIRS and SAGE II can be explained by the higher sensitivity to high thin clouds and the larger field of view of the SAGE II instrument. Since HIRS on the other side is more sensitive to cirrus and has a larger field of view than the imagers used in ISCCP, an agreement between SAGE II and HIRS can be achieved by a larger effective horizontal size of 130 km (Wylie and Wang, 1997).

1.5.2 Surface Weather Reports of Clouds
S. Warren

Synoptic weather reports are made from both land stations and ships, typically four or eight times per day, and sent by radio or electronically to the WMO's Global Telecommunications System (GTS). The reports contain information about total cloud cover, low cloud amount, cloud types at three levels, "present weather" (precipitation, fog, etc.), and cloud base height. The reports are archived at several meteorological centers around the world. About one million observations per month are reported in the synoptic code from land stations. There are about 100,000 ship observations per month, which have been archived in the Comprehensive Atmosphere-Ocean Data Set (COADS), a project of NOAA and NCAR (Woodruff et al., 1987, 1992). COADS includes not only the reports transmitted by radio but also reports that are transcribed later from the ship's logbook after the ship arrives in port. Recently the COADS has been augmented by some independent ship-observation databases, particularly those of the British and Japanese meteorological agencies, and has become the "International COADS" (ICOADS; Worley et al., 2005).

The synoptic code was defined by the International Meteorological Organization in 1929, to be used beginning in 1930 (NCDC, 1962). A major change to the classification of cloud types was made in 1949, which precludes us from analyzing cloud-type trends prior to 1949. Since then, there has been one minor change to the code: beginning in 1982, the cloud-types section of the report became optional if there are no clouds, and the present-weather code also became optional if there is no "significant" weather. This change affects our computation of the frequency of occurrence of cloud types. We have been able to take this change into account in our analysis procedure, either by the methods of Norris (1998) and Hahn and Warren (1999) for the ocean, or in the case of land data, by rejecting stations that do not normally report cloud types (Hahn and Warren, 2003).

The synoptic code defines a total of 27 cloud types, 9 for each of 3 levels (WMO 1956, 1974). For our analysis we have grouped the clouds into 9 groups: 5 low-level, 3 midlevel and 1 high-level, recognizing that the observer at the ground can most accurately report the low clouds. We did attempt a subdivision of the high clouds, but found that national boundaries appeared in our climatology, indicating subtle differences in observing practices in different countries with regard to classification of the nine types of cirriform clouds. We therefore have grouped all the high clouds together. Note that in contrast to the satellite products, the cloud level is determined by cloud base location above the local surface topographic height, not cloud top location.

We define the "amount" of a cloud type as the fraction of the sky covered by that type. The time-averaged amount can be obtained as the product of frequency-of-occurrence (fraction of weather observations in which a cloud of this type is present) and amount-when-present (the average fraction of the sky covered by this cloud type when it is present). For example, if altocumulus is present in 30% of the usable observations from a station, and if it covers on average 40% of the sky when it is present, then the average altocumulus amount at that station is 12%.

The amount, or even the presence, of a middle or high cloud may be indeterminate when a lower cloud nearly or completely covers the sky. The average amounts of middle and high cloud types can be estimated by assuming that the frequency and amount-when-present are the same in observations where they cannot be calculated as in observations where they can be calculated (subject to some adjustments). To obtain amount-when-present of upper clouds, the clouds at different levels are assumed to be randomly overlapped. These assumptions, and their justification, are discussed by Warren et al. (1986, 1988) and Norris (2005). More detail about the method is given by Hahn and Warren (2003). The first edition of cloud atlases from surface observations (Warren et al., 1986, 1988) are now superseded by the second edition at ***http://www.atmos.washington.edu/CloudMap/***.

The surface observations have uneven spatial and temporal coverage. In some continental areas (particularly Europe) there is a high density of stations reporting every 3 hours, whereas in some parts of Antarctica and North Africa there are large regions with no stations. Ships visit many areas of the ocean, but some areas are sampled so infrequently, particularly the high-latitude southern hemisphere oceans, that only multi-year seasonal averages of cloud amounts can be determined, not averages for individual years.

In addition to random sampling error, there are errors that are different from the biases that affect satellite cloud climatologies. The threshold COD for detection of cirrus clouds depends on the solar zenith angle (greater at high sun) and is greater if low-level haze is present; the threshold optical depth is apparently greater for visual observations than for the TOVS and HIRS analyses, since the cirrus amounts in the ground-based climatology are consistently lower than those in the TOVS and HIRS climatologies, even after accounting for overlap.

The night-detection bias (Hahn et al., 1995) is reduced by screening night-time observations for adequacy of moonlight. This screening appears to be adequate for the low clouds, and the diurnal cycles of middle and high clouds are much improved when compared to those obtained by using all observations. However, the diurnal cycles of the thinner middle and high clouds may still contain artifacts due to inadequate detection even under bright moonlight. In the ocean there is also the potential for sampling biases because the ships are mobile and may oversample some weather types. Such sampling biases are geographically non-uniform.

The amount of low-level clouds in the surface-based climatology is larger than in the satellite climatologies, because the satellite climatologies count only the low clouds seen from above, not the low clouds hidden below higher clouds. However, we could expect differences between cloud amounts reported from the surface and those from satellite even if only the low cloud layer is present and even if the satellite's pixel size is small enough to resolve cloud edges, because the ground observer reports sky cover whereas the satellite reports the earth cover as projected at the viewing zenith angle, which varies across the scan path. This difference will be greatest for scattered convective clouds because of their large height-to-width ratio.

1.6 Chronological Bibliography of Cloud Retrieval/Product Comparisons

The following is a chronological list of previous cloud product comparison studies as well as some algorithm comparison articles. More articles can be found in Section 4.

Hughes, N.A., 1984: Global cloud climatologies: A historical review. *J. Climate Appl. Meteor.*, **23**, 724-751.

Rossow, W.B., F. Mosher, E. Kinsella, A. Arking, M. Desbois, E. Harrison, P. Minnis, E. Ruprecht, G. Seze, C. Simmer and E. Smith, 1985: ISCCP cloud algorithm intercomparison. *J. Climate Appl. Meteor.*, **24**, 877-903.

Rossow, W.B., L.C. Garder and A.A. Lacis, 1989: Global, seasonal cloud variations from satellite radiance measurements. Part I: Sensitivity of analysis. *J. Climate*, **2**, 419-462.

Schweiger, A.J., and J.R. Key, 1992: Arctic cloudiness: Comparison of ISCCP C-2 and Nimbus-7 satellite derived cloud products with surface based cloud climatology. *J. Climate*, **5**, 1514-1527.

Wielicki, B.A., and L. Parker, 1992: On the determination of cloud cover from satellite sensors: The effects of sensor spatial resolution. *J. Geophys. Res.*, **97**, 12,799-12,823.

Rossow, W.B., A.W. Walker and L.C. Garder, 1993: Comparison of ISCCP and other cloud amounts. *J. Climate*, **6**, 2394-2418.

Mokhov, I., and M.E. Schlesinger, 1993: Analysis of global cloudiness: 1. Comparison of Meteor, Nimbus-7 and ISCCP satellite data. *J. Geophys. Res.*, **98**, 12,849-12,868.

Mokhov, I., and M.E. Schlesinger, 1994: Analysis of global cloudiness: 2. Comparison of ground-based and satellite-based cloud climatologies. *J. Geophys. Res.*, **99**, 17,045-17,065.

Liao, X., W.B. Rossow and D. Rind, 1995: Comparison between SAGE II and ISCCP high-level clouds, Part I: Global and zonal mean cloud amounts. *J. Geophys. Res.*, **100**, 1121-1135.

Liao, X., W.B. Rossow and D. Rind, 1995: Comparison between SAGE II and ISCCP high-level clouds, Part II: Locating cloud tops. *J. Geophys. Res.*, **100**, 1137-1147.

Jin, Y., W.B. Rossow and D.P. Wylie, 1996: Comparison of the climatologies of high-level clouds from HIRS and ISCCP. *J. Climate*, **9**, 2850-2879.

Lau, N-C., and M.W. Crane, 1997: Comparing satellite and surface observations of cloud patterns in synoptic-scale circulation systems. *Mon. Wea. Rev.*, **125**, 3172–3189.

Wylie, D. P., and P-H. Wang, 1997: Comparison of cloud frequency data from the high-resolution radiometer sounder and the Stratospheric Aerosol and Gas Experiment II. *J. Geophys. Res.*, **102**, 29,893-29,900.

Doutriaux-Boucher, M., and G. Seze, 1998: Significant changes between ISCCP C and D cloud climatologies. *Geophys. Res. Lett.*, **25**, doi:10.1029/1998GL900081, 4193-4196.

Descloitres, J., J.C. Buriez, F. Parol and Y. Fouquart, 1998: POLDER observations of cloud bidirectional reflectances compared to a plane-parallel model using the International Satellite Cloud Climatology Project phase functions. *J. Geophys. Res.*, **103**, D10, 11,411-11,418, doi:10.1029/98JD00592.

Stubenrauch, C.J., W.B. Rossow, F. Cheruy, A. Chedin and N.A Scott, 1999: Clouds as seen by satellite sounders (3I) and imagers (ISCCP). Part I: Evaluation of cloud parameters. *J. Climate*, **12**, 2189-2213.

Wang, J., W.B. Rossow, T. Uttal and M. Rozendaal, 1999: Variability of cloud vertical structure during ASTEX from a combination of rawinsonde, radar, ceilometer and satellite data. *Mon. Wea. Rev.*, **127**, 2484-2502.

Norris, J.R., 1999: On trends and possible artifacts in global ocean cloud cover between 1952 and 1995. *J. Climate*, **12**, 1864-1870.

Hahn, C.J., W.B. Rossow and S.G. Warren, 2001: ISCCP cloud properties associated with standard cloud types identified in individual surface observations. *J. Climate*, **14**, 11-28.

Naud, C., J-P. Muller and E.E. Clothiaux, 2002: Comparison of cloud top heights derived from MISR stereo and MODIS CO_2-slicing. *Geophys. Res. Lett.*, **29**, 10, 1795, doi:10.1029/2002GL015460.

Luo, Z., W.B. Rossow, T. Inoue and C.J. Stubenrauch, 2002: Did the eruption of the Mt. Pinatubo volcano affect cirrus properties? *J. Climate*, **15**, 2806-2820.

Stubenrauch, C. J., F. Eddounia, and L. Sauvage, 2005: Cloud heights from TOVS Path-B: Evaluation using LITE observations and distributions of highest cloud layers. J. Geophys. Res. 110, D19203,doi:10.1029/2004JD005447.

Yang, P., L. Zhang, G. Hong, S.L. Nasiri, B.A. Baum, H-L. Huang, M.D. King and S. Platnick, 2007: Differences between collection 4 and 5 MODIS ice cloud optical/microphysical products and their impact on radiative forcing simulations. *IEEE Trans. Geosci. Remote Sensing*, **45**, 2886-2899.

Horvath, A., and R. Davies, 2007: Comparison of microwave and optical cloud water path estimates from TMI, MODIS and MISR. *J. Geophys. Res.*, **112**, D01202, doi:10.1029/2006JD007101, (1-12).

Holz, R.E., S.A. Ackerman, F.W. Nagle, R. Frey, S. Dutcher, R.E. Kuehn, M.A. Vaughan and B. Baum, 2008: Global Moderate Resolution Imaging Spectroradiometer (MODIS) cloud detection and height evaluation using CALIOP. *J. Geophys. Res.*, **113**, D00A19, doi:10.1029/2008JD009837.

Rossow, W.B., and Y.-C. Zhang, 2010: Evaluation of a statistical model of cloud vertical structure using combined CloudSat and CALIPSO cloud layer profiles. *J. Climate*, **23**, 6641-6653, doi:10.1175/2010JCLI3734.1.

Stubenrauch. C.J., S. Cros, A. Guignard and N. Lamquin, 2010: A six-year global cloud climatology from the Atmospheric InfraRed Sounder aboard the AQUA Satellite: statistical analysis in synergy with CALIPSO and CloudSat. *Atmos. Chem. Phys.*, 10, 7197-7214.

Marchand, R., T. Ackerman, M. Smyth and W.B. Rossow, 2010: A review of cloud top height and optical depth histograms from MISR, ISCCP, and MODIS. *J. Geophys. Res.*, **115**, D16206, doi:10.1029/2009JD013422, (1-25).

2. Investigation of Possible Artifacts in ISCCP Cloud Amounts

William B. Rossow, CREST Institute at City College of New York

The following discussion illustrates the kinds of factors that must be investigated in a climate data record to ensure that that they do not introduce spurious signals into the record. Some of these factors are applicable to any climate data record and some are specific to satellite measurements. The key point is that any systematic change in the observing system can produce false signals. These factors have been investigated for the ISCCP D-version products.

2.1. Long-Term ISCCP Record

Figure 2.1 shows the ISCCP record as the deseasonalized monthly mean anomalies for CA, COD, CP and CT for the period July 1983 through 2009. The most notable feature in the global mean total CA anomaly time record is a slow vacillation about the mean value of 0.663 from a peak in 1986-1988 of about +0.03 to a minimum of almost -0.02 in 1999-2001. Over this same period, CT shows no systematic variations but does show occasional changes lasting 2-3 years and not associated with ENSO of up to ± 2K, especially during the Pinatubo event. CP appears to have a small linear trend, changing by 40 hPa over the whole record but this is caused by changes in the ancillary atmospheric product used to convert CT to CP. COD is relatively constant from the beginning of the period until it begins a slow increase in 2000-2002; the total change is about 0.5. We summarize the investigation of possible causes of spurious changes in global monthly mean CA. Specifically, we test whether any changes in the ISCCP observing system are systematic and continual over the whole record so as to explain the slow variation of CA.
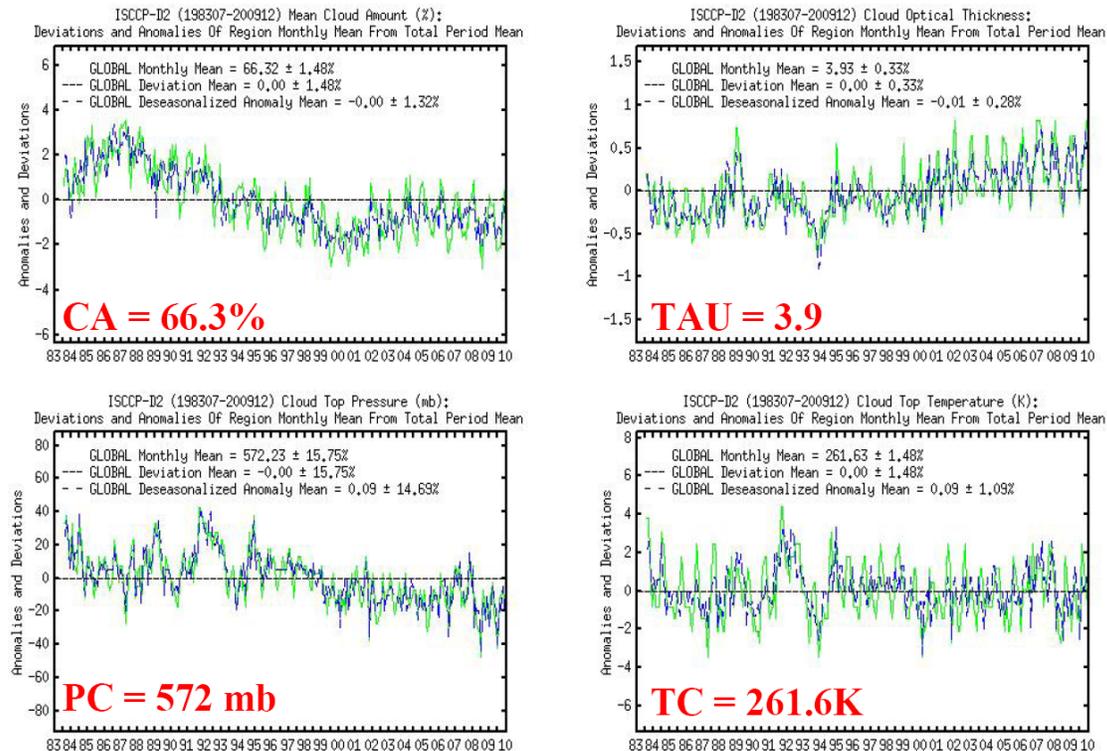
Figure 2.1: ISCCP record of global mean cloud amount as the deseasonalized monthly mean anomalies for CA, COD, CP and CT for the period July 1983 through 2009.

2.2 Effects of Radiance Calibration Changes

Most cloud detection algorithms include tests on the observed radiance values, which make their determinations of total CA dependent on the radiance calibration; any changes in calibration would introduce spurious changes in CA. In contrast, the ISCCP cloud detection algorithm is specifically

designed to perform only relative radiance comparisons: clear sky radiances are determined independently each month from the observations only and compared with observed radiances to detect the presence of clouds.

Figure 2.2 shows the effect on the total CA, as well as on four cloud types, caused by artificially changing the radiance calibrations separately for visible and infrared radiances and re-processing the data with all other factors being identical. The estimated **relative** uncertainties of the calibrations are about 3-5% for VIS and 2% absolute for IR as indicated in the figure. The test results demonstrate that the ISCCP total CA values are not dependent on radiance calibration (the very small change in total CA show is caused by the fact that the ocean reflectivity is limited by a model so that very large VIS radiance calibration changes produce a little change). The estimated calibration uncertainty translates into uncertainties of CA < 0.005 and < 0.01 for the cloud types, but we note that there is no evience for a systematic change of calibration over the whole record. Thus, the variations in Figure 2.1 cannot be explained by changes in the radiance calibrations over the ISCCP record.
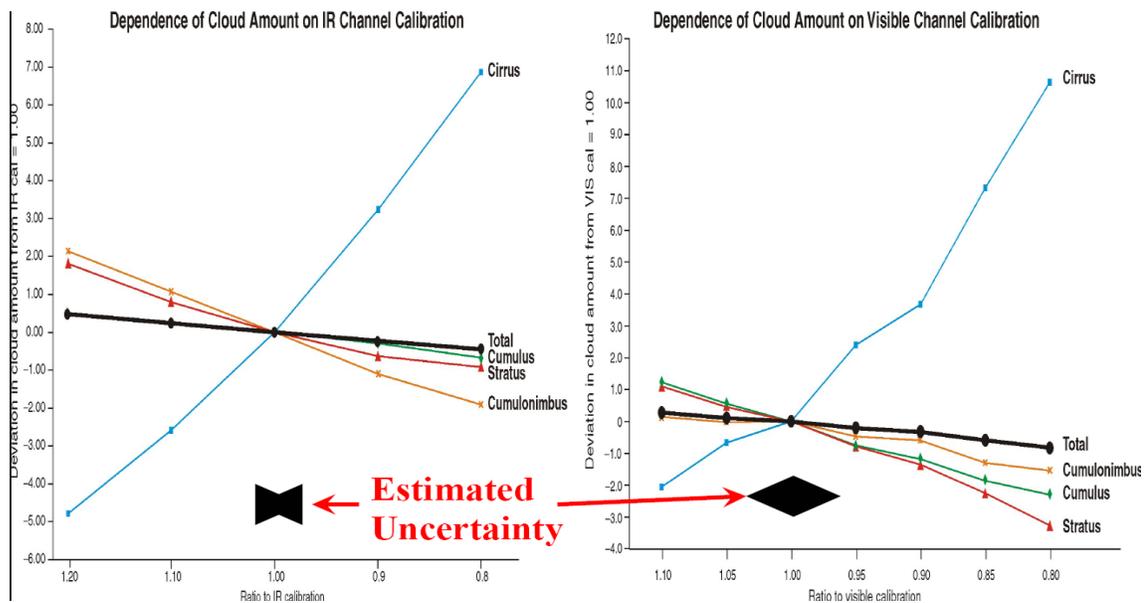
Figure 2.2: Calibration effect on CA and on cloud type CA caused by artificially changing the radiance calibrations separately for visible and infrared radiances and re-processing the data with all other factors being identical.

2.3 Effects of Geographic Coverage Changes

Since the value of CA and its variations are not uniform over the globe, any systematic variation of the spatial coverage in a data set can produce spurious changes of global mean CA. Figure 2.3 shows the time record of the monthly average fraction of the globe covered by the ISCCP data (as in Figure 2.2): the average coverage fraction is 0.92 ± 0.05. However, during the period from 1984–1986, the coverage was significantly lower. To test the effect of the missing data on the determination of global mean CA, we found the month with minimum coverage of 0.70 (August 1984) and another August with maximum coverage of 0.98 (August 1998) and re-calculated the global monthly mean CA for August 1998 after removing all of the same locations and times (at 3 hr intervals over the whole month) missing in August 1984. Although the standard deviation of geographical differences in CA is ±0.02, the global mean difference in CA is < 0.001. Apparently, the missing data is sufficiently randomly distributed in this case that the global mean CA is not affected. There is no systematic variation of the global coverage that can explain the variation in Figure 2.1.

A more specific version of this sampling problem would be caused by a change in the ratio of water and land pixel number over the data record because there is a systematic difference in CA between water

and land of about 0.15. Other systematic changes, such as in the number of samples over latitude or longitude, would produce similar effects. Figure 2.4 shows the time record of the ocean-land sampling ratio for ISCCP: the variation about the mean ratio of water to land over the record is about 5% with oceans slightly over-sampled before 1987 and slightly under-sampled afterwards. Except for the earlier reduced coverage, the variation of the ocean/land ratio is only about 2-3%. Given the average difference between ocean and land CA of 0.15, a change of 5% in the ratio translates into a high bias of < 0.01 before 1987 and a nearly constant low bias of < 0.005 afterwards. Although this effect contributes somewhat to but cannot cause the whole peak CA anomaly in 1986-1987, it is not a significant contribution after about 1990 because the bias is nearly constant.
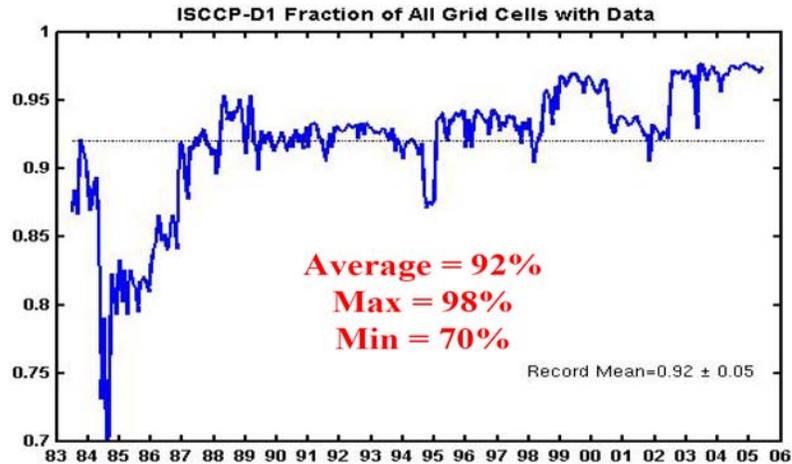
Figure 2.3: Time record of the monthly average fraction of the globe covered by the ISCCP data.
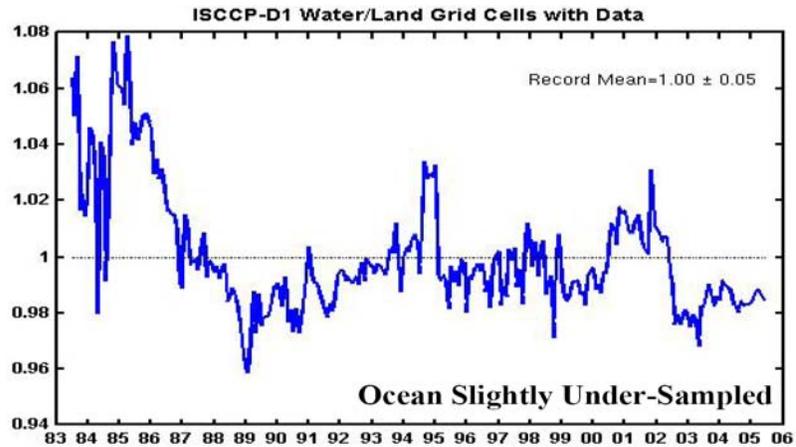
Figure 2.4: Time record of the ratio of monthly average fraction of ocean to land, covered by the ISCCP data.

2.4 Effects of Day-Night Coverage Changes

Like the effect of changing geographic coverage, systematic changes in the relative sample size between day and night would cause spurious changes in CA, both because there are systematic variations in CA with time of day and because there are algorithm differences between day and night. Figure 2.5 shows the time record of the ratio of day to night pixel number over the ISCCP record, indicating a small increase of the daytime pixel number relative to the nighttime pixel number by about 4% (the seasonal variation has to do with the changing polar illumination); this change is due almost entirely to a change in the number of daytime pixels associated with the advent of geostationary coverage of the Indian Ocean sector. Given that the systematic differences in day-night CA are < 0.10 (but of opposite sign over land and water), this change could only explain a CA increase < 0.005 (not a decrease as in Figure 2.1).

ISCCP-D1 Day/Night Grid Cells with Data

Record Mean=1.00 ± 0.02

"Daytime" Under-Sampled
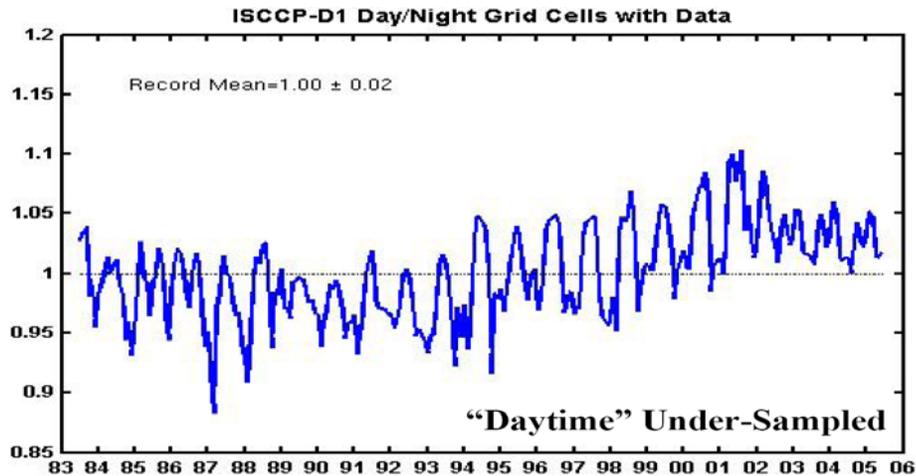
Figure 2.5: Time record of the ratio of day to night pixel number over the ISCCP record.

2.5 Effects of Satellite Viewing Geometry Changes

Evan et al. (2007) argue that the whole global mean CA variation signal shown in Figure 2.1 can be explained by systematic changes in the satellite viewing zenith angle over the ISCCP time record.

Rossow et al. (1993) already illustrated and quantified the zenith angle dependence of CA (ΔCA = 0.25 $\Delta\mu$, so $\Delta\mu < 0.3$ implies ΔCA < 0.08) and suggested that it was caused by a greater detection sensitivity to the presence of optically thin clouds at slant views compared with nadir views. The generally larger CA amounts found by CALIPSO than by ISCCP, documented in this report, support this interpretation. Figure 2.6 shows the time record of the average anomaly in $(1/\mu)$, where the globe is divided into regions with large anomaly (normalized standard deviation > 18%) and small anomaly: the latter regions should have spurious CA variations of no more than 0.00075, whereas the former regions could have spurious CA variations (peak to peak) of 0.015, based on the results in Rossow et al. (1993). Figure 2.7 shows the deseasonalized monthly CA anomalies for these same two regions: although specific CA anomaly features (spikes or sudden changes) appear in Figure 2.7a corresponding to the anomalies seen in $(1/\mu)$ in Figure 2.6a, slower CA anomaly variations occur (Figure 2.7b) in the regions where no variations in $(1/\mu)$ occur (Figure 2.6b). The CA variations in Figure 2.6b also resemble the original CA anomaly plot in Figure 2.1 but with a smaller amplitude by about one third. In other words, the variation of satellite viewing geometry cannot explain the CA variations over the portion of the globe (the majority) were the satellite viewing geometry is constant over the time record nor can it explain the whole magnitude of the CA variations even in regions of with larger $(1/\mu)$ variability. Moreover, the detailed shape of the time record of $(1/\mu)$ anomalies does not correspond to the shape of the CA anomaly time record as is required if changes in $(1/\mu)$ are to explain the changes in global mean CA.

130
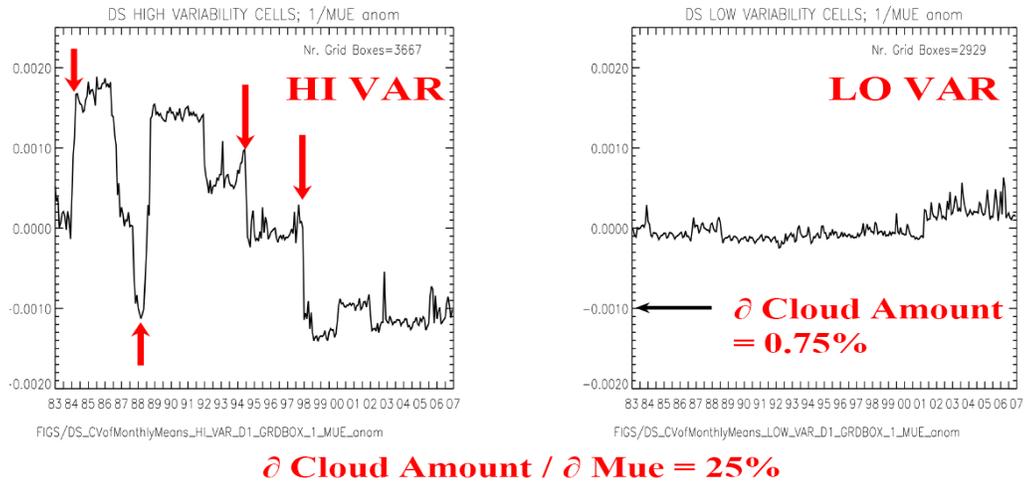
Figure 2.6: Time record of the average anomaly in (1/μ), where the globe is divided into regions with large anomaly (normalized standard deviation > 18%) and small anomaly.

Figure 2.7: Deseasonalized monthly CA anomalies for same two regions as in Figure 2.5.

2.6 Conclusions

A number of factors that might cause spurious changes in ISCCP global monthly mean total CA have been investigated: the most that can be said now is that the slow variation of global CA shown in Figure 2.1 may be somewhat exaggerated in magnitude, especially the peak values in the late 1980s, but that this variation cannot be dismissed as completely spurious. None of the hypothetical causes of spurious total CA changes is large enough to explain this variation. This conclusion is also supported indirectly by the fact that the anomalies in top-of-atmosphere radiative fluxes, calculated based on the ISCCP cloud properties, are in excellent quantitative agreement with those determined from the long-term ERBS instrument record (Zhang et al., 2004; Norris 2005). Moreover, given the stability of the ISCCP radiance calibrations, the variations of cloud types also appear to be reliable for changes larger than about 0.01-0.02.

3. Additional Analysis Figures

These additional figures may be of interest to the reader to explore more in detail differences between the data sets, essentially by the display of geographical maps.

Figures 3.1 – 3.10 present geographical maps of annual average cloud properties as determined by ISCCP and of differences between ISCCP and the other cloud data sets. These are climatological averages over the specific periods of the different data sets

Figures 3.11 – 3.17 present regional variations relative to global annual mean cloud property, determined for the same data sets.

Figures 3.18 – 3.20 present geographical maps of annual average cloud property differences between day and night in 2007, determined for data sets which include measurements at about 1h30 PM and 1h30 AM local time.

Figures 3.21 – 3.23 present geographical maps of interannual variabilities of selected cloud properties inferred from ISCCP and compared to the other data sets.

Seasonal variations of selected cloud properties are displayed separately over ocean and over land as well as over specific regions in Figures 3.24 – 3.25.

To explore the two-dimensional histograms of COD and CP, as defined for ISCCP, the two-dimensional normalized frequency distributions presented in Figure 3.27 show how the clouds are distributed in the atmosphere. This type of histogram has been valuable for climate model evaluation.
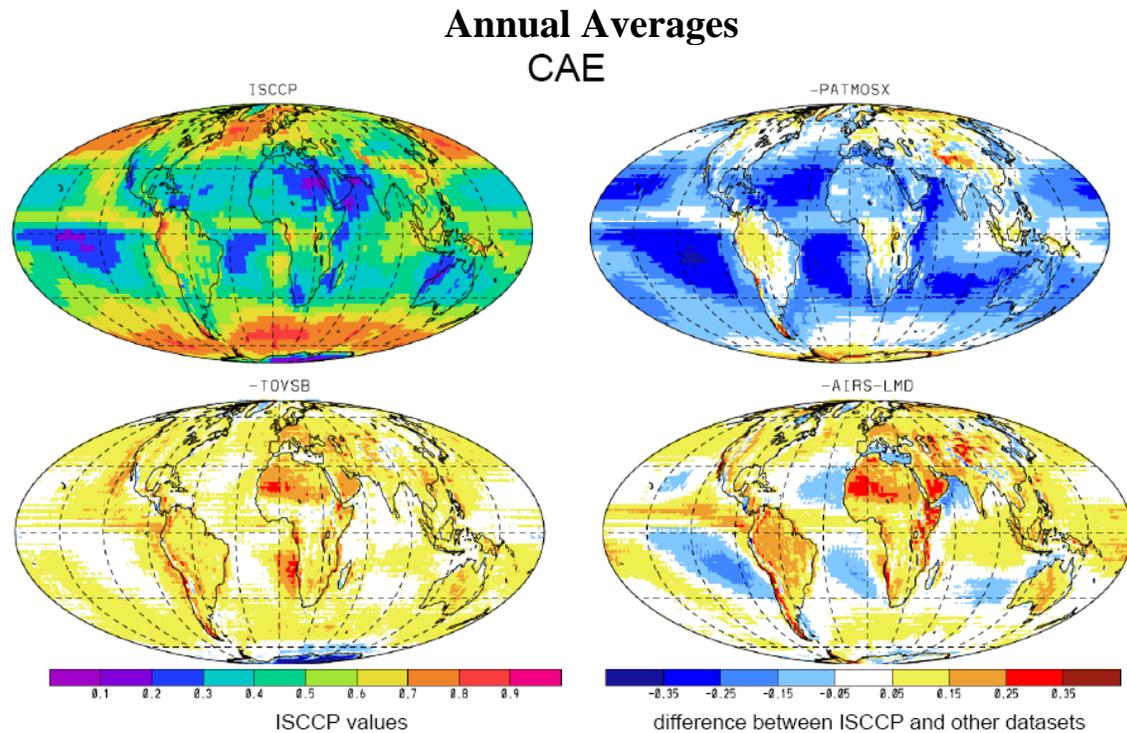
Figure 3.1: Geographical map of annual average of effective cloud amount (CAE) from ISCCP as well as geographical maps of CAE differences between ISCCP and PATMOSX, HIRS, TOVSB and AIRS-LMD.
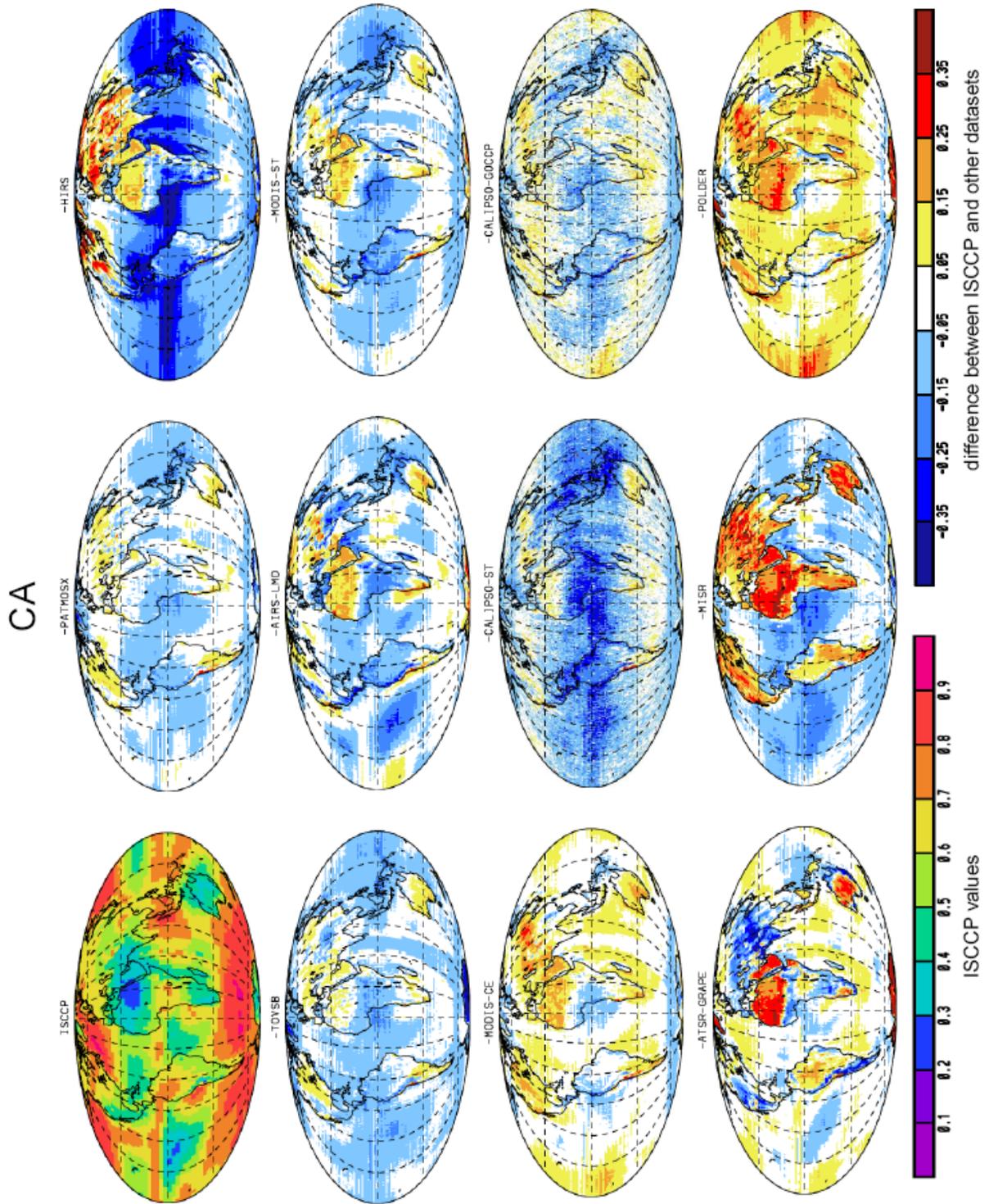
Figure 3.2: Geographical map of annual average of cloud amount (CA) from ISCCP as well as geographical maps of CA differences between ISCCP and PATMOSX, HIRS, TOVSB, AIRS-LMD, MODIS-ST, MODIS-CE, CALIPSO-ST, CALIPSO-GOCCP, ATSR-GRAPE, MISR and POLDER.
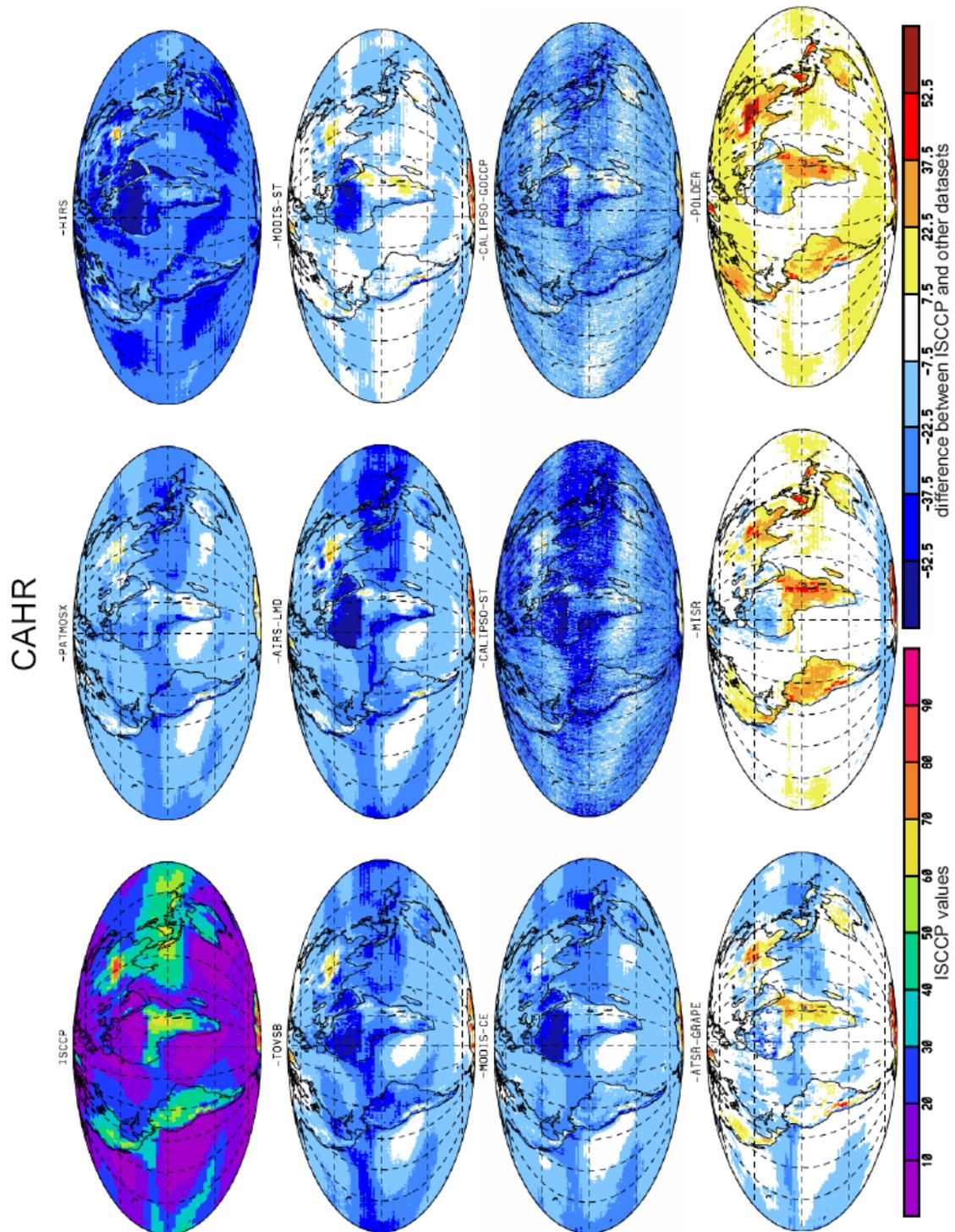
Figure 3.3: Geographical map of annual average of high-level cloud amount relative to total cloud amount (CAHR) from ISCCP as well as geographical maps of CAHR differences between ISCCP and PATMOSX, HIRS, TOVSB, AIRS-LMD, MODIS-ST, MODIS-CE, CALIPSO-ST, CALIPSO-GOCCP, ATSR-GRAPE, MISR and POLDER.
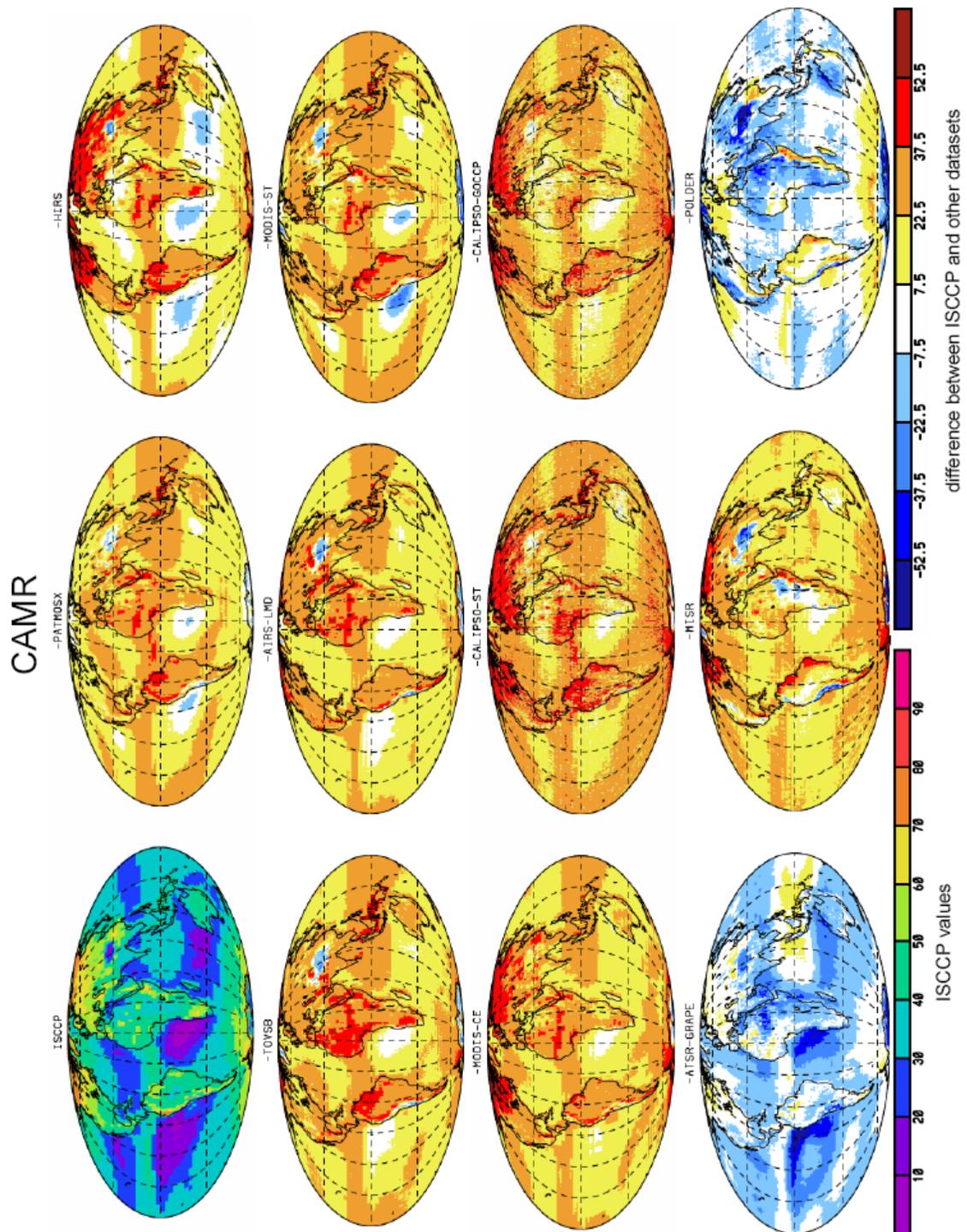
Figure 3.4: Geographical map of annual average of mid-level cloud amount relative to total cloud amount (CAMR) from ISCCP as well as geographical maps of CAMR differences between ISCCP and PATMOSX, HIRS, TOVSB, AIRS-LMD, MODIS-ST, MODIS-CE, CALIPSO-ST, CALIPSO-GOCCP, ATSR-GRAPE, MISR and POLDER.
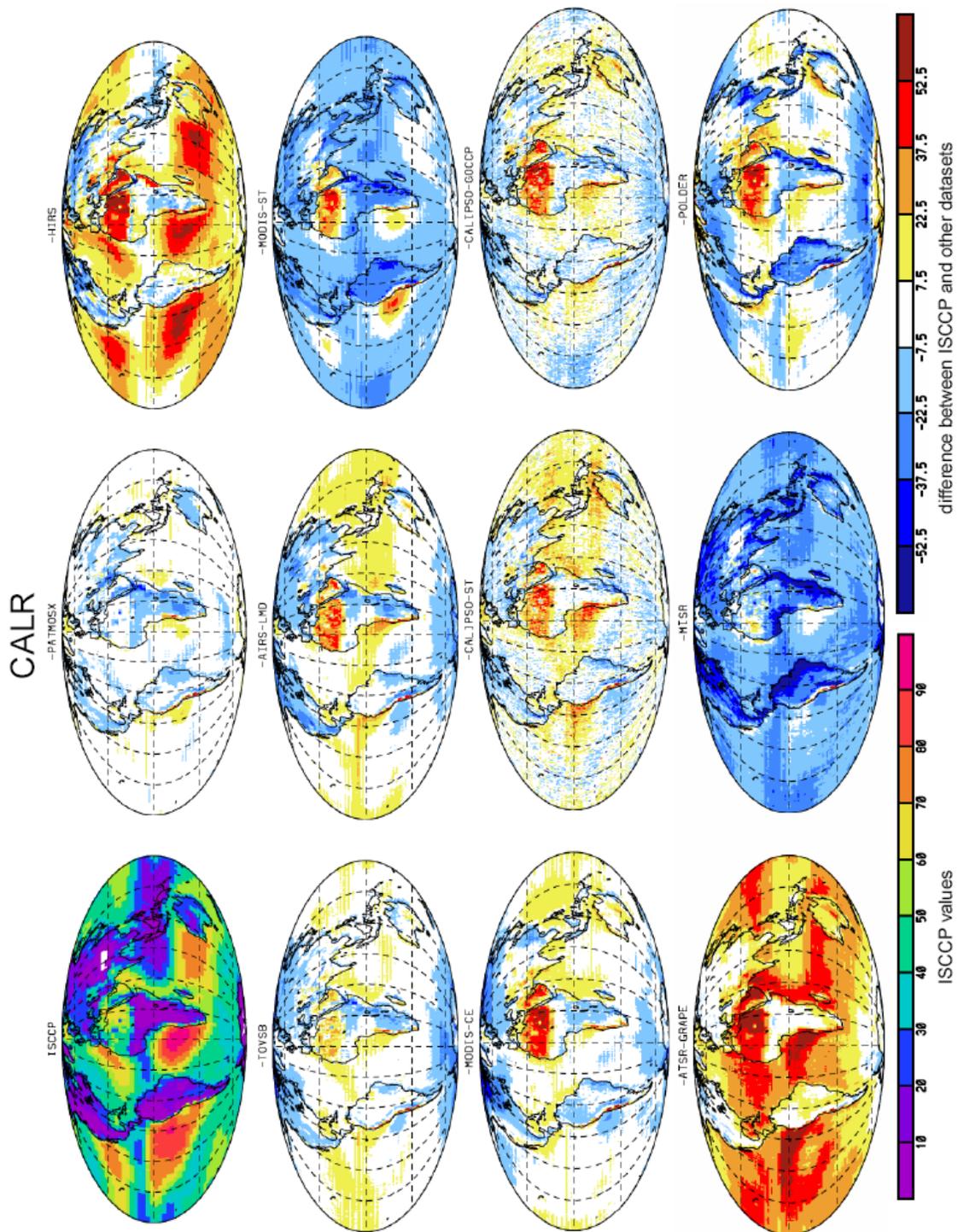
Figure 3.5: Geographical map of annual average of low-level cloud amount relative to total cloud amount (CALR) from ISCCP as well as geographical maps of CALR differences between ISCCP and PATMOSX, HIRS, TOVSB, AIRS-LMD, MODIS-ST, MODIS-CE, CALIPSO-ST, CALIPSO-GOCCP, ATSR-GRAPE, MISR and POLDER.

COD
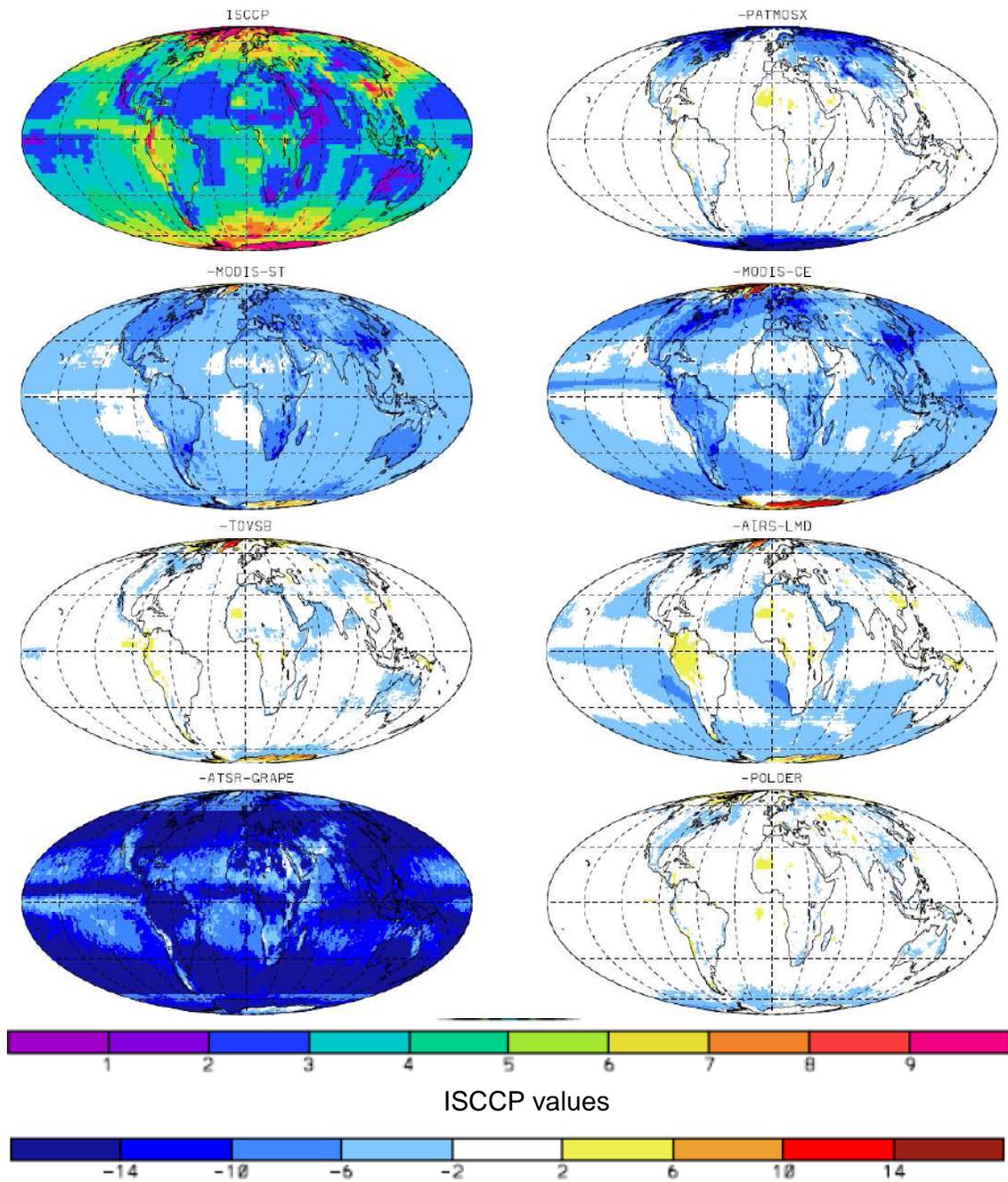
Figure 3.6: Geographical map of annual average of cloud optical depth (COD) from ISCCP as well as maps of COD differences between ISCCP and PATMOSX, MODIS-ST, MODIS-CE, TOVS Path-B, AIRS-LMD, ATSR-GRAPE and POLDER.
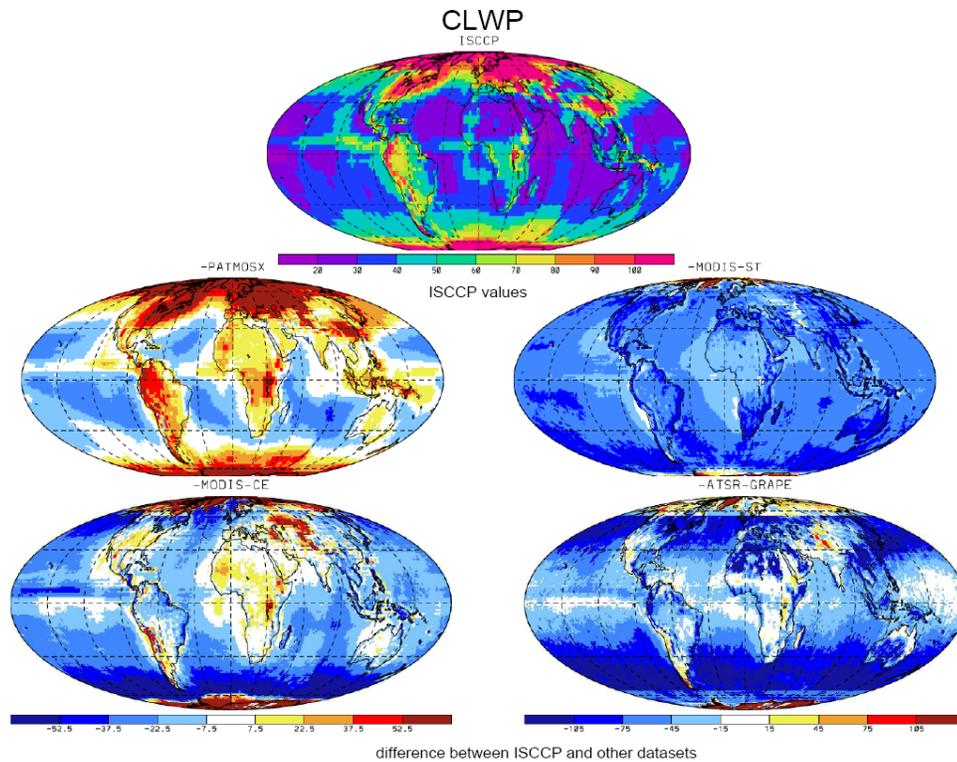
Figure 3.7: Geographical map of annual average of cloud liquid water path (CLWP) from ISCCP as well as maps of CLWP differences between ISCCP and PATMOSX, MODIS-ST, MODIS-CE and ATSR-GRAPE.
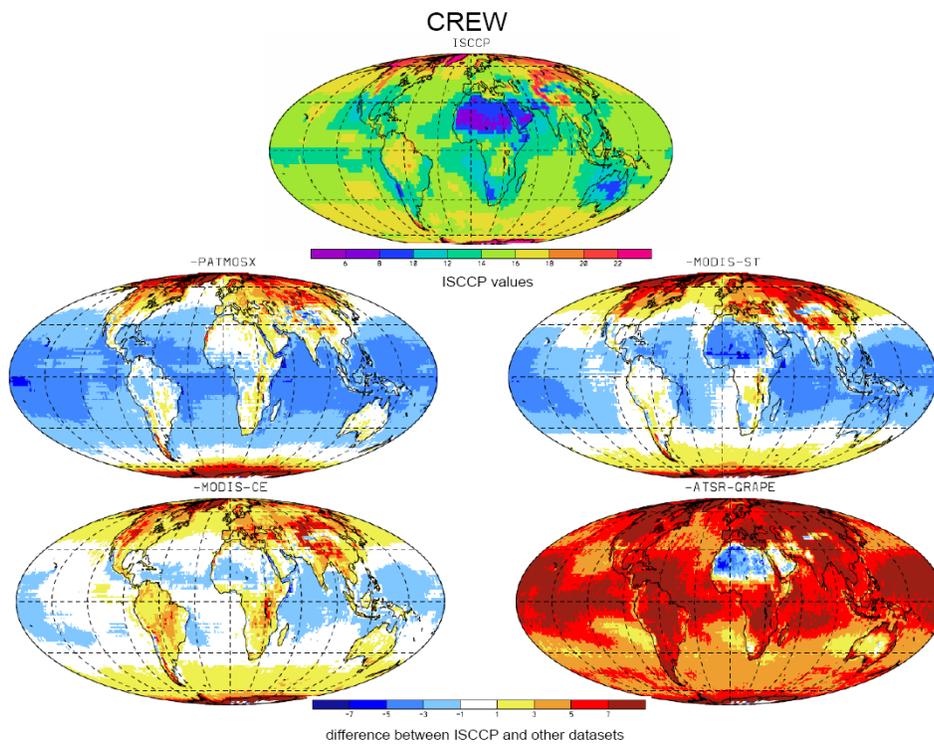
Figure 3.8: Geographical map of annual average of effective droplet radius (CREW) from ISCCP as well as maps of CREW differences between ISCCP and PATMOSX, MODIS-ST, MODIS-CE and ATSR-GRAPE.
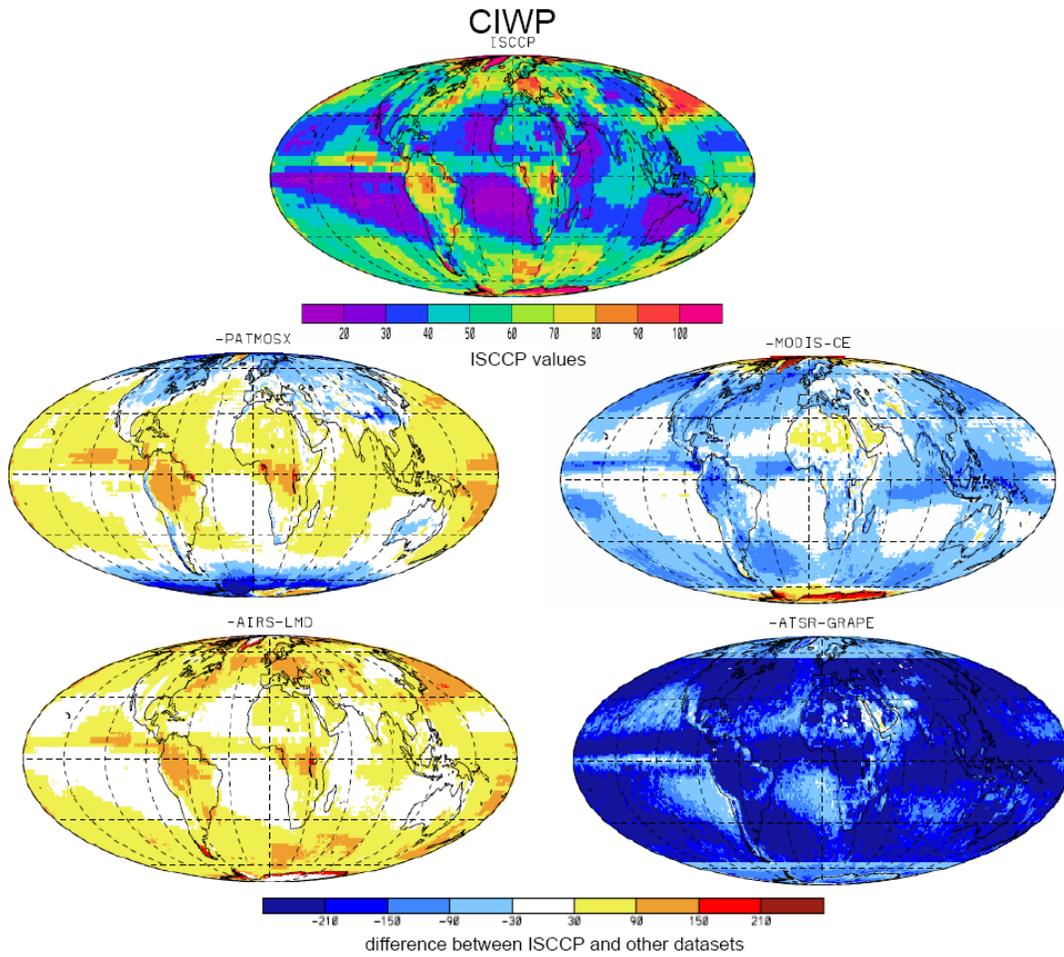
Figure 3.9: Geographical map of annual average of cloud ice water path (CIWP) from ISCCP as well as maps of CIWP differences between ISCCP and PATMOSX, MODIS-CE, AIRS-LMD and ATSR-GRAPE.
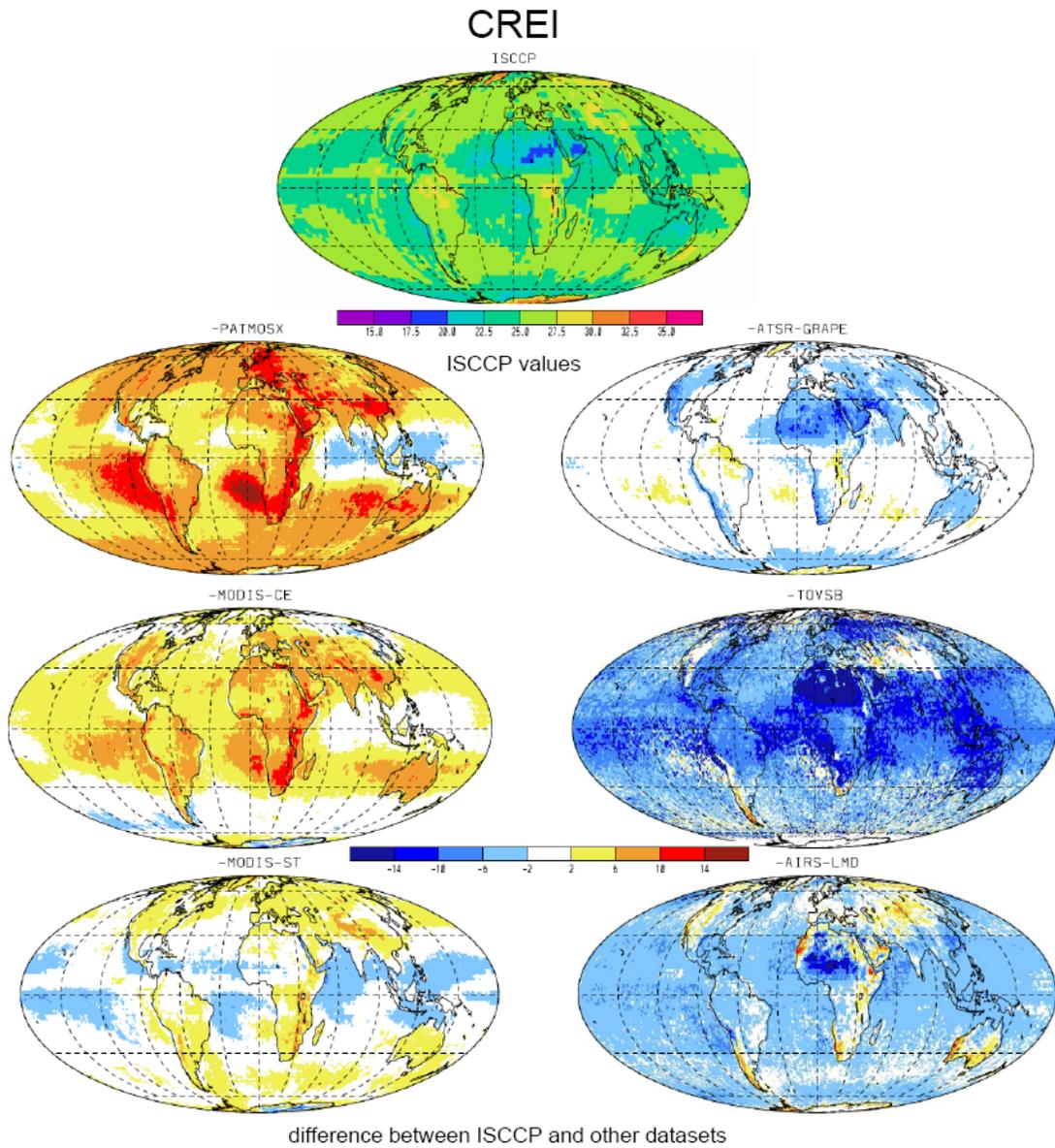
Figure 3.10: Geographical map of annual average of effective ice crystal radius (CREI) from ISCCP as well as maps of CREI differences between ISCCP and PATMOSX, ATSR-GRAPE, MODIS-CE, TOVS Path-B, MODIS-ST and AIRS-LMD.

Regional CA Variations Relative to Global Annual Mean CA
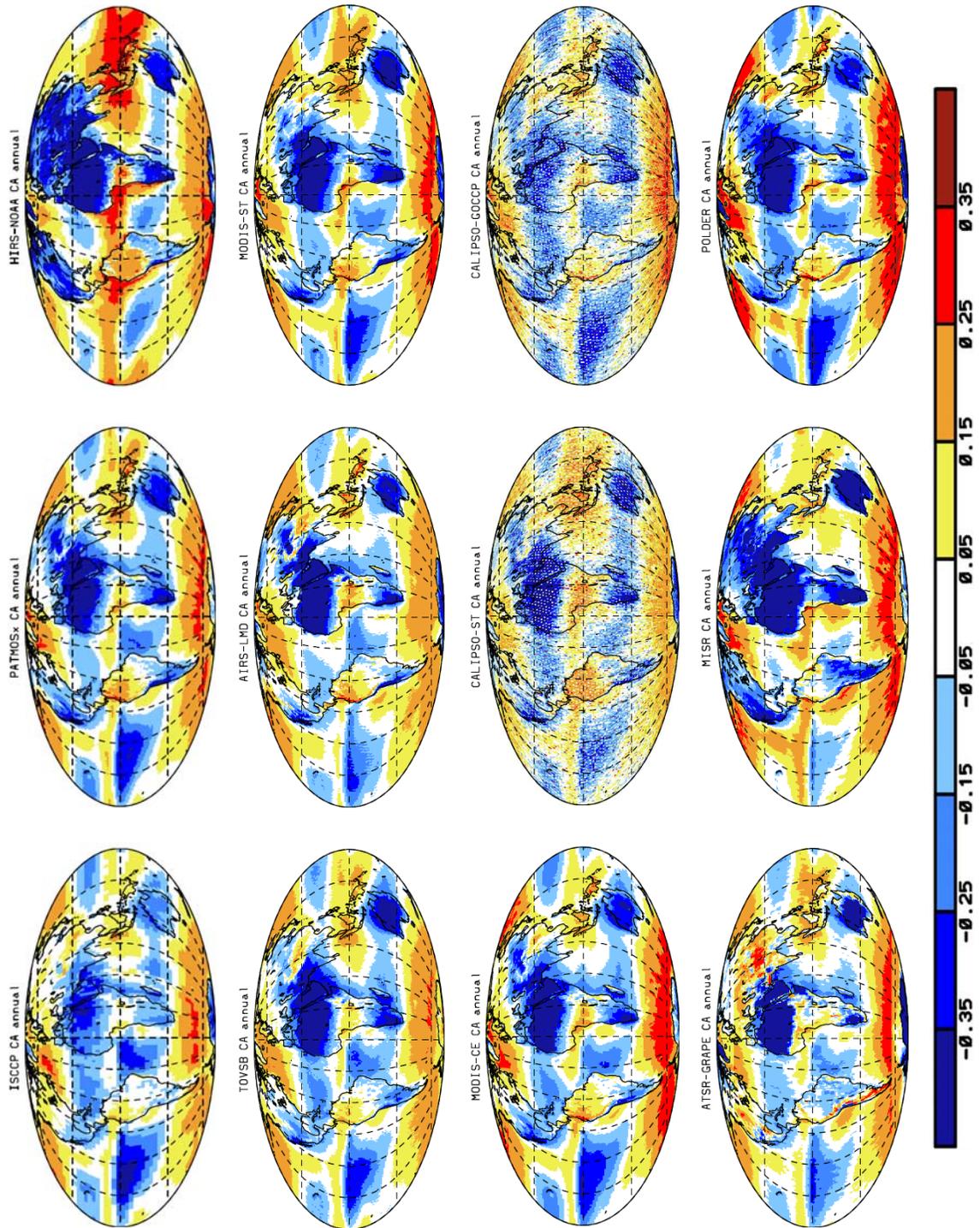
Figure 3.11: Regional variations of CA relative to global annual mean CA as determined by ISCCP, PATMOSx, HIRS-NOAA, TOVS PathB, AIRS-LMD, MODIS-ST, MODIS-CE, CALIPSO-ST, CALIPSO-GOCCP, ATSR-GRAPE, MISR and POLDER. Statistics are averaged over measurements at 1:30 – 3:00 PM, except ATSR-GRAPE and MISR (10:00 AM).

Regional CAHR Variations Relative to Global Annual Mean CAHR
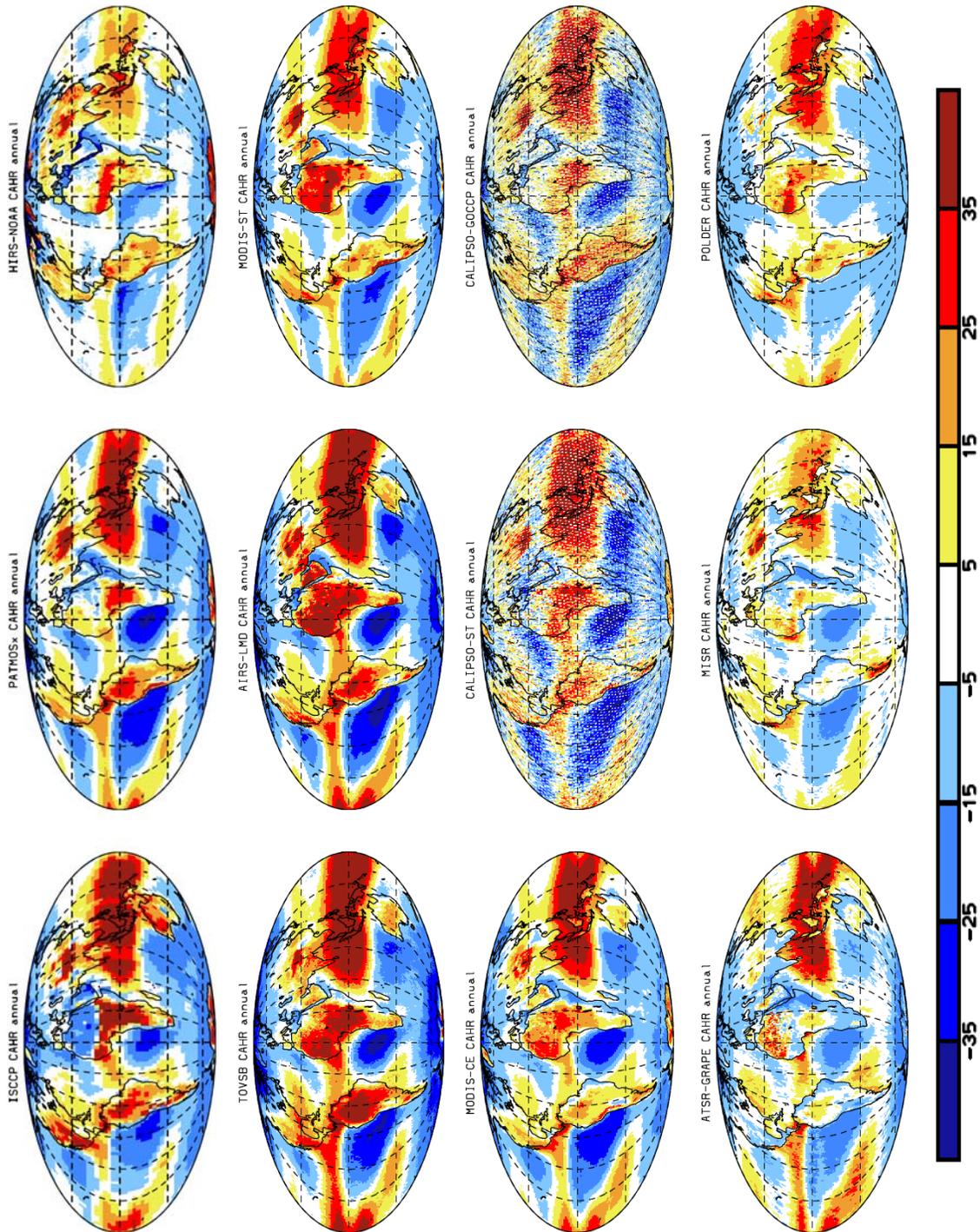
Figure 3.12: Regional variations of CAHR relative to global annual mean CAHR as determined by ISCCP, PATMOSx, HIRS-NOAA, TOVS PathB, AIRS-LMD, MODIS-ST, MODIS-CE, CALIPSO-ST, CALIPSO-GOCCP, ATSR-GRAPE, MISR and POLDER. Statistics are averaged over measurements at 1:30 – 3:00 PM, except ATSR-GRAPE and MISR (10:00 AM).

Regional CAMR Variations Relative to Global Annual Mean CAMR
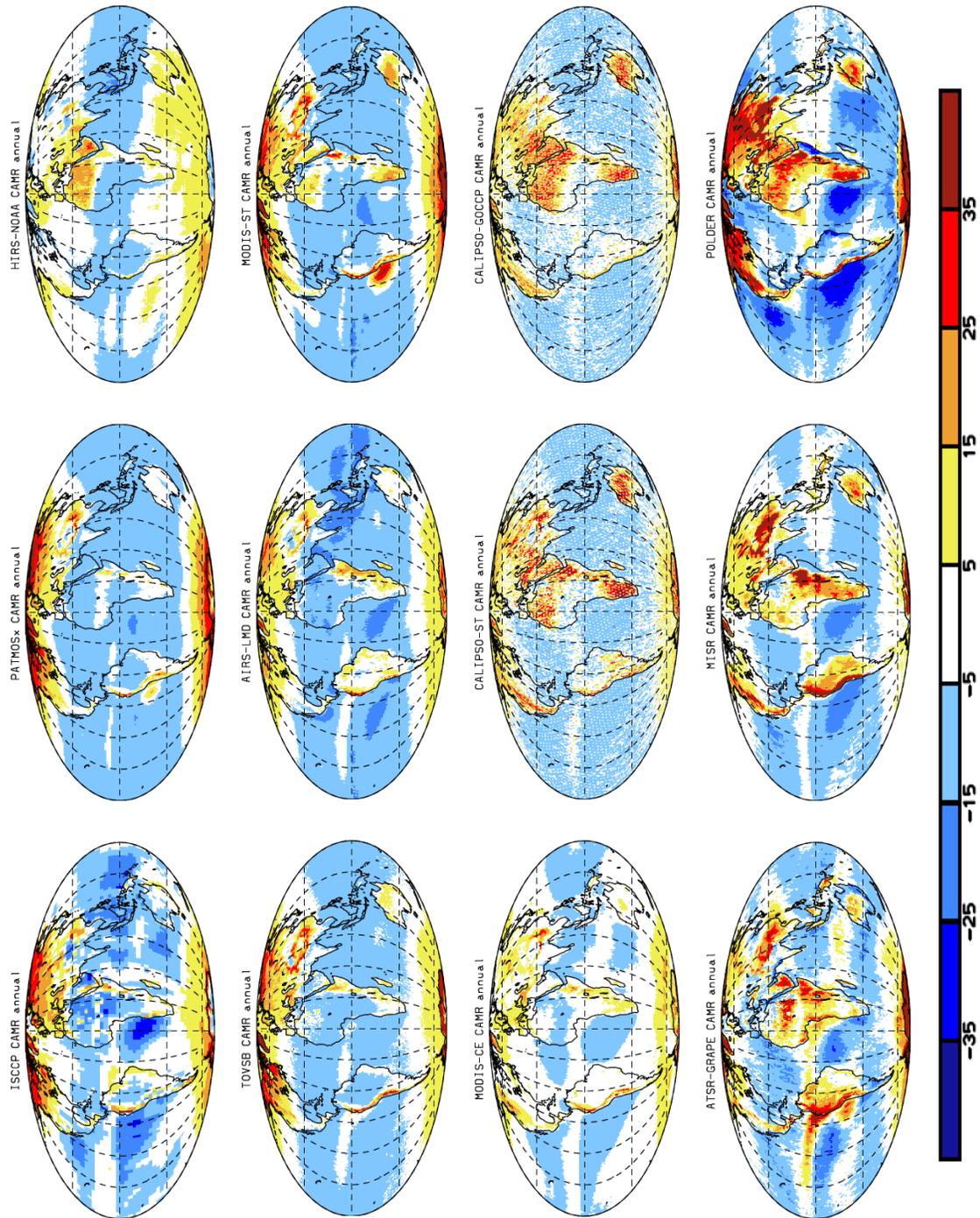
Figure 3.13: Regional variations of CAMR relative to global annual mean CAMR as determined by ISCCP, PATMOSx, HIRS-NOAA, TOVS PathB, AIRS-LMD, MODIS-ST, MODIS-CE, CALIPSO-ST, CALIPSO-GOCCP, ATSR-GRAPE, MISR and POLDER. Statistics are averaged over measurements at 1:30 – 3:00 PM, except ATSR-GRAPE and MISR (10:00 AM).

Regional CALR Variations Relative to Global Annual Mean CALR
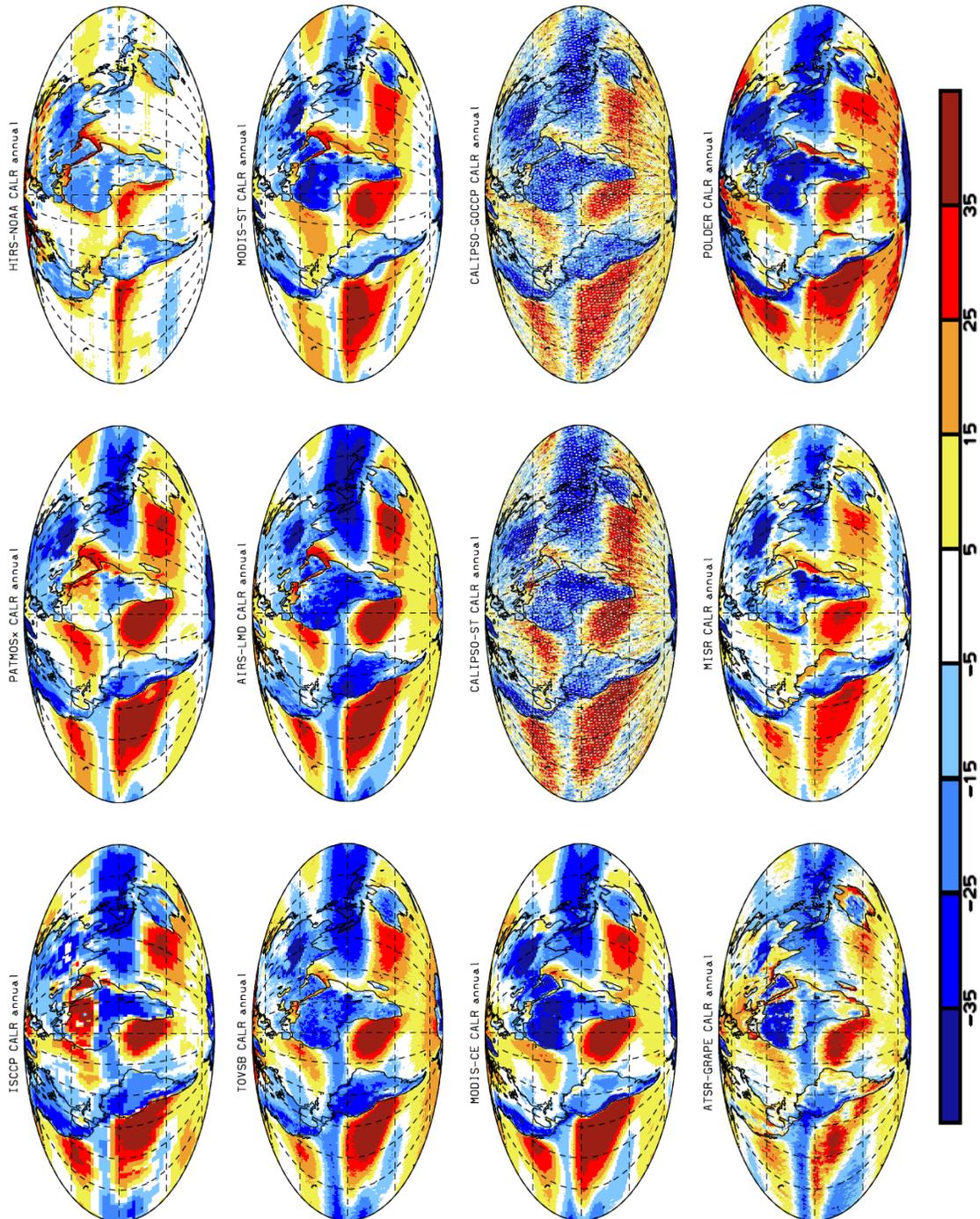
Figure 3.14: Regional variations of CALR relative to global annual mean CALR as determined by ISCCP, PATMOSx, HIRS-NOAA, TOVS PathB, AIRS-LMD, MODIS-ST, MODIS-CE, CALIPSO-ST, CALIPSO-GOCCP, ATSR-GRAPE, MISR and POLDER. Statistics are averaged over measurements at 1:30 – 3:00 PM, except ATSR-GRAPE and MISR (10:00 AM).

Regional CEM Variations Relative to Global Annual Mean CEM
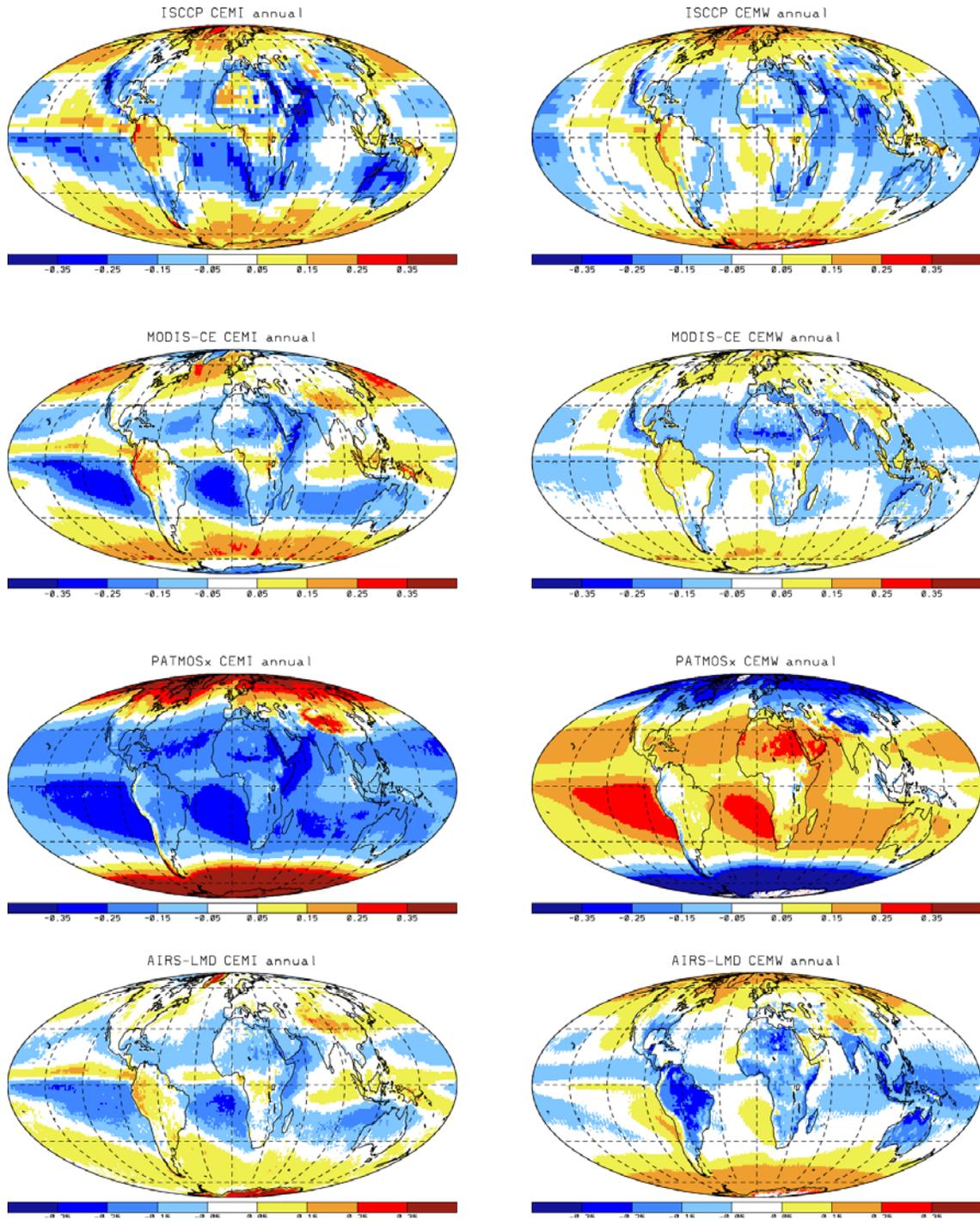
Figure 3.15: Regional variations of CALR relative to global annual mean CALR as determined by ISCCP, PATMOSx, HIRS-NOAA, TOVS PathB, AIRS-LMD, MODIS-ST, MODIS-CE, CALIPSO-ST, CALIPSO-GOCCP, ATSR-GRAPE, MISR and POLDER. Statistics are averaged over measurements at 1:30 – 3:00 PM, except ATSR-GRAPE and MISR (10:00 AM).

Regional CWP Variations Relative to Global Annual Mean CWP
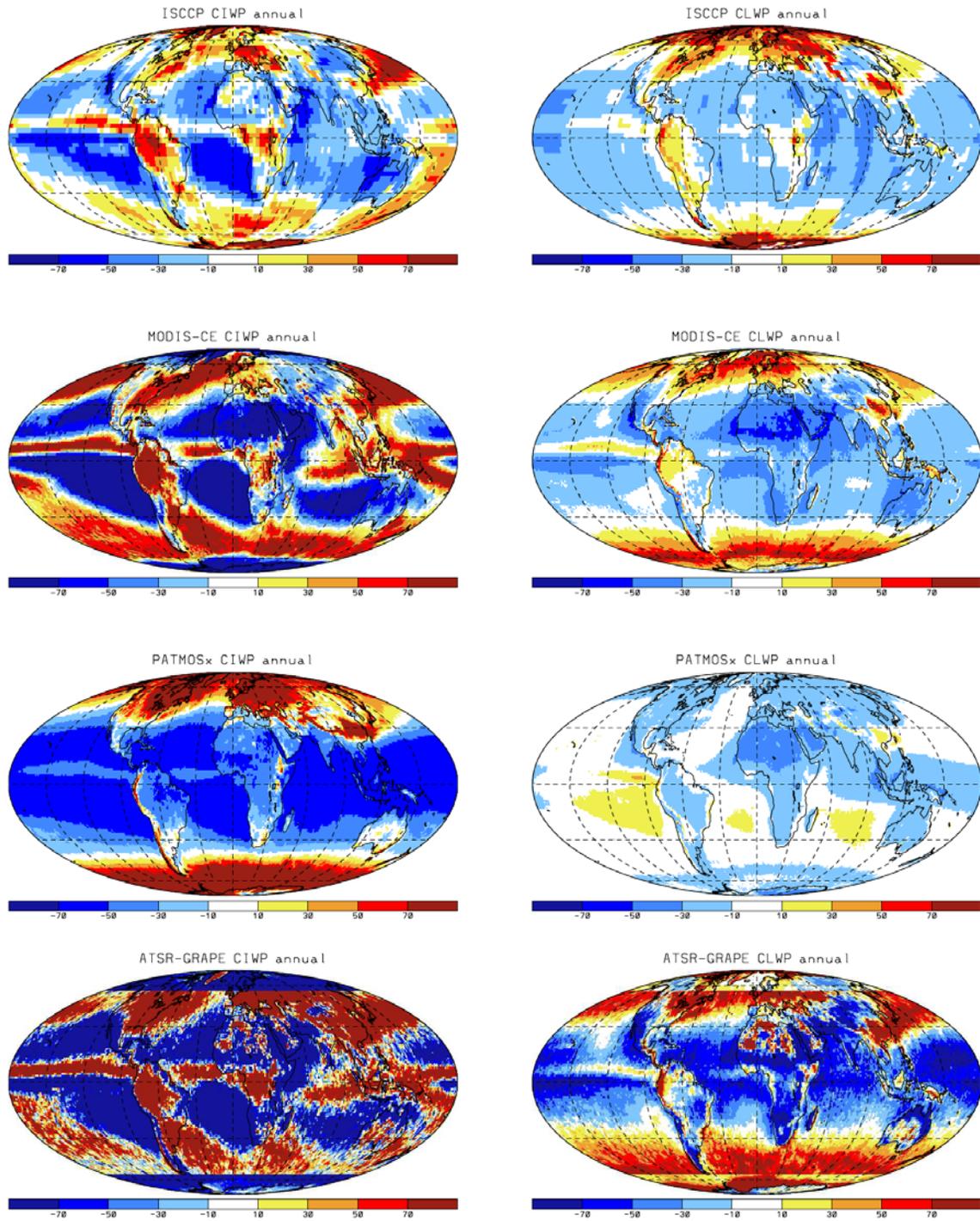
Figure 3.16: Regional variations of CALR relative to global annual mean CALR as determined by ISCCP, PATMOSx, HIRS-NOAA, TOVS PathB, AIRS-LMD, MODIS-ST, MODIS-CE, CALIPSO-ST, CALIPSO-GOCCP, ATSR-GRAPE, MISR and POLDER. Statistics are averaged over measurements at 1:30 – 3:00 PM, except ATSR-GRAPE and MISR (10:00 AM).

Regional CRE Variations Relative to Global Annual Mean CRE
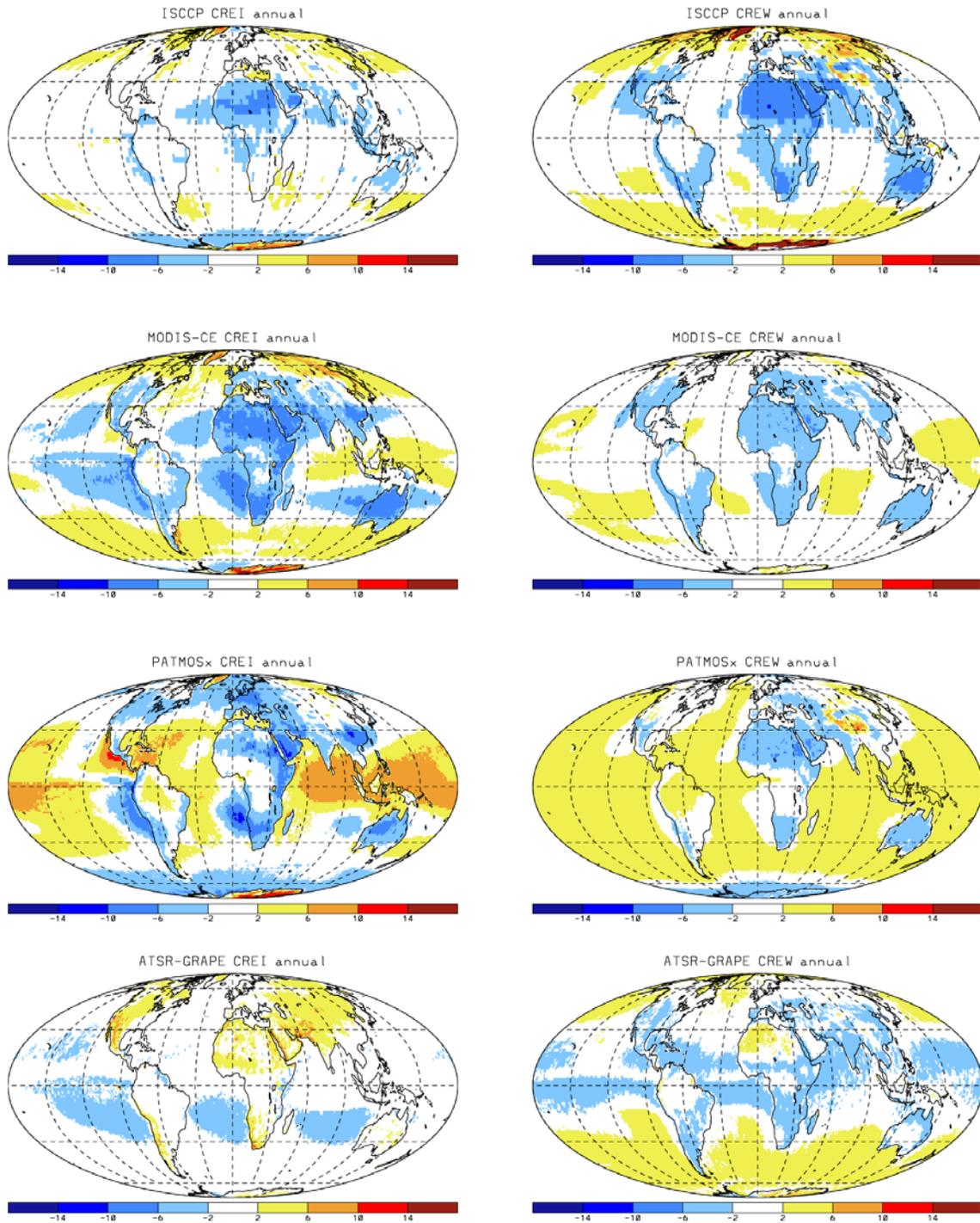
Figure 3.17: Regional variations of CALR relative to global annual mean CALR as determined by ISCCP, PATMOSx, HIRS-NOAA, TOVS PathB, AIRS-LMD, MODIS-ST, MODIS-CE, CALIPSO-ST, CALIPSO-GOCCP, ATSR-GRAPE, MISR and POLDER. Statistics are averaged over measurements at 1:30 – 3:00 PM, except ATSR-GRAPE and MISR (10:00 AM).

Day – Night Differences
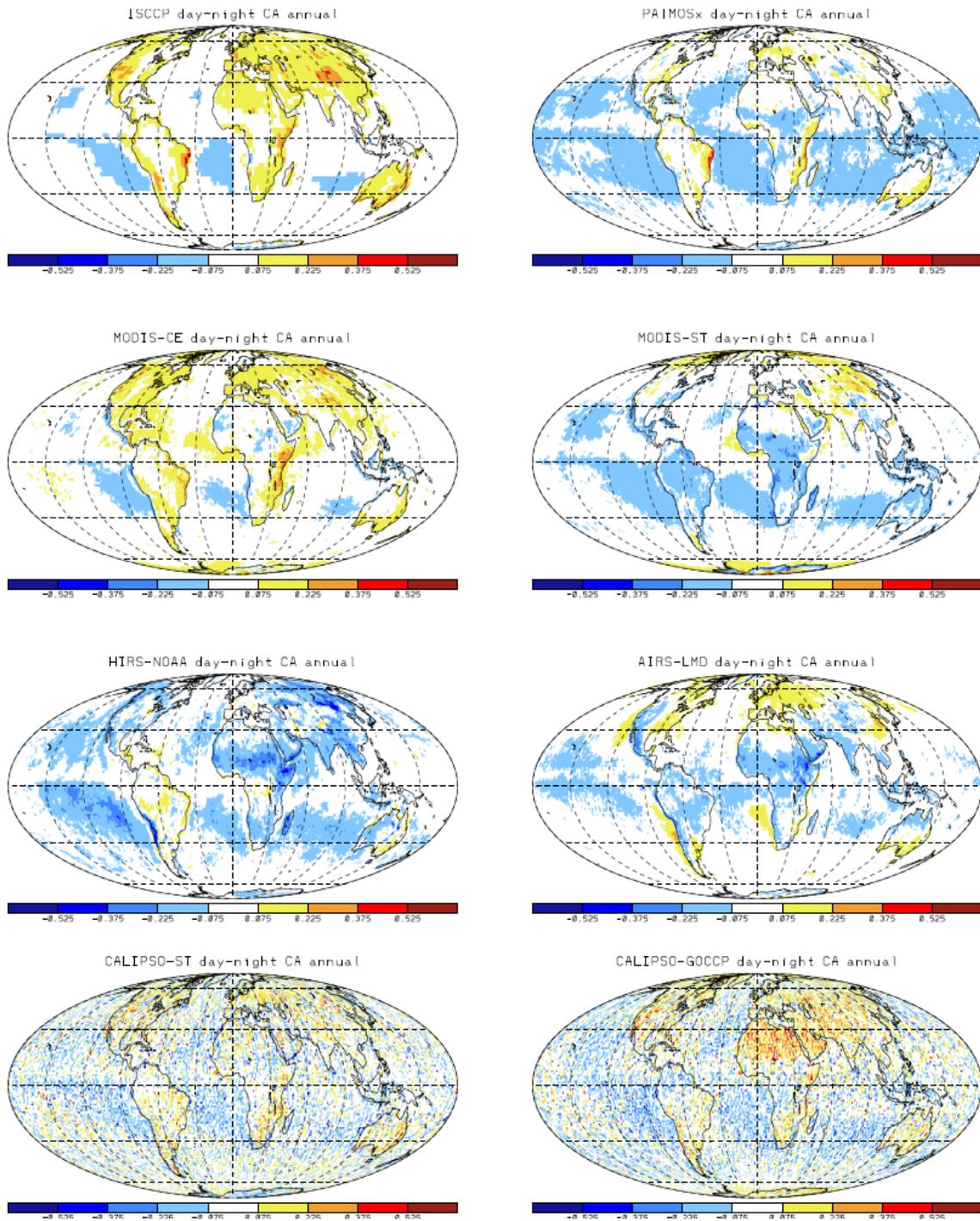
Figure 3.18: Geographical map of annual average CA differences between day (1:30 PM) and night (1:30 AM) for ISCCP, PATMOSX, MODIS-CE, MODIS-ST, HIRS-NOAA, AIRS-LMD, CALIPSO-ST and CALIPSO-GOCCP. Statistics in 2007.
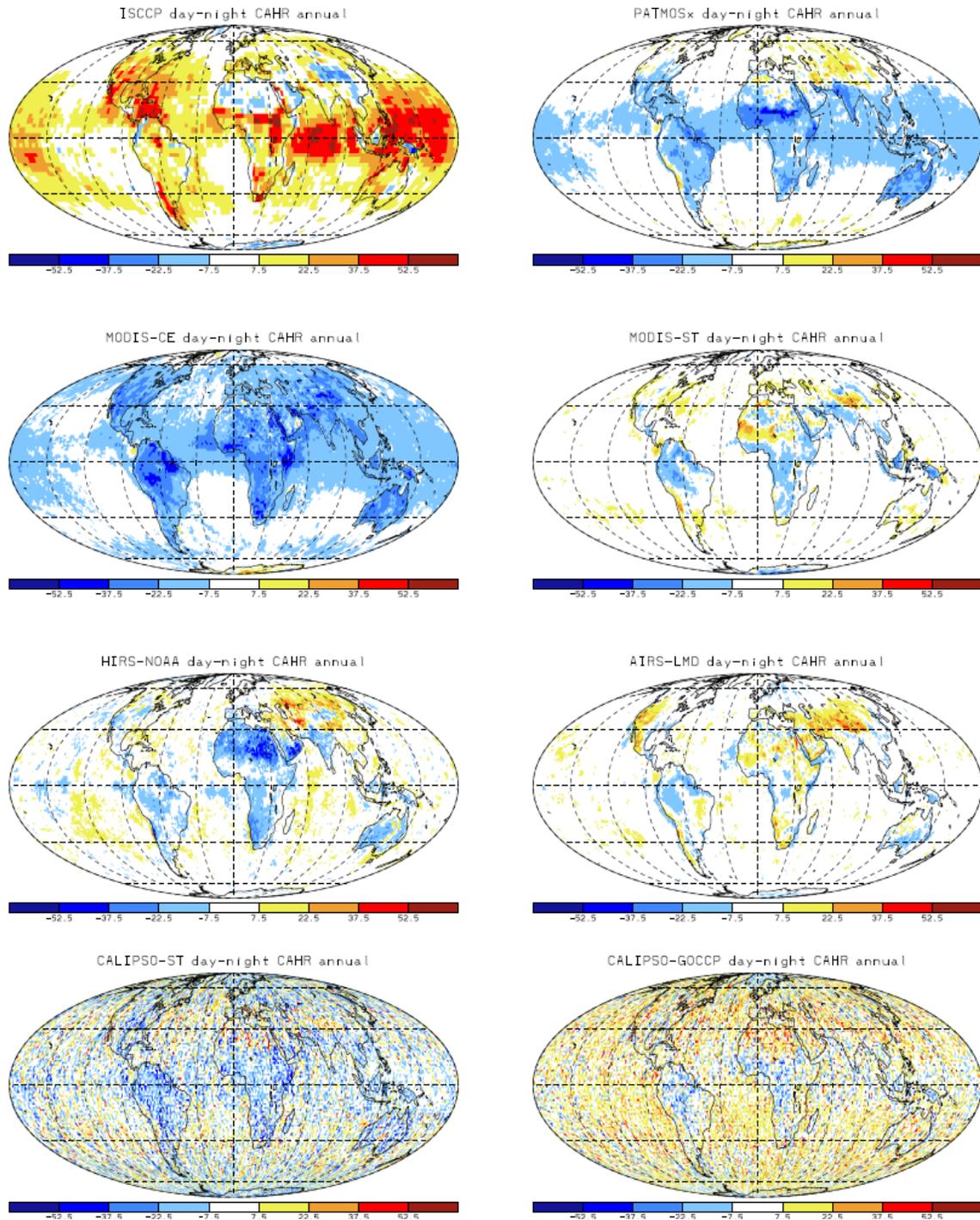
Figure 3.19: Geographical map of annual average CAHR differences between day (1:30 PM) and night (1:30 AM) for ISCCP, PATMOSX, MODIS-CE, MODIS-ST, HIRS-NOAA, AIRS-LMD, CALIPSO-ST and CALIPSO-GOCCP. Statistics in 2007.
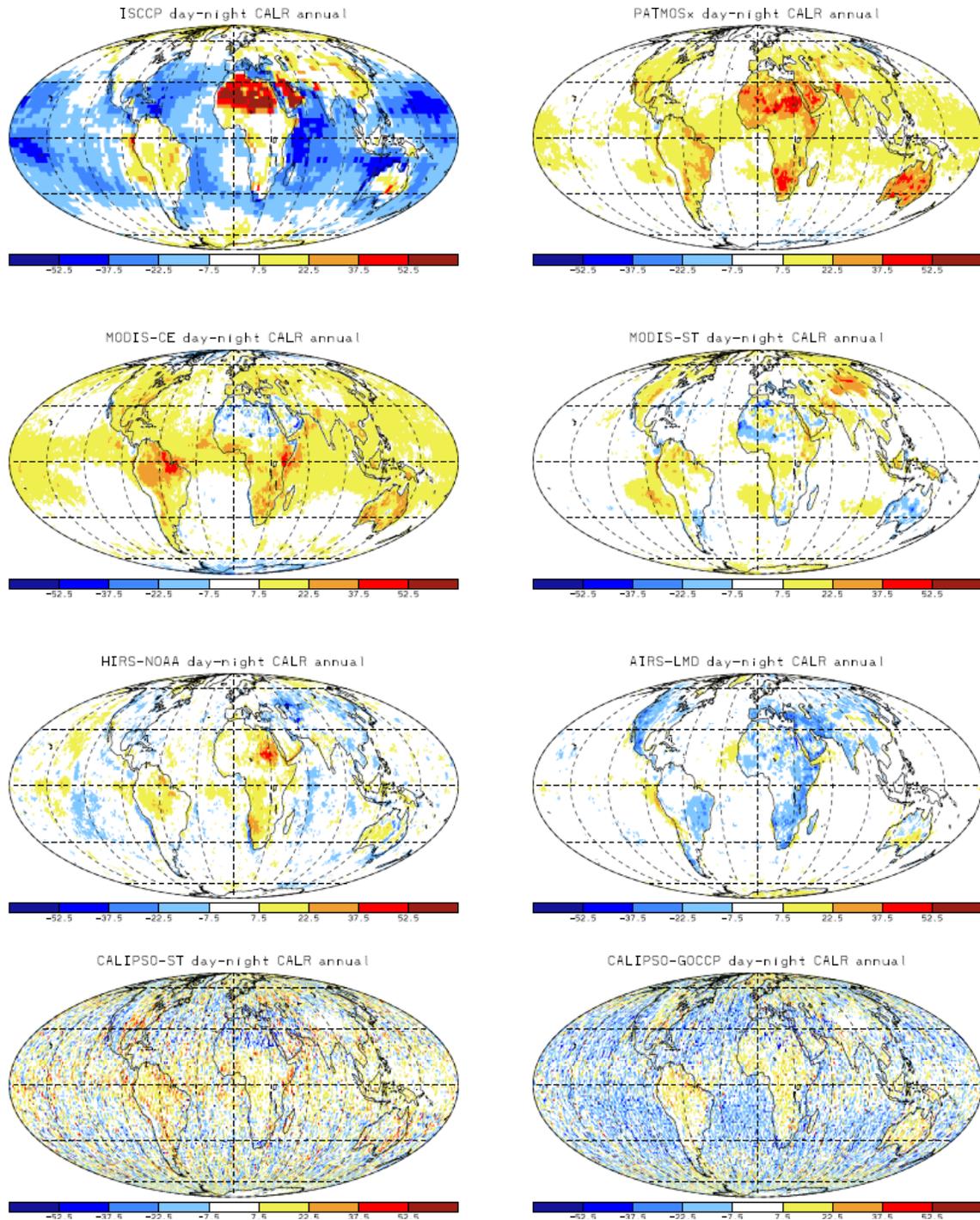
Figure 3.20: Geographical map of annual average CALR differences between day (1:30 PM) and night (1:30 AM) for ISCCP, PATMOSX, MODIS-CE, MODIS-ST, HIRS-NOAA, AIRS-LMD, CALIPSO-ST and CALIPSO-GOCCP. Statistics in 2007.

Interannual variability of CAHR
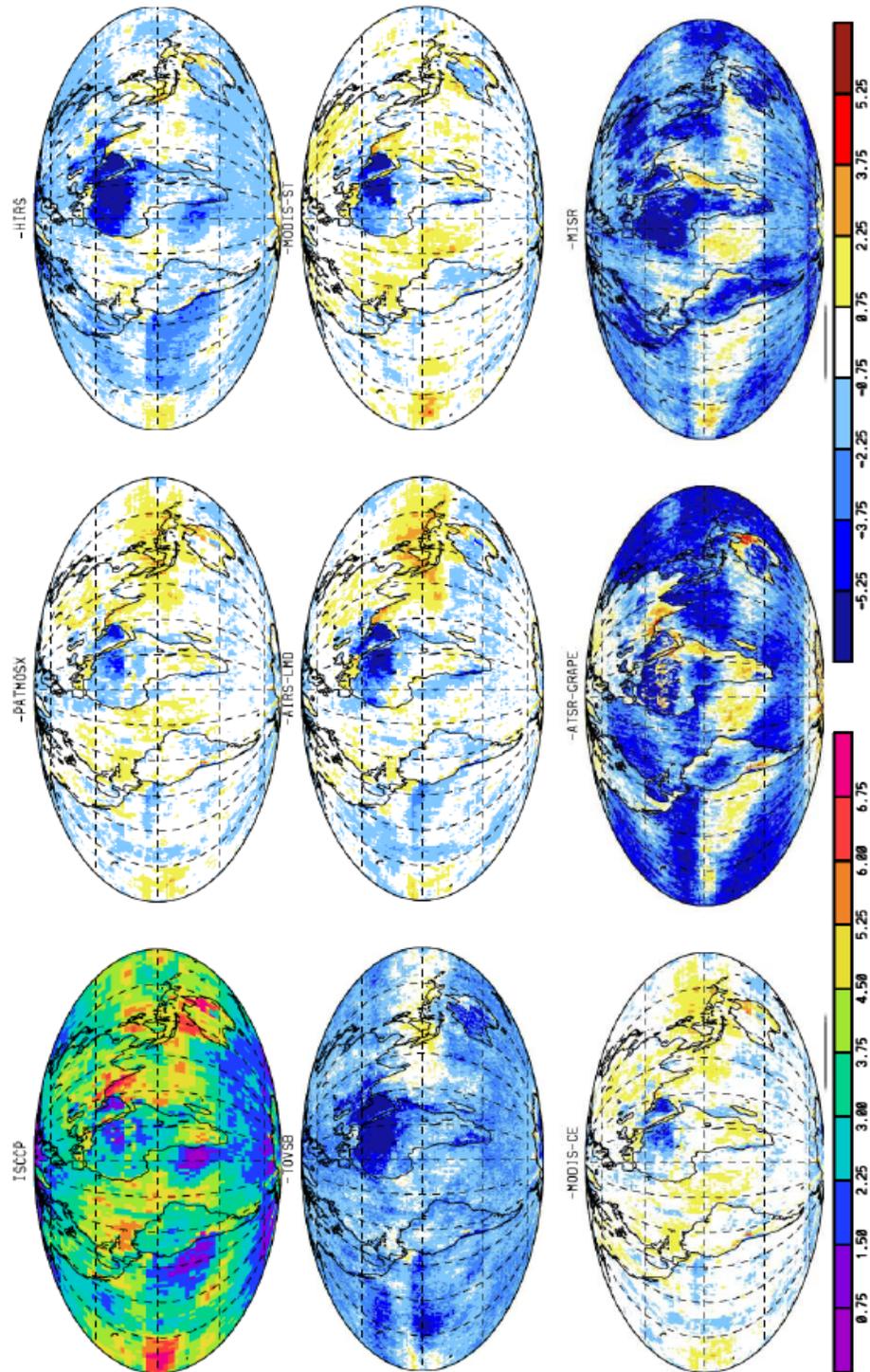
Figure 3.21: Geographical map of interannual variability inf CAHR from ISCCP as well as geographical maps of interannual CAHR variability differences between ISCCP and PATMOSX, HIRS, TOVSB, AIRS-LMD, MODIS-ST, MODIS-CE, ATSR-GRAPE and MISR.

Interannual variability of CALR
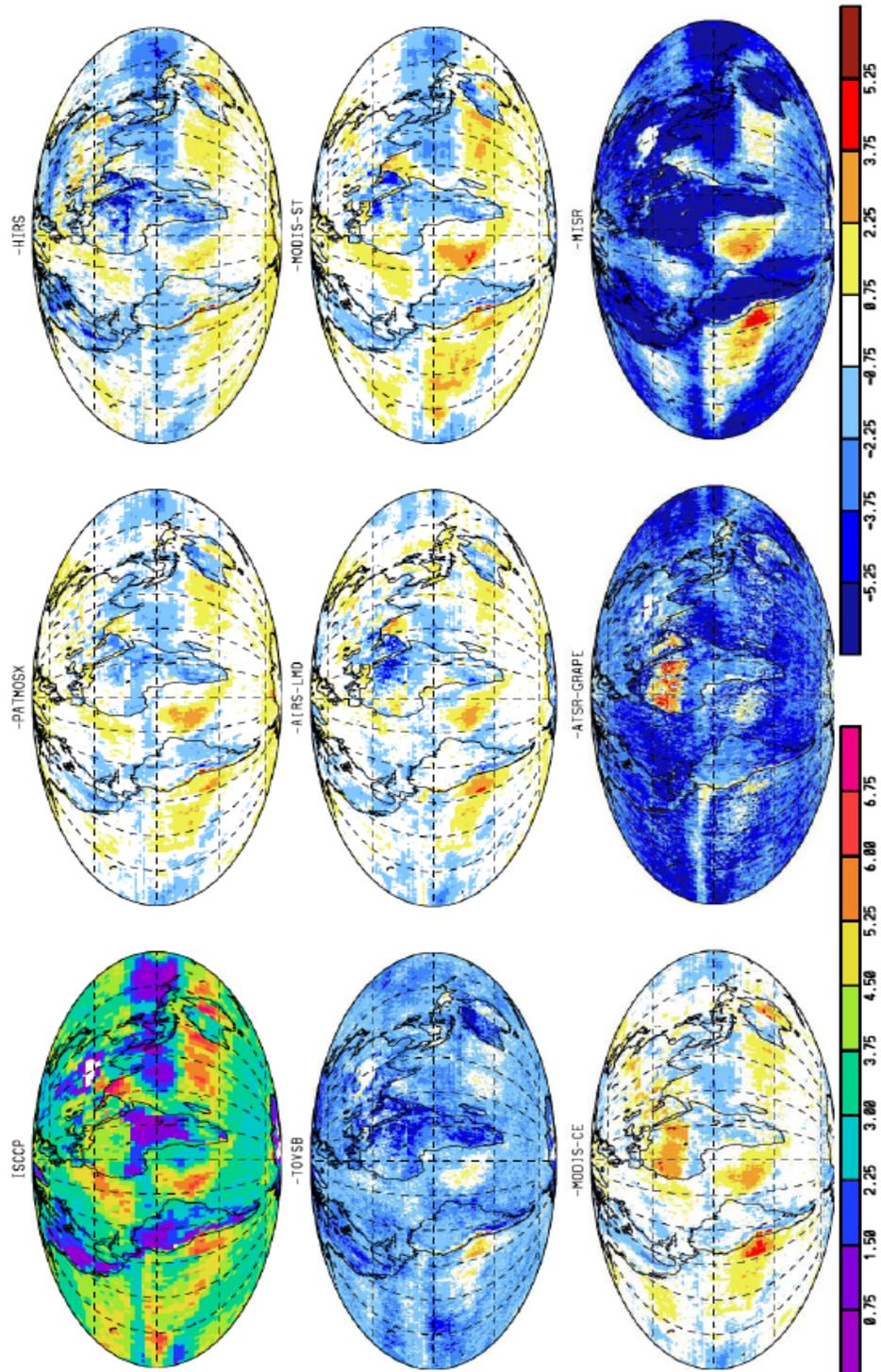
Figure 3.22: Geographical map of interannual variability of CALR from ISCCP as well as geographical maps of interannual CALR variability differences between ISCCP and PATMOSX, HIRS, TOVSB, AIRS-LMD, MODIS-ST, MODIS-CE, ATSR-GRAPE and MISR.

Interannual variability of CT
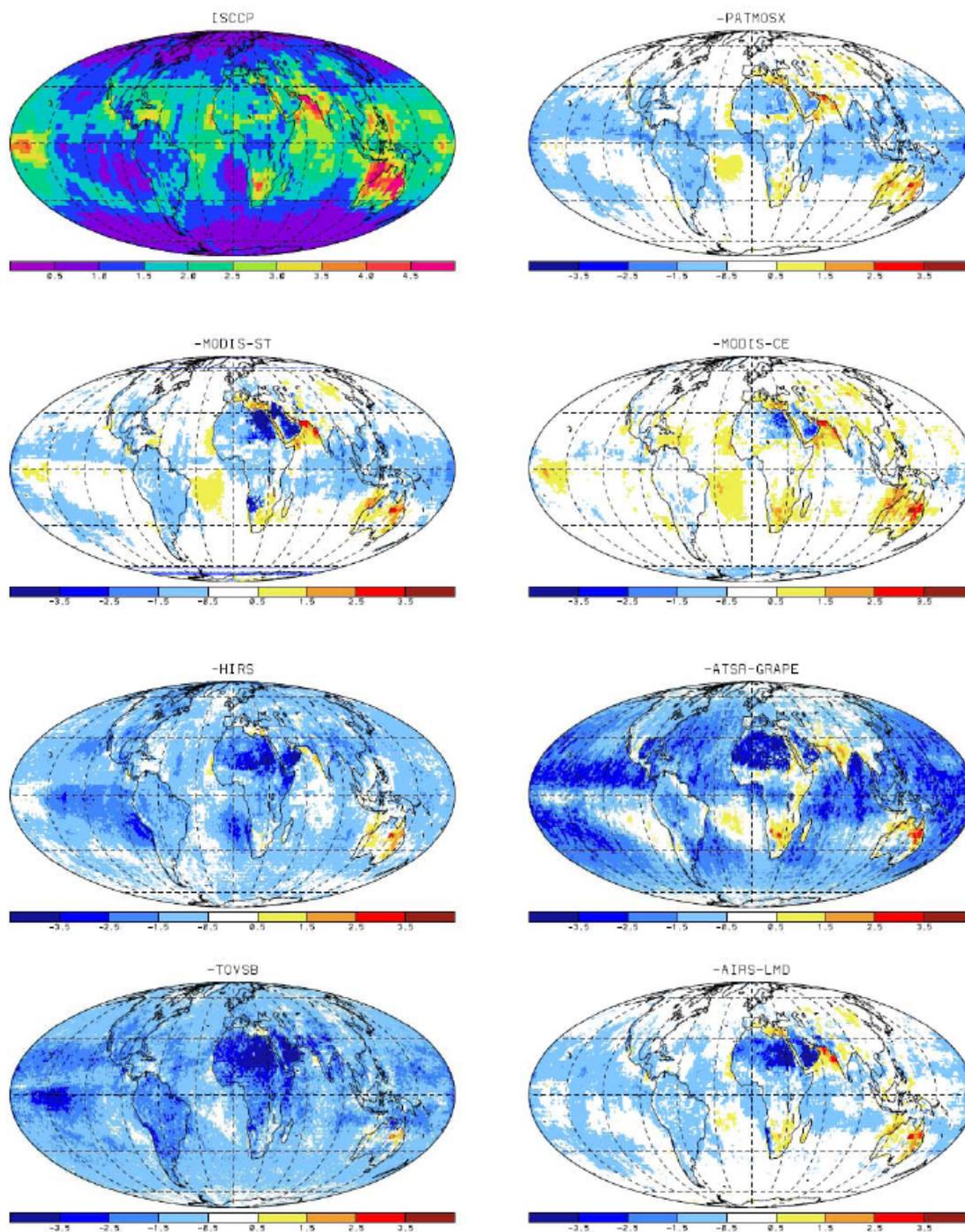
Figure 3.23: Geographical map of interannual variability of CT (in K) from ISCCP as well as geographical maps of interannual CT variability differences between ISCCP and PATMOSX, MODIS-ST, MODIS-CE, HIRS, ATSR-GRAPE, TOVSB and AIRS-LMD.

153
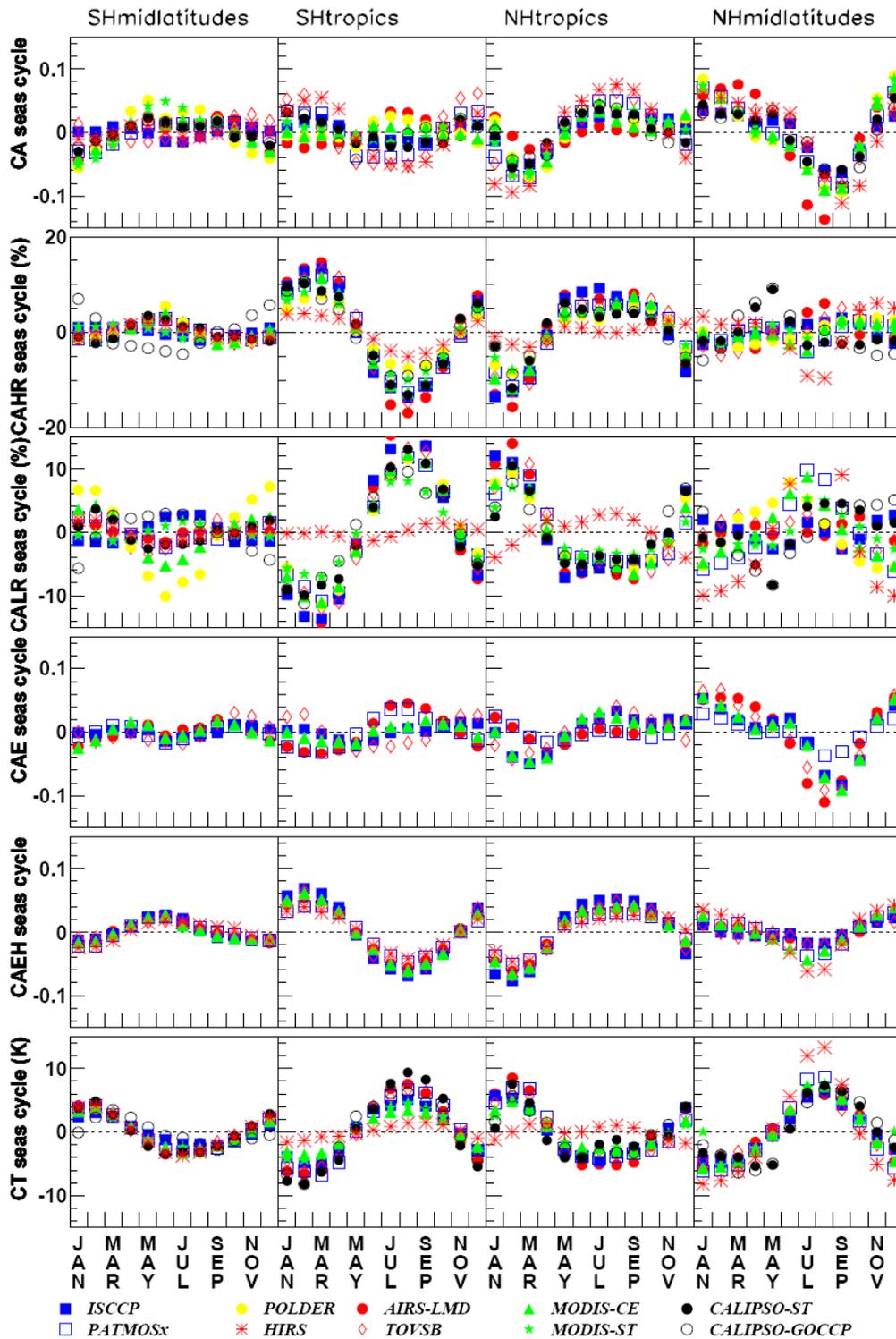
Figure 3.24: Seasonal variation of CA, CAHR, CT, CAE and CAEH over ocean in four latitude bands (60S-30S, 30S-0, 0-30N and 30N-60N), derived as the difference between monthly mean and annual mean. Statistics at 1:30 PM LT (3:00 PM for ISCCP).
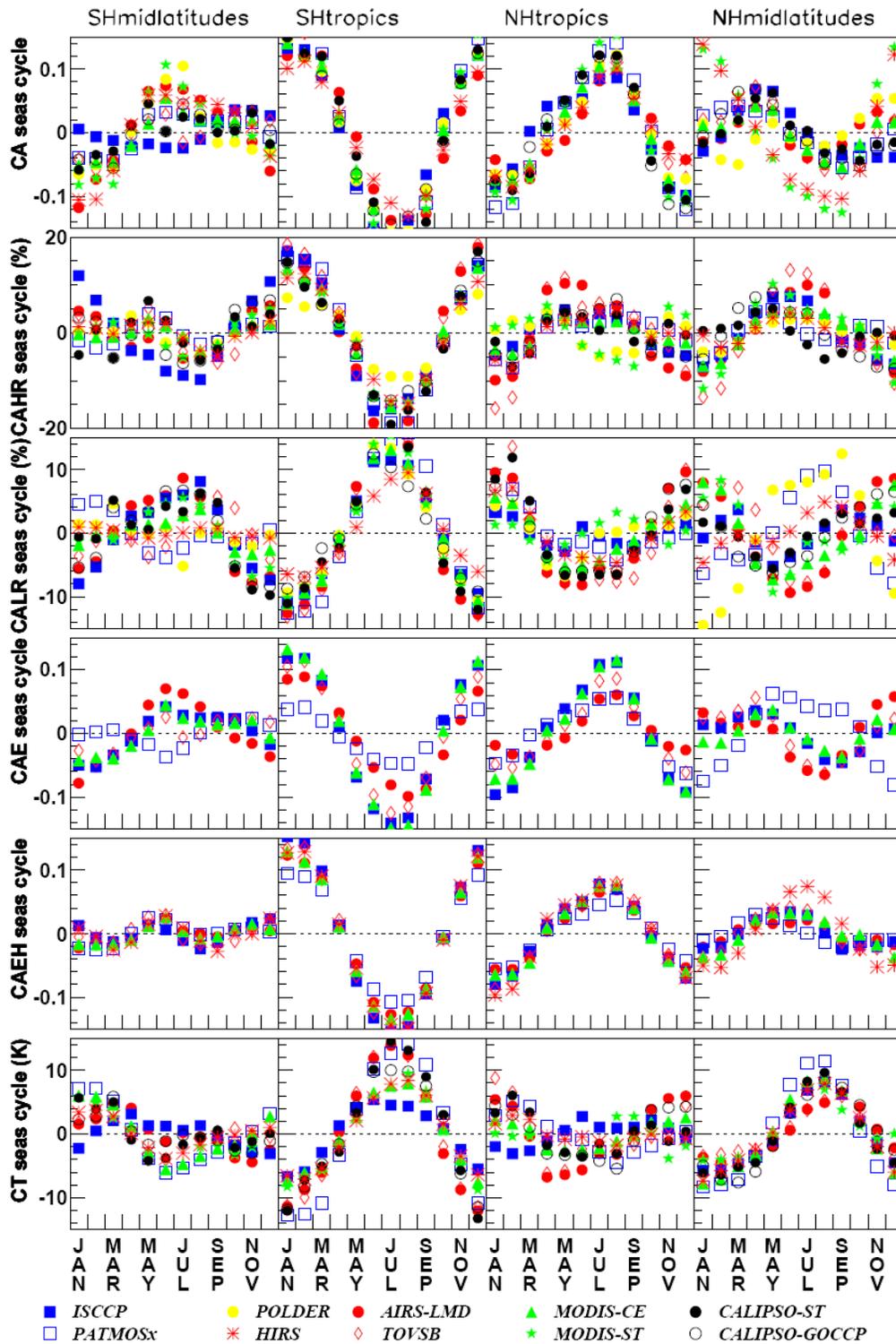
Figure 3.25: Seasonal variation of CA, CAHR, CT, CAE and CAEH over land in four latitude bands (60S-30S, 30S-0, 0-30N and 30N-60N), derived as the difference between monthly mean and annual mean. Statistics at 1:30 PM LT (3:00 PM for ISCCP).
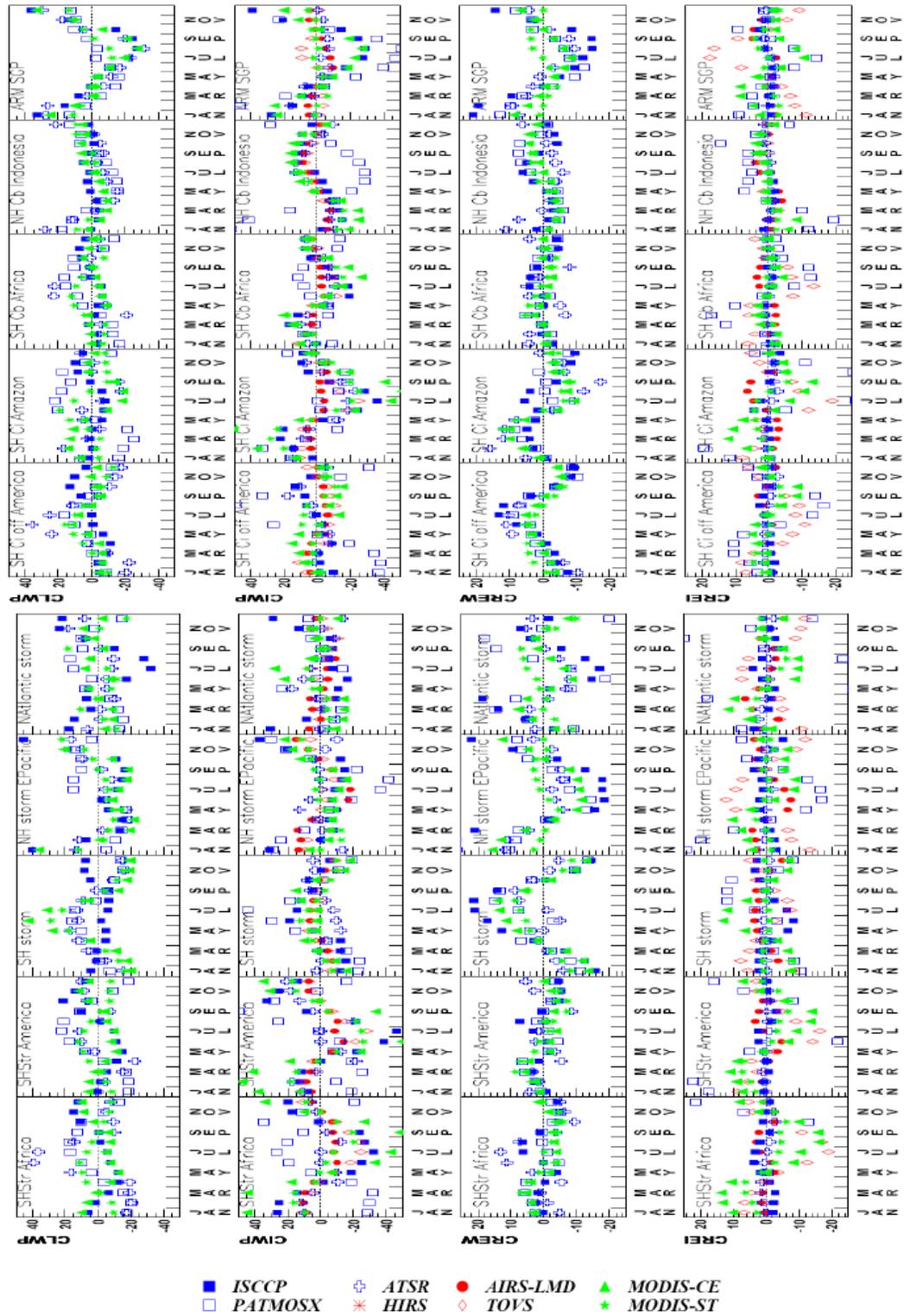
Figure 3.26: Seasonal cycles of CLWP (in gm^{-2}), CIWP (in gm^{-2}), CREW (in μm) and CREIH (in μm) for the following ten regions: 1(SH Str Africa), 2 (SH Str America), 3 (SH midlatitude storm), 4 (NH storm Eastern Pacific), 5 (NAtlantic storm), 6 (SH Ci off America), 7 (SH Ci Amazon), 8 (SH Cb Africa), 9 (NH Cb Indonesia) and 10 (ARM Southern Great Plain).
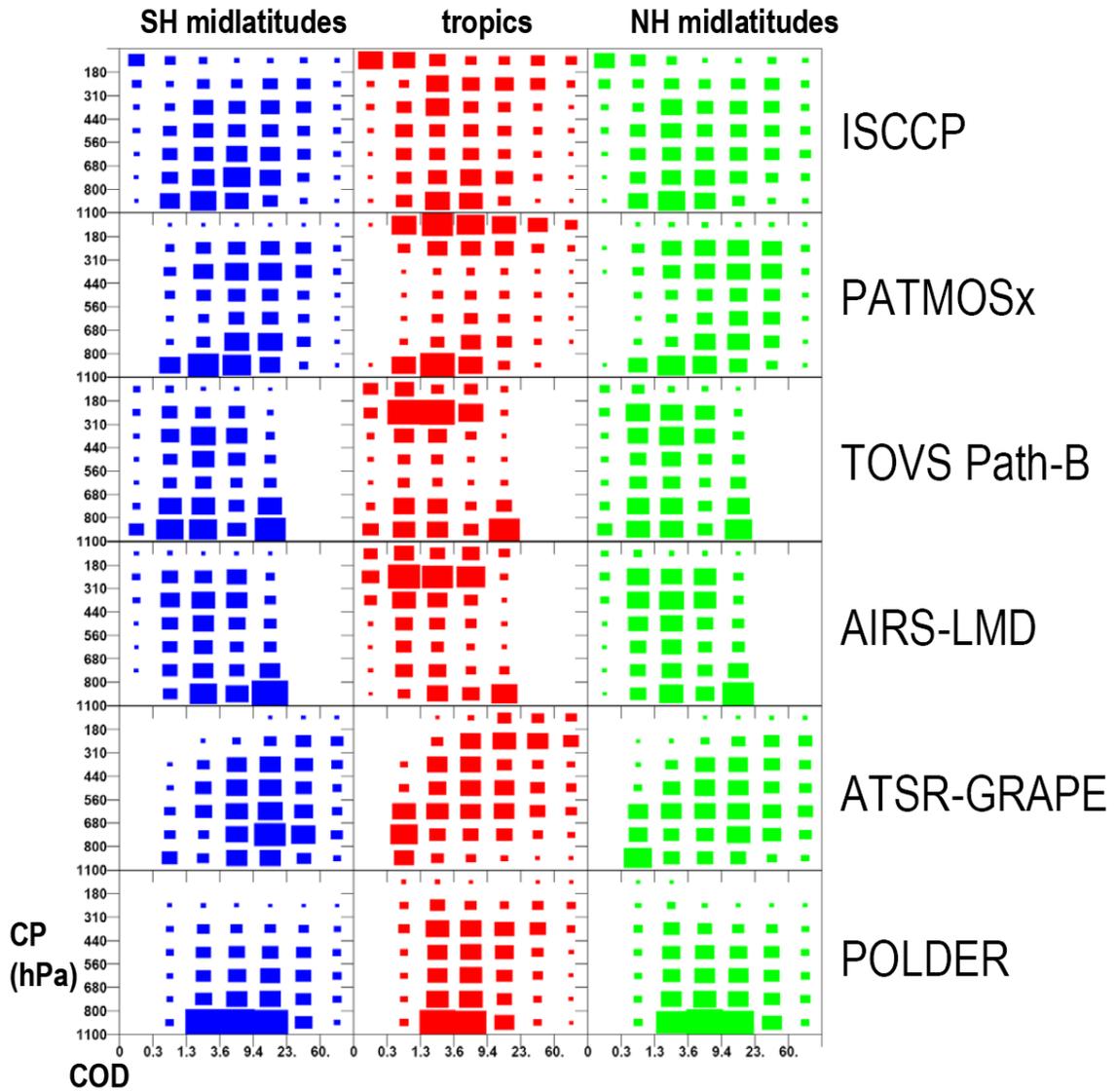
Figure 3.27: Two dimensional histograms of annual COD versus CP for three latitude bands (blue: SHmidlatitudes, red: tropics, green: NHmidlatitudes), from ISCCP, PATMOSX, TOVS Path B, AIRS-LMD, ATSR-GRAPE as well as POLDER. The size of the boxes indicates the relative frequency. This type of plot has been valuable for climate model evaluation.

157

4. References

1: ISCCP, 2: PATMOSX, 3: HIRS-NOAA, 4: TOVSB, 5: AIRS-LMD, 6: MODIS-ST, 7: MODIS-CE, 8: CALIPSO-ST, 9: CALIPSO-GOCCP, 10: POLDER, 11: MISR, 12: SAGE, 13: ATSR-GRAPE

[6]Ackerman, S.A., K.I. Strabala, W.P. Menzel, R.A. Frey, C.C. Moeller, and L.E. Gumley, 1998: Discriminating Clear-sky from Clouds with MODIS. *J. Geophys. Res.*, **103**, D24, 32141.

[11]Astin, I., L. Di Girolamo, and H.M. Van de Poll, 2001: Baysian confidence intervals for true fractional coverage from finite transect measurements: Implications for cloud studies from space. *J. Geophys. Res.*, **106**, 17303–17310.

[10]Baran, A.J., and L. C-Labonnote, 2007: A self-consistent scattering model for cirrus. I: The solar region. *Quant. J. Roy. Meteor. Soc.*, **133**, 1899-1912.

[10]Baran, A.J. and L. C-Labonnote, 2006: On the reflection and polarisation properties of ice cloud. *J. Quant. Spect. Rad. Trans.*, **100**, 41-54.

[2]Baum, B.A., A.J. Heymsfield, P. Yang, and S.T. Bedka, 2005: Bulk scattering properties for the remote sensing of ice clouds. Part I: Microphysical data and models. *J. Appl. Meteor.*, **44**, 1885-1895.

Bloom, S., A. da Silva, D. Dee, M. Bosilovich, J.-D. Chern, S. Pawson, S. Schubert, M. Sienkiewicz, I. Stajner, W.-W. Tan, M.-L. Wu, 2005: Documentation and Validation of the Goddard Earth Observing System (GEOS) Data Assimilation System - Version 4. *Technical Report Series on Global Modeling and Data Assimilation,* 104606, 165 pp.

[8,9]Bodas-Salcedo, A., M.J. Webb, S. Bony, H. Chepfer, J.-L. Dufresne, S.A. Klein, Y. Zhang, R. Marchand, J.M. Haynes, R. Pincus, and V.O. John, 2011: COSP: satellite simulation software for model assessment. *Bull. Amer. Meteor. Soc.*, **92**, 1023–1043, doi:10.1175/2011BAMS2856.1

[1]Brest, C.L., Rossow, W.B., Roiter, M.D., 1997: Update for radiance calibrations for ISCCP. *J. Atmos. Oceanic. Technol.,* **14**, 1091-1109.

[11]Bruegge, C.J., Diner, D.J., Kahn, R.A., Chrien, N., Helm-linger, M.C., Gaitley, B.J., and Abdou, W.A., 2007: The MISR radiometric calibration process. *Rem. Sens. Environ.*, **107**, 2–11, doi:10.1016/j.rse.2006.07.024.

[13]Bulgin C.E., P.I. Palmer, G.E. Thomas, C.P.G. Arnold, E. Campmany, E.Carboni, R.G. Grainger, C. Poulsen, R. Siddans, and B.N. Lawrence, 2008: Regional and seasonal variations of the Twomey indirect effect as observed by the ATSR-2 satellite instrument, *Geophys. Res. Lett.*, **35**, L02811, doi:10.1029/2007GL031394.

[10]Buriez, J.-C., C. Vanbauce, F. Parol, P. Goloub, M. Herman, B. Bonnel, Y. Fouquart, P. Couvert and G. Sèze 1997: Cloud detection and derivation of cloud properties from POLDER. *Int. J. Rem. Sens.*, **18**, 2785-2813.

[10]Buriez, J.-C., Doutriaux-Boucher M., Parol F., Loeb N.G., 2001: Angular variability of the liquid water cloud optical thickness retrieved from ADEOS-POLDER. *J. Atmos. Sci.*, **58**, 3007-3018.

[10]Buriez, J.-C., F. Parol, C. Cornet, and M. Doutriaux-Boucher, 2005: An improved derivation of the top-of-atmosphere albedo from POLDER/ADEOS-2: Narrowband albedos. *J. Geophys. Res.*, **110**, D05202, doi:10.1029/2004JD005243.

[10]Buriez, J.-C., F. Parol, Z. Poussi, and M. Viollier, 2007: An improved derivation of the top-of-atmosphere albedo from POLDER/ADEOS-2: 2. Broadband albedo. *J. Geophys. Res.*, **112**, D19201, doi:10.1029/2006JD008257.

[1]Cairns, B., 1995: Diurnal variations of cloud from ISCCP data. *Atmos. Res.,* **37**, 133-146.

[13]Campmany, E., R.G. Grainger, S.M. Dean and A.M. Sayer, 2009: Automatic detection of ship tracks in ATSR-2 satellite imagery. *Atmos. Chem. Phys.*, **9**, 1899-1905.

[5]Chahine, M.T., Pagano, T.S., Aumann, H.H., Atlas, R., and Coauthors: AIRS: Improving weather forecasting and providing new data on greenhouse gases. *Bull. Amer. Meteor. Soc.*, **87**, 911-926, 2006.

[4]Chédin, A., Scott, N.A., Wahiche, C., Moulinier, P., 1985: The Improved Initialized Inversion method: A high resolution physical method for temperature retrievals from the TIROS-N Series. *J. Clim. Appl. Meteor.,* **24**, 128-143.

[10]Chepfer H., Goloub P., Spinhirne J., et al., 2000: Cirrus cloud properties derived from POLDER-1/ADEOS polarized radiances: First validation using a ground based lidar network. *J. Appl. Meteor.*, **39**, 154-168.

[9]Chepfer H., S.Bony, D.M. Winker, G. Cesana, JL. Dufresne, P. Minnis, C.J. Stubenrauch, S. Zeng, 2010: The GCM Oriented CALIPSO Cloud Product (CALIPSO- GOCCP). *J. Geophys. Res.*, **105**, D00H16, doi:10.1029/2009JD012251.

[9]Chepfer, H., S. Bony, D. Winker, M. Chiriaco, J. Dufresne, and G. Sèze, 2008 : Use of CALIPSO lidar observations to evaluate the cloudiness simulated by a climate model. *Geophys. Res. Lett.*, **35**, L15704, doi:10.1029/2008GL034207, 2008.

[9]Chepfer H., S. Bony, D. Winker, G. Cesana, J.L. Dufresne, P. Minnis, C.J. Stubenrauch,and S. Zeng, The GCM Oriented Calipso Cloud Product (CALIPSO-GOCCP). *J. Geophys. Res.*, **115**, D00H16, doi:10.1029/2009JD012251, 2010.

[8,9]Chepfer, H., G. Cesana, D. Winker, B. Getzewich, and M. Vaughan, 2012: Comparison of two different cloud climatologies derived from CALIOP-Level 1 observations: The CALIPSO-ST and the CALIPSO-GOCCP. *J. Ocean. Atmos. Tech.*, subm.

[7]Chiriaco, M., H. Chepfer, P. Minnis, M. Haeffelin, S. Platnick, D. Baumgardner, P. Dubuisson, M. McGill, V. Noel, J. Pelon, D. Spangenberg, S. Sun-Mack, and G. Wind, 2007: Comparison of CALIPSO-like, LaRC, and MODIS retrievals of ice cloud properties over SIRTA in France and Florida during CRYSTAL-FACE. *J. Appl. Meteor. Climl.*, **46**, 249-272.

[12]Chu, W.P., M.P. McCormick, J. Lenoble, C. Brogniez, and P. Pruvost, 1989: SAGE II inversion algorithm. *J. Geophys. Res.*, **94**, 8339-8351.

[11]Davies R., A. Horváth, C. Moroney, B. Zhang, and Y. Zhu, 2007: Cloud motion vectors from MISR using sub-pixel enhancements. *Remote Sens. Environ.*, **107**.

Davis, S.M., D.L. Hlavka, E. Jensen, K.H. Rosenlof, Q. Yang, S. Schmidt, S. Borrmann, W. Frey, P. Lawson, H. Voemel, and T.P. Bui, 2010: In situ and lidar observations of tropopause subvisible cirrus clouds during TC4. *J. Geophys. Res.*, **115**, D00J17, doi:10.1029/2009JD013093.

Derber, J.C., D.F. Parrish, and S.J. Lord, 1991: The new global operational analysis system at the National Meteorological Center. *Wea. Forecasting*. **6**, 538-547.

[11]Di Girolamo, L., and R. Davies, 1997: Cloud fraction errors caused by finite resolution measurements. *J. Geophys. Res.*, **102**, 1739-1756.

[11]Di Girolamo, L., and M.J. Wilson, 2003: A first look at band-differenced angular signatures for cloud detection from MISR. *IEEE Trans. Geosci. Rem. Sens.* **41**, 1730-1734.

[11]Di Girolamo, L., A. Menzies, G. Zhao, K. Mueller, C. Moroney, and D.J. Diner, 2010: MISR Level 3 Cloud Fraction by Altitude Theoretical Basis, JPL D-62358, Jet Propulsion Laboratory, Pasadena, CA, 24 pp.

[11]Diner, D.J., J.C. Beckert, T.H. Reilly, C.J. Bruegge, J.E. Conel, R. Kahn, J.V. Martonchik, T.P. Ackerman, R. Davies, S.A.W. Gerstl, H.R. Gordon, J-P. Muller, R. Myneni, R.J. Sellers, B. Pinty, and M.M. Verstraete, 1998: Multi-angle Imaging SpectroRadiometer (MISR) description and experiment overview. *IEEE Trans. Geosci. Rem. Sens.*, **36**, 1072-1087.

[11]Diner, D. J., L. Di Girolalmo and E. Clothiaux, 1999a: MISR Level 1 cloud detection algorithm theoretical basis. *JPL D-13397, Rev. B.*, Jet Propulsion Laboratory, Pasadena, CA, 38 pp.

[11]Diner, D.J., R. Davies, L. Di Girolamo, C. Moroney, J.-P. Muller, S.R. Paradise, D. Wenkert, and J. Zong, 1999b: MISR Level 2 cloud detection and classification algorithm theoretical basis. *JPL D-11399 Rev. D*, Jet Propulsion Laboratory, Pasadena, CA, 102 pp.

[11]Diner, D.J., L. Di Girolamo, and A. Nolin, 2007: Preface to the MISR Special Issue. *Remote Sens. Environ.,* **107**, 1.

[7]Dong, X., P. Minnis, B. Xi, S. Sun-Mack, and Y. Chen, 2008: Comparison of CERES-MODIS stratus cloud properties with ground-based measurements at the DOE ARM Southern Great Plains site. *J. Geophys. Res.*, **113**, D03204, doi:10.1029/2007JD008438.

[10]Doutriaux-Boucher, M., and Quaas J., 2004: Evaluation of cloud thermodynamic phase parametrizations in the LMDZ GCM by using POLDER satellite data. *Geophys. Res. Lett*., **31**, L06126.

[1]Evan, A., A. K. Heidinger, and D. J. Vimont, 2007: Arguments against a physical long-term trend in global ISCCP cloud amounts. *Geophys. Res. Lett*., **34**, L04701.

[10]Ferlay, N., F. Thieuleux, C. Cornet, A.B. Davis, P. Dubuisson, F. Ducos, F. Parol, J. Riédi, C. Vanbauce, 2010: Toward new inferences about cloud structures from multidirectional measurements in the oxygen A band: Middle-of-cloud pressure and cloud geometrical thickness from POLDER3/PARASOL. *J. Appl. Meteor. Clim.*, doi: 10.1175/2010JAMC2550.1

[10]Fougnie, B., G. Bracco, B. Lafrance, et al., 2007: PARASOL in-flight calibration and performance. *Appl. Opt.*, **46**, 5435-5451.

[6]Frey, R.A., S.A. Ackerman, Y. Liu, K.I. Strabala, H. Zhang, J. Key and X. Wang, 2008: Cloud Detection with MODIS, Part I: Recent Improvements in the MODIS Cloud Mask. *J. Atmos. Oceanic Tech.,* **25**, 1057-1072.

[11]Garay, M.J., S.P. Szoeke, and C.M. Moroney, 2008: Comparison of marine stratocumulus cloud-top heights in the Southeastern Pacific retrieved from satellites with coincident ship-based observations. *J. Geophys. Res.*, **113**, D18204, DOI: 10.1029/2008JD009975.

[11]Genkova, I., G. Seiz, G. Zhao, P. Zuidema, and L. Di Girolamo, 2007: Trade wind cumulus cloud top height comparisons from ASTER, MISR, and MODIS. *Rem. Sens. Environ.,* **107**, 211-222.

[10]Goloub, P., M. Herman, H. Chepfer, J. Riedi, G. Brogniez, P. Couvert, G. Séze, 2000: Cloud Thermodynamic Phase Classification from the POLDER Spaceborne instrument. *J. Geophys. Res.*, **105**, 14747-14759.

[5+4]Guignard, A., C.J. Stubenrauch, A.J. Baran, and R. Armante, 2012: Bulk microphysical properties of semi-transparent cirrus from AIRS: a six year global climatology and statistical analysis in synergy with geometrical profiling data from CloudSat-CALIPSO. *Atmos. Chem. Phys.*, **12**, 503-525.

Hahn, C.J., S.G. Warren, and J. London, 1995: The effect of moonlight on observation of cloud cover at night, and application to cloud climatology. *J. Climate,* **8***,* 1429-1446.

Hahn, C.J., and S.G. Warren, 1999: Extended Edited Cloud Reports from Ships and Land Stations over the Globe, 1952-1996. Numerical Data Package NDP-026C, 79 pp., av. from Carbon Dioxide Information Analysis Center, Oak Ridge, Tennessee, USA. . (http://cdiac.ornl.gov/ftp/ndp026c/)

[1]Hahn, C.J., W.B. Rossow, and S.G. Warren, 2001: ISCCP cloud properties associated with standard cloud types identified in individual surface observations. *J. Climate,* **14**, 11-18.

Hahn, C.J., and S.G. Warren, 2003: *Cloud Climatology for Land Stations Worldwide, 1971-1996.* Report NDP-026D, 35 pp., av. from Carbon Dioxide Information Analysis Center, Oak Ridge, Tennessee, USA. (http://cdiac.ornl.gov/ftp/ndp026d/)

[1]Han, Q.-Y., W.B. Rossow, A.A. Lacis, 1994: Near-global survey of effective cloud droplet radii in liquid water clouds using ISCCP data. *J. Climate*, **7**, 465-497.

[1]Han, Q.-Y., W.B. Rossow, J. Chou, K.S. Kuo, R.M. Welch, 1999: The effect of aspect ratio and surface roughness on satellite retrievals of ice-cloud properties. *J. Quart. Spectrosc. Radiat. Trans.*, **63**, 559-583.

[11]Harshvardhan, G. Zhao, L. Di Girolamo, and R.N. Green, 2009: Satellite-observed location of stratocumulus cloud-top heights in the presence of strong inversions. *IEEE Trans. Geosci. Rem. Sens.*, **47**, 1421-1428.

[2]Heidinger, A.K., and M.J. Pavolonis, 2005: Global daytime distribution of overlapping cirrus cloud from NOAA's Advanced Very High Resolution Radiometer. *J Climate*, **18,** 4772-4784.

[2]Heidinger, A.K., C. O'Dell, R. Bennartz, and T. Greenwald, 2006: The successive-order-of-interaction radiative transfer model. Part I: Model development. *J. Appl. Meteor Clim.*, **45**, 1388-1402.

[2]Heidinger, A.K., and M.J. Pavolonis, 2009: Gazing at Cirrus Clouds for 25 Years through a Split Window. Part I: Methodology. *J. Appl. Meteor. Clim.*, **48,** 1100-1116.

[2]Heidinger, A.K., W.C. Straka A, C.C. Molling, J.T. Sullivan, and X. Wu, 2010: Deriving an inter-sensor consistent calibration for the AVHRR solar reflectance data record. *Int. J. Rem. Sens.*, **31,** 6493-6517.

[2]Heidinger, A.K., A.T. Evan, M. Foster, and A. Walther, 2012: A Naïve Bayesian Cloud Detection Scheme Derived from CALIPSO and Applied within PATMOS-x. *J. Appl. Meteor. Clim.*, **51,** 1129-1144.

[2]Heymsfield, A.J., S. Matrosov, and B. Baum, 2003: Ice water path-optical depth relationships for cirrus and deep stratiform ice cloud layers. *J. Appl Meteorol*, **42,** 1369-1390.

Hogan, R.J., and A.J. Illingworth, 2000: Deriving cloud overlap statistics from radar. *Quarterly Journal of the Royal Meteorological Society*, 126: 2903–2909. doi: 10.1002/qj.49712656914.

[6]Holz, R., S.A. Ackerman, P. Antonelli, F. Nagle, R.O. Knuteson, M. McGill, D.L. Hlavka, and W.D. Hart, 2008: An Improvement to the High Spectral Resolution CO_2 Slicing Cloud Top Altitude Retrieval. *J. Atmos. Oceanic. Technol.*, **23**, 653-670.

[11]Horváth, A., and R. Davies, 2001(a): Feasibility and error analysis of cloud motion wind extraction from near-simultaneous multiangle MISR measurements. *J. Atmos. Ocean. Technol.*, **18**.

[11]Horváth, A., and R. Davies, 2001(b): Simultaneous retrieval of cloud motion and height from polar-orbiter multiangle measurements. *Geophys. Res. Lett.*, 28, 2915–2918.

[8]Hu, Y., 2007: Depolarization ratio–effective lidar ratio relation: Theoretical basis for space lidar cloud phase discrimination. *Geophys. Res. Lett.*, **34**, L11812, doi:10.1029/ 2007GL029584.

[8]Hunt, W.H., D.M. Winker, M.A. Vaughan, K.A. Powell, P.L. Lucker, and C. Weimer, 2009: CALIPSO Lidar Description and Performance Assessment. *J. Atmos. Oceanic Technol.*, **26**, 1214–1228, doi:10.1175/2009JTECHA1223.1.

[3+1]Jin, Y., W.B. Rossow, D.P. Wylie, 1996: Comparison of the climatologies of high-level clouds from HIRS and ISCCP. *J. Climate* 9, 2850-2879.

Johnson, N.L., and Kotz, S., 1969: Discrete Distribution. *Houghton Mifflin Co.*, Boston, 328pp.

Kahn, B.H., M.T. Chahine, G.L. Stephens, G.G. Mace, R.T. Marchand, Z. Wang, C.D. Barnet, A. Eldering, R.E. Holz, R.E. Kuehn, and D.G. Vane, 2008: Cloud type comparisons of AIRS, CloudSat and CALIPSO cloud height and amount. *Atmos. Chem. Phys.*, **8**, 1231-1248.

[7]Kato, S., N.G. Loeb, P. Minnis, J.A. Francis, T.P. Charlock, D. Rutan, E.E. Clouthiaux, and S. Sun-Mack, 2006: Seasonal and interannual variations of top-of-atmosphere irradiance and cloud cover over polar regions derived from the CERES data set. *Geophys. Res. Lett.,* **33**, L19804, 10.1029/2006GL026685.

[12]Kent, G.S., D.M. Winker, M.T. Osborn, M.P. McCormick, and K.M. Skeens, 1993: A model for the separation of cloud and aerosol in SAGE II occultation data. *J. Geophys. Res.*, **98**, 20725-20735.

[6]King, M.D., W.P. Menzel, Y.J. Kaufman, D. Tanré, B.-C. Gao, S. Platnick, S.A. Ackerman, L.A. Remer, R. Pincus, P.A. Hubanks, 2003: Cloud and aerosol properties, precipitable water, and profiles of temperature and water vapor from MODIS. *IEEE Trans. Geosci. Remote Sens*. 41, 442-458.

[6]King, M.D., S. Platnick, P. Yang, G.T. Arnold, M.A. Gray, J.C. Riedi, S.A. Ackerman, K.N. Liou, 2004: Remote sensing of liquid water and ice cloud optical thickness and effective radius in the Arctic: Application of airborne multispectral MAS data. *J. Atmos. Oceanic Tech.*, **21**, 857-875.

[10]Labonnote, L., G. Brogniez, M. Doutriaux-Boucher, J.C. Buriez, J.F. Gayet, and H. Chepfer, 2000: Modelling of light scattering in cirrus clouds with inhomogeneous hexagonal monocrystals. Comparison with in-situ and ADEOS-POLDER measurements. *Geophys. Res. Lett.*, **27**, 113-116.

[10]Labonnote, L., G. Brogniez, J.C. Buriez, M. Doutriaux-Boucher, J.F. Gayet and A. Macke, 2001: Polarized light scattering by inhomogeneous hexagonal monocrystals. Validation with ADEOS-POLDER measurements. *J. Geophys. Res.*, **106**, 12139-12153.

Lee, Y., G. Wahba, and S.A. Ackerman, 2004: Cloud Classification of Satellite Radiance Data by Multicategory Support Vector Machines. *J. Atmos. Oceanic Tech.* **21**, 159-169.

[12+1]Liao, X., W.B. Rossow, D. Rind, 1995a: Comparison between SAGE II and ISCCP high-level clouds. Part II: Locating cloud tops. *J. Geophys. Res*., **100**, 1137-1147.

[12+1]Liao, X., W.B. Rossow, D. Rind, 1995b: Comparison between SAGE II and ISCCP high-level clouds. Part I: Global and zonal mean cloud amounts. *J. Geophys. Res.,* **100**, 1121-1135.

[1]Lin, B., W.B. Rossow, 1996: Seasonal variation of liquid and ice water path in nonprecipitating clouds over oceans. *J. Climate*, **9**, 2890-2902.

[1]Lin, B., W.B. Rossow, 1997: Precipitation water path and rainfall rate estimates for oceans using special sensor microwave imager and International Satellite Cloud Climatology Project data. *J. Geophys. Res.*, **102**, 9359-9374.

[1]Lin, B., P. Minnis, B. Wielicki, D.R. Doelling, R. Palikonda, D.F. Young, and T. Uttal, 1998: Estimation of water cloud properties from satellite microwave, infrared and visible measurements in oceanic environments. 2. Results. *J. Geophys. Res.,* **103**, 3887-3905.

[6]Liu, Y., J.R. Key, R.A. Frey, S.A. Ackerman, and W.P. Menzel, 2004: Nighttime polar cloud detection with MODIS. *Rem. Sens. Environ.*, **92**, 181-194.

[8]Liu, Z., M. Vaughan, D. Winker, C.A. Hostetler, L.R. Poole, D.L. Hlavka, W.D. Hart, and M.J. McGill, 2004: Use of probability distribution functions for discriminating between cloud and aerosol in lidar backscatter data. *J. Geophys. Res.*, **109**, D15202, doi: 10.1029/2004JD004732.

[8]Liu, Z., M.A. Vaughan, D.M. Winker, C. Kittaka, R.E. Kuehn, B.J. Getzewich, C.R. Trepte, and C.A. Hostetler, 2009: The CALIPSO Lidar Cloud and Aerosol Discrimination: Version 2 Algorithm and Initial Assessment of Performance. *J. Atmos. Oceanic Techn*., **26**, 1198–1213, doi:10.1175/2009JTECHA1229.1.

[6]Liu, Yinghui, Steven A. Ackerman, Brent C. Maddux, Jeffrey R. Key, Richard A. Frey, 2010: Errors in Cloud Detection over the Arctic Using a Satellite Imager and Implications for Observing Feedback Mechanisms. *J. Climate*, **23**, 1894–1907.

[10]Loeb, N., F. Parol J.C. Buriez, C. Vanbauce, 2000: Top-of-Atmosphere Albedo Estimation from Angular Distribution Models Using Scene Identification from Satellite Cloud Property Retrievals. *J. Climate*, **13**, 1269-1285.

Mace, G.G., and S. Benson-Troth, 2002: Cloud-Layer Overlap Characteristics derived from Long-Term Cloud Radar Data. *J. Climate,* **15**, 2505-2515.

Mace, G.G., Y. Zhang, S. Platnick, M.D. King, P. Minnis, and P. Yang, 2005: Evaluation of cirrus cloud properties from MODIS radiances using cloud properties derived from ground-based data collected at the ARM SGP site. *J. Appl. Meteor.*, **44**, 221-240.

Mace, G.G., Q. Zhang, M. Vaughan, R. Marchand, G. Stephens, C. Trepte, and D. Winker, 2009: A description of hydrometeor layer occurrence statistics derived from the first year of merged Cloudsat and CALIPSO data. *J. Geophys. Res*., **114**, D00A26, doi:10.1029/2007JD009755.

[6]Maddux, B.C., S.A. Ackerman, S. Platnick, 2010: Viewing Geometry Dependencies in MODIS Cloud Products. *J. Atmos. Oceanic Techn.*, **27**, 1519–1528.

[11]Marchand, R.T., T.P. Ackerman, and C. Moroney, 2007: An assessment of Multi-angle Imaging Spectroradiometer (MISR) stereo-derived cloud top heights and cloud top winds using ground-based radar, lidar, and microwave radiometers. *J. Geophys. Res.*, **112**, D06204, doi:10.1029/2006JD007091.

[12]McCormick, M.P., 1987: SAGE II: An overview. *Adv. Space Res.*, **7**, 319-326.

[12]McCormick, M.P., L.W. Thomason, C.R. Trepte, 1995: Atmospheric effects of the Mt Pinatubo eruption. *Nature*, **373**, 399-404.

[8]McGill, M.J., M.A. Vaughan, C.R. Trepte, W.D. Hart, D.L. Hlavka, D.M. Winker, and R. Kuehn, 2007: Airborne validation of spatial properties measured by the CALIPSO lidar. *J. Geophys. Res.*, **112**, D20201, doi:10.1029/2007JD008768.

[3]Menzel, W.P., D.P. Wylie, K.I. Strabala, 1992: Seasonal and Diurnal Changes in Cirrus Clouds as seen in four Years of Observations with the VAS. *J. Appl. Meteor*., **31**, 370-385.

[6]Menzel, W.P., R.A. Frey, H. Zhang, D.P. Wylie, C.C. Moeller, R.E. Holz, B. Maddux, B.A. Baum, K.I. Strabala, and L.E. Gumley, 2008: MODIS Global Cloud-Top Pressure and Amount Estimation: Algorithm Description and Results. *J. Appl. Meteor. Climl.*, **47**, 1175–1198.

[7]Minnis, P., D.P. Garber, D.F. Young, R.F. Arduini, and Y. Takano, 1998: Parameterization of reflectance and effective emittance for satellite remote sensing of cloud properties. *J. Atmos. Sci.*, **55**, 3313-3339.

[7]Minnis, P., Q.Z. Trepte, S. Sun-Mack, Y. Chen, D.R. Doelling, D.F. Young, D.A. Spangenberg, W.F. Miller, B.A. Wielicki, R.R. Brown, S.C. Gibson, and E.B. Geier, 2008a: Cloud detection in non-polar regions for CERES using TRMM VIRS and Terra and Aqua MODIS data. *IEEE Trans. Geosci. Remote Sens.*, **46**, 3857-3884.

[7]Minnis, P., C.R. Yost, S. Sun-Mack, and Y. Chen, 2008b: Estimating the physical top altitude of optically thick ice clouds from thermal infrared satellite observations using CALIPSO data. *Geophys. Res. Lett.*, **35**, L12801, doi:10.1029/2008GL033947.

[7]Minnis, P., S. Sun-Mack, D.F. Young, P.W. Heck, D.P. Garber, Y. Chen, D.A. Spangenberg, R.F. Arduini, Q.Z. Trepte, W.L. Smith, Jr., J.K. Ayers, S.C. Gibson, W.F. Miller, V. Chakrapani, Y. Takano, K.-N. Liou, Y. Xie, and P. Yang, 2011: CERES Edition-2 cloud property retrievals using TRMM VIRS and Terra and Aqua MODIS data, Part I: Algorithms. *IEEE Trans. Geosci. Remote Sens.*, **49**, *11*, 4374-4400.

[6]Moody, E.G., M.D. King, S. Platnick, C.B. Schaaf, F. Gao, 2005: Spatially complete global spectral surface albedos: Value-added datasets derived from Terra MODIS land products. *IEEE Trans. Geosci. Remote Sens.*, **43**, 144-158.

[11]Moroney C., R. Davies, and J-P. Muller, 2002(a): Operational retrieval of cloud- top heights using MISR data. *IEEE Trans. Geosci. Remote Sens.*, **40**.

[11]Moroney C., A. Horváth, and R. Davies, 2002(b): Use of stereo-matching to coreg- ister multiangle data from MISR. *IEEE Trans. Geosci. Remote Sens.*, **40**, 1541–1546.

[11]Muller J.-P., A. Mandanayake, C. Moroney, R. Davies, D.J. Diner and S. Paradise, 2002: MISR stereoscopic image matchers: techniques and results. *IEEE Trans. Geosci. Remote Sens.*, **40**, 1547-155.

Nakajima T., King, M.D., 1990: Determination of the optical thickness and effective particle radius of clouds from reflected solar radiation measurements. Part I: Theory. *J. Atmos. Sci.,* **47**, 1878-1893.

National Climatic Data Center (NCDC), 1962: History of the international code. *TDF-13 Reference Manual*, pp. 0.6-0.10, available from NCDC, Asheville, North Carolina.

[11]Naud, C.M., J.-P. Muller, and E.E. Clothiaux, 2002: Comparison of cloud top heights derived from MISR stereo and MODIS CO2-slicing. *Geophys. Res. Lett.*, **29**, 1795, doi:10.1029/2002GL015460.

[11]Naud, C.M., J.-P. Muller, M. Haeffelin, Y. Morille, and A. Delaval, 2004: Assessment of MISR and MODIS cloud top heights through intercomparison with a back-scattering lidar at SIRTA. *Geophys. Res. Lett.*, **31**, L04114, doi:10.1029/2003GL018976.

[6+11]Naud, C.M., J-P. Muller, E.E. Clothiaux, B.A. Baum, and W.P. Menzel, 2005: Intercomparison of multiple years of MODIS, MISR and radar cloud-top heights. *Annales Geophysicae*, **23**, 2415-2424.

[6+11]Naud, C.M., B.A. Baum, M. Pavolonis, A. Heidinger, R. Frey, and H. Zhang, 2007: Comparison of MISR and MODIS cloud-top heights in the presence of cloud overlap. *Remote Sens. Environ.,* **107**, 200-210.

[6]Naud, C., J.-P. Muller, and P. de Valk, 2005: On the use of ICESAT-GLAS measurements for MODIS and SEVIRI cloud-top height accuracy assessment. *Geophys. Res. Lett.*, **32**, L19815, doi:10.1029/2005GL023275.

Norris, J.R., 1998: Low cloud structure over the ocean from surface observations, Part II: Geographical and seasonal variations. *J. Climate,* **11***,* 383-403.

Norris, J.R., 2005: Multidecadal changes in near-global cloud cover and estimated cloud cover radiative forcing. *J. Geophys. Res.*, **110**, D08206, doi:10.1029/2004JD005600.

[10]Parol, F., J.C. Buriez, C. Vanbauce, J. Riedi, L.C.-Labonnote, M. Doutriaux-Boucher, M. Vesperini, G. Sèze, P. Couvert, M. Viollier, and F.M. Bréon, 2004: Review of capabilities of multi-angle and polarization cloud measurements from POLDER. *Adv. Space Res.*, **33**, 1080-1088.

[2]Pavolonis, M.J., and A.K. Heidinger, 2004: Daytime cloud overlap detection from AVHRR and IVRS. *J. Appl. Meteor.*, **43,** 762-778.

[2]Pavolonis, M.J., A.K. Heidinger, and T. Uttal, 2005: Daytime global cloud typing from AVHRR and IVRS: Algorithm description, validation, and comparisons. *J. Appl. Meteor.*, **44,** 804-826.

[5]Péquignot, E., A. Chédin, and N.A. Scott, 2008: Infrared continental surface emissivity spectra retrieved from AIRS hyperspectral sensor. *J. Appl. Meteor. Clim.*, **47**, 1619-1633.

[6]Platnick, S., M.D. King, S.A. Ackerman, W.P. Menzel, B.A. Baum, J.C. Riedi, R.A. Frey, 2003: The MODIS cloud products: Algorithms and examples from TERRA. *IEEE Trans. Geosci. Rem. Sens,*. **41**, 459-473.

[8]Powell, K.A., C.A. Hostetler, Z. Liu, M.A. Vaughan, R.E. Kuehn, W.H. Hunt, K. Lee, C.R. Trepte, R.R. Rogers, S.A. Young, and D.M. Winker, 2009: CALIPSO Lidar Calibration Algorithms: Part I - Nighttime 532 nm Parallel Channel and 532 nm Perpendicular Channel. *J. Atmos. Oceanic Techn.*, **26**, 2015–2033, doi:10.1175/2009JTECHA1242.1.

[4]Rädel, G., C.J. Stubenrauch, R. Holz, and D.L. Mitchell, 2003: Retrieval of Effective Ice Crystal Size in the Infrared: Sensitivity Study and Global Measurements from TIROS-N Operational Vertical Sounder. *J. Geophys. Res.,* **108**, 10.1029/2002JD002801.

[2]Rao, C., 1993: Nonlinearity corrections for the thermal infrared channels of the AVHRR: Assessment and recommendations.

Raschke, E., S. Kinne, and P.W. Stackhouse (lead authors), 2012: GEWEX Radiative Flux Assessment, WCRP report.

[10]Riedi J., M. Doutriaux-Boucher, P. Goloub, and P. Couvert, 2000: Global distribution of cloud top phase from POLDER/ADEOS I. *Geophys. Res. Lett.*, **27**, 1707-1710.

[10]Riedi J., P. Goloub, R.T. Marchand, 2001: Comparison of POLDER cloud phase retrievals to active remote sensors measurements at the ARM SGP site. *Geophys. Res. Lett.*, **28**, 2185-2188

[10]Riedi J., B. Marchant, S. Platnick, B. Baum, F. Thieuleux, C. Oudard, F. Parol, J-M. Nicolas, and P. Dubuisson, 2010: Cloud thermodynamic phase inferred from merged POLDER and MODIS data. *Atmos. Chem. Phys.*, **10**, 11851-11865.

[8]Rogers, R.R., C.A. Hostetler, J.W. Hair, R.A. Ferrare, Z. Liu, M.D. Obland, D.B. Harper, A.L. Cook, K.A. Powell, M.A. Vaughan, and D.M. Winker, 2011: Assessment of the CALIPSO Lidar 532 nm Attenuated Backscatter Calibration Using the NASA LaRC Airborne High Spectral Resolution Lidar. *Atmos. Chem. Phys.*, **11**, 1295–1311, doi:10.5194/acp-11-1295-2011

[1]Rossow, W.B., L.C. Garder, 1993: Cloud detection using satellite measurements of infrared and visible radiances for ISCCP. *J. Climate,* **6**, 2341-2369.

[1]Rossow, W.B., A.W. Walker, and L.C. Garder, 1993: Comparison of ISCCP and other Cloud Amounts. *J. Climate,* **6**, 2394-2418.

[1]Rossow, W.B., B. Cairns, 1995: Monitoring changes of clouds. *Climatic Change*, **31**, 305-347.

[1]Rossow, W.B., A.W. Walker, D. Beuschel, M. Roiter, 1996: International Satellite Cloud Climatology Project (ISCCP) description of new cloud datasets. *WMO/TD-No.737, World Climate Research Programme (ICSU and WMO)*, Geneva (1996) 115pp.

[1]Rossow, W.B., R.A. Schiffer, 1999: Advances in understanding clouds from ISCCP. *Bull. Amer. Meteor. Soc.,* **80**, 2261-2287.

[1]Rossow, W.B., G. Tselioudis, A. Polak, and C. Jakob, 2005: Tropical Climate Described as a Distribution of Weather States Indicated by Distinct Mesoscale Cloud Property Mixtures. *Geophys. Res. Lett.*, **32**, L21812, doi:10.1029/2005GL024584.

[1+8]Rossow, W.B., and Y.-C. Zhang, 2010: Evaluation of a statistical model of cloud vertical structure using combined CloudSat and CALIPSO cloud layer profiles. *J. Climate*, **23**, 6641-6653, doi:10.1175/2010JCLI3734.1.

Sassen, K., and B.S. Cho, 1992: Subvisual-thin cirrus lidar dataset for satellite verification and climatological research. *J. Appl. Meteor.*, **31**, 1275-1285.

Seemann, S.W., E.E. Borbas, R.O. Knuteson, G.R. Stephenson, and H.L. Huang, 2008: Development of a Global Infrared Land Surface Emissivity Database for Application to Clear Sky Sounding Retrievals from Multispectral Satellite Radiance Measurements. *J. Appl. Meteor. Clim.*, **47**, 108-123, DOI: 10.1175/2007JAMC1590.1.

[13]Sayer, A.M., C.A. Poulsen, C. Arnold, E. Campmany, S. Dean, G.B.L. Ewen, R.G. Grainger, B.N. Lawrence, R. Siddans, G.E. Thomas, and P.D. Watts, 2011: Global retrieval of ATSR cloud parameters and evaluation (GRAPE): dataset assessment. *Atmos. Chem. Phys.*, **11**, 3913-3936.

[4]Scott, N.A., A. Chédin, R. Armante, J. Francis, C.J. Stubenrauch, J.-P. Chaboureau, F. Chevallier, C. Claud, F. Chéruy, 1999: Characteristics of the TOVS Pathfinder Path-B Dataset. *Bull. Amer. Meteor. Soc.*, **80**, 2679-2701.

[10]Seze, G., C. Vanbauce, J.C. Burie, F. Parol, P. Couvert, 1999: Cloud cover observed simultaneously from POLDER and METEOSAT. *Physics and Chemistry of the Earth, Part B: Hydrology, Oceans and Atmosphere*, **24**, 921-926, ISSN 1464-1909, DOI: 10.1016/S1464-1909(99)00104-5.

[10]Sneep, M., J.F. de Haan, P. Stammes, P. Wang, C. Vanbauce, J. Joiner, A.P. Vasilkov, and P.F. Levelt, 2008: Three-way comparison between OMI and PARASOL cloud pressure products. *J. Geophys. Res.*, **113**, D15S23, doi:10.1029/2007JD008694.

Stamnes, K., S.C. Tsay W. Wiscombe, and K. Jayaweera, 1988: Numerically stable algorithm for discrete ordinate method radiative transfer in multiple scattering and emitting layered media. *Appl. Opt.*, **27**, 2502-2509.

Sherwood, S.C., J.-H. Chae, P. Minnis, and M. McGill, 2004: Underestimation of deep convective cloud tops by thermal imagery. *Geophys. Res. Lett.*, **31**, L11102, doi:10.1029/2004GL019699.

Stephens, G.L., D.G. Vane, et al., and CloudSat Science team, 2002: The CLOUDSAT mission and the A-Train. *Bull. Amer. Meteor. Soc.*, **83**, 1771-1790.

[4+1]Stubenrauch, C.J., W.B. Rossow, F. Chéruy, N.A. Scott, A. Chédin, 1999a: Clouds as seen by Infrared Sounders (3I) and Imagers (ISCCP): Part I) Evaluation of cloud parameters. *J. Climate*, **12**, 2189-2213.

[4+1]Stubenrauch, C.J., W.B. Rossow, N.A. Scott, A. Chédin, 1999b: Clouds as seen by Infrared Sounders (3I) and Imagers (ISCCP): Part III) Combining 3I Cloud Parameters and ISCCP for better understanding of Cloud Radiative Effects. *J. Climate*, **12**, 3419-3442.

[4+1]Stubenrauch, C.J., A. Chédin, R. Armante, N.A. Scott, 1999c: Clouds as seen by Infrared Sounders (3I) and Imagers (ISCCP): Part II) A New Approach for Cloud Parameter Determination in the 3I Algorithms. *J. Climate*, **12**, 2214-2223.

[4]Stubenrauch, C.J., F. Eddounia, and G. Rädel, 2004: Correlations between microphysical properties of large-scale semi-transparent cirrus and the state of the atmosphere. *Atmos. Res.*, **72**, 403-423.

[4]Stubenrauch, C.J., F. Eddounia, and L. Sauvage, 2005: Cloud heights from TOVS Path-B: Evaluation using LITE observations and distributions of highest cloud layers. *J. Geophys. Res.*, **110**, D19203,doi:10.1029/2004JD005447.

[4+1]Stubenrauch, C.J., A. Chédin, G. Rädel, N.A. Scott, S. Serrar, 2006: Cloud properties and their seasonal and diurnal variability from TOVS Path-B. *J. Climate*, **19**, 5531-5553.

[5+1+8]Stubenrauch, C.J., S. Cros, N. Lamquin, R. Armante, A. Chédin, C. Crevoisier, and N.A. Scott, 2008: Cloud properties from AIRS and evaluation with CALIPSO. *J. Geophys. Res.*, **113**, D00A10, doi:10.1029/2008JD009928.

[5+4+8]Stubenrauch. C.J., S. Cros. A. Guignard, and N. Lamquin, 2010: A six-year global cloud climatology from the Atmospheric InfraRed Sounder aboard the AQUA Satellite: statistical analysis in synergy with CALIPSO and CloudSat. *Atmos. Chem. Phys.*, **10**, 7197-7214.

Susskind, J., P. Piraino, L. Rokke, L. Iredell, A. Mehta, 1997: Characteristics of the TOVS Pathfinder Path A Dataset. *Bull. Amer. Meteor. Soc.,* **78**, 1449-1472.

Susskind, J., C. Barnet, and J. Blaisdell, 2003: Retrieval of atmospheric and surface parameters from AIRS/AMSU/HSB data in the presence of clouds. *IEEE Trans. Geosci. Remote Sens.*, 41, 390-409.

[8]Thorsen, T.J., Q. Fu, and J.M. Comstock, 2011: Comparison of the CALIPSO satellite and ground-based observations of cirrus clouds at the ARM TWP sites. *J. Geophys. Res.*, **116**, D21203, doi:10.1029/2011JD015970.

Tobin, D.C., H.E. Revercomb, R.O. Knuteson, B.M. Lesht, L.L. Strow, S.E. Hannon, W.F. Feltz, L.A. Moy, E.J. Fetzer, and T.S. Cress, 2006: Atmospheric Radiation Measurement site atmospheric state best estimates for Atmmospheric Infrared Sounder temperature and water vapour retrieval validation. *J. Geophys. Res.*, **111**, D09S14, doi:10.1029/2005JD006103.

[10]Vanbauce, C., J.-C. Buriez, F. Parol, B. Bonnel, G. Sèze and P. Couvert, 1998: Apparent pressure derived from ADEOS-POLDER observations in the Oxygen A-band over ocean. *Geophy. Res. Lett.*, **25**, 3159-3162.

[10]Vanbauce, C., B. Cadet, R.T. Marchand, 2003: Comparison of POLDER apparent and corrected oxygen pressure to ARM/MMCR cloud boundary pressures. *Geophys. Res. Lett.*, **30**-5,16.1 - 16.4

[8]Vaughan, M., K. Powell, R. Kuehn, S. Young, D. Winker, C. Hostetler, W. Hunt, Z. Liu, M. McGill, B. Getzewich, 2009: Fully Automated Detection of Cloud and Aerosol Layers in the CALIPSO Lidar Measurements. *J. Atmos. Oceanic Techn.*, **26**, 2034–2050, doi: 10.1175/2009JTECHA1228.1.

[10]Viollier, M., C. Standfuss, F. Parol, 2002: Monthly means of reflected solar flux from POLDER(ADEOS-1) and comparison with ERBE, ScaRaB and CERES. *Geophys. Res. Lett.*, **29**, 141-1-4.

Waliser, D., F. Li, C. Woods, R. Austin, J. Bacmeister, J. Chern, A. DelGenio, J. Jiang, Z. Kuang, H. Meng, P. Minnis, S. Platnick, W.B. Rossow, G. Stephens, S. Sun-Mack, W.K. Tao, A. Tompkins, D. Vane, C. Walker, and D. Wu, 2008: Cloud ice: A climate model challenge with signs and expectations of progress. *J. Geophys. Res.*

[2]Walther, A., A. Heidinger, and W. Straka, 2010: DCOMP GOES-ABI, AlgorithmTheoretical Basis Document.

[2]Walther, A., A. Heidinger, and M. Foster, 2012: Implementation of the Daytime Cloud Optical and Microphysical Properties Algorithm (DCOMP) in PATMOS-x. *J. Appl. Meteor. Clim.,* **51**, 1371-1390.

Wang, J., W.B. Rossow, 1995: Determination of cloud vertical structure from upper air observations. *J. Appl. Meteor.,* **34**, 2243-2258.

Wang, J., W.B. Rossow, T. Uttal, and M. Rozendaal, 1999: Variability of cloud vertical structure during ASTEX from a combination of rawinsonde, radar, ceilometer and satellite data. *Mon. Wea. Rev.*, **127**, 2484-2502.

Wang, J., W.B. Rossow, and Y. Zhang, 2000: Cloud Vertical Structure and its Variations from a 20-Yr Global Rawinsonde Dataset. *J. Climate*, **13**, 3041-3056.

[12]Wang, P.-H., M.P. McCormick, L.R. Poole, W.P. Chu, G.K. Yue, G.S. Kent, and K.M. Skeens, 1994: Tropical high cloud characteristics derived from SAGE II extinction measurements. *Atmos. Res.*, **34**, 53-83.

[12]Wang, P.-H., P. Minnis, M.P. McCormick, G.S. Kent, and K.M. Skeens, 1996: A 6-Year Climatology of Cloud Occurrence Frequency from Stratospheric Aerosol and Gas Experiment II Observations (1985-1990). *J. Geophys. Res.*, **101**, 29407-29429.

[12]Wang, P.-H., D. Rind, C.R. Trepte, G.S. Kent, G.K. Yue, and K.M. Skeens, 1998: An empirical model study of the tropospheric meridional circulation based on SAGE II observations. *J. Geophys. Res.*, **103**, 13801-13818.

[12]Wang, P.-H., R.E. Veiga, L.B. Vann, P. Minnis, and G.S. Kent, 2001: A further study of the method for estimation of SAGE II opaque cloud occurrence. *J. Geophys. Res.*, **106**, 12603-12613.

[12]Wang, P.-H., P. Minnis, B.A. Wielicki, T. Wong, and L.B. Vann, 2002: Satellite observations of long-term changes in tropical cloud and outgoing longwave radiation from 1985 to 1998. *Geophys. Res. Lett.*, **29**, doi:01.1029/2001GL014264.

[10]Waquet, F., J. Riedi, L. C-Labonnote, P. Goloub, B. Cairns, J.-L. Deuzé, and D. Tanré, 2009: Aerosol remote sensing over clouds using the A-Train observations. *J. Atmos. Sci.*, doi: 10.1175/2009JAS3026.1

Warren, S.G., C.J. Hahn, J. London, R.M. Chervin, and R.L. Jenne, 1986: Global Distribution of Total Cloud Cover and Cloud Type Amounts over Land. *NCAR Technical Note TN-273+STR*, Boulder, CO,

29 pp. + 200 maps (also DOE/ER/60085-H1). Available from Carbon Dioxide Information Analysis Center, Oak Ridge, Tennessee.

Warren, S.G., C.J. Hahn, J. London, R.M. Chervin, and R.L. Jenne, 1988: Global Distribution of Total Cloud Cover and Cloud Type Amounts over the Ocean. *NCAR Technical Note TN-317+STR*, Boulder, CO, 42 pp. + 170 maps (also DOE/ER-0406). Available from Carbon Dioxide Information Analysis Center, Oak Ridge, Tennessee.

Warren, S.G., R. Eastman, and C. Hahn, 2007: A Survey of Changes in Cloud Cover and Cloud Types over Land from Surface Observations, 1971-96. *J. Climate*, **20**, 717-738.

[10]Weidle F., and J. Wernli, 2008: Comparison of ERA40 cloud top phase with POLDER-1 observations. *J. Geophys Res*, **113**, D05209.

Wielicki, B.A., and L. Parker, 1992: On the determination of cloud cover from satellite sensors: The effect of sensor spatial resolution. *J. Geophys. Res.,* **97**, 12799-12823.

Wielicki, B.A., B.R. Barkstrom, B.A Baum, T.P. Charlock, R.N. Green, D.P. Kratz, R.B. Lee, P. Minnis, G.L. Smith, D.F. Young, R.D. Cess, J.A. Coakley, D.A.H. Crommelynck, L. Donner, R. Kandel, M. D. King, A.J. Miller, V. Ramanathan, D.A. Randall, L.L. Stowe, and R.M. Welch, 1998: Clouds and the Earth's Radiant Energy System (CERES): Algorithm Overview. *IEEE Trans. Geosci. and Rem. Sens.*, **36**, 1127-1141.

[8]Winker, D.M., W.H. Hunt, and M.J. McGill, 2007: Initial performance assessment of CALIOP. *Geophys. Res. Lett.*, **34**, L19803, doi:10.1029/2007GL030135.

[8]Winker, D.M., M.A. Vaughan, A.H. Omar, Y. Hu, K.A. Powell, Z. Liu, W.H. Hunt, and S.A. Young, 2009: Overview of the CALIPSO Mission and CALIOP Data Processing Algorithms. *J. Atmos. Oceanic Techn.*, **26**, 2310–2323, doi:10.1175/2009JTECHA1281.1.

[2]Wood, R., and D.L. Hartmann, 2006: Spatial variability of liquid water path in marine low cloud: The importance of mesoscale cellular convection. *J Climate*, **19,** 1748-1764.

Woodruff, S.D., R.J. Slutz, R.L. Jenne, and P.M. Steurer, 1987: A comprehensive ocean-atmosphere data set. *Bull. Amer. Meteor. Soc.*, **68**, 1239-1250.

Woodruff, S.D., S.J. Lubker, and M.Y. Liu, 1992: Updating COADS -- problems and opportunities. *Proceedings of the International COADS Workshop* (H.F. Diaz, K. Wolter, and S.D. Woodruff, Eds.), NOAA/ERL, Boulder, CO, 19-36.

World Meteorological Organization, 1956: *International Cloud Atlas*. 62 pp. + 72 plates. WMO, Geneva.

World Meteorological Organization, 1974: *Manual on Codes, Vol. 1,* WMO Publ. No. 306, WMO, Geneva.

Worley, S.J., S.D. Woodruff, R.W. Reynolds, S.J. Lubker, and N. Lott, 2005: ICOADS Release 2.1 data and products. *Int. J. Climatol.*, **25**, 823-842.

[3]Wylie, D.P., and W.P. Menzel, 1989: Two years of cloud cover statistics using VAS. *J. Climate*, **2**, 380-392.

[3]Wylie, D.P., W.P. Menzel, H.M. Woolf, K.I. Strabala, 1994: Four years of global cirrus cloud statistics using HIRS. *J. Climate*, **7**, 1972-1986.

[3]Wylie, D.P., and P.-H. Wang, 1997: Comparison of cloud frequency data from the high-resolution infrared radiometer sounder and the Stratospheric Aerosol and Gas Experiment II. *J. Geophys. Res.*, **102**, 29893-29900.

[3]Wylie, D.P., and W.P. Menzel, 1999: Eight Years of High Cloud Statistics using HIRS. *J. Climate*, **12**, 170-184.

[3]Wylie, D.P., D.L. Jackson, W.P. Menzel, and J.J. Bates, 2005: Trends in Global Cloud Cover in two Decades of HIRS Observations. *J. Climate* **18**, 3021-3031.

[3]Wylie, D.P., E. Eloranta, J.D. Spinhirne, and S.P. Palm, 2007: A comparison of cloud cover statistics from the GLAS lidar with HIRS. *J. Climate*, **20**, 4968-4981.

[7]Yang, P., G.W. Kattawar, G. Hong, P. Minnis, and Y.X. Hu, 2008: Uncertainties associated with the surface texture of ice particles in satellite-based retrieval of cirrus clouds: Part II. Effect of particle surface roughness on retrieved cloud optical thickness and effective particle size. *IEEE Trans. Geosci. Remote Sens.*, **46**, 1948-1957, doi:10.1109/TGRS.2008.916472.

[11]Yang, Y., L. Di Girolamo, and D. Mazzoni, 2007: Selection of the automated thresholding algorithm for the Multi-angle Imaging SpectroRadiometer Camera-by-camera Cloud Mask over land. *Remote Sens. Environ.,* **107**, 159-171.

[8]Yorks, J., D. Hlavka, M. Vaughan, M. McGill, W. Hart, S. Rodier, and R. Kuehn, 2011: Airborne Validation of Cirrus Cloud Properties Derived from CALIPSO Lidar Measurements, Part I: Spatial Properties. *J. Geophys. Res.*, **116**, D19207, doi:10.1029/2011JD015942.

Young, D.F., P. Minnis, D. Baumgardner, and H. Gerber, 1998: Comparison of in situ and satellite-derived cloud properties during SUCCESS. *Geophys. Res. Lett.*, **25**, 1125-1128.

[6+10]Zeng, S., F. Parol, J. Riedi, C. Cornet, and F. Thieuleux, 2011: Examination of POLDER/PARASOL and MODIS/Aqua Cloud Fractions and Properties Representativeness. *J. Climate*, **24**, 4435-4450.

[6+10]Zeng S., C. Cornet, F. Parol, J. Riedi, and F. Thieuleux, 2012: A better understanding of cloud optical thickness derived from the passive sensors MODIS/AQUA and POLDER/PARASOL in the A-Train constellation. *Atmos. Chem. Phys. Discuss.*, **12**, 11733-11764.

Zhang, M.H., W.Y. Lin, S.A. Klein, J.T. Bacmeister, S. Bony, R.T. Cederwall, A.D. Del Genio, J.J. Hack, N.G. Loeb, U. Lohmann, P. Minnis, I. Musat, R. Pincus, P. Stier, M.J. Suarez, M.J. Webb, J.B. Wu, S.C. Xie, M.-S. Yao, and J.H. Zhang, 2005: Comparing clouds and their seasonal variations in 10 atmospheric general circulation models with satellite measurements. *J. Geophys. Res.*, D15, doi:10.1029/2004JD005021.

[1]Zhang, Y., W.B. Rossow, A.A. Lacis, V. Oinas, and M.I. Mishchenko, 2004: Calculation of radiative fluxes from the surface to top of atmosphere based on ISCCP and other global data sets: Refinements of the radiative transfer model and the input data. *J. Geophys. Res.*, **109**, D19105, doi:10.1029/2003JD004457.

[6+10]Zhang, Z., P. Yang, G. Kattawar, J. Riedi, L.C. Labonnote, B. Baum, S. Platnick, and H.-L. Huang , 2009: Influence of ice particle model on satellite ice cloud retrieval: lessons learned from MODIS and POLDER cloud product comparison. *Atmos. Chem. Phys.*, **9**, 7115-7129.

[11]Zhao, G., and L. Di Girolamo, 2004: A cloud fraction versus view angle technique for automatic in-scene evaluation of the MISR cloud mask. *J. Appl. Meteorol*, **43**, 860-869.

[11]Zhao, G., and L. Di Girolamo, 2006: Cloud fraction errors for trade wind cumuli from EOS-TERRA instruments. *Geophys. Res. Lett*., **33**, L20802, doi:10.1029/2006GL027088.

5. Cloud Assessment Group

Co-Chairs:

Claudia Stubenrauch	Laboratoire de Météorologie Dynamique/IPSL/CNRS	France
Stefan Kinne	Max Planck Institut for Meteorology	Germany

Former Co-Chairs:

Bryan Baum	NASA LaRC	USA
Garrett Campbell	CIRA/Colorado	USA

Participating Cloud Teams:

Steve Ackerman	University of Wisconsin/CIMSS	USA
Bryan Baum	NASA LaRC	USA
Gregory Cesana	Laboratoire de Météorologie Dynamique/IPSL/CNRS	France
Hélène Chepfer	Laboratoire de Météorologie Dynamique/IPSL/CNRS	France
Larry Di Girolamo	University of Illinois	USA
Brian Getzewich	SSAI/NASA	USA
Anthony Guignard	Laboratoire de Météorologie Dynamique/IPSL/CNRS	France
Andrew Heidinger	NOAA, Wisconsin	USA
Brent Maddux	University of Wisconsin/CIMSS	USA
Paul Menzel	NOAA, Wisconsin	USA
Patrick Minnis	NASA LaRC	USA
Eric Olson	University of Wisconsin/CIMSS	USA
Cindy Pearl	CREST, City College of New York	USA
Robert Pincus	University of Colorado	USA
Steven Platnick	NASA Goddard Space Flight Center	USA
Caroline Poulsen	Rutherford Appleton Laboratory	UK
Jérôme Riedi	Laboratoire d'Optique Atmosphérique CNRS	France
William B. Rossow	CREST, City College of New York	USA
Andrew Sayer	Oxford University	UK
Sunny Sun-Mack	SSAI/NASA	USA
Andi Walther	University of Wisconsin/CIMSS	USA
Dave Winker	NASA LaRC	USA
Don Wylie	Univeristy of Wisconsin/CIMSS	USA
Shan Zeng	Laboratoire d'Optique Atmopsphérique CNRS	France
Guangyu Zhao	University of Illinois	USA

Other Contributors:

Sylvain Cros	Laboratoire de Météorologie Dynamique/ IPSL/CNRS	France
Artem Feofilov	Laboratoire de Météorologie Dynamique/ IPSL/CNRS	France
Nicolas Lamquin	Laboratoire de Météorologie Dynamique/ IPSL/CNRS	France

Reviewers:

Carlos Jimenez	Lab. d'Etudes du Rayonnement et Matière en Astrophyqisue	France
Chris Kummerow	Cooperative Institute for Research in the Atmosphere, Colorado	USA
Ehrhard Raschke	University of Hamburg	Germany
Rob Roebeling	EUMETSAT	Germany

Workshop Participants:

2010 *(Berlin, Germany)*

Christopher Arnold	Oxford University	UK
Ralf Bennartz	University of Wisconsin	USA
Bojan Bojkov	European Space Agency, ESRIN	Italy
Robert Burgman	University of Miami	USA
Gregory Cesana	Laboratoire de Météorologie Dynamique/IPSL/CNRS	France
Seethala Chellappan	Max Planck Institut for Meteorology	Germany
Yan Chen	SSAI/NASA	USA
Helene Chepfer	Laboratoire de Météorologie Dynamique/IPSL/CNRS	France
Alexander Chernokulsky	Obukhov Institute of Atmospheric Physics RAS	Russia
Marjolaine Chiriaco	LATMOS	France
Hartwig Deneke	Leibniz-Inst. for Tropospheric Research	Germany
Abhay Devasthale	Swedish Meteorological and Hydrological Institute	Sweden
Larry Di Girolamo	University of Illinois	USA
Salomon Eliasson Luleå	University of Technology	Sweden
Daniel Fisher	Max Planck Institute for Chemistry	Germany
Juergen Fischer	FU Berlin, Institute for Space Science	Germany
Jan Fokke Meirink	KNMI (Royal Netherlands Meteorological Institute)	Netherlands
Michael Foster	University of Wisconsin - Madison	USA
Michael Grzegorski	Mullard Space Science Lab	UK
Anthony Guignard	Laboratoire de Météorologie Dynamique/IPSL/CNRS	France
Andrew Heidinger	NOAA	USA
Georg Heygster	University of Bremen, Institute of Environmental Physics	Germany
Laura Hinkelman	JISAO/University of Washington	USA
Rainer Hollmann	Deutscher Wetterdienst	Germany
Akos Horvath	Max Planck Institut for Meteorology	Germany
Toshiro Inoue	Atmosphere & Ocean Research Institute/Tokyo University	Japan
Karl-Göran Karlsson	SMHI	Sweden
Stefan Kinne	Max Planck Institut for Meteorology	Germany
Alexander Kokhanovsky	University of Bremen	Germany
Survarchal Kumar	Max Planck Institut for Meteorology	Germany
Luca Lelli	University of Bremen	Germany
Rasmus Lindstrot	Freie Universität Berlin	Germany
Maarit Lockhoff	Deutscher Wetterdienst	Germany
Ulrike Lohmann	ETH Zurich	Switzerland
Katrin Lonitz	Max Planck Institute for Meteorology	Germany
Elke Ludewig	Max Planck Institut for Meteorology	Germany
Brent Maddux	University of Wisconsin/CIMSS	USA
Hermann Mannstein	DLR	Germany
Jana Mendrok Luleå	University of Technology	Sweden
W. Paul Menzel	University of Wisconsin	USA
Jan-Peter Muller	Mullard Space Science Lab	UK
Christine Nam	Max Planck Institut for Meteorology	Germany
Akira Noda	JAMSTEC	Japan
Robert Pincus	University of Colorado	USA
Steven Platnick	NASA Goddard Space Flight Center	USA
Caroline Poulsen	Rutherford Appleton Laboratory	UK
Vincent Puygrenier	CNRM-GAME	France
Johannes Quaas	Max Planck Institute for Meteorology	Germany
Ehrhard Raschke	University of Hamburg	Germany
Thomas Reichler	University of Utah	USA
Jérôme Riedi	Laboratoire d'Optique Atmosphérique CNRS	France
Rob Roebeling	KNMI	Netherlands

William B. Rossow	City College of New York	USA
Irina Sandu	Max Planck Institut for Meteorology	Germany
Byung Ju Sohn	Seoul National University	South Korea
Piet Stammes	KNMI	Netherlands
Bjorn Stevens	Max Planck Institut for Meteorology	Germany
Claudia Stubenrauch	Laboratoire de Météorologie Dynamique/IPSL/CNRS	France
Sunny (Szedung) Sun-Mack	SSAI/NASA	USA
Anke Thoss	SMHI	Sweden
Andi Walther	University of Wisconsin/CIMSS	USA
Dave Winker	NASA LaRC	USA
Qiuqing Zhang	University of Utah	USA
Shan Zeng	Laboratoire d'Optique Atmopsphérique CNRS	France

2008 (New York, USA)

Steve Ackerman	University of Wisconsin/CIMSS	USA
Howard Barker	Met Canada	Canada
Eugene Clothiaux	Penn State University	USA
Jason Cole	University Toronto	Canada
Roger Davies	University Auckland	New Zealand
Tony DelGenio	NASA GISS	USA
Abhay Devasthale	SMHI	Sweden
Larry DiGirolamo	University of Illinois	USA
Andy Heidinger	NOAA, Wisconsin	USA
Laura Hinkelman	University of Washington	USA
Bob Holz	University of Wisconsin/CIMSS	USA
Toshi Inoue	JMA	Japan
Brian Kahn	NASA-JPL	USA
Stan Kidder	CIRA, Colorado	USA
Stefan Kinne	MPI, Hamburg	Germany
Maarit Lockhoff	DWD	Germany
Johnny Luo	CUNY	USA
Jay Mace	University of Utah	USA
Andreas Macke	IFM-Kiel	Germany
Brent Maddux	University of Wisconsin/CIMSS	USA
Jan Fokke Meirink	KNMI	Netherlands
Pat Minnis	NASA LaRC	USA
Chris O'Dell	Colorado State	USA
Mike Pavolonis	NOAA Wisconsin	USA
Steven Platnick	NASA-GSFC	USA
Caroline Poulsen	Rutherford Lab	UK
Ehrhard Raschke	Uni Hamburg	Germany
Jerome Riedi	LOA, Lille	France
Bill Rossow	NASA GISS	USA
Ken Sassen	U. Fairbanks	USA
Genevieve Seze	LMD	France
Claudia Stubenrauch	LMD	France
Andi Walther	SSEC Wisconsin	USA
Zhien Wang	University Wyoming	USA
Dave Winker	NASA LaRC	USA
Don Wylie	University of Wisconsin/CIMSS	USA

2006 (Madison, Wisconsin, USA)

Steve Ackerman	University of Wisconsin/CIMSS	USA
Bruce Barkstrom	NOAA NCDC	USA

John Bates	NOAA NCDC	USA
Bryan Baum	NASA LaRC	USA
Ralf Bennartz	University of Wisconsin/AOS	USA
Eugene Clothiaux	Penn State University	USA
Roger Davies	University of Auckland	New Zealand
Hartwig Deneke	Royal Netherlands Meteorological Institute	Netherlands
Larry DiGirolamo	University of Illinois	USA
Ryan Eastman	University of Washington	USA
Amato Evan	University of Wisconsin/CIMSS	USA
Richard Frey	University of Wisconsin/CIMSS	USA
Iliana Genkova	NOAA/NESDIS	USA
Liam Gumley	University of Wisconsin/CIMSS	USA
Tadahiro Hayasaka	Research Institute for Humanity and Nature	Japan
Andy Heidinger	NOAA/NESDIS	USA
Bob Holz	University of Wisconsin/CIMSS	USA
Toshi Inoue	JMA	Japan
J. Adam Kankiewicz	CIRA	USA
Karl-Göran Karlsson	SMHI	Sweden
Seiji Kato	NASA LaRC	USA
Jeff Key	NOAA/NESDIS	USA
Stefan Kinne	MPI	Germany
Yinghui Liu	University of Wisconsin/CIMSS	USA
Jay Mace	University of Utah	USA
Andreas Macke	IFM-GEOMAR	Germany
Brent Maddux	University of Wisconsin/CIMSS	USA
Paul Menzel	NOAA	USA
Pat Minnis	NASA LaRC	USA
Gyula Molnar	University of Maryland	USA
Takashi Nakajima	Tokai University	USA
Shaima Nasiri	Texas A&M	USA
Joel Norris	Scripps Institution of Oceanography	USA
Chris O'Dell	University of Wisconsin/AOS	USA
Michael Pavolonis	NOAA/NESDIS	USA
Rene Preusker	Institute for Space Sciences, Free University of Berlin	Germany
Rob Roebeling	KNMI	Netherlands
Donald Reinke	CIRA	USA
Bill Rossow	NASA GISS	USA
Graeme Stephens	Colorado State University	USA
Claudia Stubenrauch	LMD, Ecole Polytechnique	France
Joel Susskind	NASA GSFC	USA
Dave Tobin	University of Wisconsin/CIMSS	USA
Yoko Tsushima		Japan
Dave Turner	University of Wisconsin/CIMSS	USA
Taneil Uttal	NOAA	USA
Pi-Huan Wang	NASA LaRC	USA
Xuanji Wang	University of Wisconsin/CIMSS	USA
Steve Warren	University of Washington	USA
Don Wylie	CIMSS, University of Wisconsin	USA
Ping Yang	Texas A&M University	USA
Yuekui Yang	University of Illinois	USA
Guangyu Zhao	University of Illinois	USA

ACKNOWLEDGMENTS

6. Acronyms

AIRS	Atmospheric Infrared Sounder
AMSR-E	Advanced Microwave Sounding Radiometer-EOS
AMSU	Advanced Microwave Sounding Unit
ATSR	Along Track Scanning Radiometer
BRF	bidirectional reflectance factor
CA	Cloud Amount
CAE	effective Cloud Amount
CAH	highlevel Cloud Amount
CAHR	relative highlevel Cloud Amount
CAI	ice Cloud Amount
CAL	low-level Cloud Amount
CALR	relative low-level Cloud Amount
CAM	midlevel Cloud Amount
CAMR	relative midlevel Cloud Amount
CAW	liquid Cloud Amount
CEM	Cloud emissivity
COD	Cloud Optical Depth
CP	Cloud Pressure
CRE	Cloud effective radius
CT	Cloud Temperature
CWP	Cloud Water Path
CZ	Cloud Altitude
CALIPSO	Cloud Aerosol Lidar and Infrared Pathfinder Satellite Observations
CCI	Climate Change Initiative
CNES	Centre National d'Etudes Spatiales
CNRS	Centre National de la Recherche Scientifique
COADS	Comprehensive Ocean-Atmosphere Data Set
CREW	Cloud Retrieval Evaluation Workshop
ECMWF	European Centre for Medium-Range Weather Forecasts
ECV	Essential Climate Variable
ENSO	El Niño Southern Oscillation
EOS	Earth Observation System
ERBS	Earth Radiation Budget Satellite
ERS	European Remote sensing Satellite
ESA	European Space Agency
EUMETSAT	European Organisation for the Exploitation of Meteorological Satellites
FCDR	Fundamental Climate Data Record
GCM	General Circulation Model
GEWEX	Global Energy and Water Cycle Experiment
GEOS	Goddard Earth Observing System Model
GMAO	Global Modeling and Assimilation Office
HIRS	High resolution Infrared Radiation Sounder
IASI	Infrared Atmospheric Sounding Interferometer
IIR	Imageur Infrarouge
IPCC	Intergovernmental Panel on Climate Change
IPSL	Institut Pierre Simon Laplace
ISCCP	International Satellite Cloud Climatology Project
ITCZ	InterTropicsl Convergence Zone
LT	local time
LUT	Look Up Table
MISR	Multi-angle Imaging SpectroRadiometer

MODIS	MODerate resolution Imaging Spectroradiometer
MSU	Microwave Sounding Unit
NASA	National Aeronautics and Space Administration
NCAR	National Center for Atmospheric Research
NCEP	National Centers for Environmental Prediction
NESDIS	National Environmental Satellite, Data, and Information Service
NH	Northern Hemisphere
NOAA	National Oceanic and Atmospheric Administration
POLDER	POLarization and Directionality of the Earth's Reflectances
SAGE	Stratospheric Aerosol Gas Experiment
SCF	Southern Great Plains Central Facility
SH	Southern Hemisphere
SSM/I	Special Sensor Microwave Imager
TOVS	TIROS-N Operational Vertical Sounder
WCRP	World Climate Research Programme